SOLID-STATE NUCLEAR MAGNETIC RESONANCE STUDIES OF THE STRUCTURES, MEMBRANE LOCATIONS, CHOLESTEROL CONTACT, AND MEMBRANE MOTIONS OF MEMBRANE-ASSOCIATED HIV FUSION PEPTIDE (HFP)

By

Lihui Jia

A DISSERTATION

Submitted to
Michigan State University
in partial fulfillment of the requirements
for the degree of

Chemistry—Doctor of Philosophy

2017

ABSTRACT

SOLID-STATE NUCLEAR MAGNETIC RESONANCE STUDIES OF THE STRUCTURES, MEMBRANE LOCATIONS, CHOLESTEROL CONTACT, AND MEMBRANE MOTIONS OF MEMBRANE-ASSOCIATED HIV FUSION PEPTIDE (HFP)

By

Lihui Jia

Membrane fusion is the key step during HIV viral entry to cells, and the process is catalyzed by HIV membrane fusion protein gp41. HFP is the ~25-residue N-terminal domain of gp41 and is required for membrane fusion with significant decreases in fusion activity with point mutations. Both viral and host cell membrane contain ~30mol % cholesterol (CHOL), and HFP induced fusion is faster in membrane with CHOL. However, how HFP interacts with membrane lipids and CHOL is unknown. In this thesis, we used the newly developed ^{13}C-^{2}H Rotational Echo Double Resonance (REDOR) solid-state NMR method to study the membrane location of HFP in chemically-native membrane environment.

HFP is ^{13}CO labeled at specific residue, and the membrane is deuterated at specific regions of the membrane using selective regions deuterated phosphatidylcholine (PC) and CHOL. We study HFP wild type, HFP_V2E and L9R mutants because these two mutants eliminate and decrease fusion respectively. HFP is predominantly β sheet structure in bilayer membrane for both HFP wild type and HFP_V2E mutant, HFP_L9R has a different structure and is likely helical. Both HFP and HFP_V2E mutant have major deeply-inserted membrane location contacting membrane center and minor shallowly-inserted membrane location contacting half way of one membrane leaflet. The HFP_V2E mutant has bigger fraction of molecules with shallower membrane location, which is consistent with the strong correlation between membrane location insertion depth and the peptide fusogenicity. HFP_L9R mutant has majorly deeply inserted into membrane.

By comparing the HFP- PC and HFP- CHOL contact, there is preferential contact between HFP and CHOL vs PC at several residues including G5, G10 and G16. The free energy difference for contacting PC vs CHOL is ~ 0.57(5) kcal.mol^{-1} for T= 300K. HFP- CHOL contact geometry is successfully modeled by Swiss Dock and YASARA energy minimization with two strands antiparallel HFP (1→16/16→1 registry). There are two energetically favorable binding models between HFP and CHOL, from docking, energy minimization and consistency with REDOR results. The contact models reveal tilted and curved-up tail orientation of Chol_d7. Fusion may be catalyzed by matching the curvature of lipids contacting HFPs with the membrane curvature during the fusion intermediates like the stalk.

Membrane motion perturbation by HFP is studied by static deuterium NMR from deuterium powder pattern spectrum, order parameter profile and T_2 relaxation time. The DMPC-d54 spectrum becomes ~10% narrower in membrane without CHOL with 4% HFP and in membrane with 33% CHOL with 1% HFP. Accordingly, the order parameter of lipid acyl chain becomes ~ 1-10% disordered by HFP. However, the spectrum becomes 20% broader in membrane with 33% CHOL with 4% HFP, and the order parameter of lipid acyl chain becomes ~ 20- 30% ordered by HFP. With HFP at 37 °C, DMPC-d54 T_2 decreases ~ 70 %, and the CHOL T_2 decreases ~ 30%. T_2 reduction is probably associated with increased membrane curvature induced by HFP. With greater membrane curvature, the C-D bond will experience more orientation diversity relative to the external magnetic field. Thus, the quadrupolar field will have greater change, leading to faster relaxation and shorter T_2.

Gp41_V2E mutant eliminates cell-cell fusion. Our CD spectroscopy studies show that the FPHM_V2E mutant is helical and the melting temperature is above 90 °C in 10mM Tris buffer + 0.2 % SDS at pH 7.4. Protein is trimer and induces no lipid mixing in PC: CHOL= 2:1 vesicles.

Dedicated to Xinliang Ding and Joshua J. Ding

ACKNOWLEDGEMENTS

First of all, I would like to thank my PhD advisor, Dr. David P. Weliky for his tremendous guidance, patience and encouragement through my graduate life. Dr. Weliky has been very nice and always supportive when I have questions and concerns. He always encourages me to ask questions and teaches me to solve problems and become a scientist. I am very grateful for his support and help.

I would like to acknowledge my committee members, Prof. John L. McCracken, Prof. A. Daniel Jones and Prof. Benjamin G. Levine for their time, generous help and guidance through my PhD life, which is very valuable for my research and development to a scientist. Prof. A. Daniel Jones has also provided valuable suggestions to the peptide and protein purification and characterization in my research. He also gives me helpful suggestions for my interview preparations and future career development. I really appreciate that.

I would like to acknowledge MSU Mass Spectrometry Facility, Max. T. Rogers NMR Facility for their assistance to my research. I thank Dr. Daniel Holmes and Dr. Li Xie for trouble shooting the NMR instruments and willingness to devote time and effort to help.

I am also very grateful for the help and support from all the Dr. Weliky group members, Dr. Charles Gabrys, Dr. Li Xie, Dr. Ujjayini Ghosh, Dr. Punsisi Ratnayake, Dr. Koyeli banerjee, Shuang Liang, Robert Wolfe and Ahinsa Ranaweera. They have been very helpful in my research, and very friendly in many other aspects.

At the end, I would like to thank all my friends for their support and best wishes. I thank my family for their encouragement and unconditional love.

TABLE OF CONTENTS

LIST OF TABLES

LIST OF FIGURES

KEY TO ABBREVIATIONS

AIDS: acquired immunodeficiency syndrome

CD: circular dichroism

CHR: C-terminal heptad repeat region

CHOL: cholesterol

Chol-d6: cholesterol-2,2,3,4,4,6-d6

Chol-d7: cholesterol-25,26,26,26,27,27,27-d7

CP: Cross polarization

CSA: chemical shift anisotropy

DMPC: 1,2-dipalmitoyl-*sn*-glycerol-3-phosphocholine

DMPC-d54: 1,2-dimyristoyl-d54-sn-glycero-3-phosphocholine

DMPG: 1,2-dipalmitoyl-*sn*-glycero-3-phospho-(1'-*rac*-glycerol) (sodium salt)

DOPC: 1,2-dioleoyl-*sn*-glycero-3-phosphocholine

DOPG: 1,2-dioleoyl-*sn*-glycero-3-phospho-(1'-*rac*-glycerol) (sodium salt)

DPC: dodecylphosphocholine

DPPC: 1,2-dipalmitoyl-*sn*-glycero-3-phosphocholine

DPPG: 1,2-dipalmitoyl-*sn*-glycero-3-phospho-(1'-*rac*-glycerol) (sodium salt)

DTPG: dipalmitoylphosphatidylglycerol

Endo: endo-domain

FACTS: fast analytical continuum treatment of solvation

FID: free induction decay

FMOC: 9-Fluorenylmethoxycarbonyl

FP: fusion peptide

FPPR: fusion peptide proximal region

FT: Fourier Transform

FWHM: full width at half maximum

HEPES: 2-(4-(2-hydroxyethyl)piperazin-1-yl) ethanesulfonic acid

HFP: HIV fusion peptide

HIV: Human immunodeficiency virus

HPLC: high pressure liquid chromatography

MALDI-TOF: matrix-assisted laser desorption ionization- time of flight

MAS: Magic angle spinning

MES: 2-(N-morpholino) ethanesulfonic acid

MPER: membrane-proximal external region

N-NBD-PE: N-(7-nitro-2, 1, 3-benzoxadiazol-4-yl) (ammonium salt)
dipalmitoylphosphatidylethanolamine

N-Rh-PE: N-(lissamine rhodamine B sulfonyl) (ammonium salt)
dipalmitoylphosphatidylethanolamine

NHR: N-terminal heptad repeat region

na: natural abundance

NMR: nuclear magnetic resonance

PC: phosphatidylcholine

PC-d4: 1,2-(dipalmitoyl-2,2,2,2-d4)-*sn*-glycero-3-phosphocholine

PC-d8: 1,2-(dipalmitoyl-7,7,7,7,8,8,8,8-d8)-*sn*-glycero-3-phosphocholine

PC-d10: 1,2-(dipalmitoyl-15,15,15,15,16,16,16,16,16,16-d10)-*sn*-glycero-3-phosphocholine

PG: phosphatidylglycerol

PHI: pre-hairpin intermediate

POPC: 1-palmitoyl-2-oleoyl-*sn*-glycero-3-phosphocholine

POPG: 1-palmitoyl-2-oleoyl-*sn*-glycero-3- phospho-(1'-*rac*-glycerol) (sodium salt)

QCC: quadrupolar coupling constant

QUECHO: quadrupolar echo

REDOR: Rotational echo double resonance

RMSD: root mean square deviation

SDS: sodium dodecyl sulfate

SHB: six helical bundles

SPPS: solid phase peptide synthesis

ssNMR: solid state nuclear magnetic resonance

TFA: trifluoroacetic acid

TM: transmembrane domain

TPPM: tow-pulse phase modulated

Tris: (hydroxymethyl)aminomethane

Chapter 1 - Introduction

1.1 NMR Introduction

NMR spectroscopy bases on the properties of nuclear spin, and studies the nuclei with spin quantum number $I \neq 0$. The nucleus involves in multiple types of electric and magnetic field interactions and each interaction type has its corresponding Hamiltonians.[1] The total Hamiltonian expression is:

$$\hat{H}_t = \hat{H}_{ext} + \hat{H}_{int} = \left(\hat{H}_Z + \hat{H}_{RF}\right) + \left(\hat{H}_{CS} + \hat{H}_J + \hat{H}_D + \hat{H}_Q\right) \quad 1.1$$

Where $\hat{H}_{ext}$ is the Hamiltonian for the interaction between the nuclear spin and the external magnetic field, including $\hat{H}_Z$ and $\hat{H}_{RF}$, which corresponds to the static magnetic field $\mathbf{B_0}$ and the radio frequency (r.f.) field $\mathbf{B_1}$ respectively;

$\hat{H}_{int}$ is the Hamiltonian for the interaction between the nuclear spin and the intrinsic field within the sample including:

$\hat{H}_{CS}$ is chemical shift interaction between the nuclear spin and the chemical shift field (electronic shielding field) induced by $\mathbf{B_0}$;

$\hat{H}_J$ is J coupling interaction or spin-spin coupling within one molecule;

$\hat{H}_D$ is the direct dipolar coupling interaction between two nuclear spins;

$\hat{H}_Q$ is quadrupole interaction between the nucleus ($I \geq 1$) quadrupole moment and surrounding electric filed gradient.

In the dissertation a vector is displayed in bold letters, the quantum mechanical operators are shown with "^" above the letters and the vector-operators are shown in bold letters with "^" above them.

1.1.1 Zeeman interaction

The interaction between the nuclear spin and the external static magnetic field ($\mathbf{B_0}$) is Zeeman interaction and the Hamiltonian is:

$$\hat{H}_Z = -\hat{\boldsymbol{\mu}} \cdot \mathbf{B_0} \qquad 1.2$$

Where $\hat{\boldsymbol{\mu}}$ is the nuclear magnetic moment operator, and it is related to nuclear spin operator $\hat{\mathbf{I}}$ as

$$\hat{\boldsymbol{\mu}} = \gamma\hbar\hat{\mathbf{I}} \qquad 1.3$$

Where γ is the gyromagnetic ratio; and $\hbar$ is the reduced Plank's constant. Then,

$$\hat{H}_Z = -\hat{\boldsymbol{\mu}} \cdot \mathbf{B_0} = -\gamma\hbar\hat{\mathbf{I}} \cdot \mathbf{B_0} = -\gamma\hbar\left(\hat{I}_x\mathbf{i} + \hat{I}_y\mathbf{j} + \hat{I}_z\mathbf{k}\right) \cdot B_0 \cdot \mathbf{k} = -\gamma\hbar\hat{I}_z B_0 \qquad 1.4$$

Where **i**, **j** and **k** is the x, y and z direction's unit vector respectively.

For a spin I nucleus, it has 2I+1 energy states in B_0 field and each state has Eigen function as Ψ_{Im} or written as |I, m>. The m is the magnetic spin quantum number, and has the value of −I, −I+1, ….., I−1, and I. $\hat{H}_Z$ and $\hat{I}_z$ have the same sets of eigenfunctions because $\hat{H}_Z$ is proportional to $\hat{I}_z$. The energy value of eigenstate |I, m> is $E_{I,m}$ and

$$\hat{H}_Z|I, m> = E_{I,m}|I, m> = -\gamma\hbar\hat{I}_z B_0|I, m> = -\gamma\hbar B_0 m|I, m> \qquad 1.5$$

So,

$$E_{I,m} = -\gamma\hbar B_0 m \qquad 1.6$$

For a spin 1/2 nucleus, I = 1/2 and m= 1/2. Then there are two possible eigenstates, $|\frac{1}{2}, +\frac{1}{2}>$, and $|\frac{1}{2}, -\frac{1}{2}>$, which are also called α and β states respectively. $E_{\frac{1}{2},\frac{1}{2}} = -\frac{1}{2}\gamma\hbar B_0$, and $E_{\frac{1}{2},-\frac{1}{2}} = \frac{1}{2}\gamma\hbar B_0$. The energy difference between the two states is ΔE. $\Delta E = \hbar\gamma B_0$, and the corresponding frequency is $\omega_0 = \gamma B_0$. This frequency is the rotation frequency of the net magnetization (**M**) about the $\mathbf{B_0}$ field, and is Larmor frequency (Figure 1.1). The rotation of **M** comes from the

torque (**T**) derived from the net spin angular momentum (**J**) in the magnetic field. The relation is derived as following: [1]

$$\mathbf{M} = \sum_i \boldsymbol{\mu}_i = \sum_i \gamma\hbar\mathbf{I}_i = \gamma\mathbf{J} \qquad 1.7$$

$$\mathbf{T} = \mathbf{M} \times \boldsymbol{B} = \frac{d\mathbf{J}}{dt} = \frac{1}{\gamma}\frac{d\mathbf{M}}{dt} \qquad 1.8$$

$$\text{So } \frac{d\mathbf{M}}{dt} = \gamma\mathbf{M} \times \boldsymbol{B} \qquad 1.9$$

Equation 1.9 predicts that **M** rotates about $\mathbf{B_0}$ with frequency $\omega_0 = \gamma B_0$.

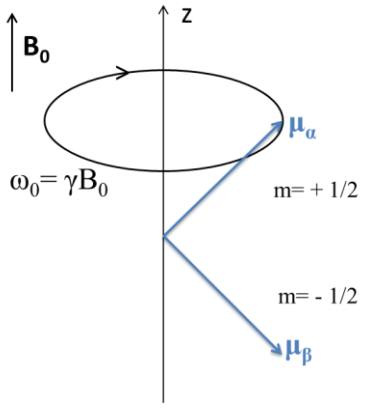

Figure 1.1 The two spin states m= $\pm$1/2 of a nucleus with I= 1/2 in the static magnetic field $\mathbf{B_0}$. The corresponding magnetic moments $\boldsymbol{\mu}_\alpha$ and $\boldsymbol{\mu}_\beta$ make precession about $\mathbf{B_0}$ in the **z** direction with Larmor frequency $\omega_0 = \gamma B_0$.

Compared to internal magnetic fields such as dipolar field, the external magnetic field is million times bigger, and the Zeeman interaction is a much stronger interaction. The local field $\mathbf{B_{loc}}$ is divided into secular parts ($\mathbf{B_{locz}}$) along $\mathbf{B_0}$ direction that commute with $\mathbf{B_0}$ and non-secular part ($\mathbf{B_{locp}}$) perpendicular to $\mathbf{B_0}$ direction that does not commute with $\mathbf{B_0}$. The secular part of the Hamiltonian commutes with Zeeman Hamiltonian and will affect the energy level correction to the first order, while the non-secular part does not commute with Zeeman Hamiltonian and is

thousand times smaller, thus it is not considered. This is Zeeman truncation or secular approximation. [2, 3]

1.1.2 Radio frequency (RF) B_1 field interaction

In NMR experiments, we apply radiofrequency (RF) pulse that produce time dependent $\mathbf{B_1}$ field to the spin system. $\mathbf{B_1}$ field is oscillating magnetic field. There are two components, the resonant $\mathbf{B_1^{res}}$ and the non-resonant $\mathbf{B_1^{non\text{-}res}}$ part.

$$\mathbf{B_1^{res}} = \frac{1}{2}\mathrm{B_1}(\cos(\omega t)\mathbf{x} - \sin(\omega t)\,\mathbf{y}) \qquad 1.10$$

$$\mathbf{B_1^{non-res}} = \frac{1}{2}\mathrm{B_1}(\cos(\omega t)\mathbf{x} + \sin(\omega t)\,\mathbf{y}) \qquad 1.11$$

Where **x** and **y** are the x and y direction's unit vector respectively.

Only the $\mathbf{B_1^{res}}$ part affects the spin states because $\mathbf{B_1^{res}}$ part rotates about $\mathbf{B_0}$ clockwise in xy plane, the same direction as the spin does while $\mathbf{B_1^{non-res}}$ rotates about $\mathbf{B_0}$ counter clockwise.

The $\mathbf{B_1}$ field produced by a 90X pulse is:

$$\mathbf{B_1} = \mathrm{B_1}\,(\cos\omega t)\,\mathbf{x} = \mathrm{B_1}\,(\cos 2\pi\nu t)\,\mathbf{x} \qquad 1.12$$

Where ν = the frequency of the 90X pulse.

With $\mathbf{B_1}$ field, the spin will experience a torque $\mathbf{T} = \mathbf{M} \times \boldsymbol{B_1}$, and rotates about B1 field with frequency of γB_1, which is Rabi frequency, and the precession is Rabi precession, determined by the cross product or right hand rule. If **M** is in **z** direction, and $\mathbf{B_1}$ is in **x** direction, then from $\mathbf{T} = \mathbf{M} \times \boldsymbol{B_1} = \boldsymbol{z} \times \mathbf{x} = \mathbf{y}$, the **M** will process toward **y** direction. The right hand rule would be placing the four fingers of the right hand along **M** (z- axis), followed by curving the four fingers

toward $\mathbf{B_1}$ direction (x- axis), and the direction the thumb is pointing to is the direction that the **M** is rotating to (which is y- axis direction in this example).

The flip angle θ_{rf} of **M** generated by $\mathbf{B_1}$ field is $\theta = \omega_1\tau_p = \gamma B_1\tau_p$, where τ_p is the duration of the pulse. If **M** is originally along z- axis, for a 90X pulse, θ= 90°, and M rotates 90° about x axis to the y- axis; for a 180X pulse, θ= 180°, and M rotates 180° about x- axis to the z- axis. The Hamiltonian for X pulse in rotating frame (see rotating frame section) is

$$\hat{H}_{RF} = -\gamma B_1 \hat{I}_x \qquad 1.13$$

$\hat{H}_{RF}$ is time independent in rotating frame and $\mathbf{B_1}$ appears static.

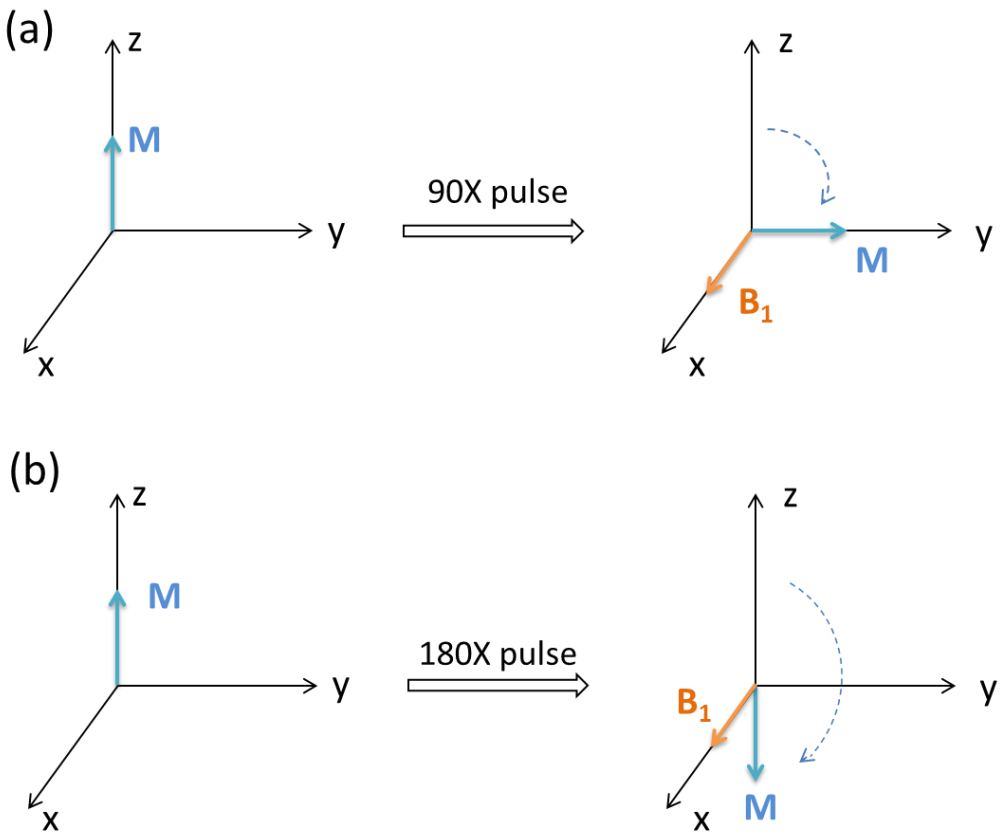

Figure 1.2 Vector representation of **M** precession with 90X (a) and 180X (b) pulse.[4]

1.1.3 Rotating frame

In laboratory frame, when placed in static magnetic field $\mathbf{B_0}$, **M** rotates about $\mathbf{B_0}$ with rapid frequency γB_0 about hundreds of MHz. RF-pulses introduce $\mathbf{B_1}$ field and **M** rotates about $\mathbf{B_1}$ field with a much slower precession frequency γB_1. $\mathbf{B_1}$ rotates about $\mathbf{B_0}$ with frequency ω_{RF}.[4, 5] The motion of **M** is complicated in laboratory frame for NMR experiments and it is not obvious to analyze the effect of $\mathbf{B_1}$ field on the motion of **M**. It is very helpful to consider the motion of **M** in rotating frame. The frequency of the rotating frame is ω_{RotF}. In rotating frame, the x-y plane rotates about $\mathbf{B_0}$ with ω_{RotF} set as the transmitter frequency. When transmitter frequency is set at $\mathbf{B_1}$ precession frequency ω_{RF}, $\mathbf{B_1}$ will appear static in the rotating frame.

In the rotating frame, the apparent precession frequency of **M** would be $(\omega_0 - \omega_{RotF})$, where ω_0 is the Larmor precession frequency and $\omega_0 = \gamma B_0$. Then the resonance offset $\Omega = \omega_0 - \omega_{RotF}$, and the offset field is $B_{o.f.} = \Omega/\gamma = (\omega_0 - \omega_{RotF})/\gamma$ according to the relation of $\omega = \gamma B$.[6] $\mathbf{B_{o.f.}}$ is along z-axis and is the reduced magnetic field in the rotating frame. When we set transmitter frequency ω close to ω_0 and ω_{RotF} the same as ω, $\mathbf{B_{o.f}}$ would be close to zero, then the $\mathbf{B_1}$ field would be dominant relative to $\mathbf{B_{o.f.}}$ **M** would majorly rotate about $\mathbf{B_1}$ field in the rotating frame. See example in Figure 1.2.

1.1.4 Chemical shift interaction

Chemical shift interaction arises from electron behavior in magnetic field $\mathbf{B_0}$. There are electrons around the nucleus and within the chemical bond in a molecule. When place the molecule in external magnetic field $\mathbf{B_0}$, the electron motions react to $\mathbf{B_0}$ and move under the Lorentz force from $\mathbf{B_0}$. This type of electron movement produces a secondary magnetic field that contributes to the total field that the spin feels and thus affects the resonance frequency. Shielding interaction

(or chemical shift interaction) is the interaction of the nucleus with the secondary field that the electrons produced. Shielding field decreases the magnitude of $\mathbf{B_0}$ experienced by a nucleus in most cases. Chemical shift is the frequency shift the shielding interaction causes in the spectrum. The shielding field can be in any direction because of various molecular orientations relative to $\mathbf{B_0}$. However, only the $\mathbf{B_0}$ direction component is relevant according to secular approximation. The Hamiltonian for this chemical shift interaction is,

$$\hat{H}_{CS} = \gamma \hat{\mathbf{I}} . \boldsymbol{\sigma} . \mathbf{B_0} \qquad 1.14$$

When $\mathbf{B_0}$ is in z direction,

$$\hat{H}_{CS} = -\gamma \hbar B_0 \boldsymbol{\sigma} . \hat{\mathbf{I}} \qquad 1.15$$

Where $\hat{\mathbf{I}}$ is the spin operator; $\boldsymbol{\sigma}$ is the shielding tensor. The electron distribution around the nucleus interested is generally not spherically symmetric, and the size of the shielding is dependent on the molecular orientation relative to $\mathbf{B_0}$. The shielding tensor $\boldsymbol{\sigma}$ is associated with the principal axis frame (PAF), which has three axes of x^{PAF}, y^{PAF} and z^{PAF} with corresponding values of σ_{xx}, σ_{yy} and σ_{zz} (see Figure 1.3 a). The three values are also the three principal chemical shifts in the chemical shift anisotropy (CSA) powder pattern. The orientation of PAF is dependent on the electron cloud orientation relative to the $\mathbf{B_0}$ and is certain for a certain molecule. The chemical shift is:

$$\sigma = \sigma_{xx} \cos^2 \alpha + \sigma_{yy} \cos^2 \beta + \sigma_{zz} \cos^2 \gamma \qquad 1.16$$

Where α, β and γ are the Euler angles and corresponds to the angles between $\mathbf{B_0}$ and the three PAF axes (see figure 1.3 b).

(a) (b)

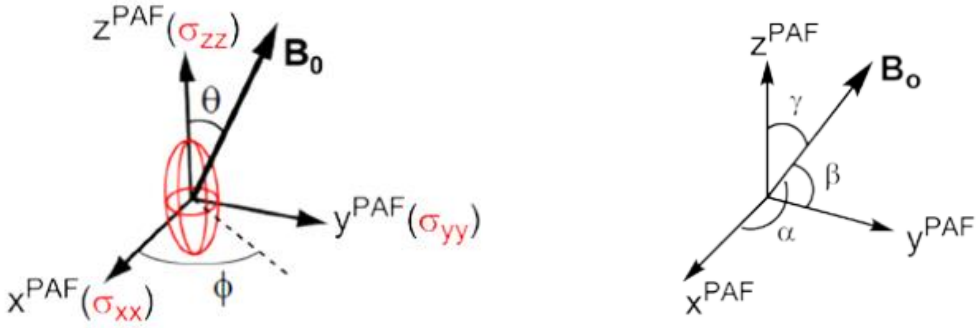

Figure 1.3 Shielding tensor (red) relative to the $\mathbf{B_0}$ field in PAF with principal axes values of σ_{xx}, σ_{yy} and σ_{zz} (a), where θ is the angle between the z-axis of PAF and $\mathbf{B_0}$, and ϕ is the angle between the x-axis of PAF and the projection of $\mathbf{B_0}$ on the x-y plane of PAF. PAF associated Euler angles, α, β, and γ with respect to $\mathbf{B_0}$ field (b). [7]

For liquid which has rapid molecular tumbling motion and solids under magical angle spinning (MAS) (see MAS section), the chemical shift orientation dependence (CAS) is averaged out and isotropic chemical shift is observed. [7, 8].

$$\sigma_{iso} = \frac{1}{3}(\sigma_{xx} + \sigma_{yy} + \sigma_{zz}) \qquad 1.17$$

Without rapid molecular tumbling or MAS for a peptide or protein, a powder pattern is observed (Figure 1.7 c). The total Hamiltonian for chemical shift contains isotropic and anisotropic and is:

$$\hat{H}_{CS} = \sigma_{iso}\gamma\hbar B_0 + \frac{1}{2}\delta_{CS}\hbar(3\cos^2\theta - 1 - \eta_{CS}\sin^2\theta\cos(2\phi)) \qquad 1.18$$

Where the first part is for isotropic chemical shift and the second part is for the anisotropic chemical shift; σ_{iso} is the isotropic chemical shift, δ_{CS} is the reduced anisotropy, η_{CS} is the asymmetry parameter, θ and ϕ (see Figure 1.3 a) are the polar angles of $\mathbf{B_0}$ in PAF. $\delta_{CS} =$

$-\gamma B_0(\sigma_{zz} - \sigma_{iso})$ and $\eta_{CS} = -\frac{\sigma_{yy}-\sigma_{xx}}{\sigma_{zz}-\sigma_{iso}}$.[9] Figure 1.4a displays a powder pattern of ^{13}CO nucleus. A powder pattern contains all the possible orientations of the molecule and the intensity reflects the population of the molecule with that orientation. σ_{zz} is the most shielded chemical shift principal component, and σ_{xx} is the least shielded chemical shift principal component. Figure 1.4 b shows the PAF for ^{13}CO. z^{PAF} with principal chemical shift value of σ_{zz} is perpendicular to the Cα-CO-N peptide bond plane, y^{PAF} with principal chemical shift value of σ_{yy} is along the CO bond direction, and x^{PAF} with principal chemical shift value of σ_{xx} is perpendicular to CO bond in the peptide bond plane. [8]

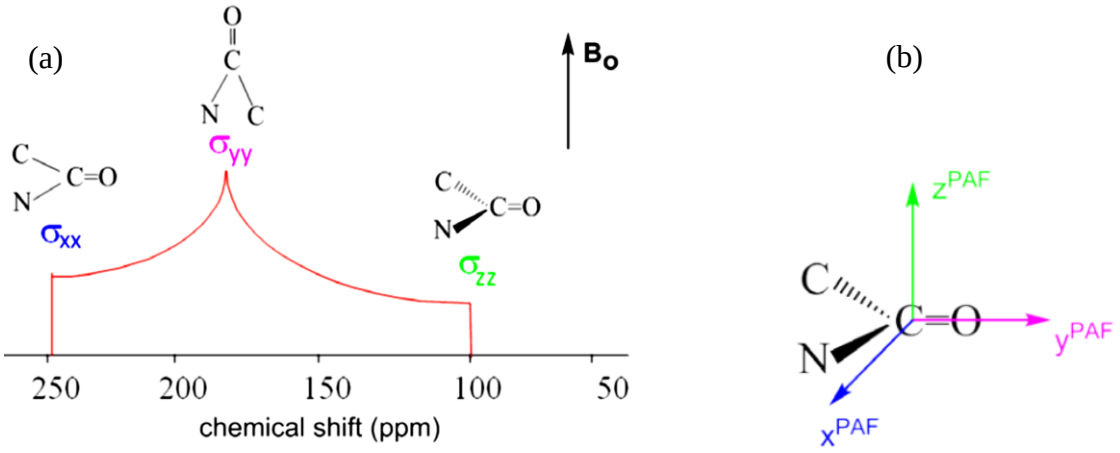

Figure 1.4 (a) CSA powder pattern of ^{13}CO with the three principal chemical shift values of σ_{xx} = 247 ppm, σ_{yy} = 176 ppm and σ_{zz} = 99 ppm. (b) The PAF of ^{13}CO in peptide or protein backbone with z^{PAF} perpendicular to the peptide bone C-CO-N plane, y^{PAF} alone the CO bond direction, and x^{PAF} perpendicular to the CO bond in the C -CO- N plane.

1.1.5 J coupling interaction

J coupling is also scaler coupling. It is the indirect dipole- dipole coupling between two nuclear spins connected through chemical bonds. The coupling depends on the interaction between the

nuclear spins and the bonding electron spins.[10] The Hamiltonian for J coupling between spin **j** and **k** is

$$\hat{H}_J = 2\pi \mathbf{J}_{jk} \hat{\mathbf{I}}_\mathbf{j} \cdot \hat{\mathbf{I}}_\mathbf{k} \qquad 1.19$$

Where $\mathbf{J_{jk}}$ is the J-coupling tensor, $\hat{\mathbf{I}}_\mathbf{j}$ and $\hat{\mathbf{I}}_\mathbf{k}$ are the nuclear spin operator for the j^{th} and k^{th} nuclei. From the Hamiltonian, the J-coupling is only dependent on the molecular structure and independent on magnetic field.[11] Therefore, J coupling remains a constant with differing magnetic field. J coupling tensor becomes a number in isotropic liquids. In liquid state NMR, the line width is usually narrow with a few hertz. Therefore, J coupling is an important interaction because J coupling magnitude is about 10 Hz for a three bond ^{1}H-^{1}H J coupling of ^{1}H-C-C-^{1}H, and about 140 Hz for ^{1}H-C J coupling of C-H bond.[12] However, in solid state NMR, the line width is generally about a few hundred hertz, and J- coupling will be within the broad linewidth. [13]

1.1.6 Dipolar coupling interaction

Dipolar coupling is the direct magnetic dipole- dipole interaction through space. It arises from the interaction of one nuclear spin with the magnetic field generated at its site from another nuclear spin nearby. The strength of the interaction depends on the inter-nuclear distance r and the angle θ between the inter-nuclear distance vector and the magnetic field $\mathbf{B_0}$ along the z-axis (shown in Figure 1.5).

The secular Hamiltonian for homonuclear dipolar coupling is

$$\hat{H}_D^{II} = -\frac{\mu_0}{4\pi}\hbar\frac{\gamma^2}{r_{12}^3}\frac{1}{2}(3\cos^2\theta - 1)\left(3\hat{I}_{1z}\hat{I}_{2z} - \hat{\mathbf{I}}_\mathbf{1}\cdot\hat{\mathbf{I}}_\mathbf{2}\right) \qquad 1.20$$

Where I_1 and I_2 are two different spin of the same nucleus type, μ_0 is the permeability of free space, $\hat{\mathbf{I}}_1$ and $\hat{\mathbf{I}}_2$ are the vector operators of spin 1 and 2, θ and r are the angles shown in Figure 1.5. The Hamiltonian for heteronuclear dipolar coupling for spin I and S of different nucleus type is:

$$\hat{H}_D^{IS} = -\frac{\mu_0}{4\pi}\hbar\frac{\gamma_I\gamma_S}{r_{IS}^3}\frac{1}{2}(3\cos^2\theta - 1)\left(2\hat{I}_z\hat{S}_z\right) \qquad 1.21$$

For dipolar coupling, $\frac{\mu_0}{4\pi}\hbar\frac{\gamma_I\gamma_S}{r_{IS}^3}$ is dipolar coupling constant in unit of rad/s, and heteronuclear dipolar coupling constant in unit of Hz is

$$d = \frac{\mu_0}{4\pi}\hbar\frac{\gamma_I\gamma_S}{r_{IS}^3} \times \frac{1}{2\pi} = \frac{\mu_0 h\gamma_I\gamma_S}{16\pi^3 r_{IS}^3} \qquad 1.22$$

For ^{13}C-^{31}P dipolar coupling, d=12250/r^3, for ^{13}C-^{15}N dipolar coupling, d=3066/r^3, while for ^{13}C-^{2}H dipolar coupling, d=4662/r^3, where d is in unit of Hz and r is in unit of angstroms.[14-16]

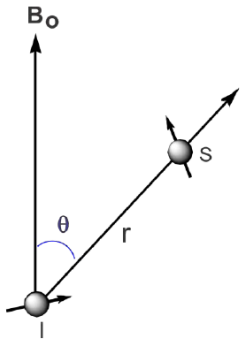

Figure 1.5 Dipolar coupling between nuclear spin I and S with inter-nuclear distance (r) and azimuthal angle (θ). θ is the angle between the inter-nuclear vector and the magnetic field $\mathbf{B_0}$ which is alone z axis.

$\hat{\mathbf{I}}_{\mathbf{1}} \cdot \hat{\mathbf{I}}_{\mathbf{2}} = \hat{I}_{1x}\hat{I}_{2x} + \hat{I}_{1y}\hat{I}_{2y} + \hat{I}_{1z}\hat{I}_{2z}$. $\hat{H}_Z$ is the Zeeman Hamiltonian for homonuclear dipolar coupling. For homonuclear dipolar coupling, $\hat{H}_Z = -\gamma\hbar B_0(\hat{I}_{1z} + \hat{I}_{2z})$, and following calculation can be done to see whether $\hat{H}_Z$ commutes with $\hat{\mathbf{I}}_{\mathbf{1}} \cdot \hat{\mathbf{I}}_{\mathbf{2}}$.

$[\hat{H}_Z,\ \hat{\mathbf{I}}_{\mathbf{1}} \cdot \hat{\mathbf{I}}_{\mathbf{2}}] = -\gamma\hbar B_0[(\hat{I}_{1z} + \hat{I}_{2z}), \hat{\mathbf{I}}_{\mathbf{1}} \cdot \hat{\mathbf{I}}_{\mathbf{2}}]$

$$= -\gamma\hbar b_0\left[(\hat{I}_{1z} + \hat{I}_{2z}), (\hat{I}_{1x}\hat{I}_{2x} + \hat{I}_{1y}\hat{I}_{2y} + \hat{I}_{1z}\hat{I}_{2z})\right] = 0$$

The Zeeman Hamiltonian for heteronuclear dipolar coupling is $\hat{H}_Z = -\hbar B_0(\gamma_I\hat{I}_z + \gamma_S\hat{I}_z)$. The $\left[\gamma_I\hat{I}_z + \gamma_S\hat{I}_z, \hat{\mathbf{I}} \cdot \hat{\mathbf{S}}\right] \neq 0$ because the two different γ present.[2, 17]

Therefore, $\hat{\mathbf{I}} \cdot \hat{\mathbf{S}}$ commutes with $\hat{H}_Z$ for homonuclear dipolar coupling, but does not commute with $\hat{H}_Z$ for heteronuclear coupling. According to secular approximation or Zeeman truncation, the Hamiltonian is truncated more for heteronuclear dipolar coupling than homonuclear dipolar coupling.

1.1.7 Quadrupolar coupling interaction

Quadrupolar coupling interaction exists in quadrupolar nuclei with spin quantum number I > 1/2 due to non-spherical charge distribution around the nucleus. Figure 1.6 shows the nucleus charge distribution and the corresponding quadrupole moment.

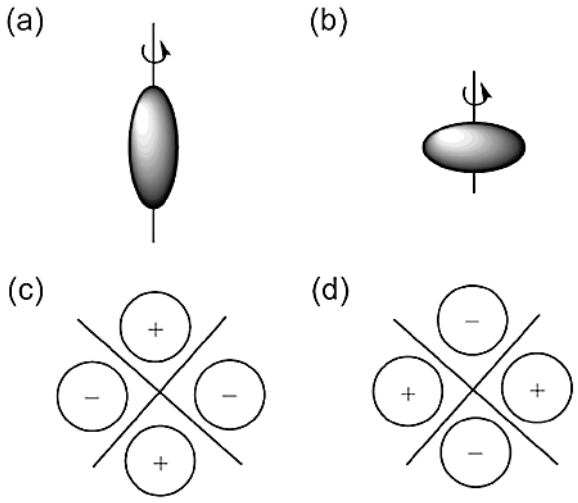

Figure 1.6 Prolate (a) and Oblate (b) charge distribution of quadrupolar nucleus and the corresponding quadrupole moment shown in (c) and (d) respectively. Prolate moment (c) is positive and Oblate moment (d) is negative. [2, 18]

The quadrupolar nuclei has electric quadrupole moment, which interacts with the electric field gradient produced by the distribution of other nuclei and the electrons near the nucleus at the nucleus site, and this is known as quadrupolar coupling.[18] The coupling strength depends on the magnitude of the quadrupole moment and the electric field gradient strength. The electric quadrupole moment is eQ, where e is the proton charge and Q is the quadrupole moment specific to nucleus type. Quadrupolar interaction is a relatively stronger interaction (~170 kHz for aliphatic C- ^{2}H) and affects the energy levels of the nuclear spin like other magnetic interactions previously discussed. The secular quadrupolar interaction Hamiltonian is

$$\hat{H}_D = \frac{eQeq}{2I(2I-1)\hbar}\frac{1}{2}(3\cos^2\theta - 1 - \eta_Q \sin^2\theta\cos(2\emptyset))\frac{1}{2}(3\hat{I}_z^2 - I(I+1)) \qquad 1.22$$

Where e = the proton charge, Q = the quadrupole moment specific to nucleus type, q is associated with electric field gradient tensor, I is the nucleus spin quantum number, θ and ϕ are

the polar angles of magnetic field $\mathbf{B_0}$ in PAF, η_Q is the asymmetry parameter of the electric field tensor, and $\hat{I}_z$ is the z-component of the spin operator.

$\frac{eQeq}{\hbar}$ = the quadrupolar coupling constant (QCC), in unit of rad/s. QCC in Hz is

$$\chi = \frac{eQeq}{\hbar}\frac{1}{2\pi} = \frac{eQeq}{h} \qquad 1.23$$

The term $(3\cos^2\theta - 1 - \eta_Q \sin^2\theta\cos(2\emptyset))$ is from the orientation dependence of the electric field gradient tensor.

For ^{2}H nucleus, spin quantum number I =1, and $\chi \approx 170$ kHz in aliphatic C-D bond[19]. Because deuterated lipids and cholesterol have been widely used to study membrane structure and dynamics, we are going to analyze the effect of orientation on the observed resonance frequency of ^{2}H. Since η_Q is ~ 0 for aliphatic C-D bond due to the approximate uniaxiality of electron density in the σ bond, and $\hat{I}_z^2|I,m>= m^2|I,m>$, the ^{2}H quadrupolar energy is written as,

$$E_Q = \frac{eQeq}{2I(2I-1)\hbar}\frac{1}{2}\left(3\cos^2\theta - 1 - \eta_Q \sin^2\theta\cos(2\emptyset)\right)\frac{1}{2}\left(3m^2 - I(I+1)\right)$$

$$= \frac{\pi}{4}\chi\hbar(3\cos^2\theta - 1)(3m^2 - 2) \qquad 1.24$$

Where m= -1, 0 and +1 for ^{2}H. The allowed transitions are $\Delta m = \pm 1$ in NMR spectroscopy. Therefore, there are two allowed transitions, m = +1 → m = 0, and m = 0 → m = -1. Next, we are going to discuss orientation dependence of E_Q by analyzing a few typical θ value, and see how it affects the ^{2}H transition frequency and the resulting ^{2}H spectrum.

Example (1)**:** When θ = 0°, $E_Q = \frac{\pi}{4}\chi\hbar(3\cos^2\theta - 1)(3m^2 - 2) = \frac{\pi}{2}\chi\hbar(3m^2 - 2)$. For the three possible values of m: +1, 0, and -1, the corresponding E_Q would be $\frac{\pi}{2}\chi\hbar$, $-\pi\chi\hbar$ and $\frac{\pi}{2}\chi\hbar$. Besides the quadrupolar interaction, there is also Zeeman interaction, which is the strongest interaction in

NMR. We assume the Zeeman energies for m = +1, 0, and -1 are – Ez, 0 and + Ez. For transition m = +1 →m = 0, $\Delta E = E_{+1\rightarrow 0} = E_z - \pi\chi\hbar - \frac{\pi}{2}\chi\hbar = E_z - \frac{3\pi}{2}\chi\hbar$. From ΔE = hν, the transition frequency $\nu_{+1\rightarrow 0} = \nu_z - \frac{3}{4}\chi$. Similarly, for transition m = 0 →m = -1, $\Delta E = E_{0\rightarrow -1} = E_z + \frac{\pi}{2}\chi\hbar - (-\pi\chi\hbar) = E_z + \frac{3\pi}{2}\chi\hbar$, thus the transition frequency $\nu_{0\rightarrow -1} = \nu_z + \frac{3}{4}\chi$. ν_z is the Larmor frequency of ^{2}H in absence of quadrupolar interaction and ν_z = Ez / h. When the spectrometer transmitter frequency is set at the ^{2}H Larmor frequency ν_z, there will be two discrete signals observed in the ^{2}H spectrum, one at $-\frac{3}{4}\chi$ corresponding to transition of m = +1 →m = 0, and the other one at $\frac{3}{4}\chi$ corresponding to transition of m = 0 →m = -1. The spectrum frequency axis is in unit of Hz. This spectrum for this specific angle is shown in Figure 1.7 a.

Example (2): When θ = 54.7°, $E_Q = \frac{\pi}{4}\chi\hbar(3\cos^2\theta - 1)(3m^2 - 2) = \frac{\pi}{2}\chi\hbar(3m^2 - 2) = 0$ because $(3\cos^2\theta - 1) = 0$. E_Q = 0 regardless of m value. $\Delta E = E_{0\rightarrow -1}$ = Ez for transition m = +1 →m = 0 and $\Delta E = E_{0\rightarrow -1}$ = Ez for transition m = 0 →m = -1. Therefore, $\nu_{+1\rightarrow 0} = \nu_z$ and $\nu_{0\rightarrow -1} = \nu_z$. When the transmitter frequency is set at the ^{2}H Larmor frequency ν_z, both transitions will give signal at the same frequency and appears at 0 Hz in the spectrum. Figure 1.7 b shows the spectrum for this specific angle.

Example (3): When θ = 90°, $E_Q = \frac{\pi}{4}\chi\hbar(3\cos^2\theta - 1)(3m^2 - 2) = -\frac{\pi}{4}\chi\hbar(3m^2 - 2)$. For the three possible values of m: +1, 0, and -1, the corresponding E_Q would be $-\frac{\pi}{4}\chi\hbar$, $\frac{\pi}{2}\chi\hbar$ and $-\frac{\pi}{4}\chi\hbar$. For transition m = +1 →m = 0, $\Delta E = E_{+1\rightarrow 0} = E_z + \frac{\pi}{2}\chi\hbar + \frac{\pi}{4}\chi\hbar = E_z + \frac{3\pi}{4}\chi\hbar$. From ΔE = hν, the transition frequency $\nu_{+1\rightarrow 0} = \nu_z + \frac{3}{8}\chi$, where $\nu_z = E_z/h$. Similarly, for transition m = 0 →m = -1, $\Delta E = E_{0\rightarrow -1} = E_z - \frac{\pi}{4}\chi\hbar - \left(\frac{\pi}{2}\chi\hbar\right) = E_z - \frac{3\pi}{4}\chi\hbar$, thus the transition frequency $\nu_{0\rightarrow -1} = \nu_z -$

$\frac{3}{8}\chi$. In this example, there will be two discrete signals observed in the ^{2}H spectrum, one at $\frac{3}{8}\chi$ corresponding to transition of m = +1 →m = 0, and the other one at $-\frac{3}{8}\chi$ corresponding to transition of m = 0 →m = -1. Figure 1.7 c shows the spectrum for this specific angle.

For a static sample that θ could have all possible values, the observed ^{2}H spectrum would have a powder pattern with doublet (Figure 1.7 d). The doublet corresponds to the two possible transitions for the three spin states m=1, 0 and -1. The transitions are m = +1 →m = 0 and m = 0 →m = -1 for θ= 90^o. The splitting of the two horns in the spectrum is $\frac{3}{4}\chi$, which would be 127 kHz for aliphatic C-D bond.

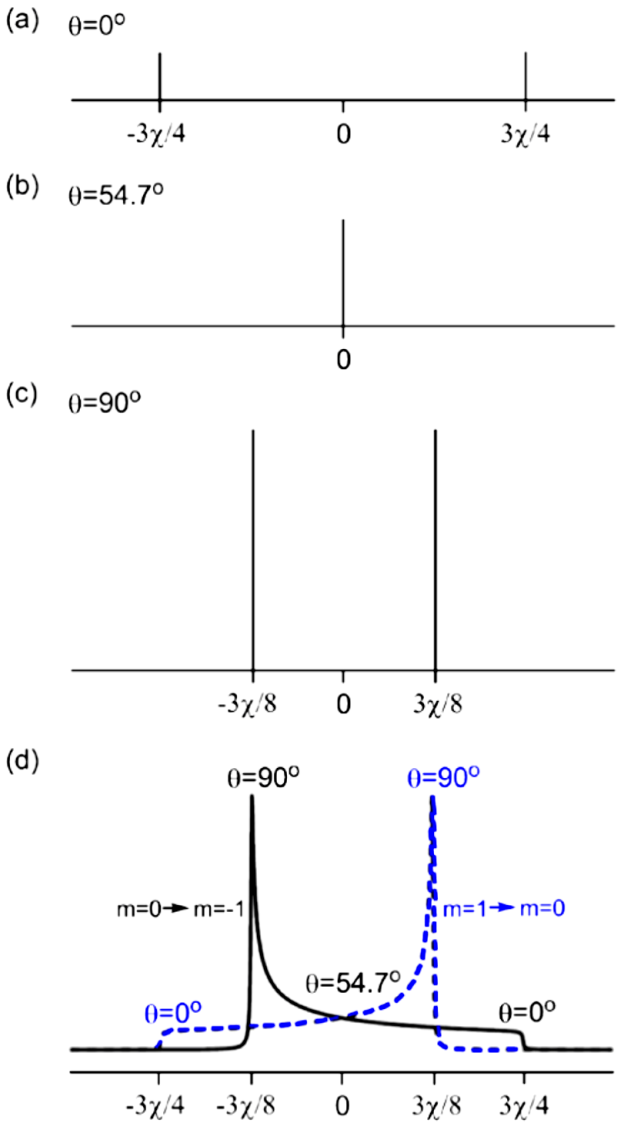

Figure 1.7 The orientation dependence of static ^{2}H spectra. Discrete lines are observed for the allowed two transitions ($m = +1 \rightarrow m = 0$, and $m = 0 \rightarrow m = -1$) with (a) $\theta = 0°$, (b) $\theta = 54.7°$ and (c) $\theta = 90°$ where θ is the angle between the C – ^{2}H bond and $\mathbf{B_0}$ field. (d) The quadrupolar powder pattern for the allowed two transitions for all possible θs in static sample.[2, 18]

1.1.8 Magic angle spinning (MAS)

Magic angle spinning (MAS) is a widely used technique to achieve high-resolution spectrum in solid state NMR.[1, 20, 21] In liquid sate NMR, the observed high-resolution spectrum with narrow peaks is because of rapid molecular tumbling in solution. The rapid motion in liquids can average out the orientation dependence of CSA and dipolar coupling. In solid state NMR, the rapid molecular reorientation is absent, so the peaks are generally broad due to anisotropic interactions like CSA and dipolar coupling. In order to get high resolution spectrum in solids, MAS was invented.[20] The angle between the rotor spinning axis and the external magnetic field $\mathbf{B_0}$ equals magic angle 54.7° (Figure 1.8). In MAS, the sample-containing rotor spins at speed ranging from a few to tens of kHz. Rapid MAS could average out chemical shift anisotropy and only leave isotropic chemical shift observed. Spinning side bands shows up with slow spinning speed in addition to the isotropic chemical shift (Figure 1.9).

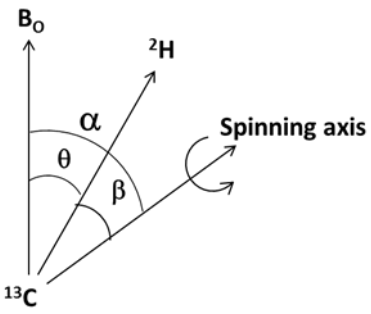

Figure 1.8 Magic angle spinning (MAS) for ^{13}C- ^{2}H inter-nuclear vector, the angle α is the angle between the external magnetic field $\mathbf{B_0}$ and sample- spinning axis. When the angle α is fixed at 54.7°, the sample spinning is called magic angle spinning.[18] θ and β is the angle between ^{13}C-^{2}H distance vector and $\mathbf{B_0}$ and spinning axis respectively.

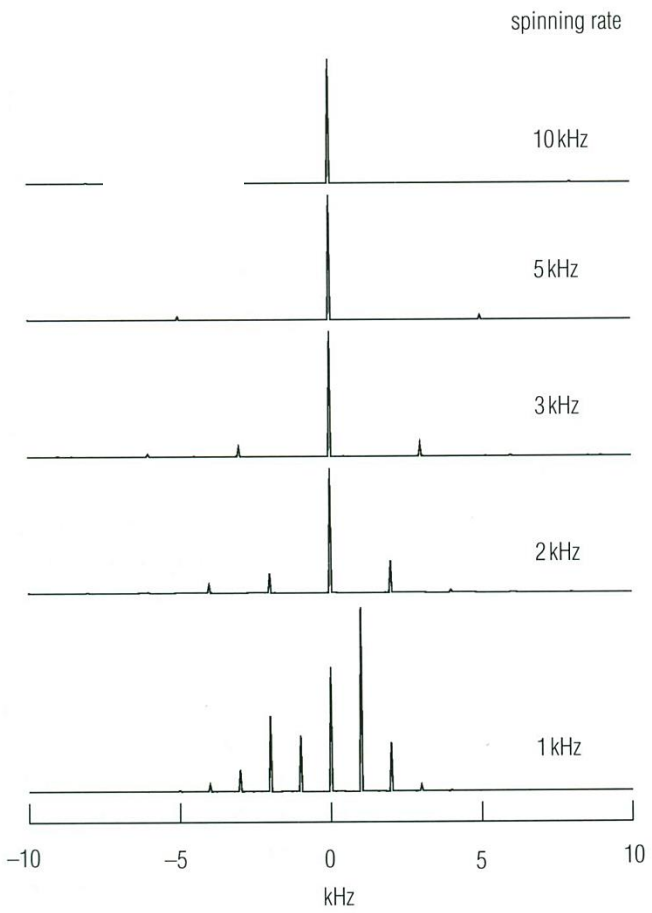

Figure 1.9 The effect of different spinning speed on the observed spectrum. For this example, the isotropic chemical shift is set at 0 Hz, the CSA is 5 kHz, and the asymmetry is 0. When the spinning speed is slow, there are spinning sidebands spaced at spinning frequency; when the spinning speed is fast enough to overcome the CAS, only isotropic chemical shift is observed with high intensity.[1] And the figure is from reference 1.

Another important effect of MAS is to average out dipolar coupling which also broadens spectrum line width. Take ^{13}C-^{2}H dipolar coupling for example, the ^{13}C-^{2}H distance geometry is shown in Figure 1.8, α is 54.7° (magic angle) and is the angle between the rotor spinning axis and $\mathbf{B_0}$. θ and β is the angle between ^{13}C- ^{2}H distance vector and $\mathbf{B_0}$ and spinning axis

respectively. The θ varied with time when the sample spins about the spinning axis. Over each rotor period, the average of $(3\cos^2\theta - 1)$ becomes 0.[1]

$$< 3\cos^2\theta(t) - 1 > = \frac{1}{2}(3\cos^2\alpha - 1)(3\cos^2\beta - 1) = 0 \qquad 1.25$$

Where θ, α, and β are defined in Figure 1.8.

1.1.9 Rotational echo double resonance (REDOR)

Rotational echo double resonance (REDOR) solid state NMR has been widely used to study the inter-nuclear distance by recovering the heteronuclear dipolar coupling under MAS. Dipolar coupling has a distance dependence of $1/r^3$. From REDOR, we can get both dipolar coupling and inter-nuclear distance r. REDOR was developed by Terry Gullion and Jacob Schaefer and originally illustrated with ^{13}C- and ^{15}N labeled alanine.[22] Typical REDOR pulse sequence is shown in Figure 1.10 with example spins of ^{13}C (detect) and ^{15}N (dephasing).

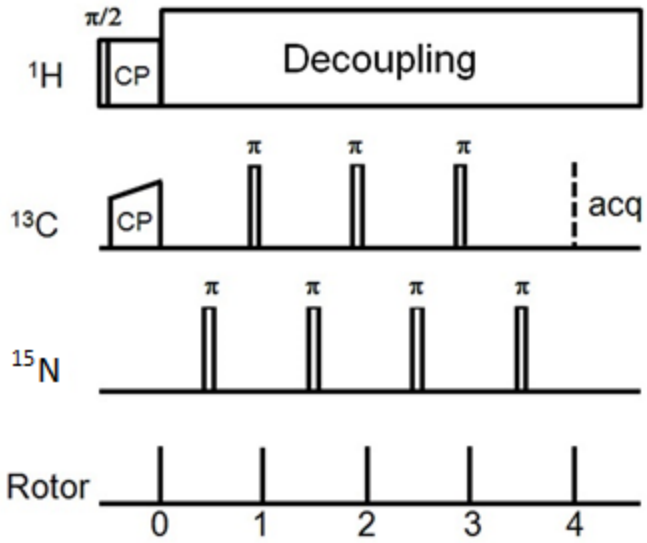

Figure 1.10 Pulse sequence for ^{13}C - ^{15}N REDOR.

REDOR experiments require a three- channel spectrometer and a triple resonance probe for peptide and protein studies. For ^{13}C -^{15}N REDOR, the three channels are ^{1}H, ^{13}C and ^{15}N. 90° pulse is initially applied to ^{1}H nuclei to generate a transverse magnetization by rotating the ^{1}H magnetization from $\mathbf{B_0}$ direction to the x-y plane; cross polarization (CP) is applied to both ^{1}H and ^{13}C channels to generate ^{13}C transverse magnetization by transferring ^{1}H transverse magnetization to ^{13}C nucleus.

Cross polarization (CP) is a commonly used method to study rare spins like ^{13}C with low abundance and very long relaxation times, which causes poor signal/noise ratio and requires long gaps between scans respectively. A decent spectrum with good signal signal/noise ratio would take long time due to thousands of scans needed in solid state NMR. CP could solve the problems by transferring the magnetization from the nearby network of abundant spins like ^{1}H to the rare spins like ^{13}C. The process is mediated by ^{1}H -^{13}C dipolar coupling and can be understood through doubly rotating frame.[1] In one rotating frame, the ^{1}H $\mathbf{B_1}$ field is static; while in the other rotating frame, the ^{13}C $\mathbf{B_1}$ field is static. In both rotating frames, it assumes $\mathbf{B_1}$ field is the only magnetic field considering no resonance offset present. The ^{1}H and ^{13}C contact pulses during CP must meet the Hartmann-Hahn matching condition:

$$\gamma_{1_H} B_1(^{1}H) = \gamma_{13_C} B_1(^{13}C) \qquad 1.26$$

Where $B_1(^{1}H)$ and $B_1(^{13}C)$ is the magnitude of ^{1}H $\mathbf{B_1}$ field and ^{13}C $\mathbf{B_1}$ field respectively. Equation 1.26 applies when there is no resonance offset. However, in real samples, there is resonance offset $\mathbf{B_{o.f.}}$. Then the matching conditions become

$$\gamma_{1_H} B_{eff}(^{1}H) = \gamma_{13_C} B_{eff}(^{13}C) \qquad 1.27$$

Where B_{eff} is the magnitude of $\mathbf{B_{eff}}$ and $\mathbf{B_{eff}} = \mathbf{B_1} + \mathbf{B_{o.f.}}$ $B_{eff} = \sqrt{(\mathbf{B_1} + \mathbf{B_{o.f.}})^2}$.

The transition energy gaps for the two hetero-nuclei are equal in the doubly rotating frame. The energy required for a ^{13}C $\alpha \rightarrow \beta$ transition is from the energy released by a nearby ^{1}H $\beta \rightarrow \alpha$ transition. There is energy redistribution between ^{1}H and ^{13}C spins, but the total energy of the spin system is conserved.

The Hartmann-Hahn matching condition described in equation 1.26 and 1.27 is for static sample. However, in REDOR, MAS is used and MAS with CP complicates the Hartmann-Hahn matching condition because MAS affects dipolar coupling by creating time dependent orientation dependence $<3\cos^2\theta(t) - 1>$. The strength of the dipolar coupling depends on the orientation between inter-nuclear distance vector and the $\mathbf{B_0}$ field as well as the magnitude of γ. For the ^{1}H –^{13}C dipolar coupling, the largest ^{13}CO – ^{1}H dipolar coupling is ~ 4 kHz in a peptide because the closest distance between ^{1}H and a labeled ^{13}CO is ~ 2Å, which is between ^{13}CO and ^{1}H in the peptide bond. In REDOR with 10 kHz MAS, the largest 4 kHz ^{13}CO – ^{1}H dipolar coupling is supposed to be averaged out. However, the ^{1}H – ^{1}H dipolar coupling is not averaged out with 10 kHz MAS. The ^{1}H – ^{1}H dipolar coupling is much stronger due to 4 times bigger γ compared to ^{13}CO, and is typically 10-50 kHz.[23] The ^{1}Hs are dipolar coupled as a network in peptide, and there are rapid spin states exchange ($\alpha \leftrightarrow \beta$ transition) between ^{1}Hs through the homonuclear dipolar coupling. The spin states exchange rate is roughly equal to the ^{1}H – ^{1}H homonuclear dipolar coupling. Therefore, the ^{1}Hs will change its spin state over each rotor period with a rate comparable or even faster than the 10 kHz MAS speed. Then the ^{13}CO – ^{1}H dipolar coupling is not averaged to zero over each rotor period because the heteronuclear dipolar coupling is disrupted by the fast ^{1}H spin states exchange. This is also the reason that ^{13}CO – ^{1}H CP can be achieved through the ^{13}CO – ^{1}H heteronuclear dipolar coupling under 10 kHz MAS. The Hartmann-Hahn matching condition under MAS is

$$\gamma_{1_H} B_{eff}(^1H) = \gamma_{13_C} B_{eff}(^{13}C) + n\omega_R \quad 1.28$$

Where n= 0, ±1, ±2 and represents the nth spinning sideband in the ^{13}C spectrum, and ω_R is the MAS frequency.[24] From equation 1.28, $\gamma_{1_H} B_{eff}(^1H) \neq \gamma_{13_C} B_{eff}(^{13}C)$, and the total energy of the spins are not conserved.

MAS disrupt the ^{13}CO – ^{1}H dipolar coupling by averaging out the orientation dependence. Besides, there is distribution of resonance-offset frequency due to different molecular orientation, chemical environment and dipolar couplings. Therefore, a ramp field is applied to ^{13}C during CP to increase the CP transfer efficiency. In REDOR, the maximum CP ^{13}C signal is achieved by optimizing the field strength and ramp of ^{13}C pulses.

Following CP, rotor synchronized π pulses are applied to ^{13}C channel at the end of each rotor period except the last rotor period, and to ^{15}N channel at the middle of each rotor period. Two types of signals are detected, the control signal S_0 and the reduced signal S_1. To obtain S_0 signal, ^{13}C π pulses are applied and no ^{15}N π pulses. To get S_1, ^{15}N π pulses are applied in the middle of each rotor period along with ^{13}C π pulses applied at the end of each rotor period. To understand how MAS and π pulses affect dipolar coupling over each rotor period, we can look at the ^{13}CO – ^{15}N heteronuclear dipolar coupling Hamiltonian:

$$\hat{H}_D^{CN} = -\frac{\mu_0}{4\pi}\hbar\frac{\gamma_C\gamma_N}{r_{CN}^3}\frac{1}{2}(3\cos^2\theta - 1)(2\hat{I}_z\hat{S}_z) \quad 1.29$$

Where $\hat{I}_z$ and $\hat{S}_z$ are the z-component of spin operator for ^{13}C and ^{15}N respectively.

The ^{13}CO – ^{15}N dipolar coupling depends on spatial part, and ^{13}C and ^{15}N spin parts. MAS affect the spatial part, and π pulses affect the spin parts. MAS average out the ^{13}CO – ^{15}N dipolar coupling over each rotor period. π pulses change the sign of dipolar coupling. ^{13}C π pulses change the sign of magnetic moment of the observed spins (^{13}C), while ^{15}N π pulses change the

sign of magnetic moment of the dephasing spins (^{15}N) and thus alter the sign of the dipolar field experienced by the observed spin (^{13}C).

In S_0, ^{13}C π pulses can refocus the isotropic chemical shift and average out chemical shift anisotropy by MAS. Full ^{13}C signal is observed, and the dipolar coupling is averaged to zero (Figure 1.11). In S_1 experiment, the dipolar coupling is reintroduced, and results in reduced ^{13}C signal S_1 (Figure 1.12). The reintroduced dipolar coupling causes phase accumulation of the magnetization over each rotor period. S_1/S_0= cos (ϕ). $\phi = \frac{N_c T_r d}{\pi}\sqrt{2}\sin 2\beta \sin\alpha$; $\frac{S_1}{S_0} = \frac{1}{2\pi}\int_0^{\pi}\int_0^{2\pi}\cos\emptyset \sin\beta \, d\alpha d\beta$, where Nc is number of rotor periods, Tr is rotor period, d is dipolar coupling in rad/s, and figure 1.8 shows the angle of θ and β. The observed S_1 signal is reduced because of all the possible θ and β values in the sample. The dephasing is given by the equation $\Delta S/S_0 = (S_0 - S_1)/S_0$ and is dependent on a dimensionless parameter $\lambda = d\times\tau$, where d is the dipolar coupling, τ is the dephasing time. ^{13}C – ^{15}N dipolar coupling $d = \frac{\mu_0 h \gamma_{^{13}C}\gamma_{^{15}N}}{16\pi^3 r_{IS}^3} = \frac{3066}{r_{CN}^3}$, where d is in unit of Hz and internuclear distance r is in unit of Å. d can be obtained by simulating the dephasing buildup with SIMPSON program.[25] Once d is known, the inter-nuclear distance can be calculated.

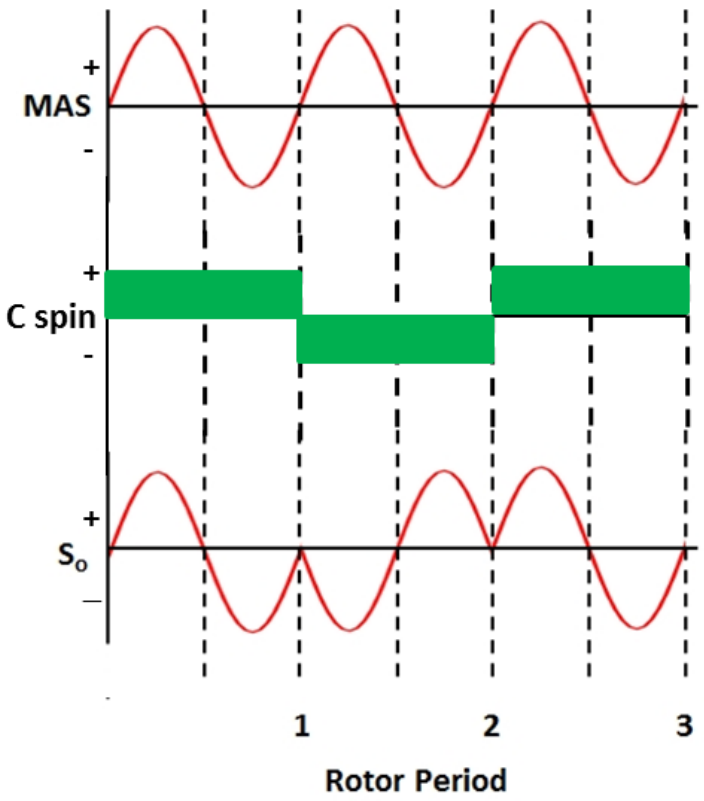

Figure 1.11 Diagram of heteronuclear dipolar coupling evolution over rotor period for S_0 experiment in REDOR. The + and – sign represent positive and negative dipolar coupling respectively. MAS represents the dipolar coupling spatial dependence over each rotor period; C spin represents the observing spin operator and π pulse changes the sign of dipolar coupling; S_0 represents the overall effects from MAS and C spin π pulses on dipolar coupling over each rotor period. As we can see, the dipolar coupling for S_0 is averaged to zero over each rotor period.

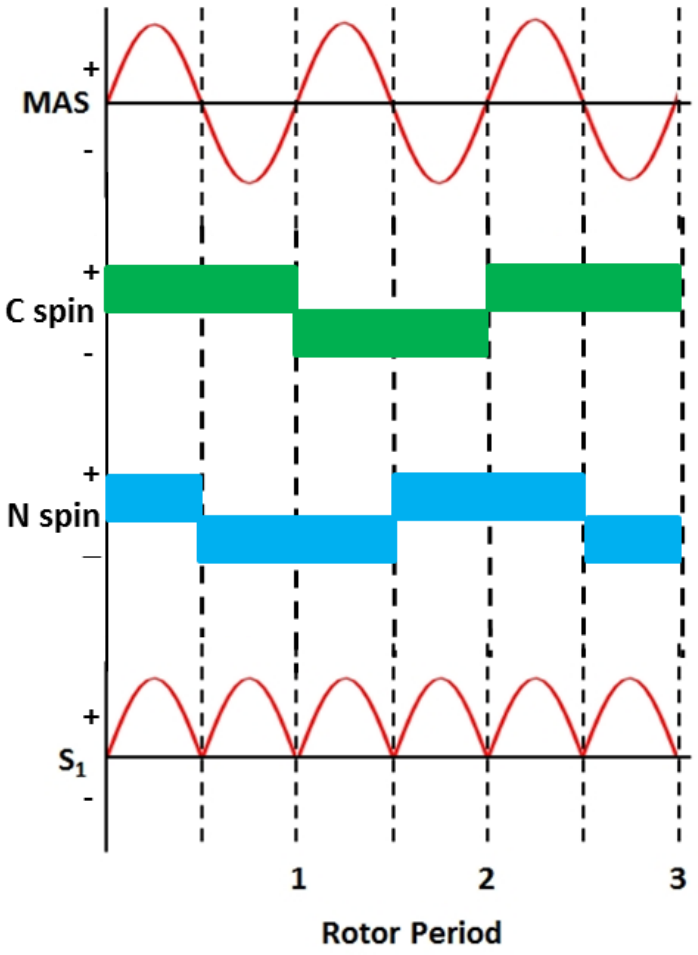

Figure 1.12 Diagram of heteronuclear dipolar coupling evolution over rotor period for S_1 experiment in REDOR. The + and – sign represent positive and negative dipolar coupling respectively. MAS represents the dipolar coupling spatial dependence over each rotor period; C spin and N spin represent the observing and dephasing spin operator respectively and π pulse changes the sign of dipolar coupling. S_1 represents the overall effects from MAS, C spin (detecting) and N (dephasing) spin π pulses on dipolar coupling over each rotor period. As we can see, the dipolar coupling for S_1 is re-introduced and is nonzero over each rotor period.

1.1.10 Quadrupolar echo (QUECHO)

In ^{2}H NMR experiment, the spectrum lines are broad due to quadrupolar coupling. Broad lines generally have rapid decaying FID. Pulse ringing-down is much stronger signal relative to the weak sample signal, thus prevents the measurement of sample signal until a short time (dead time) after pulse.[1] For solid ^{2}H NMR experiment with broad NMR resonance frequencies, the proportion of signal loss during the dead time is significant and is overcome by using quecho pulse sequence (shown in Figure 1.13) which refocuses the time evolution of spins.

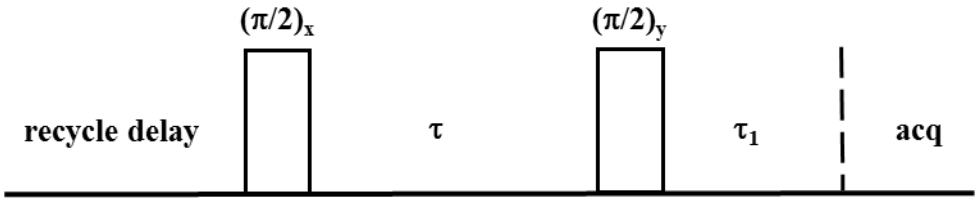

Figure 1.13 "Quecho" pulse sequence. Theoretically, $\tau = \tau_1$.

In the sequence, the first π/2 pulse is used to generate transverse magnetization, a sencond π/2 pulse is used to refocus the time evolution of spins and quadrupolar coupling. The two π/2 pulse must be out of phase. τ is the time interval between the first and the second π/2 pulse. τ_1 is the time interval after the second π/2 pulse and before acq. When the time interval $\tau_1 = \tau$, the echo appears with its maximum intensity. The can be understood through time evolution of density operator $\hat{\rho}(t)$.

The first π/2 pulse generates M along y axis, density operator at time 0 is $\hat{\rho}(0) = \hat{I}_y$. The time evolution of density operator is[17]

$$\hat{\rho}(t) = \hat{U}(t)\hat{\rho}(t)\hat{U}^{-1}(t) \qquad 1.30$$

Where $\hat{U}(t)$ is the time evolution operator.

$$\widehat{U}(2\tau) = e^{-i\widehat{H}_Q\tau}e^{i\frac{\pi}{2}\hat{I}_y}e^{i\widehat{H}_Q\tau} = e^{-i\omega_\theta(3\hat{I}_z^2-\hat{\boldsymbol{I}}^2)\tau}e^{i\frac{\pi}{2}\hat{I}_y}e^{i\omega_\theta(3\hat{I}_z^2-\hat{\boldsymbol{I}}^2)\tau}$$

$$= e^{-i\omega_\theta(3\hat{I}_z^2-\hat{\boldsymbol{I}}^2)\tau}e^{i\frac{\pi}{2}\hat{I}_y}e^{i\omega_\theta(3\hat{I}_z^2-\hat{\boldsymbol{I}}^2)\tau}e^{-i\frac{\pi}{2}\hat{I}_y}e^{i\frac{\pi}{2}\hat{I}_y}$$

$$= e^{-i\omega_\theta(3\hat{I}_z^2-\hat{\boldsymbol{I}}^2)\tau}e^{-i\omega_\theta(3\hat{I}_x^2-\hat{\boldsymbol{I}}^2)\tau}e^{i\frac{\pi}{2}\hat{I}_y} \qquad 1.31$$

$$= e^{i\omega_\theta(3\hat{I}_y^2-\hat{\boldsymbol{I}}^2)\tau}e^{i\frac{\pi}{2}\hat{I}_y}$$

by using $\hat{1} = e^{-i\frac{\pi}{2}\hat{I}_y}e^{i\frac{\pi}{2}\hat{I}_y}$ and $\hat{\boldsymbol{I}}^2 = \hat{I}_x^2 + \hat{I}_y^2 + \hat{I}_z^2$.

Then $\hat{\rho}(2\tau) = \widehat{U}(2\tau)\hat{I}_y\widehat{U}^{-1}(2\tau)$

$$= e^{i\omega_\theta(3\hat{I}_y^2-\hat{\boldsymbol{I}}^2)\tau}e^{i\frac{\pi}{2}\hat{I}_y}\hat{I}_y e^{-i\frac{\pi}{2}\hat{I}_y}e^{-i\omega_\theta(3\hat{I}_y^2-\hat{\boldsymbol{I}}^2)\tau} \qquad 1.32$$

$$= e^{i\omega_\theta(3\hat{I}_y^2-\hat{\boldsymbol{I}}^2)\tau}\hat{I}_y e^{-i\omega_\theta(3\hat{I}_y^2-\hat{\boldsymbol{I}}^2)\tau}$$

$$= \hat{I}_y$$

by using $\left[3\hat{I}_y^2 - \hat{\boldsymbol{I}}^2, \hat{I}_y\right] = 0$.

By replacing the second $(\pi/2)_y$ pulse propogator $e^{i\frac{\pi}{2}\hat{I}_y}$ with $(\pi/2)_{-y}$ pulse propogator $e^{-i\frac{\pi}{2}\hat{I}_y}$, same results will be obtained, which means the solid echo is independent of the sign of the second pulse.

Therefore, the time evolution results of $\hat{\rho}(2\tau) = \hat{I}_y$ is the same as $\hat{\rho}(0) = \hat{I}_y$ which is generated by the first $(\pi/2)_x$ pulse in the "quecho" pulse sequence. So the spin states and the signal at time 2τ is the same as at time 0. $2\tau = \tau + \tau_1$.

1.2 HIV Introduction

1.2.1 HIV virus and infection

Human immunodeficiency virus (HIV) is a kind of retrovirus that causes disease of acquired immunodeficiency syndrome (AIDS). The size of the mature HIV virus is 110 – 128 nm.[26]

Globally in 2015, an estimated 36.7 million people were living with HIV, ~ 1.1 million died because of AIDS, and the newly infected people were ~ 2.1 million. Each year from 2000 to 2015, there were ~ 28 to 40 million people living with HIV with an increasing trend, 2 to 1 million people died of AIDS related diseases with a decreasing trend, and 3 to 2 million people got newly infected with HIV with a decreasing trend. From the start of the epidemic, there have been ~ 78 million people infected with HIV and ~ 35 million people died from AIDS related illness.[27] Because increasing number of people living with HIV have access to the HIV antiretroviral therapy, the number of death is decreasing, and the newly infection number is bigger than the death number, the total number of people living with HIV has an increasing trend. Even though the number of AIDS death has declined due to HIV antiretroviral treatments, there is still no vaccine available against HIV. The typical cost for HIV treatment is ~ $ 25,000 /year.[28, 29]

HIV virus enters host cell through two different pathways. One is through direct membrane fusion between the viral and host cell membrane; the other one is through endocytosis.[30-32] There were electron microscopy studies of the HIV viral entry process in early 1990s. There were major steps for the direct membrane fusion pathway. First, the HIV virus binds to host cell membrane, then the outer leaflet of HIV and host cell membranes merge, followed by a membrane pore formation, and the entry of the HIV contents into the host cell during infection. Figure 1.14 shows the direct membrane fusion process and relevant fusion model. This process is pH independent and the viral entry process happens within 1-3 mins at 37 °C. The endocytic pathway was also observed by electron microscopy and the viral entry process happens a few mins later.[30]

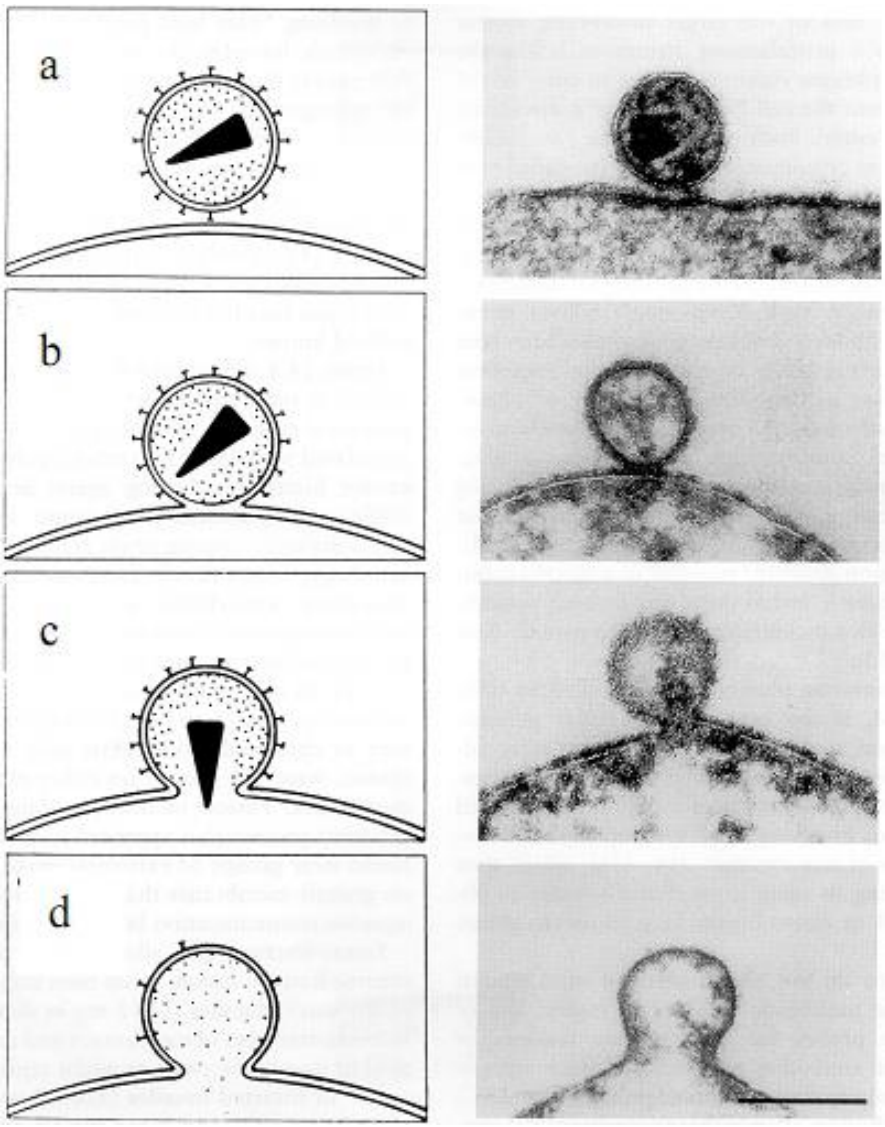

Figure 1.14 Electron microscopy (right panel) and the relevant model (left panel) of HIV- host cell viral entry process. (a) HIV virus binding to host cell, (b) HIV and host cell membrane hemifusion, (c) large viral pore formation and (d) HIV viral components released into host cell. In the model, the spikes represent HIV viral membrane protein, black triangle is the viral RNA and black dots are other components including proteins.[30]

Membrane fusion between the HIV virus and the target host cell membrane is the initial process of AIDS infection. The fusion is mediated by the viral glycoproteins gp160, which is a dimer composed of gp120 and gp41 via non-covalent interaction.[33] gp120 is the receptor binding protein and gp41 is the transmembrane fusion protein.[34] gp120 and gp41 dimers are assembled as trimers and there are ~ 14 trimers on each virion by cryoelectron microscopy.[35, 36] gp120 interacts with cell surface protein CD4 and chemokine receptor CXCR4 or CCR5 sequentially. Then gp120 moves away and gp41 is exposed to interact with host cell membrane.[32, 37]

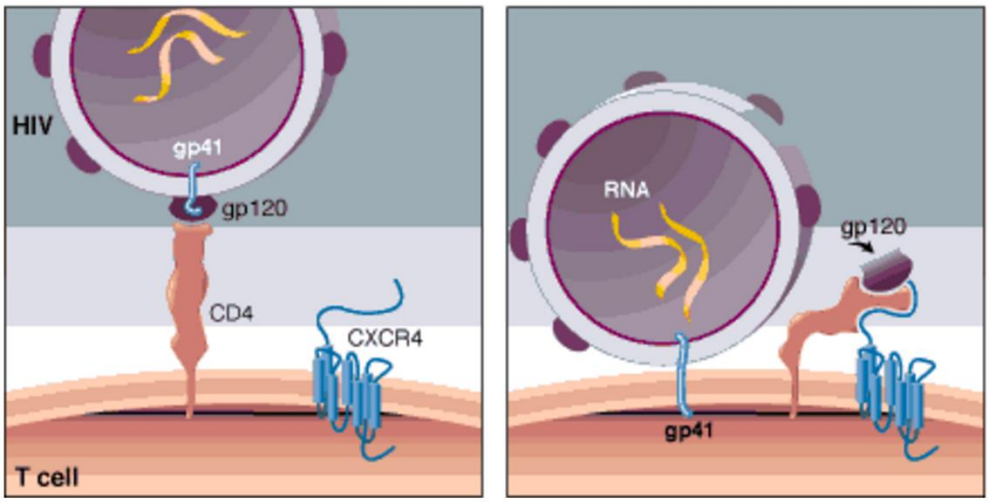

Figure 1.15 HIV interacts with T cell surface protein CD4 and chemokine receptor CXCR4. HIV gp120 protein interacts with T cell CD4 and CXCR4 sequentially and moves away, then gp41 get exposed to interact with cell membrane.[38]

1.2.2 HIV gp41

Transmembrane protein gp41 catalyzes the membrane joining or fusion between the viral and host cell membrane. A general feature of HIV gp41 is shown in figure 1.16 A. From N- to C-terminal, it is the fusion peptide (FP), N-heptad repeat (NHR), loop linker, C-heptad repeat (CHR), the transmembrane domain (TM) and the endo-domain (Endo) or cytoplasmic domain.

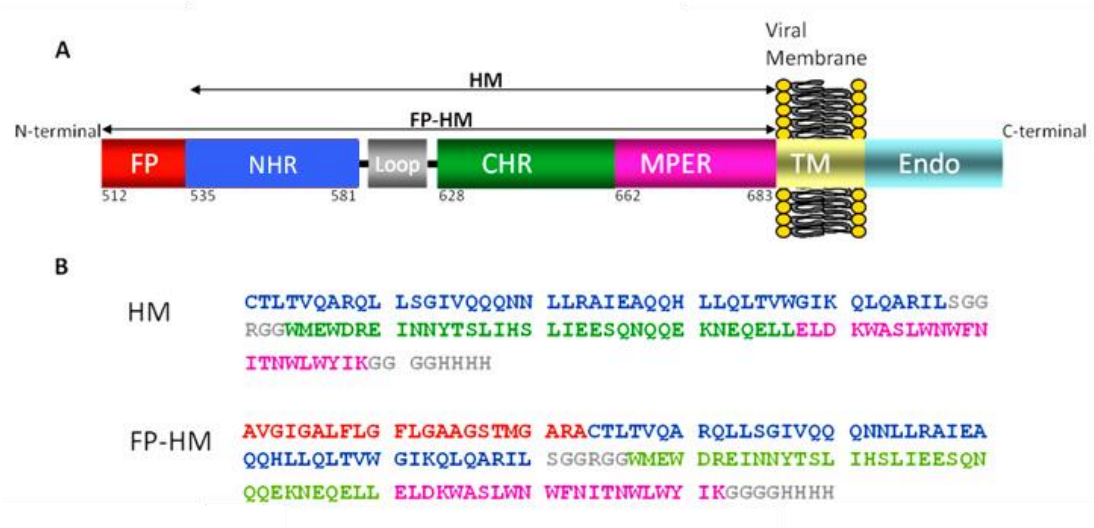

Figure 1.16 Schematic representation (A) and partial sequences (B) of HIV-1 gp41 protein. Colored boxes show the functional regions of gp41. Form N terminal to C terminal, FP is fusion peptide region, NHR and CHR is N- heptad repeat and C-heptad repeat respectively, Loop is the loop region, MPER is the membrane proximal external region, TM is the transmembrane domain, and Endo is the endodomain or cytoplasmic domain. The ectodomain without FP is HM protein, and the full ectodomain including FP of gp41 is FP-HM. FP containing protein could induce more fusion.[39, 40] The amino acid sequence of HM and FP-HM (B) is color coded according to the different domains.[39] A minimal six residues loop SGGRGG replaces the native loop and does not affect the SHB assembly.[41, 42]

During fusion, fusion protein gp41 undergoes three major states, which are pre- fusion native state, extended pre- hairpin state, and post fusion hairpin state (six helical bundle or SHB) (figure 1.17).[43-45] In native state before fusion, gp41 exists as trimers covered by three gp120s. X-ray crystallography reveals the native trimer state of soluble trimer gp140; a near-native gp160 with N-terminal four residues of MPER and without transmembrane and cytoplasmic domains of gp41.The electron density for FP part is weak and diffuse and is likely lack of regular secondary

structure.[46] gp41 interacts with the cell membrane with FP part and exists as extended pre-hairpin state after gp120 moves away due to receptor binding. The structure of gp41 fusion intermediates is not clear. There is evidence to support the existence of pre-hairpin folding by inhibited membrane fusion with treatment of CHR analog short peptide such as C34 and T20 designed to bind to NHR and prevent CHR and NHR from folding to SHB state.[47-50] The completion of SHB formation is essential for membrane fusion pore enlargement and inhibition of SHB formation could cause low temperature (4 °C)- arrested fusion pore quickly and irreversibly close.[51] There is high- resolution crystal structure for the final hairpin or SHB state that contains the CHR and NHR part.[52-54]

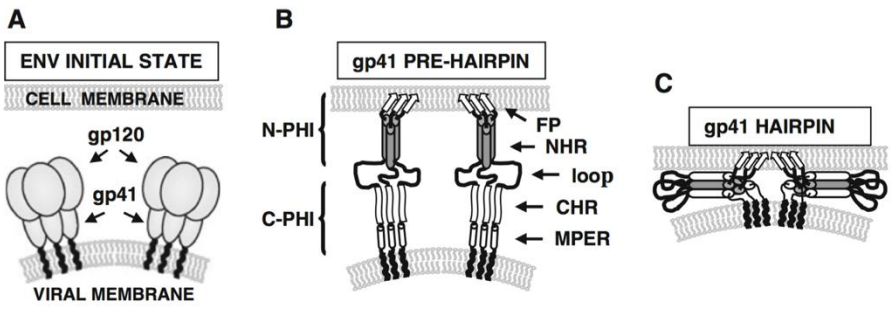

Figure 1.17 Three major states of gp41 during fusion: (A) pre- fusion native state where gp41 is trimeric and non-covalently associated with gp120, (B) extended pre-hairpin state where gp41 has conformational change and interacts with host cell membrane, (C) post fusion hairpin state (six helical bundle states).[41, 43] Figures in (B) and (C) do not show gp120 to focus on the change of gp41.

(a) (b)

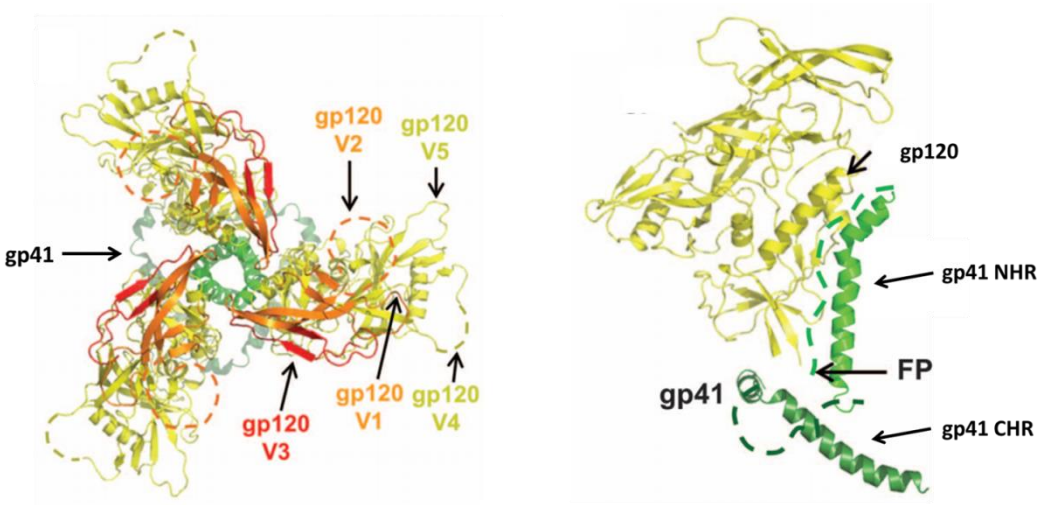

Figure 1.18 X- ray crystallography of soluble gp140 (PDB: 4NCO), a near-native gp160 without MPER and transmembrane domain of gp41 with N-terminal 4 residues of MPER and without transmembrane and cytoplasmic domains of gp41: (a) trimer of gp140, gp120 is in yellow, orange, and red; gp41 is in green. (b) Close view of dimer of gp120 and gp41 in the trimer of gp140.[46]

In SHB, the NHR helices form the interior parallel trimer through hydrophobic interaction and the CHR helices pack in to the grooves on the surface of the interior trimer in an antiparallel orientation to the NHR helices. Figure 1.19 shows a crystal structure of gp41 ectodomain including MPER and part of FP region.

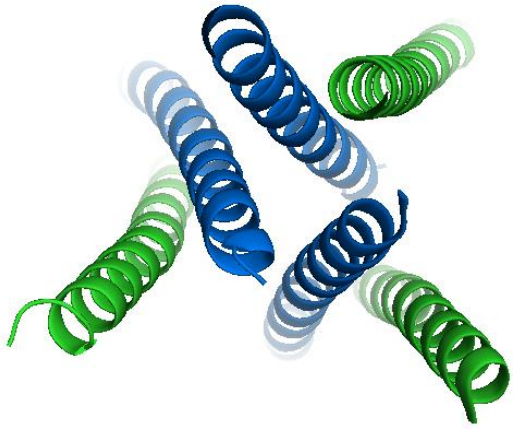

Figure 1.19 Crystal structure of HIV gp41 ectodomain composed of FPPR-CHR-NHR-MPER (Gly^{531} to Leu^{581} in blue and Met^{628} to Tyr^{681} in green; gp41 531-681) (PDB: 2X7R). The gp41 does not include the N-terminal fusion peptide (gp41 512-530). Residues are numbered according to their positions in gp160 complex).[54]

1.2.3 HIV fusion peptide (HFP)

HIV fusion peptide is the N terminal ~ 20 residues. Figure 1.16 displays the amino acid sequence in red. Mutations in FP region of gp41 eliminate/decrease the membrane fusion activity as well as infectivity compared to wild type protein.[55, 56] There is more membrane fusion induced by gp41 ectodomain including the FP region compared to gp41 ectodomain without FP region.[39, 40, 43, 57] It is very important to study HFP to help understand the HIV fusion mechanism. HFP is reasonable substitution as model peptides for gp41 because HFP itself can cause rapid fusion and leakage of lipid vesicles.[57-60] There are HFP structure studies in both detergent micelles and lipid membranes. HFP is majorly helical in dodecylphosphocholine (DPC) or sodium dodecyl sulfate (SDS) micelles studied by liquid state NMR and CD spectroscopy.[61-63] HFP is majorly helical from I4 to L12 in DPC micelles and from I4 to A15 in SDS micelles. In membrane lipid bilayers, there is significant helical, or β sheet structures by CD spectroscopy

depending on the membrane lipid compositions or peptide to lipid ratio.[64, 65] Infrared spectroscopy shows significant helical, or β sheet or a mixture of both structures depending on membrane lipid composition and peptide to lipid ratio.[65, 66] Solid-state NMR chemical shift measurements and 2D ^{13}C- ^{13}C correlation spectroscopy give continuous β stand conformation in the first 16 residues in model membrane that reflects approximate lipid head-group and CHOL composition of host cell of HIV-1 virus.[67-69] β sheet structure of HFP is probably the biological relevant structure. There is FP structure dependence on CHOL. HFP has major β sheet structure in membrane with CHOL, and has a mixture of β sheet and α helical structure in membrane without CHOL.[56, 70, 71] There is a significant population of antiparallel β stand oligomer/aggregate states by both close proximity studies via 2D ^{13}C- ^{13}C correlation experiments and distance measurements by ^{13}C-^{15}N REDOR.[68] A minor fraction of parallel β strand structure, which is at most 0.15, and a major antiparallel is confirmed by quantitative analysis of ^{13}C-^{15}N REDOR data of HFP constructs with selected labeling at specific residues.[72] A major antiparallel structure of FP is also supported for the strand conformation when it is in the SHB state (FP-Hairpin) by SSNMR.[73]

Studies have shown that FP membrane location correlates with fusion. There is a strong correlation between HFP insertion depth and fusion activity by REDOR SSNMR and lipid mixing assays.[14, 55, 74] In SSNMR experiments, a specific residue of HFP backbone is ^{13}CO labeled. ^{13}C-^{31}P REDOR is extensively used to measure the distance from membrane surface since ^{31}P comes from the lipid head-group. ^{13}C- ^{19}F REDOR is widely used to study the proximity to the membrane center or the middle of one leaflet, while there is $^{1}H \rightarrow ^{19}F$ substitution at 16-C or 5-C respectively. It turns out that HFP V2E mutant is located at the membrane surface, while HFP monomer inserts into a single membrane leaflet and HFP trimer

inserts more deeply into the membrane center. Lipid mixing data shows that the membrane fusion rate of HFP trimer is 15-40 times higher than that of HFP monomer.[74] Thus, there is strong correlation between HFP membrane insertion depth and fusogenicity. Although fluorinated lipid is widely used to study the peptide location in the membrane hydrophobic core, using fluorinated lipid has the potential to change membrane bilayer structure.[75] A recent developed ^{13}C- ^{2}H REDOR by Dr. WELIKY has been used to study peptide location in native membrane lipid bilayer because ^{2}H substitution of ^{1}H in the lipid is chemically equivalent and will not change the structure of membrane.[2, 16, 70]

Besides FP membrane location, studies have shown that Cholesterol (CHOL) also correlates with HFP fusogenicity. Depletion of cellular CHOL reduces HIV-1 binding to cells and inhibits HIV virus induced cell-cell fusion. HFP induced model membrane fusion studies indicate that there is faster fusion in membranes that contain CHOL and more fusion when there is more CHOL.[60, 74, 76, 77]

Our current work focuses on structure, membrane location and membrane dynamics study of HFP- the N- terminal 23 residues of gp41 to help understand HIV membrane fusion mechanism. We study the peptide structure and membrane location by peptide ^{13}C – membrane ^{2}H REDOR SSNMR with deuterated phospholipid and CHOL. To understand the role of CHOL in fusion, we compare the peptide contact to phospholipid vs CHOL. We study deuterated phospholipid and CHOL ^{2}H relaxation times to help understand membrane perturbation by HFP and role of CHOL in this membrane perturbation by static ^{2}H – NMR method.

REFERENCES

REFERENCES

1. Duer, M.J., *Solid-State NMR Spectroscopy Principles and Applications*. 2002: Blackwell Science.

2. Xie, L., *Solid State Nuclear Magnetic Rosonance Studies of Structures and Membrane Locations of Peptides*, in *Chemistry*. 2014, Michigan State University.

3. Ghosh, U., *Solid State NMR Studies of Structure and Dynamics of Membrane Associated Influenza Fusion Peptides*, in *Chemistry*. 2016, Michigan State University.

4. Thomas C. Farrar, E.D.B., *Pulse and Fourier transform NMR Introduction to theory and methods*. 1971: Academic Press.

5. Rabi, II, N.F. Ramsey, and J. Schwinger, *USE OF ROTATING COORDINATES IN MAGNETIC RESONANCE PROBLEMS.* Reviews of Modern Physics, 1954. **26**(2): p. 167-171.

6. Keeler, J., *Understanding NMR spectroscopy*. 2005, Wiley.

7. Cisnetti, F., et al., *Determination of chemical shift anisotropy tensors of carbonyl nuclei in proteins through cross-correlated relaxation in NMR.* Chemphyschem, 2004. **5**(6): p. 807-814.

8. Loth, K., P. Pelupessy, and G. Bodenhausen, *Chemical shift anisotropy tensors of carbonyl, nitrogen, and amide proton nuclei in proteins through cross-correlated relaxation in NMR spectroscopy.* Journal of the American Chemical Society, 2005. **127**(16): p. 6062-6068.

9. Baldus, M.W.a.M., *CHAPTER 1 Introduction to biological solid-state NMR*, in *Advances in Biological Solid-State NMR: Proteins and Membrane-Active Peptides*, A.N. Frances Separovic, Editor. 2014, Royal Society of Chemistry. p. P001-608.

10. Ramsey, N.F. and E.M. Purcell, *INTERACTIONS BETWEEN NUCLEAR SPINS IN MOLECULES.* Physical Review, 1952. **85**(1): p. 143-144.

11. Hahn, E.L. and D.E. Maxwell, *SPIN ECHO MEASUREMENTS OF NUCLEAR SPIN COUPLING IN MOLECULES.* Physical Review, 1952. **88**(5): p. 1070-1084.

12. *Coupling constants*. Available from: http://sopnmr.ucsd.edu/coupling.htm.

13. Nethercott, M.J., *Sample Preparation and 2D Solid State Nuclear Magnetic Resonance Studies of the FP-Hairpin Construct of the HIV gp41 protein*, in *Chemistry*. 2012, Michigan State University.

14. Qiang, W., Y. Sun, and D.P. Weliky, *A strong correlation between fusogenicity and membrane insertion depth of the HIV fusion peptide.* Proceedings of the National Academy of Sciences of the United States of America, 2009. **106**(36): p. 15314-15319.

15. Ghosh, U., et al., *Closed and Semiclosed Interhelical Structures in Membrane vs Closed and Open Structures in Detergent for the Influenza Virus Hemagglutinin Fusion Peptide and Correlation of Hydrophobic Surface Area with Fusion Catalysis.* Journal of the American Chemical Society, 2015. **137**(24): p. 7548-7551.

16. Xie, L., et al., *Residue-specific membrane location of peptides and proteins using specifically and extensively deuterated lipids and C-13-H-2 rotational-echo double-resonance solid-state NMR.* Journal of Biomolecular Nmr, 2013. **55**(1): p. 11-17.

17. Spiess, K.S.-R.H.W., *Multidimensional solid-state NMR and polymers*. 1994: ACADEMIC PRESS INC.

18. Harris, R.K., *Nuclear Magnetic Resonance Spectroscopy*. Longman Scientific & Technical. 1986, England.

19. Seelig, J., *DEUTERIUM MAGNETIC-RESONANCE - THEORY AND APPLICATION TO LIPID-MEMBRANES.* Quarterly Reviews of Biophysics, 1977. **10**(3): p. 353-418.

20. Andrew, E.R., A. Bradbury, and R.G. Eades, *NUCLEAR MAGNETIC RESONANCE SPECTRA FROM A CRYSTAL ROTATED AT HIGH SPEED.* Nature, 1958. **182**(4650): p. 1659-1659.

21. Tycko, R., *Biomolecular solid state NMR: Advances in structural methodology and applications to peptide and protein fibrils.* Annual Review of Physical Chemistry, 2001. **52**: p. 575-606.

22. Gullion, T. and J. Schaefer, *ROTATIONAL-ECHO DOUBLE-RESONANCE NMR.* Journal of Magnetic Resonance, 1989. **81**(1): p. 196-200.

23. Yannoni, C.S., *HIGH-RESOLUTION NMR IN SOLIDS - THE CPMAS EXPERIMENT.* Accounts of Chemical Research, 1982. **15**(7): p. 201-208.

24. Meier, B.H., *CROSS POLARIZATION UNDER FAST MAGIC ANGLE SPINNING - THERMODYNAMICAL CONSIDERATIONS.* Chemical Physics Letters, 1992. **188**(3-4): p. 201-207.

25. Bak, M., J.T. Rasmussen, and N.C. Nielsen, *SIMPSON: A general simulation program for solid-state NMR spectroscopy.* Journal of Magnetic Resonance, 2000. **147**(2): p. 296-330.

26. Gentile, M., et al., *DETERMINATION OF THE SIZE OF HIV USING ADENOVIRUS TYPE-2 AS AN INTERNAL LENGTH MARKER.* Journal of Virological Methods, 1994. **48**(1): p. 43-52.

27. *http://www.unaids.org/sites/default/files/media_asset/UNAIDS_FactSheet_en.pdf*. 2016.

28. *cdc.gov.*

29. *https://aidsinfo.nih.gov/guidelines*.

30. Grewe, C., A. Beck, and H.R. Gelderblom, *HIV - EARLY VIRUS-CELL INTERACTIONS.* Journal of Acquired Immune Deficiency Syndromes and Human Retrovirology, 1990. **3**(10): p. 965-974.

31. Miyauchi, K., et al., *HIV Enters Cells via Endocytosis and Dynamin-Dependent Fusion with Endosomes.* Cell, 2009. **137**(3): p. 433-444.

32. White, J.M., et al., *Structures and mechanisms of viral membrane fusion proteins: Multiple variations on a common theme.* Critical Reviews in Biochemistry and Molecular Biology, 2008. **43**(3): p. 189-219.

33. Chan, D.C. and P.S. Kim, *HIV entry and its inhibition.* Cell, 1998. **93**(5): p. 681-684.

34. Rizzuto, C.D., et al., *A conserved HIV gp120 glycoprotein structure involved in chemokine receptor binding.* Science, 1998. **280**(5371): p. 1949-1953.

35. Zhu, P., et al., *Distribution and three-dimensional structure of AIDS virus envelope spikes.* Nature, 2006. **441**(7095): p. 847-852.

36. Wyatt, R. and J. Sodroski, *The HIV-1 envelope glycoproteins: Fusogens, antigens, and immunogens.* Science, 1998. **280**(5371): p. 1884-1888.

37. Liu, J., et al., *Molecular architecture of native HIV-1 gp120 trimers.* Nature, 2008. **455**(7209): p. 109-U76.

38. Balter, M., *AIDS Research: New Hope in HIV Disease.* Science, 1996. **274**(5295): p. 1988.

39. Banerjee, K. and D.P. Weliky, *Folded Monomers and Hexamers of the Ectodomain of the HIV gp41 Membrane Fusion Protein: Potential Roles in Fusion and Synergy Between the Fusion Peptide, Hairpin, and Membrane-Proximal External Region.* Biochemistry, 2014. **53**(46): p. 7184-7198.

40. Ratnayake, P.U., et al., *pH-dependent vesicle fusion induced by the ectodomain of the human immunodeficiency virus membrane fusion protein gp41: Two kinetically distinct processes and fully-membrane-associated gp41 with predominant beta sheet fusion peptide conformation.* Biochimica Et Biophysica Acta-Biomembranes, 2015. **1848**(1): p. 289-298.

41. Sackett, K., et al., *Hairpin Folding of HIV gp41 Abrogates Lipid Mixing Function at Physiologic pH and Inhibits Lipid Mixing by Exposed gp41 Constructs.* Biochemistry, 2009. **48**(12): p. 2714-2722.

42. Tan, K.M., et al., *Atomic structure of a thermostable subdomain of HIV-1 gp41.* Proceedings of the National Academy of Sciences of the United States of America, 1997. **94**(23): p. 12303-12308.

43. Sackett, K., A. TerBush, and D.P. Weliky, *HIV gp41 six-helix bundle constructs induce rapid vesicle fusion at pH 3.5 and little fusion at pH 7.0: understanding pH dependence of*

protein aggregation, membrane binding, and electrostatics, and implications for HIV-host cell fusion. European Biophysics Journal with Biophysics Letters, 2011. **40**(4): p. 489-502.

44. Melikyan, G.B., *Common principles and intermediates of viral protein-mediated fusion: the HIV-1 paradigm.* Retrovirology, 2008. **5**: p. 13.

45. Tamm, L.K., J. Lee, and B.Y. Liang, *Capturing Glimpses of an Elusive HIV Gp41 Prehairpin Fusion Intermediate.* Structure, 2014. **22**(9): p. 1225-1226.

46. Julien, J.P., et al., *Crystal Structure of a Soluble Cleaved HIV-1 Envelope Trimer.* Science, 2013. **342**(6165): p. 1477-1483.

47. Kilby, J.M., et al., *Potent suppression of HIV-1 replication in humans by T-20, a peptide inhibitor of gp41-mediated virus entry.* Nature Medicine, 1998. **4**(11): p. 1302-1307.

48. Kliger, Y., et al., *Mode of action of an antiviral peptide from HIV-1 - Inhibition at a post-lipid mixing stage.* Journal of Biological Chemistry, 2001. **276**(2): p. 1391-1397.

49. Weissenhorn, W., et al., *Structural basis for membrane fusion by enveloped viruses.* Molecular Membrane Biology, 1999. **16**(1): p. 3-9.

50. Furuta, R.A., et al., *Capture of an early fusion-active conformation of HIV-1 gp41.* Nature Structural Biology, 1998. **5**(4): p. 276-279.

51. Markosyan, R.M., F.S. Cohen, and G.B. Melikyan, *HIV-1 envelope proteins complete their folding into six-helix bundles immediately after fusion pore formation.* Molecular Biology of the Cell, 2003. **14**(3): p. 926-938.

52. Weissenhorn, W., et al., *Atomic structure of the ectodomain from HIV-1 gp41.* Nature, 1997. **387**(6631): p. 426-430.

53. Chan, D.C., et al., *Core structure of gp41 from the HIV envelope glycoprotein.* Cell, 1997. **89**(2): p. 263-273.

54. Buzon, V., et al., *Crystal Structure of HIV-1 gp41 Including Both Fusion Peptide and Membrane Proximal External Regions.* Plos Pathogens, 2010. **6**(5): p. 7.

55. Freed, E.O., et al., *A MUTATION IN THE HUMAN-IMMUNODEFICIENCY-VIRUS TYPE-1 TRANSMEMBRANE GLYCOPROTEIN-GP41 DOMINANTLY INTERFERES WITH FUSION AND INFECTIVITY.* Proceedings of the National Academy of Sciences of the United States of America, 1992. **89**(1): p. 70-74.

56. Gabrys, C.M., et al., *Solid-State Nuclear Magnetic Resonance Measurements of HIV Fusion Peptide (CO)-C-13 to Lipid P-31 Proximities Support Similar Partially Inserted Membrane Locations of the alpha Helical and beta Sheet Peptide Structures.* Journal of Physical Chemistry A, 2013. **117**(39): p. 9848-9859.

57. Cheng, S.F., et al., *The fusion peptide domain is the primary membrane-inserted region and enhances membrane interaction of the ectodomain of HIV-1 gp41.* Molecular Membrane Biology, 2010. **27**(1): p. 31-44.

58. Durell, S.R., et al., *What studies of fusion peptides tell us about viral envelope glycoprotein-mediated membrane fusion.* Molecular Membrane Biology, 1997. **14**(3): p. 97-112.

59. Epand, R.M., *Fusion peptides and the mechanism of viral fusion.* Biochimica Et Biophysica Acta-Biomembranes, 2003. **1614**(1): p. 116-121.

60. Lai, A.L., et al., *Fusion Activity of HIV gp41 Fusion Domain Is Related to Its Secondary Structure and Depth of Membrane Insertion in a Cholesterol-Dependent Fashion.* Journal of Molecular Biology, 2012. **418**(1-2): p. 3-15.

61. Li, Y.L. and L.K. Tamm, *Structure and plasticity of the human immunodeficiency virus gp41 fusion domain in lipid micelles and bilayers.* Biophysical Journal, 2007. **93**(3): p. 876-885.

62. Jaroniec, C.P., et al., *Structure and dynamics of micelle-associated human immunodeficiency virus gp41 fusion domain.* Biochemistry, 2005. **44**(49): p. 16167-16180.

63. Gabrys, C.M. and D.P. Weliky, *Chemical shift assignment and structural plasticity of a HIV fusion peptide derivative in dodecylphosphocholine micelles.* Biochimica Et Biophysica Acta-Biomembranes, 2007. **1768**(12): p. 3225-3234.

64. Chang, D.K., S.F. Cheng, and W.J. Chien, *The amino-terminal fusion domain peptide of human immunodeficiency virus type 1 gp41 inserts into the sodium dodecyl sulfate micelle primarily as helix with a conserved glycine at the micelle-water interface.* Journal of Virology, 1997. **71**(9): p. 6593-6602.

65. Rafalski, M., J.D. Lear, and W.F. Degrado, *PHOSPHOLIPID INTERACTIONS OF SYNTHETIC PEPTIDES REPRESENTING THE N-TERMINUS OF HIV GP41.* Biochemistry, 1990. **29**(34): p. 7917-7922.

66. Castano, S. and B. Desbat, *Structure and orientation study of fusion peptide FP23 of gp41 from HIV-1 alone or inserted into various lipid membrane models (mono-, bi- and multibi-layers) by FT-IR spectroscopies and Brewster angle microscopy.* Biochimica Et Biophysica Acta-Biomembranes, 2005. **1715**(2): p. 81-95.

67. Yang, J., et al., *Oligomeric beta-structure of the membrane-bound HIV-1 fusion peptide formed from soluble monomers.* Biophysical Journal, 2004. **87**(3): p. 1951-1963.

68. Qiang, W., M.L. Bodner, and D.P. Weliky, *Solid-state NMR Spectroscopy of human immunodeficiency virus fusion peptides associated with host-cell-like membranes: 2D correlation spectra and distance measurements support a fully extended conformation and models for specific antiparallel strand registries.* Journal of the American Chemical Society, 2008. **130**(16): p. 5459-5471.

69. Aloia, R.C., H.R. Tian, and F.C. Jensen, *LIPID-COMPOSITION AND FLUIDITY OF THE HUMAN-IMMUNODEFICIENCY-VIRUS ENVELOPE AND HOST-CELL PLASMA-MEMBRANES.* Proceedings of the National Academy of Sciences of the United States of America, 1993. **90**(11): p. 5181-5185.

70. Jia, L.H., et al., *REDOR solid-state NMR as a probe of the membrane locations of membrane-associated peptides and proteins.* Journal of Magnetic Resonance, 2015. **253**: p. 154-165.

71. Yang, J., C.M. Gabrys, and D.P. Weliky, *Solid-state nuclear magnetic resonance evidence for an extended beta strand conformation of the membrane-bound HIV-1 fusion peptide.* Biochemistry, 2001. **40**(27): p. 8126-8137.

72. Schmick, S.D. and D.P. Weliky, *Major Antiparallel and Minor Parallel beta Sheet Populations Detected in the Membrane-Associated Human Immunodeficiency Virus Fusion Peptide.* Biochemistry, 2010. **49**(50): p. 10623-10635.

73. Kelly Sackett, M.J.N., Zhaoxiong Zheng and David P. Weliky, *Solid-State NMR Spectroscopy of the HIV gp41 Membrane Fusion Protein Supports Intermolecular Antiparallel β Sheet Fusion Peptide Structure in the Final Six- Helix Bundle State.* Journal of molecular biology, 2014. **426**(5): p. 1077-1094.

74. Rong Yang, M.P., ‡ Francis J. Castellino,‡ and David P. Weliky*,†, *A Trimeric HIV-1 Fusion Peptide Construct Which Does Not Self-Associate in Aqueous Solution and Which Has 15-Fold Higher Membrane Fusion Rate.* Journal of American Chemical Society, 2004. **126**(45): p. 14722-14723.

75. Hirsh, D.J., et al., *A new monofluorinated phosphatidylcholine forms interdigitated bilayers.* Biophysical Journal, 1998. **75**(4): p. 1858-1868.

76. Liao, Z.H., et al., *Lipid rafts and HIV pathogenesis: Host membrane cholesterol is required for infection by HIV type 1.* Aids Research and Human Retroviruses, 2001. **17**(11): p. 1009-1019.

77. Yang, S.T., et al., *HIV gp41-mediated membrane fusion occurs at edges of cholesterol-rich lipid domains.* Nature Chemical Biology, 2015. **11**(6): p. 424-+.

Chapter 2 - Materials and methods

2.1 Materials

Protected amino acids and Wang resins were purchased from Peptides International (Louisville, KY), Sigma-Aldrich (St. Louis, MO) and Dupont, and lipids were purchased from Avanti Polar Lipids (Alabaster, Al). The phosphatidylcholine (PC) lipid was typically 1,2-dipalmitoyl-*sn*-glycero-3-phosphocholine (DPPC) and the phosphatidylglycerol (PG) lipid was typically 1,2-dipalmitoyl-*sn*-glycero-3-phospho-(1'-*rac*-glycerol) (sodium salt) (DPPG). Some other lipids were also used, including 1-palmitoyl-2-oleoyl-*sn*-glycero-3-phosphocholine (POPC), 1-palmitoyl-2-oleoyl-*sn*-glycero-3- phospho-(1'-*rac*-glycerol) (sodium salt) (POPG), 1,2-dioleoyl-*sn*-glycero-3-phosphocholine (DOPC), 1,2-dioleoyl-*sn*-glycero-3-phospho-(1'-*rac*-glycerol) (sodium salt) (DOPG), 1,2-dipalmitoyl-*sn*-glycerol-3-phosphocholine (DMPC) and 1,2-dipalmitoyl-*sn*-glycero-3-phospho-(1'-*rac*-glycerol) (sodium salt) (DMPG). 1,2-(dipalmitoyl-2,2,2,2-d4)-*sn*-glycero-3-phosphocholine (PC-d4), 1,2-(dipalmitoyl-7,7,7,7,8,8,8,8-d8)-*sn*-glycero-3-phosphocholine (PC-d8) and 1,2-(dipalmitoyl-15,15,15,15,16,16,16,16,16,16-d10)-*sn*-glycero-3-phosphocholine (PC-d10) lipids were custom-synthesized by Avanti (Alabaster, Al) using deuterated palmitic acids obtained from CDN Isotopes. Protected labeled amino acids were obtained from Cambridge Isotopes (Andover, MA) or Sigma-Aldrich (St. Louis, MO). Other reagents including cholesterol-2,2,3,4,4,6-d6 (Chol-d6) and cholesterol-25,26,26,26,27,27,27-d7 (Chol-d7) were typically obtained from Sigma-Aldrich (St. Louis, MO).

2.2 Peptide sequences, preparation and purification

HFP: AVGIGALFLGFLGAAGSTMGARSWKKKKKKG;

HFP_V2E: AEGIGALFLGFLGAAGSTMGARSWKKKKKKG;

HFP_L9R: AVGIGALFRGFLGAAGSTMGARSWKKKKKKG;

KALP: Acetyl-GKKLALALALALALALALALKKA-NH_2.

The underlined residues of HFPs are N-terminal fusion peptide (FP) residues of fusion protein gp41 subunit of the HIV virus, LAV_{1a} strain, without (HFP) and with point mutation (HFP_V2E and HFP_L9R).[1, 2] The HFP peptides have a non-native W to permit FP quantitation by 280 nm absorbance, and a non-native C-terminal tag to increase the aqueous solubility of the peptides which helps purification and further NMR sample preparation. Manual solid-phase peptide synthesis (SPPS) was done using Fmoc chemistry for all the peptide sequences.[3, 4] Wang resin with attached glycine and alanine were used for HFP sequences and KALP, respectively. HFP was ^{13}CO labeled at G5, G10, L12 and G16. HFP_V2E was ^{13}CO labeled at G5, and HFP_L9R was ^{13}CO labeled at G5 and G10. KALP was ^{13}CO labeled at A5, A7, A17 and A19. There was only one residue ^{13}CO labeled in each labeling sequence. The synthesized peptides were purified using reversed phase HPLC with a preparative C4 column using water - acetonitrile gradient containing 0.1% TFA. TFA is the ion- pair reagent and helps maintain the acidic pH (~ 2) of the eluting solution and also neutralizes the carboxylate group of the peptide. The HPLC purification program for each peptide is in Appendix. Peptide content in the fractions was analyzed by matrix assisted laser desorption/ionization (MALDI)- TOF mass spectrometry using the intensity of the peptide mass peak relative to the sum of mass peak intensities. The purest fraction contained 90-95% peptide and was used to make solid-state NMR (SSNMR) samples. For a 200 μmole scale synthesis, this fraction contained ~ 12 μmole HFP.

2.3 Peptide associated membrane sample preparation for MAS and static solid state NMR

Samples for NMR experiments were prepared by the same procedure to better analyze the data in terms of dependence on sample composition. Each sample contained ~1μmole peptide, 40μmole PC, 10μmole PG, and either 25, 12.5, 6.25, or 0μmole CHOL, which respectively correspond to

cholesterol lipid fraction f_{Chol} = 0.33, 0.20, 0.11, and 0. NMR samples were typically prepared by organic cosolubilization method as following: phospholipids (with and without CHOL) were dissolved in chloroform and solvent was then removed with nitrogen gas and overnight vacuum pumping.[5, 6] The dry lipid film and lyophilized peptide were dissolved in 2,2,2-trifuoroethanol:1,1,1,3,3,3-hexafluoroisopropanol:chloroform with 2:2:3 volume ratio, and solvent was then removed with nitrogen gas and overnight vacuum pumping. The peptide +lipid film was suspended in 3 mL aqueous buffer containing 5mM HEPES and 10mM MES at pH 7.4 with 0.01 % NaN_3 preservative. The suspension was subjected to ten freeze/thaw cycles and each cycle includes rapid freezing in liquid nitrogen followed by thawing in hot water at ~ 60 °C, then with addition of 20 mL more buffer, and ultracentrifugation at 270000g for four hours, with free peptide soluble in the supernatant. There was typically 0.85 fraction membrane-bound FP, as compared to 0.5 fraction for samples without anionic lipid, which evidences both hydrophobic and electrostatic contributions to binding. The centrifugation pellet was harvested, lyophilized, and packed in a 4 mm diameter magic angle spinning (MAS) rotor which contained 10μL buffer. An additional 10μL buffer was added after packing.

Some FP samples were prepared by initial FP binding to unilamellar vesicles in aqueous solution which is also named as aqueous vesicle binding method as following: Lipids were dissolved in chloroform and the solvent was removed by nitrogen gas followed by vacuum pumping overnight. The lipid film was suspended in 2mL aqueous buffer at pH 7.4 followed by 10 freeze/thaw cycles. Large unilamellar vesicles were prepared by extrusion through a polycarbonate filter with 100 nm diameter pores. The extrusion was repeated 20-25 times. There is probably 10 % lipid loss during extrusion process, but the loss of lipid is minimized by extruding ~ 1 mL buffer through the apparatus after collecting the vesicle suspension. The buffer

extrusion mixture is also harvested and the lipid loss is not considered. ~ 20 mL 0.1mM peptide stock solution in pH 7.4 buffer was added dropwise to the extruded vesicles while maintaining the pH 7.4. The feeding peptide: lipid mole ratio is 1:25. The lipid and peptide solution was vortexed overnight and ultra-centrifuged at 270000 g for four hours. The quantity of membrane bound peptide is considered the difference between the total and unbound quantities, which are obtained by measuring A_{280} with ε_{280} = 5700 cm^{-1} M^{-1}. The membrane bound peptide: lipid mole ratio is 1:50 in the pellet. The membrane bound peptide fraction relative to total feed peptide is typically 0.5, and this is probably because there is kinetic barrier for peptide incorporation into the membrane. The typical fraction of membrane-bound FP is 0.85 in organic cosolubilization method where there is no kinetically trapped peptide because peptide and lipids were premixed. The pellet was lyophilized overnight and packed in 4 mm MAS rotor. Typically, ~ 10 μL of buffer (pH 7.4) was added to the rotor before and after packing the sample to rehydrate the peptide bound membrane pellet.

The packed NMR sample was rehydrated overnight at room temperature before NMR experiments.

2.4 Solid state NMR

2.4.1 MAS solid state NMR spectroscopy

Experiments were done with a 9.4 T Agilent Infinity Plus spectrometer using a MAS probe tuned to ^{1}H, ^{13}C, and ^{2}H frequencies. The sample was typically cooled with nitrogen gas at –50 °C with corresponding sample temperature of ~ –30 °C. The REDOR pulse sequence was in time: (1) ^{1}H $\pi/2$ pulse; (2) ^{1}H-^{13}C cross polarization (CP); (3) dephasing period of duration (τ); and (4) ^{13}C detection. S_0 and S_1 REDOR data were acquired alternately and differed in the pulses applied during the dephasing period.[5] For both acquisitions, there was a ^{13}C π pulse at the end of each

rotor cycle except the final cycle, and for S_1, there was also a ^2H π pulse at the midpoint of each cycle. Typical parameters included: (1) ^{13}C transmitter at 160 ppm and ^2H transmitter at the center of the powder pattern; (2) 10 kHz MAS frequency and 1.5ms CP contact time; (3) 50 kHz ^1H π /2 pulse and CP fields; (3) 55-68 kHz ^{13}C CP ramp; (4) 60 kHz ^{13}C π pulses and 100 kHz ^2H π pulses with XY-8 phase cycling applied to all π pulses; and ~70 kHz two-pulse phase-modulated (TPPM) ^1H decoupling during dephasing and acquisition.[7, 8] Pulses were calibrated using a lyophilized peptide that included a single ^{13}CO- ^2H spin pair with r_{CD} = 5.0 Å.[9] Typical recycle delays were 1 s (τ = 2, 8, 16ms), 1.5 s (τ = 24, 32ms), and 2 s (τ = 40 and 48ms). The typical numbers of summed S_0 or S_1 scans were ~ 4000, 7000, 12000, 22000, 32000, 40000, and 50000 for τ= 2, 8, 16, 24, 32, 40, and 48ms, respectively. ^{13}C shifts were externally referenced to the adamantane methylene peak at 40.5 ppm which allows direct comparison to liquid-state NMR databases.[10] Data processing included 100 Hz Gaussian line broadening and baseline correction. S_0 and S_1 are typically integrals over 3 ppm intervals, with $\Delta S/S_0 = (S_0 - S_1)/S_0$ and $\sigma_{\triangle S/S0} = ((\sigma_{S0}/S_0)^2 + (\sigma_{S1}/S_1)^2)^{½} \times (S_1/S_0)$, where σ_{S0} and σ_{S1} are the standard deviations of 10 spectral noise regions with 3 ppm integration width.[11]

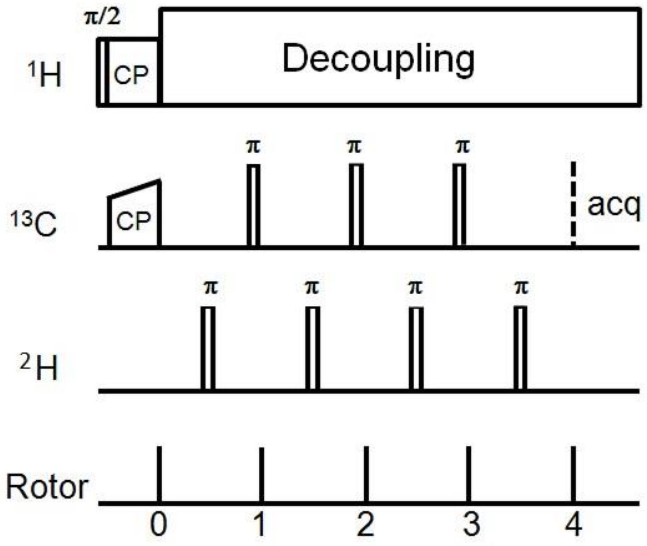

Figure 2.1 ^{13}C – ^{2}H REDOR pulse sequence. Each sequence starts with a CP from ^{1}H to the observed ^{13}C nucleus to enhance the intensity of ^{13}C signal followed by a dephasing and acquisition period. TPPM ^{1}H decoupling was applied during the dephasing and the acquisition periods.

NMR parameters were optimized using I4 peptide with sequence of Acetyl-AEAAAKEAAAKEAAAKA-NH_2 with C-terminal amidation and N-terminal Acetylation.[9] The I4 peptide was synthesized by solid phase peptide synthesis (SPPS) and A8 Cα- ^{2}H and A9 ^{13}CO labeled.[5] Solid state NMR studies have shown that lyophilized I4 peptide has majorly α helical conformation. The distance between A8 Cα- ^{2}H and A9 ^{13}CO labeled nuclei is 5.0 Å with a corresponding ^{13}C- ^{2}H dipolar coupling of 37 Hz.

2.4.2 Static solid state NMR spectroscopy

The overall membrane (lipid/CHOL) structure and motions with and without HFP were evaluated using static ^{2}H NMR spectroscopy typically with quadrupolar echo (quecho) pulse

sequence.[12] The experiments were done on a 9.4 T Agilent Infinity Plus spectrometer with a MAS triple resonance probe tuned to ^2H frequency. The ^2H frequency was 61. 2023333 MHz, and the ^2H $\pi/2$ pulses were calibrated using D_2O (99%). The quecho pulse sequence is, $(\pi/2)_x$ - τ - $(\pi/2)_y$ - τ_1 - detect (Figure 2.2), and this sequence is used to minimize the effects of pulse ring-down.[13, 14] The first $\pi/2$ pulse is the excitation pulse and the second $\pi/2$ pulse is the refocusing pulse. The phase of the first $\pi/2$ pulse is x and the phase of the second $\pi/2$ pulse is alternated between y and –y. The recycle delay is 1s. ^2H spectra were acquired for a fixed τ and τ_1 value at different temperatures. To obtain the ^2H T_2, decay of the acquired signals was measured for different τ and τ_1 with synchronous increment of τ and τ_1. Typical static solid state NMR parameters include 2.2μs ^2H $\pi/2$ pulse, dwell time = 2μs, τ = 40μs and τ_1 = 21μs. The quecho ^2H FID data was typically processed with dc offset because uncorrected dc offset could result a spike at the middle of the spectrum.[15] Experimentally, τ_1 is shorter than τ, so we also need to do data shift to move the maximum echo signal at t = 0 before Fourier Transform (FT) was performed, typically with -11 data shifts and 200 Hz Gaussian line broadening.

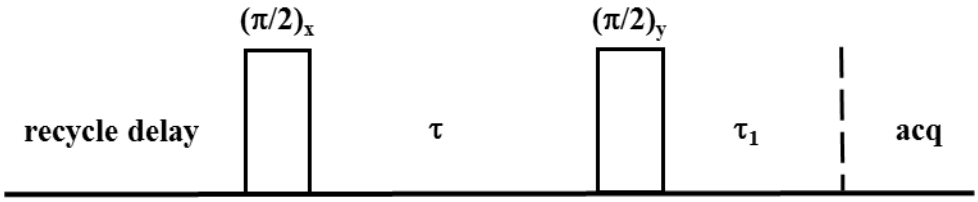

Figure 2.2. "Quecho" pulse sequence.

REFERENCES

REFERENCES

1. Qiang, W. and D.P. Weliky, *HIV Fusion Peptide and Its Cross-Linked Oligomers: Efficient Syntheses, Significance of the Trimer in Fusion Activity, Correlation of beta Strand Conformation with Membrane Cholesterol, and Proximity to Lipid Headgroups.* Biochemistry, 2009. **48**(2): p. 289-301.

2. Freed, E.O., et al., *A MUTATION IN THE HUMAN-IMMUNODEFICIENCY-VIRUS TYPE-1 TRANSMEMBRANE GLYCOPROTEIN-GP41 DOMINANTLY INTERFERES WITH FUSION AND INFECTIVITY.* Proceedings of the National Academy of Sciences of the United States of America, 1992. **89**(1): p. 70-74.

3. Fields, G.B. and R.L. Noble, *SOLID-PHASE PEPTIDE-SYNTHESIS UTILIZING 9-FLUORENYLMETHOXYCARBONYL AMINO-ACIDS.* International Journal of Peptide and Protein Research, 1990. **35**(3): p. 161-214.

4. Merrifield, R.B., *SOLID PHASE PEPTIDE SYNTHESIS .1. SYNTHESIS OF A TETRAPEPTIDE.* Journal of the American Chemical Society, 1963. **85**(14): p. 2149-&.

5. Xie, L., et al., *Residue-specific membrane location of peptides and proteins using specifically and extensively deuterated lipids and C-13-H-2 rotational-echo double-resonance solid-state NMR.* Journal of Biomolecular Nmr, 2013. **55**(1): p. 11-17.

6. Jia, L.H., et al., *REDOR solid-state NMR as a probe of the membrane locations of membrane-associated peptides and proteins.* Journal of Magnetic Resonance, 2015. **253**: p. 154-165.

7. Bennett, A.E., et al., *HETERONUCLEAR DECOUPLING IN ROTATING SOLIDS.* Journal of Chemical Physics, 1995. **103**(16): p. 6951-6958.

8. Terry Gullion, D.B.B., Mark S Conradi, *New, compensated Carr-Purcell sequences.* Journal of Magnetic Resonance, 1990. **89**(3): p. 479-484.

9. Long, H.W. and R. Tycko, *Biopolymer conformational distributions from solid-state NMR: alpha-helix and 3(10)-helix contents of a helical peptide.* Journal of the American Chemical Society, 1998. **120**(28): p. 7039-7048.

10. Morcombe, C.R. and K.W. Zilm, *Chemical shift referencing in MAS solid state NMR.* Journal of Magnetic Resonance, 2003. **162**(2): p. 479-486.

11. Zheng, Z., et al., *Conformational flexibility and strand arrangements of the membrane-associated HIV fusion peptide trimer probed by solid-state NMR spectroscopy.* Biochemistry, 2006. **45**(43): p. 12960-12975.

12. Davis, J.H., *THE DESCRIPTION OF MEMBRANE LIPID CONFORMATION, ORDER AND DYNAMICS BY H-2-NMR*. Biochimica Et Biophysica Acta, 1983. **737**(1): p. 117-171.

13. Duer, M.J., *Solid-State NMR Spectroscopy Principles and Applications*. 2002: Blackwell Science.

14. Spiess, K.S.-R.H.W., *Multidimensional solid-state NMR and polymers*. 1994: ACADEMIC PRESS INC.

15. Christian Schorn, B.T., *NMR Spectroscopy: Data Acquisition*. 2004, WILEY-VCH Verlag GmbH & Co. KGaA.

Chapter 3 - Structure and Membrane Location Studies of HIV Fusion Peptide (HFP) and KALP Peptide

3.1 Introduction

The cell membrane is the stable lamellar bilayer structure composed of lipids and is the physical barrier to molecular diffusion. Aside from lipids, the membrane also contains many types of proteins. And the membrane mass is about equal between lipids and protein for plasma membranes of most animal cells.[1] The protein membrane locations and contacts between protein specific residues and membrane lipid specific regions are important for their functions and can also give insight to protein/membrane biophysical interaction.[2-4] There have been high-resolution protein crystal structures that are obtained generally in non-lamellar media like detergent micelles, detergent-rich bicelles, or lipidic cubic phase. These high resolution structures sometimes provide the protein location information in the non-lamellar phase but typically not in the bilayer phase which is the most relevant model of the cell membrane. Structure of HFP studied in detergent micelle shows majorly helical conformation, while structure of HFP studied in membrane without CHOL show both helical and β sheet secondary structure, and studies in membrane containing ~ 33% CHOL show predominant β strand structure.[5-10]

The membrane locations of HFP have been studied by REDOR NMR method.[11-14] The peptide location relative to the membrane surface can be studied by ^{13}C-^{31}P REDOR. The peptide location in the membrane hydrocarbon core has been extensively studied by incorporating fluorinated lipids. DPPC (C5- ^{19}F) and DPPC (C16- ^{19}F) were fluorinated at C5 and C16. DPPC (C5- ^{19}F) is used to investigate the location of the peptide relative to the half way of one membrane leaflet, and DPPC (C16- ^{19}F) to study the location of the peptide relative

to the membrane center. However, fluorinated DPPC is chemically modified lipid and there is potential perturbation to the membrane structure. Studies have shown that 100% DPPC (C16- ^{19}F) would form interdigitated membrane.[15] To maintain membrane bilayer and achieve maximum REDOR dephasing, generally only 10% fluorinated lipids were incorporated, but these dilute and randomly distributed nuclei would give rise to the inaccuracy of inter-nuclear distance correlation with membrane insertion depth.[16]

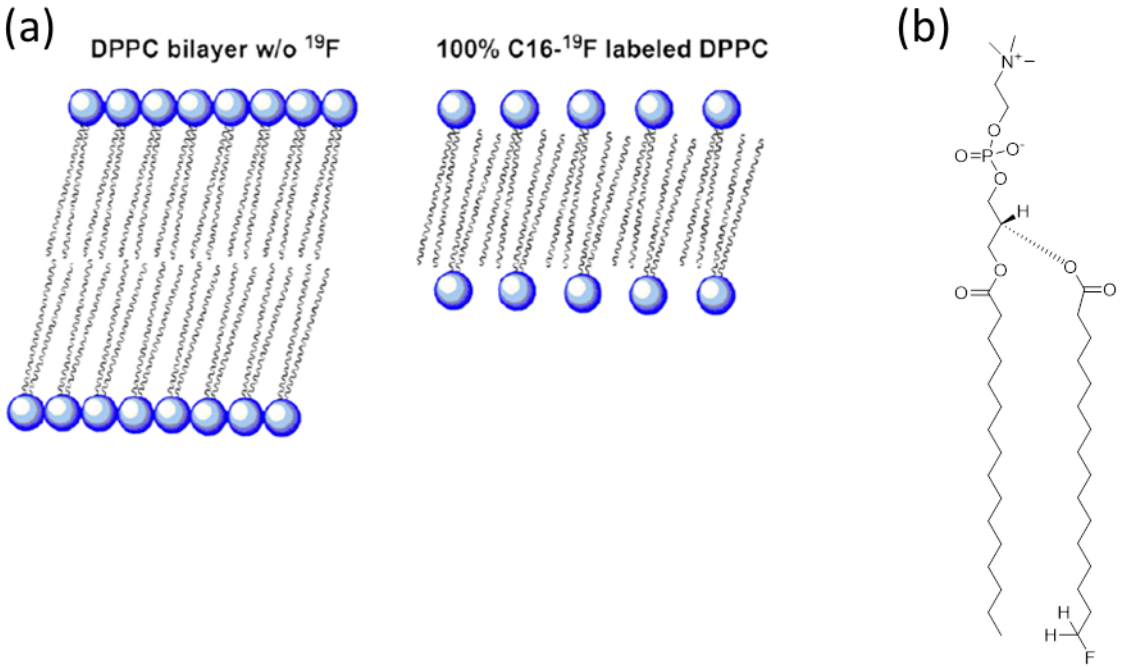

Figure 3.1 (a) DPPC bilayer regular membrane (left) without chemically modified lipid and interdigitated membrane (right) composed of C16- ^{19}F DPPC with a ^{1}H→ ^{19}F substitution at C16, (b) chemical structure of C16- ^{19}F DPPC lipid.[15, 17]

A recently developed method in our group is to use ^{13}C-^{2}H REDOR method to study peptide membrane location in the membrane hydrophobic core using deuterated lipids or CHOL.[11, 13, 14, 18, 19] This method is advantageous because, ^{2}H is chemically equivalent to ^{1}H, and would not cause perturbation to the membrane. Besides, it would have a continuous band of ^{2}H labeling

in the membrane, which could more accurately reflect the membrane location according to the closest peptide −membrane contact (see figure 3.2B). Non−chemically modified phosphatidylcholine (PC) and CHOL are available with a wide variety of ^{2}H labeling patterns located in different bilayer regions (Figure 3.2A).

Previous studies have shown that HFP forms a small intermolecular antiparallel β sheet with a distribution of antiparallel registries.[9, 20] Studies of HFP_F8c and HFP_G5c by ^{13}C- ^{2}H REDOR support major deeply inserted and minor shallowly inserted membrane locations for HFP.[18] In this thesis, the membrane locations of HFP ware studied in membrane both without and with CHOL. In membrane without CHOL, HFP was ^{13}CO labeled at either G5 or L12. In membrane with CHOL, HFP was ^{13}CO labeled at residue G5 and G16. To help understand HFP induced membrane fusion mechanism, fusogenic L9R and non-fusogenic V2E mutants were also studied in membrane without CHOL.[21] This method has also been applied to study the membrane locations of the model transmembrane KALP peptide.

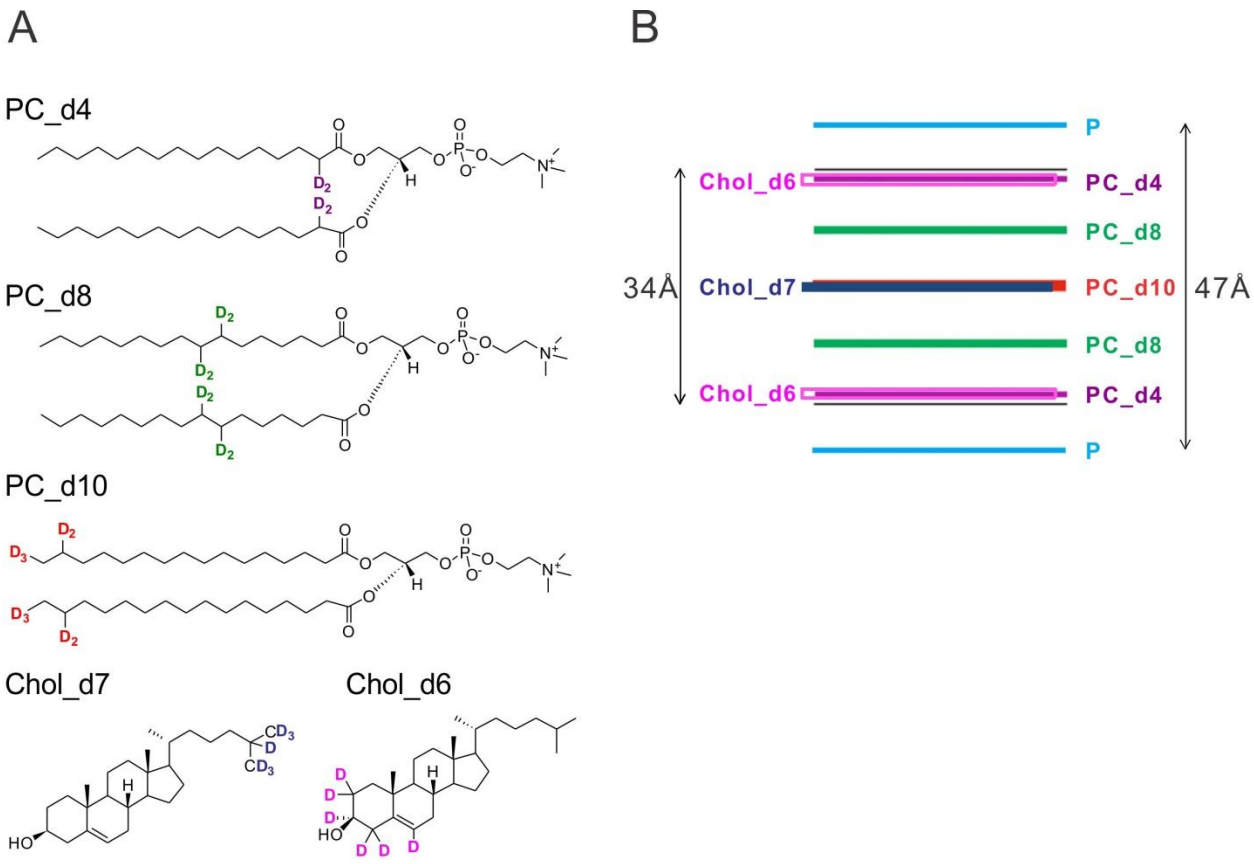

Figure 3.2 (A) ^{2}H patterns and structures of deuterated DPPC lipids and CHOL and (B) approximate ^{2}H's and ^{31}P's (P) membrane locations in the membrane without protein. DPPC lipids are deuterated at different regions of the acyl chain. The lipid ^{2}H and ^{31}P locations are for the membrane gel-phase without CHOL and CHOL ^{2}H locations are for the liquid-ordered phase with CHOL. The same color-coding is used in other figures through this thesis.

The peptides were chemically synthesized with specific ^{13}CO labeling by FMOC solid phase peptide synthesis (SPPS).[22] The method was described in Chapter 2, where the NMR sample preparation method and NMR parameters were also discussed.

3.2 Results

3.2.1 Fitting of the ^{13}C-^{2}H REDOR data

Dephasing buildup plot is obtained from dephasing ($\Delta S/S_0$) at different dephasing time (τ).[23] The S_0 and S_1 peak intensities are also denoted S_0 and S_1, and are obtained typically from 3ppm integration windows of major peak. The dephasing ($\Delta S/S_0$) is calculated as

$$\frac{\Delta S}{S_0} = \frac{(S_0 - S_1)}{S_0} \qquad 3.1$$

The S_0 and S_1 error is based on spectral noise, which is the standard deviation of 10 spectral noise regions with 3ppm integration window.[24]

$$\sigma_{\Delta S/S_0} = \sqrt{\left(\frac{\sigma_{S_0}}{S_0}\right)^2 + \left(\frac{\sigma_{S_1}}{S_1}\right)^2} \times \frac{S_1}{S_0} \qquad 3.2$$

The dephasing is directly related to the dipolar coupling between the ^{13}C (detecting) and ^{2}H (dephasing) nuclei. The ^{13}C – ^{2}H inter-nuclear dipolar coupling (d) is dependent on the ^{13}C – ^{2}H inter-nuclear distance (r), and

$$d(\text{Hz}) = \frac{4642}{r(\text{Å})^3} \qquad 3.3$$

The buildup of experimental dephasing $(\Delta S/S_0)^{exp}$ as a function of τ provides the experimental basis for evaluating the protein labeled (lab) ^{13}CO - to - lipid ^{2}H proximity and the labeled inter-nuclear distance (r) values. The uncertainty of $(\Delta S/S_0)^{exp}$ is based on spectral noise and calculated according to equation 3.2. The sample analyzed is 0.5μmol HFP G5c in 50μmol PC_d10 membrane with peptide to lipid ratio of 1:100.

The data are fitted with three approaches that are denoted ***I***, ***II*** and ***III***. And best fit parameters are based on the minimum χ^2 value. Method ***I*** and ***II*** are simulated by quantum mechanics- based SIMPSON program with a model of isolated ^{13}CO – ^{2}H spin-pairs that has a single dipolar

coupling (d).[25] ***I*** is obtained with two populations (P's) of peptides (HFP G5c molecules), and one population (P) (single ^{13}CO – ^{2}H spin-pair) has a nonzero dipolar coupling (d) and contributes to the experimental dephasing buildup while the rest population (1−P) has a dipolar coupling of zero and does not contribute to the experimental dephasing buildup. ***II*** is obtained with three populations (P's) of peptides, and two populations (two different ^{13}CO – ^{2}H spin-pairs) have nonzero dipolar couplings and contribute to the experimental dephasing, while the rest population has a dipolar coupling of zero and does not contribute to the experimental dephasing. For approach ***I*** and ***II***, each population has a single ^{13}CO – ^{2}H spin-pairs and a single d, and the $(\Delta S/S_0)$ is quantum mechanically calculated by SIMPSON program. For ***III***, the $(\Delta S/S_0)^{exp}$ is fitted to a single exponential buildup equation $A \times (1 - e^{-\gamma \tau})$ with A and γ as the fitting parameters. A is assigned as the approximate fraction of peptide (HFP molecule) with $d \approx 3\gamma/2$. The 3/2 ratio is based on approximately equal time spent in the three ^{2}H m states (m= -1, 0, +1 states) during τ because of the ^{2}H T_1 relaxation. Experimental dephasing time τ typically goes up to 48ms, and there are $m=0 \leftrightarrow m=\pm 1$ ^{2}H transitions during the dephasing period because the ^{2}H $T_1 \approx 50$ms.[17, 26] There isn't buildup for a *lab* ^{13}CO during the $m = 0$ times of ^{2}H nuclei. The stochastic variability of the $m = 0$ times due to ^{2}H T_1 relaxation among the sample ^{13}CO's is not straightforwardly incorporated into quantum mechanical calculation of the buildup in SIMPSON program. We approximate that each ^{2}H is in the $m = 0$ state for 1/3 of the dephasing period so that the observed buildup rate $\gamma \approx 2d/3$. $(1 - A)$ is the fraction of peptide (HFP molecule) with $d \approx 0$.

The data are fitted poorly by method ***I*** in part because the $(\Delta S/S_0)^{exp}$ buildup has exponential shape whereas the calculated buildup by SIMPSON program gives sigmoidal shape. Method ***II*** gives better fitting and applied three populations of HFP G5 ^{13}CO with four fitting parameters:

fractional populations A_1 and A_2 with couplings d_1 and d_2, respectively. The $A_3 = 1 - A_1 - A_2$ and $d_3 = 0$. Method ***III*** also has good fitting with a single exponential buildup from equation: $A \times (1 - e^{-\gamma\tau})$. Method ***III*** is consistent with a model of two populations. Population P_1 has fraction A with ^{13}CO-^{2}H proximity of $d \approx 3\gamma/2$ and population P_2 has fraction $1 - A$ and $d \approx 0$. We approximate that the dipolar coupling is dominated by the closest ^{2}H and the ^{13}CO-^{2}H distance r is calculated from the d of P_1 using equation 3.3.

There are several reasons for choosing method ***III*** rather than ***II*** for general fitting of sample buildups. (1) The $\chi 2_{\mathbf{III}}$ is lowest for most samples fitting, and it is generally close to the number of degrees of fitting ≡ 5 and this is statistically reasonable. The lowest $\chi 2_{\mathbf{III}}$ is achieved with two fitting parameters instead of four fitting parameters in method ***II*** which also gives good fitting buildups. This difference is especially significant because there are only seven data points to be fitted. We choose method ***III*** also because it is simpler and probably more biophysically plausible to have two instead of three peptide membrane locations. Additionally, stochastic processes such as the non-radiative m=0 ↔ m=±1 transitions commonly have exponential dependence as a function of time.[26]

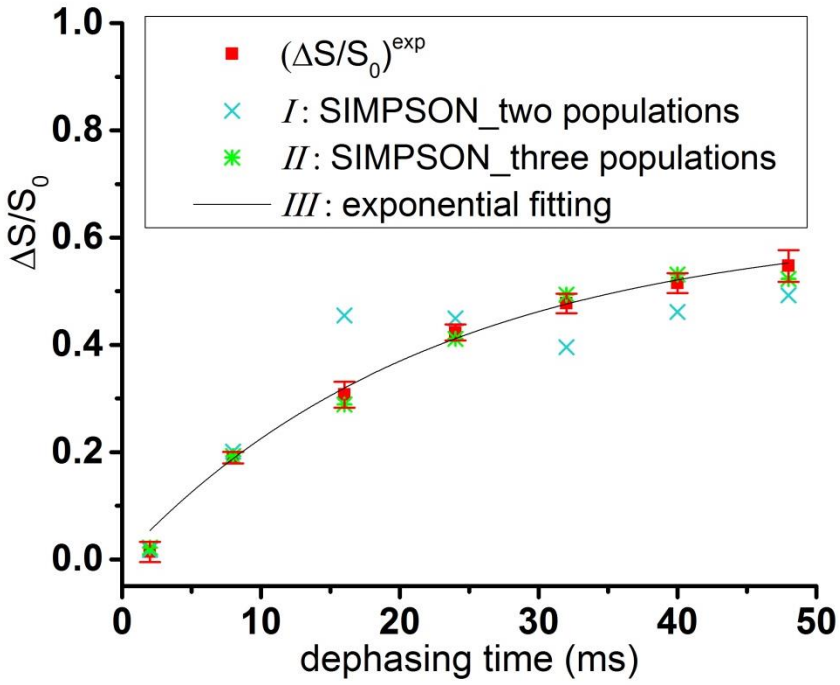

Figure 3.3 Experimental ^{13}CO-^{2}H $(\Delta S/S_0)^{exp}$ (red squares with error bars) for sample HFP_G5$_C$ in PC_d10 membrane. The $(\Delta S/S_0)^{exp}$ are for the major *lab* G5 peak with β sheet structure and error bars are calculated from spectral noise. Fitted $(\Delta S/S_0)$ are displayed for three different fitting approaches. The blue crosses (Approach ***I***) and green stars (Approach ***II***) are based on models of two- (P_1 and P_2) and three-populations (P_1, P_2, and P_3) of HFP_G5$_C$ molecules, respectively. The $(\Delta S/S_0)$ for each population is calculated with the quantum mechanics-based SIMPSON program using a model of isolated ^{13}CO-^{2}H spin-pairs with a single dipolar coupling (d). For the two population model, the best-fit parameter values for P_1 are d = 53 Hz and fractional population A = 0.71. The corresponding $P_2 = 1 - A = 0.29$ with d = 0 Hz. For the three-population model, the best-fit values are d_1 = 90 Hz, A_1 = 0.27, d_2 = 25 Hz, and A_2 = 0.50 with $P_3 = 1 - A_1 - A_2 = 0.23$ and d_3 = 0 Hz. The black line (Approach ***III***) is the best-fit to the exponential buildup function $A \times (1 - e^{-\gamma\tau})$ with A = 0.63 and γ = 44 Hz.

3.2.2 Effect of sample preparation methods on $^{13}C–^{2}H$ REDOR $\Delta S/S_0$

To evaluate whether HFP achieves thermodynamic structure and membrane location, two different sample preparation methods were compared, which is organic cosolubilization method and aqueous vesicle binding method and the two different sample preparation methods have been described in detail in Chapter 2. Most samples were prepared by organic cosolubilization method. Vesicle binding method is more like peptide incorporation during viral fusion. In organic sample preparation method, the lipids and peptides are well mixed in organic solvent mixtures, so there will be no kinetic trapped structure and membrane location. In these samples, the HFP is ^{13}CO labeled at Gly5 residue. The membrane is composed of PC_d10: DTPG with 4:1mol ratio. And the peptide to lipid ratio is 1:25. Both samples have similar spectrum (Figure 3.3) with a major ^{13}CO peak centered at 171ppm chemical shift which suggests HFP form majorly β sheet structure in membrane. The higher chemical shift 175ppm peak is from lipid carbonyl natural abundance and peptide carbonyl natural abundance of residues other than glycine and methionine.[27]

The dephasing buildups (Figure 3.4) are also similar with $(\Delta S/S_0)^{exp} \approx 0.7$ for large τ. The results support that HFP achieves thermodynamic equilibrium structure and membrane location.

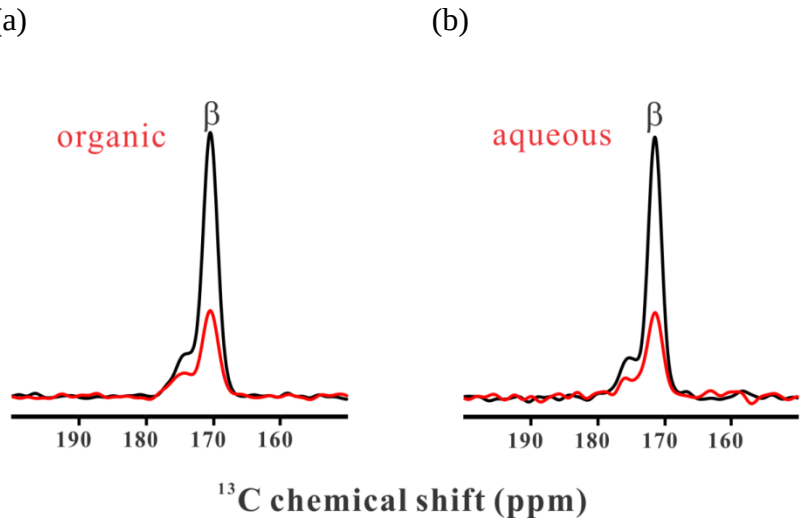

Figure 3.4 ^{13}C-detect / ^{2}H-dephase REDOR S_0 (black) and S_1 (red) experimental spectra of membrane - associated HFP G5c at τ = 40ms by different sample preparation methods, (a) organic cosolubilization method (organic) and (b) aqueous vesicle binding method (aqueous). Each spectrum is the sum of ~ 40000 scans and processed with 150 Hz Gaussian line broadening and polynomial baseline correction. The observed chemical shifts for G5 are 171ppm from both organic and aqueous methods, and this is consistent with major β sheet structure of HFP in membrane. The similar structure supports that HFP achieves thermodynamic equilibrium structure when it's associated with membrane. The membrane is composed of 40μmol DPPC_d10 and 10μmol DTPG lipids. Sample prepared by organic methods contains ~ 2μmol and sample prepared by aqueous method contains ~ 1.3μmol HFP. The cooling N_2 gas temperature is ~ - 50 °C with corresponding sample temperature of ~ - 30 °C.

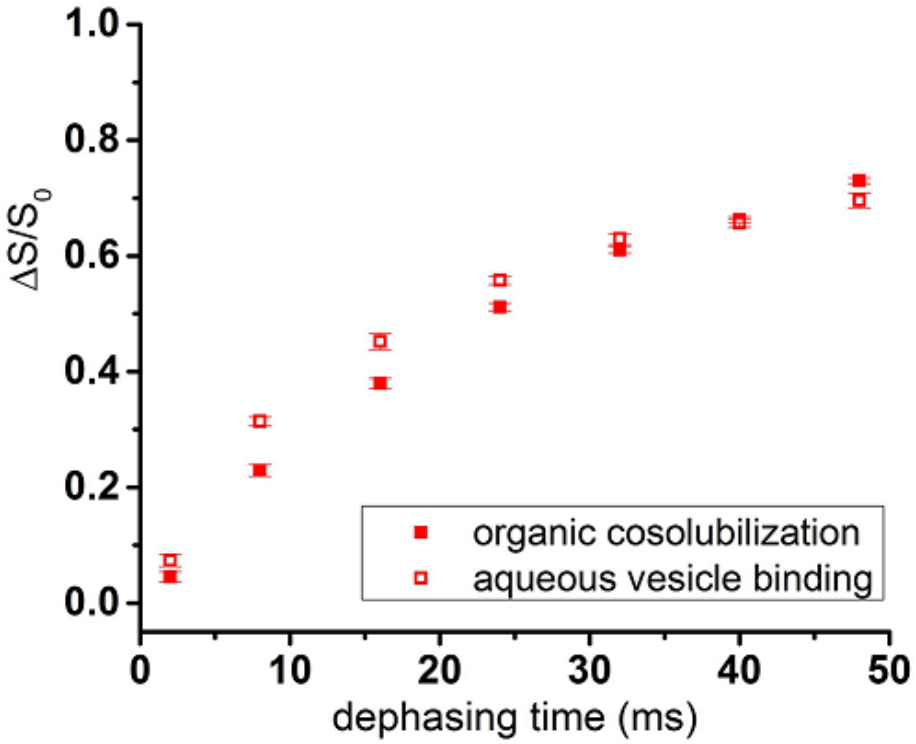

Figure 3.5 The dephasing buildups of $\Delta S/S_0$ vs dephasing time (τ) for different NMR sample preparation methods: organic cosolubilization (closed square) and aqueous vesicle binding (open square). The intensity for S_0 and S_1 were obtained by integration over a 3ppm width centered at the highest peak intensity. The similar dephasing buildups support thermodynamic equilibrium membrane location of HFP when it's associated with membrane.

3.2.3 Effect of temperature on experimental $\Delta S/S_0$

The effect of temperature on the experimental dephasing buildup is compared with sample temperature at ~ - 30 °C and ~ - 0 °C with corresponding cooling gas temperature of - 50 °C and ~ - 20 °C. The sample analyzed is HFP_G5c in PC_d10: DTPG (4:1) membrane. And the sample is prepared by organic cosolubilization sample preparation method. The same sample is investigated at different temperature. The spectra acquired at the two different temperatures are similar with a major peak at 171 ppm chemical shift corresponding to β sheet secondary structure. The same β sheet structure at higher temperature supports that HFP structure doesn't change significantly when temperature varies and probably represents the most relevant structure at physiological temperature. The dephasing buildup is smaller at higher temperature and the $(\Delta S/S_0)^{exp}{}_{0\,°C}/\ (\Delta S/S_0)^{exp}{}_{-30\,°C}) \approx 0.7$ for a given τ. At higher temperature the signal per scan S_0 is decreased when τ increases. For τ=2ms, $(S_0)^{exp}{}_{0\,°C}/\ (S_0)^{exp}{}_{-30\,°C}) \approx 1.0$, and it's only 0.13 for τ = 48ms. This suggests that the $^1H \rightarrow {}^{13}C$ CP is temperature independent and the T_2 of peptide ^{13}CO is shorter at higher temperature. The T_2 is shorter probably because the peptide motion increases at higher temperature. And the increased peptide and lipids motions likely cause motional averaging of the ^{13}CO- ^2H dipolar coupling and thus a reduced $(\Delta S/S_0)^{exp}$ is observed.[18] In order to obtain the biggest experimental $(\Delta S/S_0)$, all samples are investigated at ~ - 30 °C.

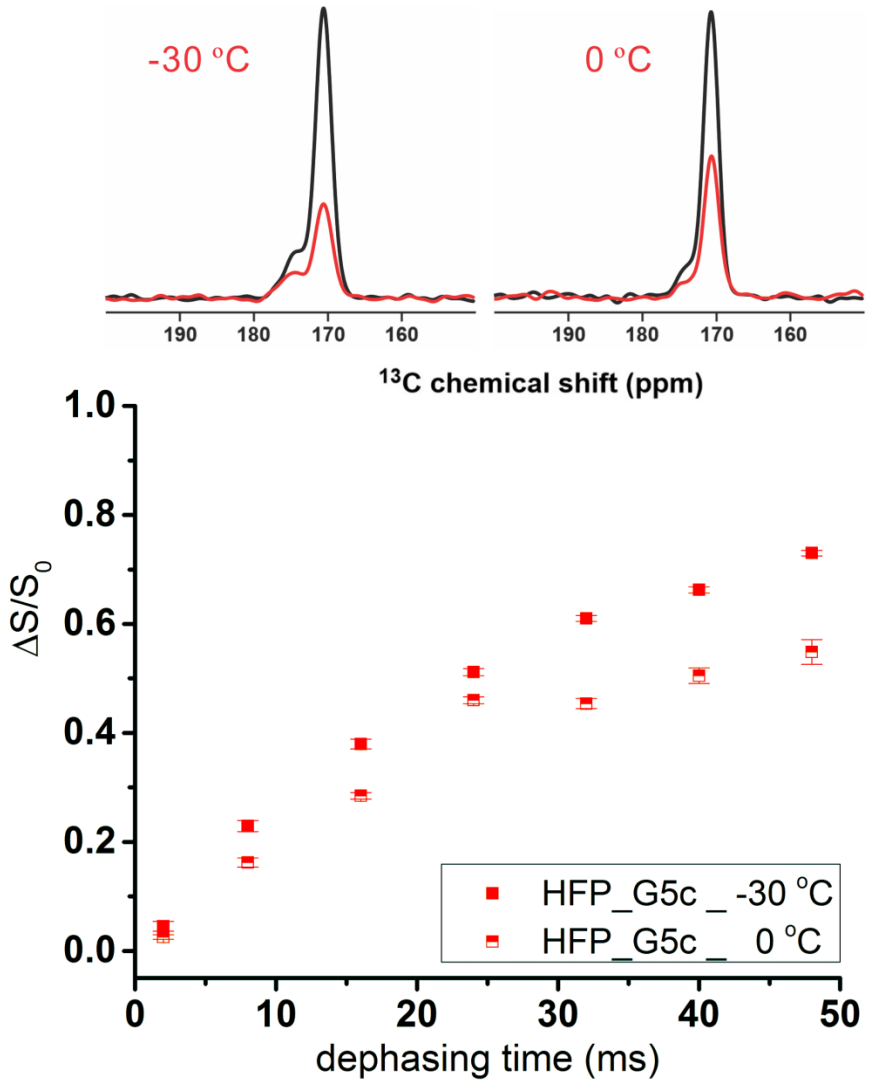

Figure 3.6 The spectra (top panel) and dephasing buildups (bottom panel) of $\Delta S/S_0$ vs dephasing time (τ) for sample investigated at ~ - 30 °C and ~ - 0 °C: the spectrum is for τ = 40ms and the black is S_0 and red is S_1. The data is processed with 150Hz Gaussian line broadening.

3.2.4 Effect of membrane charge on experimental $\Delta S/S_0$

The membrane charge effect on HFP structure and membrane location is investigated with HFP G5c in neutral membrane with 50μmol PC_d10, PC_d8 and PC_d4 with ^2H labeling. The negatively charged membrane has the same lipid labeling but with addition of anionic PG lipid

and the PC: PG mole ratio is 4:1. The negative charged lipid is added because most human cell membranes including the HIV host cell include 0.1~ 0.2mol fraction of anionic lipids.[28] The S_0 spectra of HFP G5c samples are similar with predominant 171ppm chemical shift peak regardless of the membrane charge. The 171ppm chemical shift corresponds to β sheet structure of the lab G5 ^{13}CO's. The dephasing buildups also show similar trends. There are significant buildups for HFP G5 ^{13}CO in membranes labeled with PC_d10 and PC_d8 lipids, but negligible buildups in membranes with labeling in PC_d4 lipid. The chemical shift and dephasing buildups features support that HFP β sheet is inserted into the membrane hydrophobic core. Exponential fitting of the significant dephasing buildups give 4~5 Å closest inter-nuclear distances, which indicates Van der Waals contact between HFP G5 ^{13}CO and the lipid ^{2}Hs in PC_d8 and PC_d10. The NMR sample is generally prepared with organic cosolubilization method if without special instructions. The peptide incorporation efficiency is generally greater for sample in negatively charged membrane. This greater bound peptide fraction is probably due to the electrostatic attraction between the positively charged solubility tag in HFP and the negatively charged lipids head-group in the membrane. Therefore, extra peptides were added to compensate the binding efficiency difference when preparing samples with neutral membrane. Since the NMR sample is the centrifuged pellet containing the membrane and the bound HFP, the unbound HFP was in the supernatant and separated from and not contained in the NMR sample. Because of better binding of HFP in anionic membrane, it gives better prediction of the quantity of HFP incorporated in membrane. Thus, most samples in this thesis are prepared in membrane with negatively charged lipids and the PC: PG = 4:1 mole ratio.

(a)

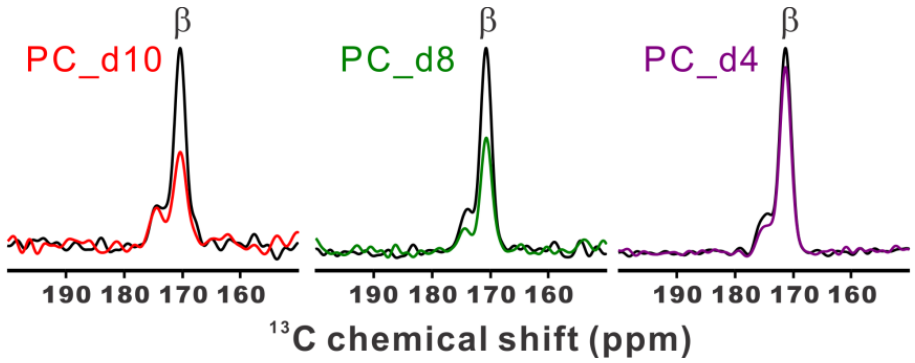

(b)

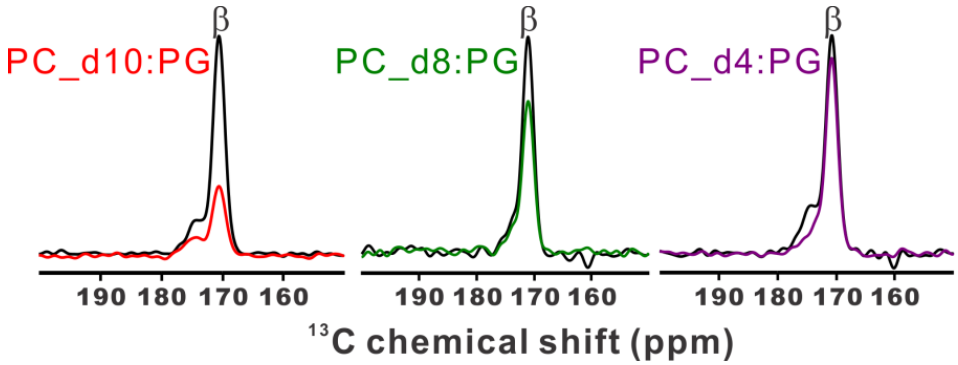

Figure 3.7 ^{13}C-detect / ^{2}H-dephase REDOR S_0 (black) and S_1 (colored) experimental spectra of HFP_G5c in (a) neutral membrane and (b) negatively charged membrane at τ = 40ms. The data is processed with 100Hz Gaussian line broadening and polynomial baseline correction. The 171 ppm chemical shift indicates that HFP has predominant β sheet structure at the labeled Gly5 residue site.

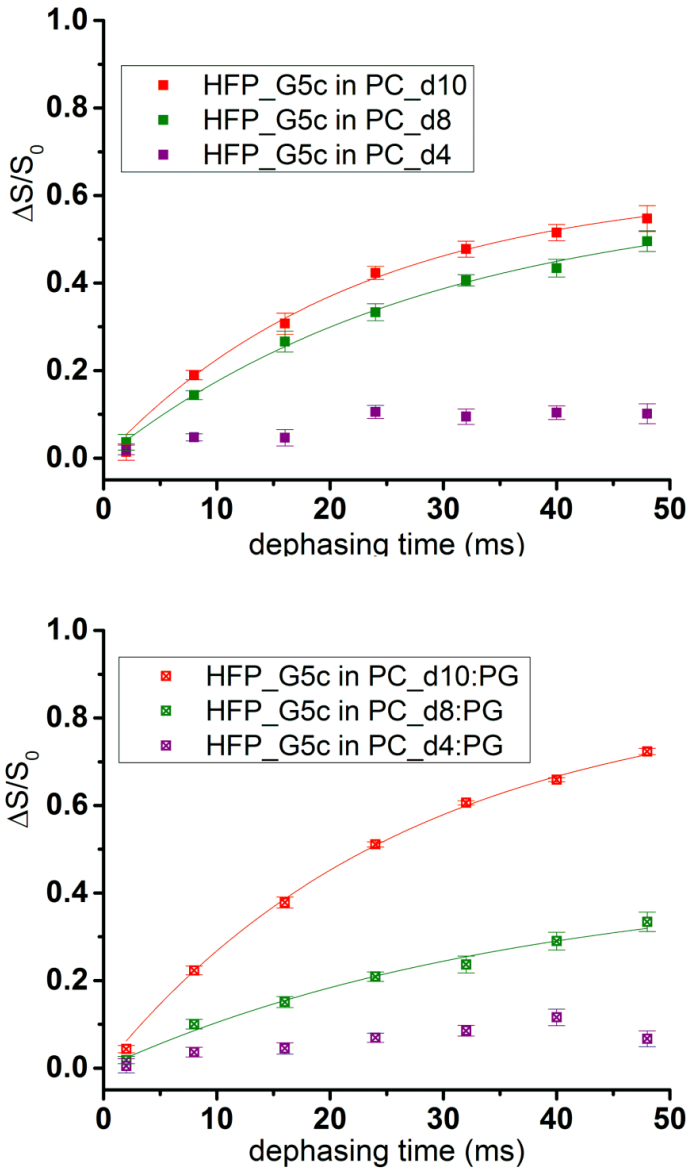

Figure 3.8 The dephasing buildups of $\Delta S/S_0$ (colored squares) with error bars vs dephasing time (τ) for HFP_G5c in (top panel) neutral membrane and (bottom panel) negatively charged membrane. The neutral membrane is composed of PC lipid, and the negative membrane is PC: PG lipids of 4:1mol ratio. The dephasing buildups are for the major peak at 171 ppm with integration window of 3ppm for both S_0 and S_1. The colored line is the best fit exponential buildup curve fitted by $A \times (1 - e^{-\gamma\tau})$ for samples with significant dephasing buildups.

Table 3.1 Best-fit exponential buildup parameters for HFP_G5c in membrane [a]

Membrane	A	γ (Hz)	r (Å)
PC_d10	0.63(4)	44(5)	4.1(2)
PC_d8	0.60(3)	34(3)	4.5(1)
PC_d10:PG	0.89(2)	36(2)	4.4(1)
PC_d8:PG	0.44(6)	27(6)	4.9(3)

[a] A and γ are fitting parameters for experimental dephasing buildup from fitting equation of $A \times (1 - e^{-\gamma\tau})$, and r is calculated as $d = 3\gamma/2 = 4642/r^3$.

3.2.5 HFP location in membrane without CHOL studied by ^{13}C–^{2}H REDOR

To study the membrane locations of HFP, we used deuterated PC lipids with addition of a small fraction of anionic PG lipids and PC: PG = 4:1 mole ratio. The negative charged lipid is added because the HIV host cell includes 0.1~ 0.2mol fraction of anionic lipids and also because better peptide binding to membrane.[28] The HFP is ^{13}CO labeled at G5 and L12 residues. Former student Dr. Li XIE from our group has studied the membrane contact of HFP with F8 ^{13}CO labeled in neutral membrane with deuterated PC lipid and showed that HFP_F8 has β sheet structure and is inserted in the membrane hydrophobic core.[26] Additionally, for HFP_F8 studied in DMPC_d54 with per-deuterated lipid acyl chain, the dephasing goes up to ~ 1 rapidly,

which supports that all HFP molecules are deeply inserted into the membrane hydrocarbon core. ^{13}C – ^{15}N REDOR studies have shown that HFP forms majorly β antiparallel sheet registry when associated with ~ 30mol % CHOL. In membrane without CHOL, each HFP ^{13}CO labeled sample is studied with PC_d10, PC_d8 and PC_d4 ^{2}H labeling in the membrane to fully understand the ^{13}CO contacts with different regions of the membrane. For HFP_G5c in PC: PG (4:1) membrane, the spectrum is displayed in Figure 3.7 (b), the dephasing buildup is displayed in Figure 3.8, and the fitting results of significant buildups for PC_d10 and PC_d8 labeling is shown in Table 3.1. The major peak for G5 has 171 ppm chemical shift, and the major peak for L12 has 175 ppm chemical shift, these results support major β sheet structure at both G5 and L12 residue. The data for sample containing HFP_L12c is processed with 20Hz Gaussian line broadening and polynomial baseline correction. L12 and G5 have similar dephasing buildup features with biggest dephasing with PC_d10, significant dephasing with PC_d8 and smallest dephasing with PC_d4. Similar features are also observed for HFP_F8 samples.[26] Fitting of PC_d10 and PC_d8 experimental dephasing buildups all give 4 ~ 5 Å inter-nuclear distances, which supports Van der Waals contacts between HFP_G5 and L12 ^{13}CO and ^{2}H of membrane lipid PC_d10 and PC_d8. At τ= 48ms, the $(\Delta S/S_0)_{d10}/(\Delta S/S_0)_{d8}$ is $\approx$ 7:3 and A_{d10}: A_{d8} $\approx$ 2:1 supports that there are multiple membrane locations of HFP in membrane. And the major population is deeply inserted into the membrane in contact with d10 ^{2}Hs, and the minor population is shallowly inserted into the membrane and contacts d8 ^{2}Hs.

The interior of the HFP β sheet is likely located within the hydrophobic hydrocarbon core in the membrane, because there is lower free energy due to hydrophobic effect from many of the nonpolar sidechains of HFP amino acids. On the contrary, the terminal part of HFP is probably located in near the membrane head group region rather than the membrane hydrocarbon region.

There are registry distributions of antiparallel HFP registry in membrane. The HFP terminal residues have incomplete inter–residue hydrogen bonds with the neighbor strands. The free energy is lowered by forming additional hydrogen bonds with water which has higher content near the membrane head group region instead of the hydrocarbon core. The interior residues can form nearly complete inter–residue hydrogen bonds in membrane hydrocarbon core. All HFP antiparallel β sheet registries have G5 and L12 in the registry interior and G16 near the registry terminal.[18, 29] There is probably small number (~ 10) of HFP molecules in the antiparallel β sheet registries and is consistent with gp41 oligomerization including establishment of a dimer of trimers of gp41ectodomain.[30]

It's not clear how the major deeply inserted and minor shallowly inserted membrane location is advantageous to HFP induced membrane fusion. The majorly deep inserted HFP may reduce the fusion activation energy to the membrane fusion intermediate by perturbing the local membrane. The multiple membrane location of HFP may be correlated with HFP antiparallel β sheet registry distributions and hydrophobicity in membrane. How the lipids are displaced by HFP molecule is not known and neither the orientation of the contact lipids relative to the rest bulk lipid. Our data is most consistent with insertion of the antiparallel β sheet registries in a single membrane leaflet, but we can’t rule out a transmembrane model.

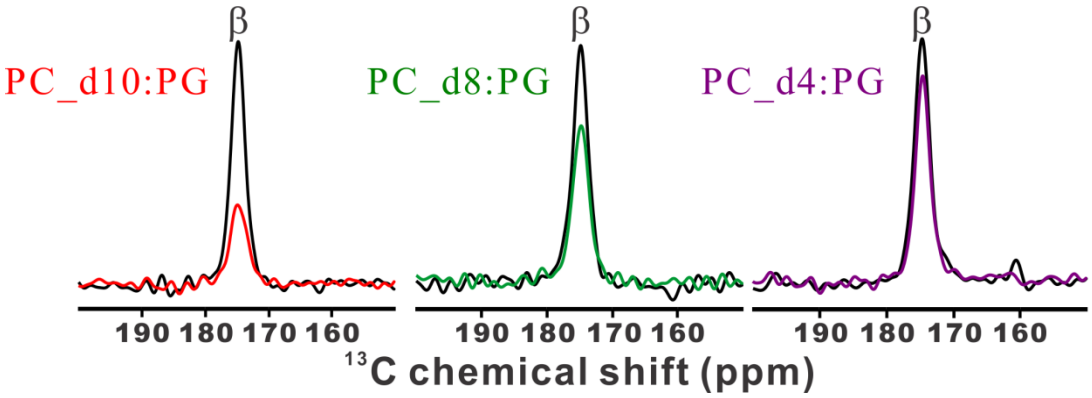

Figure 3.9 ^{13}C-detect / ^{2}H-dephase REDOR S_0 (black) and S_1 (colored) experimental spectra of HFP_L12c in PC: PG =4:1 membrane. The data is processed with 20Hz Gaussian line broadening and polynomial baseline correction.

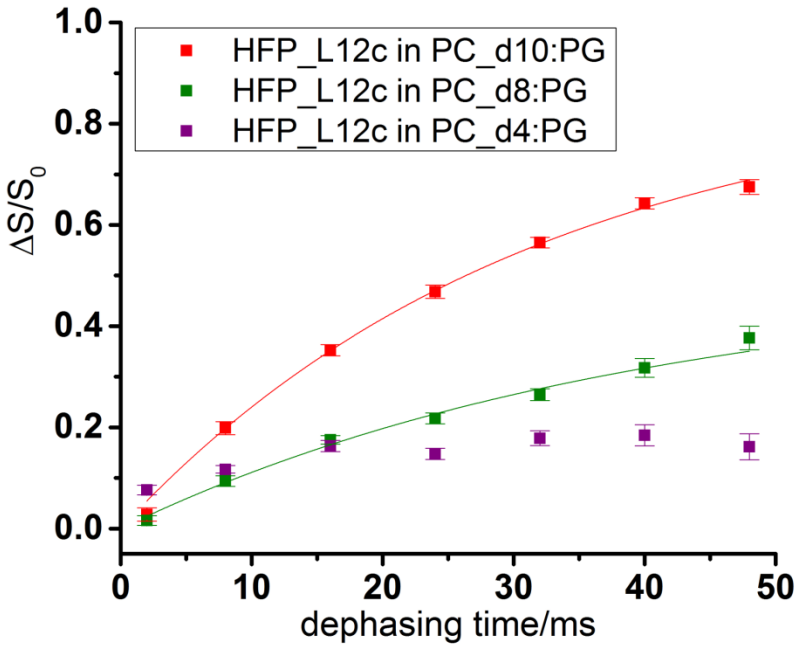

Figure 3.10 The dephasing buildups of $\Delta S/S_0$ (colored squares) with error bars vs dephasing time (τ) for HFP_G12c in membrane composed of PC: PG = 4:1 ratio. The $\Delta S/S_0$ data is for the major peak of β sheet conformation and the S_0 and S_1 is integration with 3ppm integration window. The colored line is the best fit exponential buildup curve fitted by $A \times (1 - e^{-\gamma\tau})$.

Table 3.2 Best-fit exponential buildup parameters for HFP_L12c in membrane [a]

Membrane	A	γ (Hz)	r (Å)
PC_d8	0.50 (8)	25 (5)	5.0 (4)
PC_d10	0.88 (5)	31 (3)	4.6 (2)

[a] A and γ are fitting parameters for experimental dephasing buildup from fitting equation of $A \times (1 - e^{-\gamma\tau})$, and r is calculated as $d = 3\gamma/2 = 4642/r^3$.

(a) Major population

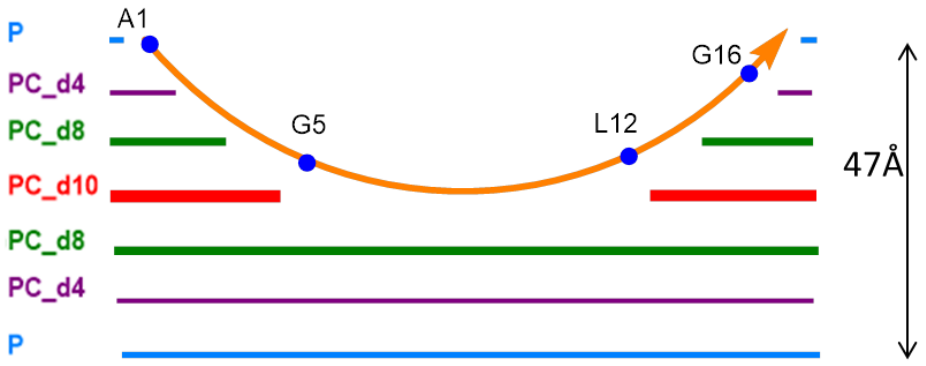

(b) Minor population

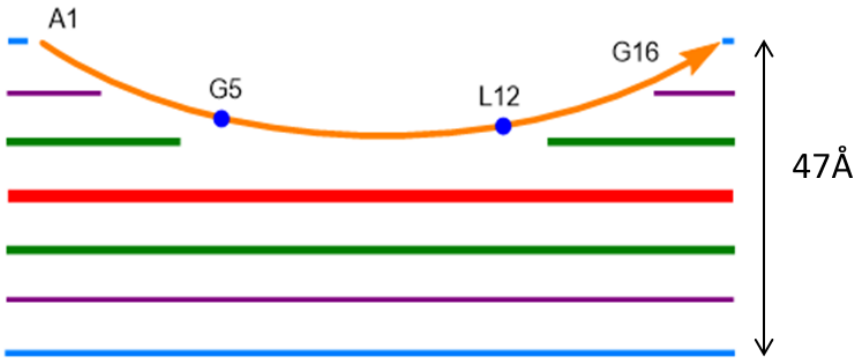

Figure 3.11 HFP membrane location model in anionic membrane without CHOL: (a) major deeply inserted membrane location and (b) minor shallowly inserted membrane location. The membrane ^{2}H positions represent the location without protein.

3.2.6 HFP location in membrane with CHOL studied by ^{13}C–^{2}H REDOR

3.2.6.1 HFP location in DPPC: DPPG: CHOL membrane studied by ^{13}C–^{2}H REDOR

HIV host cell membrane contains ~ 30mol % CHOL, so it's important to study HFP membrane location in membrane containing CHOL.[31] The HFP is ^{13}CO labeled at G5 and G16 residue. One advantage of Gly-^{13}CO labeling is that HFP has majorly β sheet structure in membrane. The

171ppm major peak of HFP Gly-^{13}CO is separated from 175ppm lipid carbonyl natural abundance peak. Previous ^{13}C– ^{2}H REDOR data shows that G5 is majorly deeply inserted into membrane center contacting PC_d10 ^{2}Hs in membrane without CHOL, and ^{13}C– ^{31}P REDOR data suggests that G5 is far away (at least 10 Å) from phosphorous head group. ^{13}C–^{31}P REDOR data also suggests that G16 is close to phosphorous head group because A14 and A15 is ~ 5 Å away from the phosphorous group.[16, 32] Therefore, G5 and G16 are reasonable candidates to study HFP contacts to Chol_d7 and Chol_d6 with ^{2}Hs located near the center and edge of the membrane, respectively. Chol_d7 and Chol_d6 have ^{2}Hs deuterated at the methyl and hydroxyl regions, respectively. The membrane studied is PC: PG: CHOL (8:2:5) and the CHOL amount is 25μmol.

In the spectrum, both G5 and G16 have the major peak at 171ppm, which corresponds to sheet secondary structure of HFP in membrane containing 33mol % CHOL. G16 also has a slightly smaller peak at 174 ppm compared to the 171 ppm major peak. The 174 ppm peak likely corresponds to coil conformation according to the glycine chemical shift distributions in proteins.[27] Coil formation means lack of regular secondary structure (helix and β sheet), and the dihedral angles could be any of the angles sterically allowed while different dihedral angles give different chemical shifts. Those G16 residues form hydrogen bonds with water near the membrane head group.[18, 27] A single major peak at 171 ppm for G5 suggests that almost all HFP antiparallel registries include G5 residue and G5 forms complete inter-residue hydrogen bonds.

The dephasing is calculated for major 171ppm peak corresponding to β sheet HFP structure. The dephasing buildup trends are strikingly different for Chol_d7 and Chol_d6 labeling. G5 has large and small dephasing buildup with Chol_d7 and Chol_d6, respectively. For G16, the trend is

opposite, with large and small dephasing buildup with Chol_6 and Chol_d7, respectively. Since Chol_d7 have ^{2}Hs located in the membrane center, the G5 dephasing buildup supports that most HFP G5 residue is deeply inserted into the membrane hydrophobic core near the membrane center in CHOL containing membrane. And this result is consistent with the G5 and L12 major deeply insertion membrane location model discussed earlier in this chapter. The G16 dephasing buildup evidences G16 is located near membrane surface, and this result is consistent with the ^{13}C–^{31}P REDOR data. Exponential fitting of the significant buildups give ~ 4 Å ^{13}CO–^{2}H inter-nuclear distances for G5 ^{13}CO – Chol_d7 ^{2}H and G16 ^{13}CO – Chol_d6 ^{2}H, which support Van der Waals contact between HFP and CHOL.

HFP–CHOL contact results support that there is multiple membrane locations of HFP in membrane containing CHOL because $(\Delta S/S_0)_{Chol\_d7}$ /$(\Delta S/S_0)_{Chol\_d6} \approx$ 3:1 at τ = 40ms. The 3:1 ratio suggests that G5 has major population deeply inserted to the membrane center contacting Chol_d7 ^{2}Hs and minor population shallowly inserted to the membrane surface contacting Chol_d6 ^{2}Hs. The HFP membrane location model is similar in membrane containing 33mol % and membrane without CHOL.

The CHOL contact studies of HFP with Chol_d7 and Chol_d6 labeling scheme strongly suggests that this ^{13}C–^{2}H REDOR methodology is effective to study HFP specific residue contact to specific regions of CHOL. And this method is promising to be applied to study protein–CHOL van der Waals contact with other proteins.

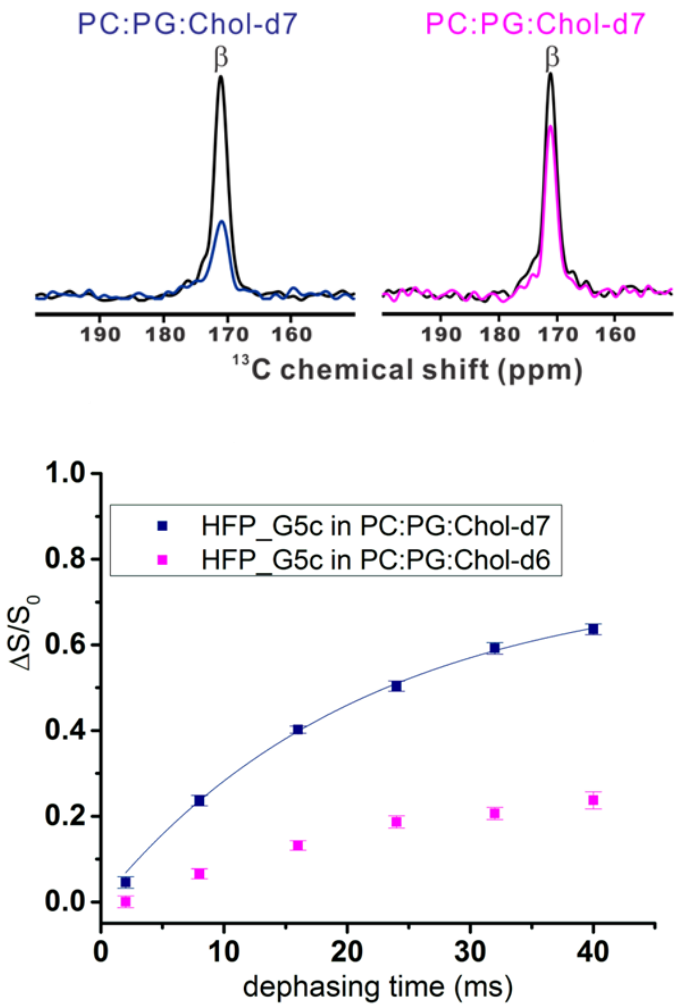

Figure 3.12 ^{13}C-detect / ^{2}H-dephase REDOR S_0 (black) and S_1 (colored) experimental spectra (top panel) and the dephasing buildups (bottom panel) of $\Delta S/S_0$ (colored squares) with error bars vs dephasing time (τ) for HFP_G5c in membranes with Chol_d7 and Chol_d6. The S_0 and S_1 spectra displayed are for τ =40ms. The data is processed with 100Hz Gaussian line broadening and polynomial baseline correction. The dephasing buildup is for the major β peak. S_0 and S_1 is integration through 3ppm integration window. The colored line is the best fit exponential buildup curve fitted by $A \times (1 - e^{-\gamma\tau})$

(a)

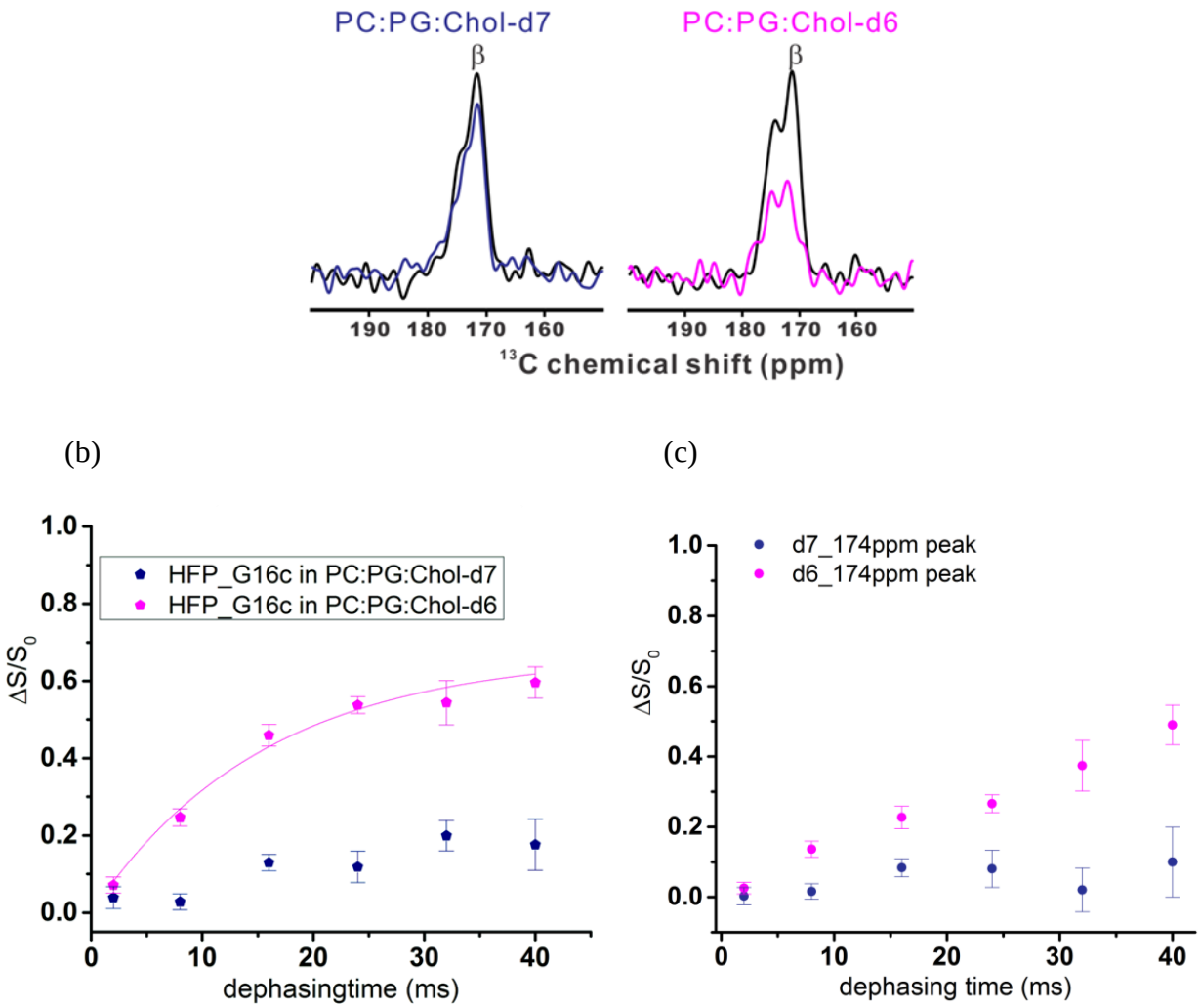

Figure 3.13 ^{13}C-detect / ^{2}H-dephase REDOR S_0 (black) and S_1 (colored) experimental spectra (a) and the dephasing buildups of $\Delta S/S_0$ (colored squares) with error bars vs dephasing time (τ) for HFP_G16c in membranes with Chol_d7 and Chol_d6 for 171ppm peak (b) and 174ppm peak (c). The S_0 and S_1 spectra displayed are for τ =40ms. The data is processed with 100Hz Gaussian line broadening and polynomial baseline correction. The dephasing buildup is for the major β peak with 171ppm chemical shift. S_0 and S_1 is integration through 1ppm integration window. The colored line is the best fit exponential buildup curve fitted by $A \times (1 - e^{-\gamma\tau})$.

Table 3.3 Best-fit exponential buildup parameters for HFP_G5c and G16c in membrane with Chol_d7 and Chol_d6 [a]

Peptide	Membrane	A	γ (Hz)	r (Å)
HFP_G5c	PC:PG:Chol_d7	0.76 (3)	47 (3)	4.0 (1)
HFP_G16c	PC:PG:Chol_d6	0.67 (5)	64 (10)	3.6 (2)

[a] A and γ are fitting parameters for experimental dephasing buildup from fitting equation of $A \times (1 - e^{-\gamma\tau})$, and r is calculated as $d = 3\gamma/2 = 4642/r^3$. The membrane composition is PC: PG: CHOL (8:2:5) with ~ 1μmol peptide. The peptide to lipids (not including CHOL) ratio is 1:50.

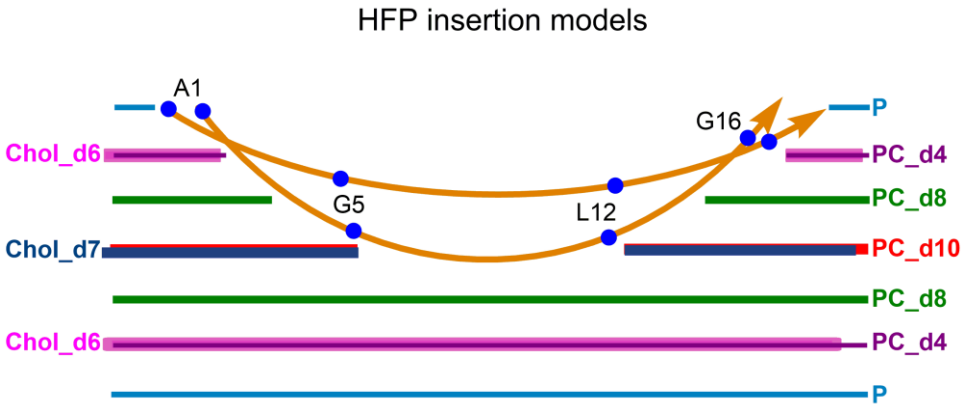

Figure 3.14 Semi-quantitative HFP membrane location model with major population deeply inserted and minor population shallowly inserted to the membrane hydrophobic core. The membrane ^2H positions represent the location without protein.

3.2.6.2 HFP location in POPC: POPG: CHOL membrane studied by $^{13}C–^{2}H$ REDOR

$^{13}C–^{2}H$ REDOR method is evaluated in POPC: POPG: CHOL membrane which is typically used to study the fusion activity of fusion proteins such as HIV gp41 and influenza hemagglutinin.[33-36] So it's important to study the membrane locations in this membrane composition to help correlate the membrane location function relationship. POPC and POPG lipids have lower melting temperature, which is −2 °C compared to 41°C of DPPC and DPPG lipids. The membrane will be in gel phase below the lipid melting temperature and liquid disordered phase above the lipid melting temperature. Using POPC lipid, because it represents the most abundant lipid head-group and common lipid acyl chains in HIV host cell membrane.[28] In this study, HFP is ^{13}CO labeled at G10 and G16. The membrane composition studied with both G10 and G16 labeling is POPC: POPG: CHOL with 8:2:5 mole ratios. The membrane is labeled at CHOL with Chol_d7 and Chol_d6. Less CHOL content membrane with POPC: POPG: CHOL of 8:2:2.5 is compared with HFP_G10c and Chol_d7 labeling. The data is processed with Gaussian 100Hz line broadening and polynomial baseline correction. S_0 and S_1 are integrated with 3ppm integration window. Substantial dephasing buildups with exponential buildup trends are fitted with equation $A \times (1 - e^{-\gamma\tau})$.

All G10 samples have predominant peak with ~ 171ppm chemical shift, which is consistent with β sheet structure in both 33mol % and 20mol % CHOL content membranes. G16 samples have predominant peak with ~ 171ppm chemical shift, which is consistent with β sheet structure. G16 samples also have a significant peak at ~ 174ppm, which is consistent with coil conformation and corresponding to the G16s that are not included in the peptide antiparallel registries and have hydrogen bonding with water molecules near the membrane surface.[29] These spectra features are similar to those in DPPC: DPPG: CHOL membrane, which suggests the HFP peptide

antiparallel β sheet with registration distribution structure is robust and likely the most biological relevant structure. In membrane with POPC: POPG: CHOL= 8:2:5, the quantitative dephasing trend is opposite for G10 and G16 samples. For G10, the dephasing is much bigger with Chol_d7 than Chol_d6, while the dephasing is bigger with Chol_d6 than Chol_d7 for G16. The experimental dephasing results are consistent with G10 is inserted in the membrane hydrocarbon core and G16 has a shallower location near the membrane surface. Compared to samples in DPPC: DPPG: CHOL membrane, the experimental dephasing at longer dephasing time is generally smaller and the buildup rate is also slower in POPC: POPG: CHOL membrane. This might due to shallower membrane locations of HFP in the hydrophobic core relative to the membrane center compared to membrane location in DPPC membrane. The contrary dephasing buildup trends with Chol_d7 and Chol_d6 labeling for both G10 and G16 supports that this ^{13}C–^{2}H REDOR method can be used to differentiate residue specific membrane locations. 20mol % Chol_d7 labeling for G10c gives about half the dephasing than 33mol % Chol_d7 labeling. This is probably due to spin dilutions with less amount of Chol_d7. More residue specific labeling will be necessary for a complete membrane location model of HFP in this POPC: POPG: CHOL membrane system.

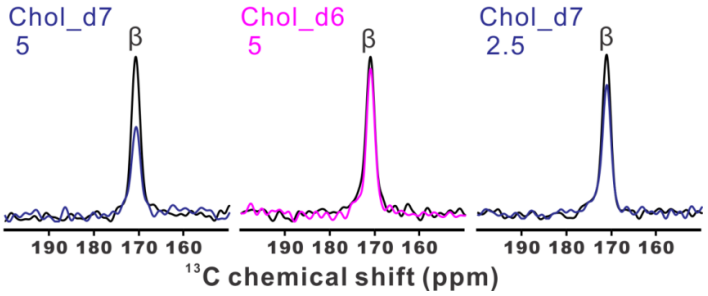

Figure 3.15 ^{13}C-detect / ^{2}H-dephase REDOR S_0 (black) and S_1 (colored) experimental spectra for HFP_G10c at τ = 40ms. The data is processed with 100 Hz Gaussian line broadening and polynomial baseline correction. POPC: POPG: CHOL = 8:2:5 and 8:2:2.5 mole ratios.

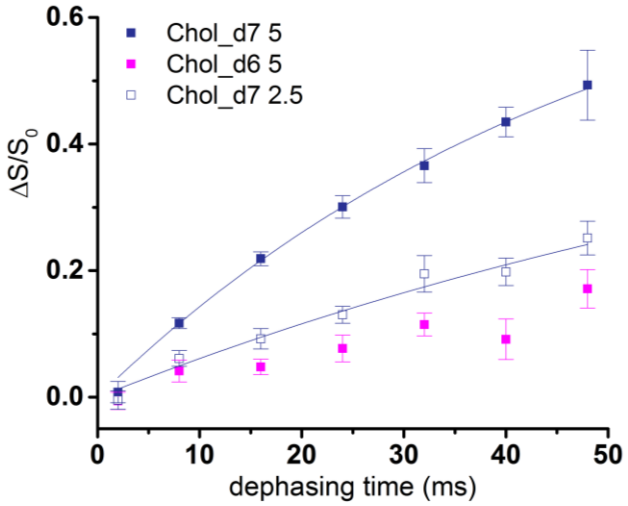

Figure 3.16 The dephasing buildups of $\Delta S/S_0$ (colored squares) with error bars vs dephasing time (τ) for HFP_G10c in membrane composed of POPC: POPG: CHOL = 8:2:5 and 8:2:2.5 ratios. The $\Delta S/S_0$ data is for the major peak of β sheet conformation and the S_0 and S_1 is integration with 3 ppm integration window. The colored line is the best fit exponential buildup curve fitted by $A \times (1 - e^{-\gamma\tau})$.

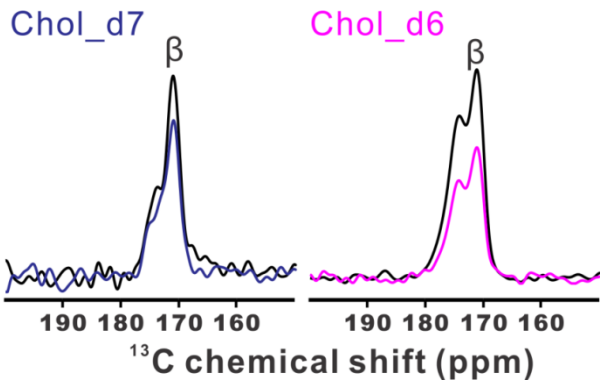

Figure 3.17 ^{13}C-detect / ^{2}H-dephase REDOR S_0 (black) and S_1 (colored) experimental spectra for HFP_G16c at τ = 40ms. The data is processed with 100 Hz Gaussian line broadening and polynomial baseline correction. POPC: POPG: CHOL = 8:2:5.

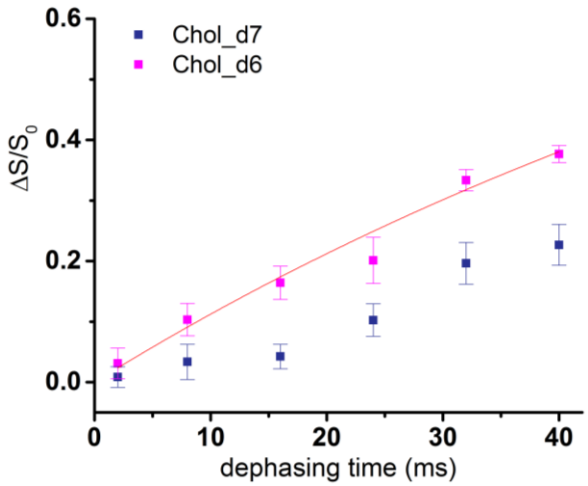

Figure 3.18 The dephasing buildups of $\Delta S/S_0$ (colored squares) with error bars vs dephasing time (τ) for HFP_G16c in membrane composed of POPC: POPG: CHOL = 8:2:5 ratio. The $\Delta S/S_0$ data is for the major peak of β sheet conformation and the S_0 and S_1 is integration with 1 ppm integration window. The colored line is the best fit exponential buildup curve fitted by $A \times (1 - e^{-\gamma\tau})$.

Table 3.4 Best-fit exponential buildup parameters for HFP_G10c and G16c in POPC: POPG membrane with Chol_d7 and Chol_d6 [a]

Peptide	Membrane	A	γ (Hz)	r (Å)
HFP_G10c	PC:PG:Chol_d7 (8:2:5)	0.79 (10)	20 (3)	5.4 (3)
HFP_G16c	PC:PG:Chol_d6 (8:2:5)	1.02 (61)	12 (9)	6.4 (1.6)
HFP_G10c	PC:PG:Chol_d7 (8:2:2.5)	0.60 (38)	11 (8)	6.6 (17)

[a] A and γ are fitting parameters for experimental dephasing buildup from fitting equation of $A \times (1 - e^{-\gamma\tau})$, and r is calculated as $d = 3\gamma/2 = 4642/r^3$. Each sample typically contains ~ 1μmol peptide. The peptide to lipids (not including CHOL) ratio is typically 1:50.

3.2.6.3 HFP location in DOPC: DOPG: CHOL membrane studied by ^{13}C–^{2}H REDOR

The ^{13}C–^{2}H REDOR NMR method is also employed to study the membrane locations of HFP in DOPC: DOPG: CHOL membrane. DOPC and DOPG lipids have much lower melting temperature, which is −17 °C and −18 °C, respectively, compared to 41°C of DPPC and DPPG lipids. The sample temperature during NMR data acquisition is ~ −30 °C. The lipids and peptides would have much more motion compared to the POPC and DPPC membranes. The peptide is ^{13}CO labeled at G5. The NMR sample is prepared by aqueous vesicle binding method which is described in chapter 2. The data is processed with 100 Hz Gaussian line broadening and polynomial baseline correction. The spectra feature for Chol_d7 and Chol_d6 are consistent with

the membrane compositions studied earlier. Major peak has 171ppm chemical shift, which is corresponding to β sheet structure. For HFP_G5c in DOPC and DPPC containing membrane, the full width at half maximum (FWHM) is 2.4 ppm and 2.7 ppm at τ = 2ms; 2.2 ppm and 2.5 ppm respectively at τ = 40ms. The $(S/N/scan)_{DPPC}$: $(S/N/scan)_{DOPC} \approx 1$ and 5 for S_0 at τ = 2ms and τ = 40ms respectively. Compared to DPPC membrane, the FWHM is a little bit narrower and S/N/scan is much worse in DOPC membrane. This is probably because increased membrane and peptides motion, which leads to shorter T_2 for HFP. S_0 and S_1 are integrated with 2 ppm integration window because the peak is narrower, and the dephasing results are superimposable to those obtained with 3 ppm integration window for HFP_G5c with Chol_d7 labeling. The quantitative dephasing is calculated for major β peak. HFP_G5c has much greater dephasing with Chol_d7 than Chol_d6, which supports that major HFP_G5c is inserted into the membrane hydrocarbon core and contacting Chol_d7 ^{2}Hs. The membrane location features are consistent with the results studied earlier with other model membranes. However, the dephasing buildups are not showing exponential trends. The buildup rate is much slower; the $(\Delta S/S_0)_{16ms}$ is 13 % in DOPC membrane, but 40% in DPPC membrane, and the $(\Delta S/S_0)_{40ms}$ is 46% in DOPC membrane, but 76% in DPPC membrane. This is likely due to increased motional averaging of the coupling. The initial data shows that the ^{13}C–^2H REDOR NMR method is also able to differentiate membrane core and membrane surface contacts of peptide. More residue specific labeling is needed to obtain a complete membrane location model of HFP in the DOPC: CHOL membrane system. This method should also be able to be applied to study residue specific contacts of other peptides or proteins in this model membrane system.

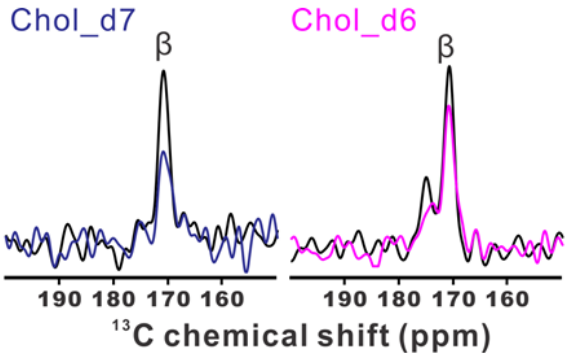

Figure 3.19 ^{13}C-detect / ^{2}H-dephase REDOR S_0 (black) and S_1 (colored) experimental spectra for HFP_G5c at τ = 40ms. The data is processed with 100 Hz Gaussian line broadening and polynomial baseline correction. DOPC: DOPG: CHOL = 8:2:5. Chol_d7 sample contains ~ 1.5μmol peptides, and Chol_d6 sample contains ~ 1.3μmol peptides.

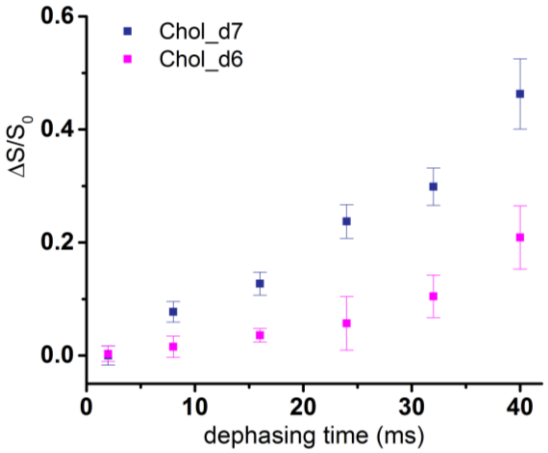

Figure 3.20 The dephasing buildups of $\Delta S/S_0$ (colored squares) with error bars vs dephasing time (τ) for HFP_G5c in membrane composed of DOPC: DOPG: CHOL = 8:2:5 ratio. The $\Delta S/S_0$ data is for the major peak of β sheet conformation and the S_0 and S_1 is integration with 2 ppm integration window.

The membrane location of HFP in 33mol % CHOL with DPPC, POPC, and DOPC membrane is compared by analyzing the average dephasing of 8- 40ms dephasing. The ratio of dephasing with Chol_d7 to Chol_d6 is calculated for G5 labeling, and the ratio of dephasing with Chol_d6 to Chol_d7 is calculated for G16. The average dephasing ratio is 2.9 for G5c in both DPPC and POPC membrane, which supports similar membrane locations for G5 in both model membrane studied. For Gl6c, the average dephasing of Chol_d6 relative to Chol_d7 is 3.7 and 2.0 in DPPC and POPC membrane respectively, which support major fraction of G16 is located near the membrane surface in both model membranes studied.

3.2.7 HFPV2E $^{13}C–^{2}H$ REDOR results in membrane without CHOL

It's interesting and significant to study V2E mutant because studies have shown that this mutant could significant decrease fusion.[16, 21] A single residue V2E mutation in the whole HIV gp41 protein eliminates fusion, and even a mixture of small fraction of the V2E mutant protein significantly decreases fusion. These results suggest that gp41 acts as oligomers during catalysis of fusion. It has been proposed that wild type and V2E mutant HFP peptides have different secondary structure and membrane locations.[8, 22, 37, 38] In membrane without CHOL, HFP_V2E mutant has greater population of helical structure than HFP wild type.[8] $^{13}C–^{31}P$ REDOR data supports that HFP_V2E has much shallower membrane location then HFP wildtype with greater contact to the membrane surface phosphorous head group.[16] In this thesis, we are studying the membrane contacts with specific regions of the membrane by $^{13}C–^{2}H$ REDOR method, the advantage of which has been discussed earlier.

The HFP_V2E peptide is ^{13}CO labeled at G5 residue. The peptide is chemically synthesized by FMOC SPPS method, and purified by reverse phase HPLC. The peptide purity was checked by

MALDI–TOF mass spectrometry and the purity is ≥ 90 %. The membrane is PC: PG =4:1 mole ratio and ^{2}H labeled with PC_d10/d8/d4.

Compared to the spectra of wild type G5, the V2E mutant G5 has a greater 175ppm chemical shift peak. This is probably due to higher fraction of helical conformation at G5 site compared to wild type, which is consistent with the previous study results. There are substantial dephasing buildups for samples with both PC_d10 and PC_d8 labeling, and smallest dephasing buildup for PC_d4 labeling. The substantial buildups are well fitted to exponential equation $A \times (1 - e^{-\gamma\tau})$. Fitting of both PC_d10 and PC_d8 sample give 4 ~ 5 Å ^{13}C–^{2}H inter-nuclear distance. These results support HFP_V2E G5 ^{13}CO has Van der Waals contact with both PC_d10 and PC_d8 ^{2}Hs, which also support major deeply inserted and minor shallowly inserted membrane locations of G5 residue. And the multiple membrane location feature of HFP_V2E is similar to G5 wild type. However, the PC_d8 dephasing buildup is much bigger for the V2E mutant than the wild type, which suggests bigger fraction of G5 in the V2E mutant has shallower membrane location than wild type G5. The bigger fraction of shallower membrane location for V2E molecules positively correlates with its less fusogenicity. There is antiparallel registry distribution difference between V2E and wild type β sheet molecules.[29] There is major longer antiparallel β sheet registry for HFP_V2E mutant than wildtype. For V2E mutant, ~ 0.44 fraction of antiparallel β sheet registry is with residues 20→1/1→20. For wild type, ~ 0.30 fraction of antiparallel β sheet registry is with residues 16→1/1→16 and 17→1/1→17.[29] The hydrophobic patch is formed by the most hydrophobic first 12 residues of HFP N-terminal based on amino acid hydrophobicity. The non-fusogenicity of V2E is associated with the hydrophobic patch size formed from its registry. For 20→1/1→20 registry, the hydrophobic patch is formed from residue 9 to residue 12. However, for 16→1/1→16 registry, the hydrophobic patch is formed from residue 5 to residue 12 (shown

in Figure 3.21). Thus, the hydrophobic patch is shorter with longer 20→1/1→20 antiparallel β sheet registry compared to 16→1/1→16 registry. The bigger fraction of shallower membrane location for V2E is probably due to the shorter hydrophobic patch which causes less perturbation of the membrane. A semi quantitative membrane location model is proposed, but a more complete model will need membrane contact studies of some other residue labeling.

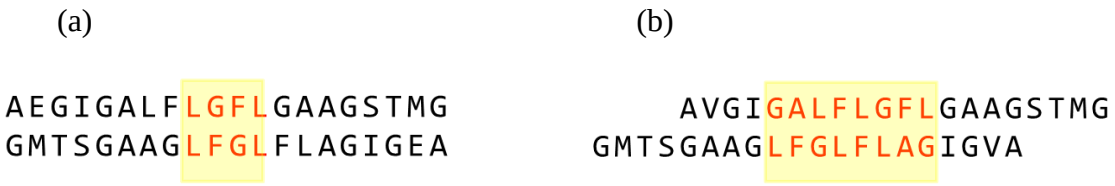

Figure 3.21 Schematic pictures of the hydrophobic patch (yellow shaded area) formed by the N-terminal most hydrophobic 12 residues of HFP based on amino hydrophobicity. (a) 20→1/1→20 registry for HFP_V2E mutant. (b) 16→1/1→16 registry for HFP wild type.

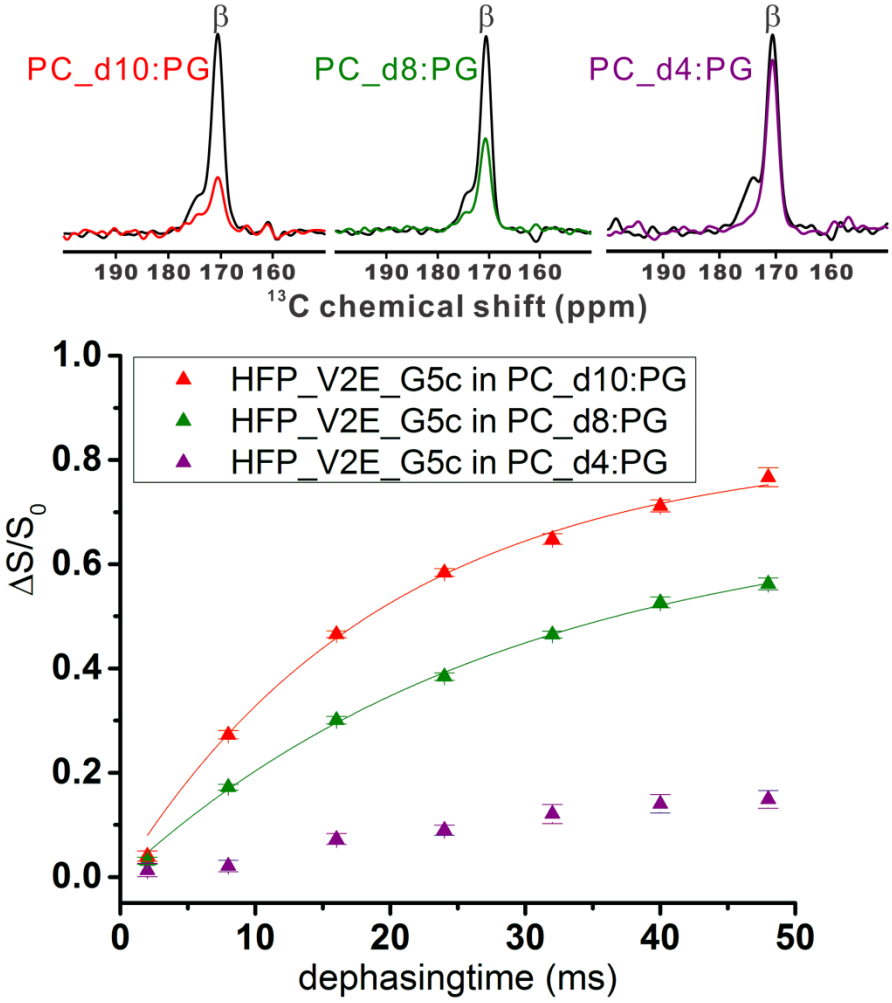

Figure 3.22 ^{13}C-detect / ^{2}H-dephase REDOR S_0 (black) and S_1 (colored) experimental spectra (top panel) and the dephasing buildups (bottom panel) of $\Delta S/S_0$ (colored triangles) with error bars vs dephasing time (τ) for HFP_V2E_G5c. The spectra displayed is for τ =40ms. The data is processed with 100Hz Gaussian line broadening and polynomial baseline correction. The quantitative dephasing buildup is for the major β peak with 171ppm chemical shift. S_0 and S_1 is integration through 3ppm integration window. The colored line is the best fit exponential buildup curve fitted by $A \times (1 - e^{-\gamma\tau})$.

Table 3.5 Best-fit exponential buildup parameters for HFP_V2E_G5c in membrane without CHOL [a]

Membrane	A	γ (Hz)	r (Å)
PC_d8:PG	0.70 (3)	35 (3)	4.5 (1)
PC_d10:PG	0.82 (4)	51 (4)	4.0 (1)

[a] A and γ are fitting parameters for experimental dephasing buildup from fitting equation of $A \times (1 - e^{-\gamma\tau})$, and r is calculated as $d = 3\gamma/2 = 4642/r^3$. The membrane composition is PC: PG (4:1) with ~ 1μmol peptide. The peptide to lipids ratio is 1:50.

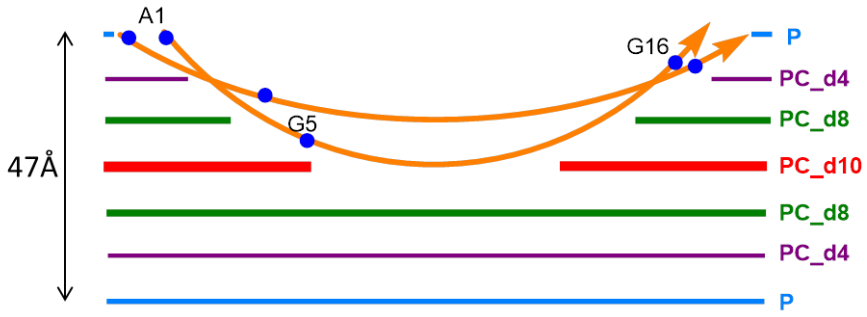

Figure 3.23 Semi-quantitative HFP_V2E membrane location model with major population deeply inserted and minor population shallowly inserted to the membrane hydrophobic core. There is more minor population compared to HFP wildtype with shallowly inserted membrane location. How the lipids and CHOL are displaced by HFP molecules is not known and neither the orientation the neighbor lipids and CHOL of HFP.

3.2.8 HFPL9R results in membrane without CHOL

L9R mutant is another mutant that is worth study because L9R mutant could also significantly reduce membrane fusion.[21] The fusion reduction effect is much less for L9R than V2E mutant. In order to help understand HIV membrane fusion mechanism, we study the structure and membrane contacts of HFP_L9R in lipid membrane.

The HFP_L9R peptide is chemically synthesized by FMOC SPPS method and purified by reverse phase HPLC. The peptide purity is checked by MALDI-TOF mass spectrometry, and the purity is ≥ 90 %. Each sample contains ~ 1.5μmol peptide. And the membrane is PC: PG =4:1.

The spectra have a major ^{13}CO peak at 176ppm for both HFP_L9R G5 and G10 samples, which is not corresponding to β sheet structure.[27] Then 176ppm chemical shift might indicate α helical structure because ^{13}CO chemical shift for glycine in α helical protein is 175.51 (1.23)ppm,

where 175.51 ppm is the average value and 1.23ppm is the standard deviation.[27] G5 sample has biggest dephasing with PC_d10 labeling, significant dephasing with PC_d4 labeling and negligible dephasing for PC_d8. These results suggest that there are multiple locations of L9R G5 reside, with most population deeply inserted into the membrane hydrocarbon core and contacting PC_d10 ^{2}Hs, and minor population located near the membrane surface contacting PC_d4 ^{2}Hs, and almost no contact to PC_d8 ^{2}Hs. At τ = 48ms, $(\Delta S/S_0)_{d10}/(\Delta S/S_0)_{d4} \approx 2{:}1$. G10 sample has similar buildup trends with G5, biggest dephasing obtained with PC_d10 labeling, some dephasing with PC_d4 and negligible dephasing buildup with PC_d8 labeling. It's just the buildup extents for both PC_d10 and PC_d4 are different. For G10 sample, there is rapid dephasing buildup and goes up to 90% at τ = 48ms, which supports most G10 ^{13}CO are making contacts with PC_d10 ^{2}Hs, and most L9R peptide molecules are deeply inserted into the membrane center. There are ~ 25% molecules making contact with PC_d4 ^{2}Hs near the membrane surface based on the τ = 48ms dephasing ratio, $(\Delta S/S_0)_{d10}/(\Delta S/S_0)_{d4} \approx 3{:}1$. Substantial buildups with PC_d10 labeling are fitted by $A \times (1 - e^{-\gamma\tau})$ with two options. One is with the limitation of $A \leq 1$, because A is the molecular fraction, the maximum of which is 1. The other one is without limitation of A. The best fitted 4 ~ 5 Å distance supports Van der Waals contact between HFP_L9R molecule and PC_d10 at both G5 and G10 ^{13}CO site.

A more quantitative fitting of the PC_d4 buildups might need lipid natural abundance correction because the lipid ^{13}CO group is directly bonded to the carbon that has d4 ^{2}Hs attached. So there will be a small fraction of rapid buildup from lipid ^{13}CO group due to ^{13}C–^{2}H dipolar coupling. The lipid ^{13}CO–^{2}H distance is ~ 2.1 Å according to the distance between Cα–^{1}H and ^{13}CO within the same residue in β strand structure. The corresponding d would be ~ 500Hz and $\gamma \approx$ 333 Hz. And the resulting dephasing would increase rapidly to ~1 at τ = 16ms according to fitting

equation of $A \times (1 - e^{-\gamma\tau})$ with A= 1. So the dephasing from lipid natural abundance (na) at longer dephasing time would depend on the fraction which is A value from lipid na ^{13}CO. For a typical sample containing 1.5μmol peptide in 50μmol lipids,

$f_{Lip-na} = \frac{Lip-na}{Lip-na+pep-na+lab} = \frac{50\mu mol \times 1.1\%}{50\mu mol \times 1.1\% + 30 \times 1.5\mu mol \times 1.1\% + 0.99 \times 1.5\mu mol} = 0.23$, where Lip-na is the amount of lipid natural abundance ^{13}CO, pep–na is the amount of peptide natural abundance ^{13}CO, and lab is the amount of labeled peptide ^{13}CO. The corresponding $(\Delta S/S_0)_{2ms}^{Lip-na}$ is ~ 0.10. For both G5 and G10 labeling, the $(\Delta S/S_0)_{2ms}$ is ~ 0.10, which is mostly from the Lip-na dephasing. For G5 sample with PC_d4 labeling, $(\Delta S/S_0)_{48ms}^{exp}$ is ~ 0.45, then the corrected $(\Delta S/S_0)_{48ms}^{cor}$ ~ 0.22. $(\Delta S/S_0)_{d10}/ (\Delta S/S_0)_{d4}^{cor} \approx 7{:}2$, which still supports major deeply inserted and minor shallowly inserted membrane location for G5. For G10 sample with PC_d4 labeling, $(\Delta S/S_0)_{48ms}^{exp}$ is ~ 0.32, then the corrected $(\Delta S/S_0)_{48ms}^{cor}$ ~ 0.10, which supports almost no dephasing buildup from the peptide with PC_d4. And the $(\Delta S/S_0)_{d10}/ (\Delta S/S_0)_{d4}^{cor} \approx 9{:}1$. So, there is likely single deeply inserted membrane location of HFP_L9R at G10 residue.

A membrane location model consistent with our experimental results is that G10 is located near the membrane center, and G5 is also close to the membrane center but relatively shallower compared to G10 because $(\Delta S/S_0)_{G5}/ (\Delta S/S_0)_{G10} \approx 0.7{:}\ 0.9$. The complete membrane location model would need more dephasing data from other residue labeling as well as the confirmation of the secondary structure of the HFP_L9R mutant.

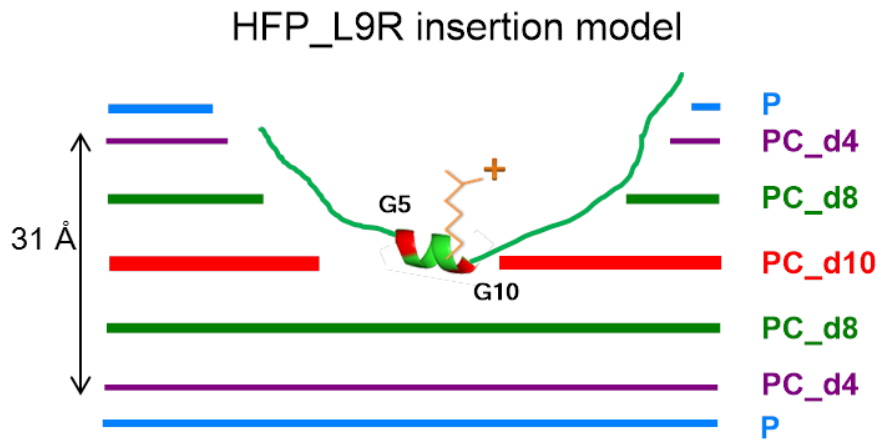

Figure 3.24 Membrane location model of HFP_L9R mutant consistent with our REDOR experimental data. A short helix is shown from G5 to G10 to reflect the helical conformation for G5 and G10 residues. And the secondary structure of other residues in HFP_L9R mutant is not determined and shown as line. The R9 sidechain is likely pointing out to the direction of the membrane surface. However, the arginine side chain length is ~ 7.5 Å, which is shorter than the hydrophobic thickness of half membrane leaflet. HFP_L9R mutant probably induces local membrane thinning, and similar membrane curvature relative to membrane fusion intermediate. This might help explain the fusogenicity of L9R mutant.

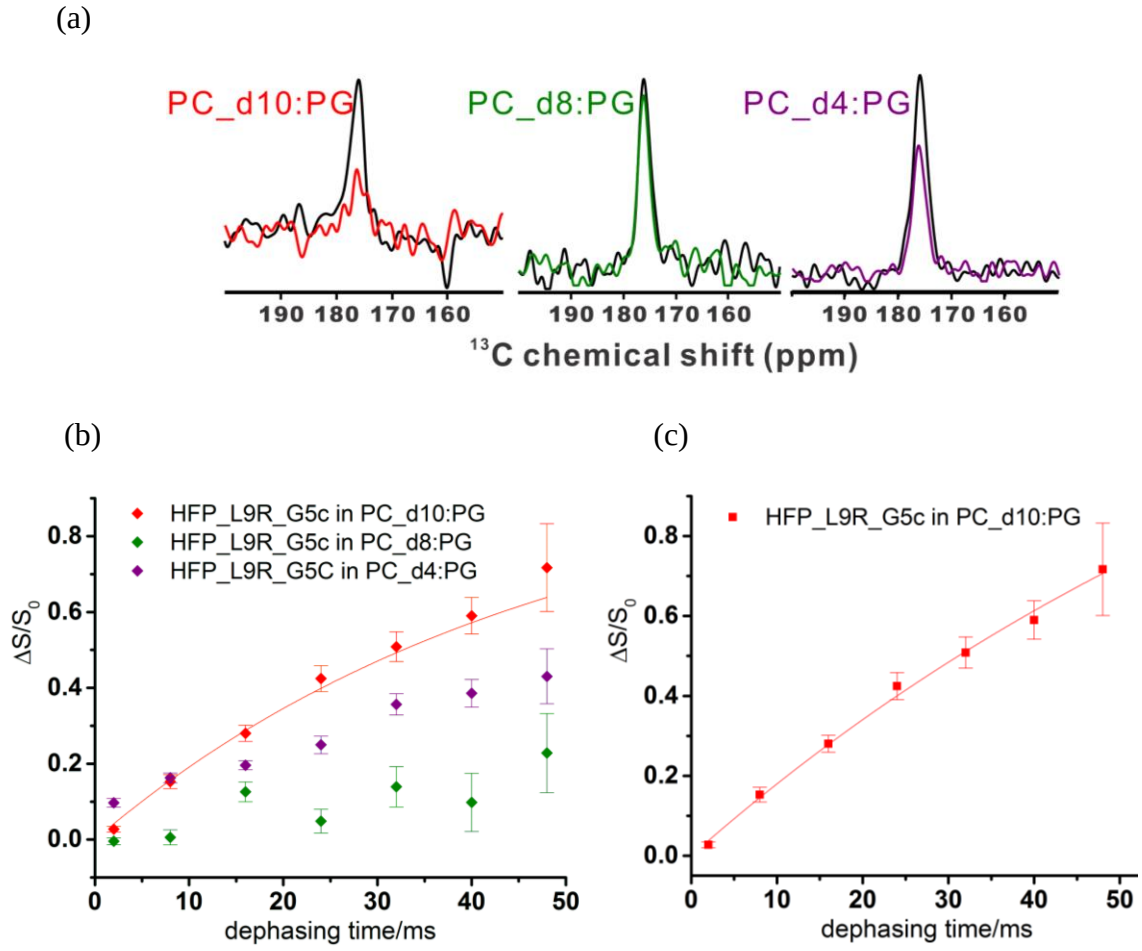

Figure 3.25 ^{13}C-detect / ^{2}H-dephase REDOR S_0 (black) and S_1 (colored) experimental spectra (a) and the dephasing buildups (b) of $\Delta S/S_0$ (colored squares) with error bars vs dephasing time (τ) for HFP_L9R_G5c. The spectra displayed is for τ =40ms. The data is processed with 100Hz Gaussian line broadening and polynomial baseline correction. The quantitative dephasing buildup is for the major peak with 176 ppm chemical shift. S_0 and S_1 is integration through 3ppm integration window. The colored line is the best fit exponential buildup curve fitted by $A \times (1 - e^{-\gamma\tau})$. Fitting in (b) in done with A≤1, the χ^2 for d10 fitting is 5. Fitting in (c) is done with no limitation on A, and the χ^2 for d10 fitting is 2.5.

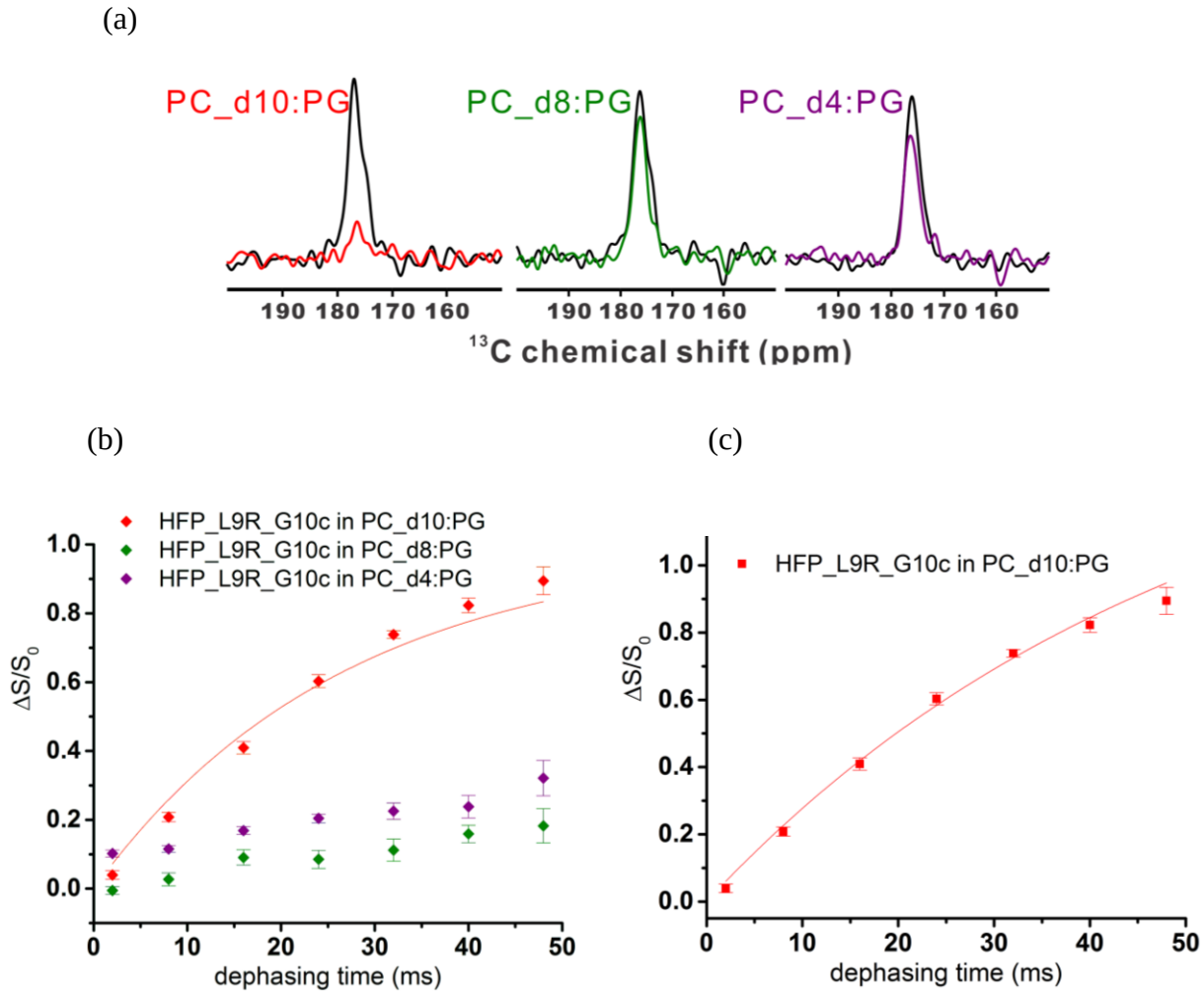

Figure 3.26 ^{13}C-detect / ^{2}H-dephase REDOR S_0 (black) and S_1 (colored) experimental spectra (a) and the dephasing buildups (b) of $\Delta S/S_0$ (colored squares) with error bars vs dephasing time (τ) for HFP_L9R_G10c. The spectra displayed is for τ =40ms. The data is processed with 100Hz Gaussian line broadening and polynomial baseline correction. The quantitative dephasing buildup is for the major peak with 176 ppm chemical shift. S_0 and S_1 is integration through 3ppm integration window. The colored line is the best fit exponential buildup curve fitted by $A \times (1 - e^{-\gamma\tau})$. Fitting in (b) in done with A≤1, the χ^2 for d10 fitting is 45. Fitting in (c) is done with no limitation on A, and the χ^2 for d10 fitting is 10.

Table 3.6 Best-fit exponential buildup parameters for HFP_L9R in membrane without CHOL [a]

Peptide	Membrane	A	γ (Hz)	r (Å)
G5	PC_d10:PG	1.0 (3) [b]	21(7)	5.3 (6)
G5	PC_d10:PG	1.7 (7) [c]	11(5)	6.5(10)
G10	PC_d10:PG	1.0 (2) [b]	37 (11)	4.4 (4)
G10	PC_d10:PG	1.5 (2) [c]	30 (7)	5.4 (4)

[a] A and γ are fitting parameters for experimental dephasing buildup from fitting equation of $A \times (1 - e^{-\gamma\tau})$ with limitation of A≤ 1, and r is calculated as d= 3γ/2 = 4642/r^3. The membrane composition is PC: PG (4:1) with ~ 1.5μmol peptide. The peptide to lipids ratio is 3:100. The uncertainty is in the parenthesis, and a sample 1.0 (3) means an error of ±0.3.

[b] data is fitted with limitation of A≤ 1.

[c] data is fitted with no limitation on A .

To summarize, our study supports that L9R mutant is non β sheet structure at G5 and G10 residues. Membrane contacts between the peptide backbone and specific regions of membrane support multiple membrane locations for G5 with major deeply inserted population contacting the membrane center and a minor shallowly inserted population contacting the membrane surface

lipid carbonyl region. Different from G5, G10 likely has a single membrane location which is deeply inserted into the membrane center contacting the lipid tail.

3.2.9 KALP results in membrane without CHOL

KALP peptide is a transmembrane α helical peptide in membrane.[39, 40] The ^{13}C–^{2}H REDOR method is applied to study the residue specific membrane locations of helical transmembrane peptide. The KALP peptide is chemically synthesized by Fmoc SPPS method and ^{13}CO labeled at A5, A7, A17 and A19. The crude peptides are purified by reverse phase HPLC with a C4 column. The purification program is different than any HFP purification program and is shown in appendix. To make NMR sample, 9.7 mg peptides are weighed and dissolved in 3mL 2,2,2-trifuoroethanol, 3mL 1,1,1,3,3,3-hexafluoroisopropanol, and 4.5 mL chloroform. The mixture is then divided into 3 portions, and each portion is added to PC_d10: PG, PC_d8: PG and PC_d4: PG lipid films, respectively. So each membrane is feed 1.4μmol KALP peptides. The peptide lipids mixture is mixed by sonication, and solvent is removed by a steam of N_2 (g), followed by vacuum overnight to remove any residual solvents. The dry film is then hydrated in 3 mL buffer with pH 7.4, homogenized by 10 freeze– thaw cycles. Extra 20 mL buffer is added. The pellet is harvested after centrifugation at ~ 270000g. Any unbound KALP peptide is in the supernatant.

All KALP samples with Ala ^{13}CO labeling have dominant peak with ~ 179 ppm chemical shift, which is consistent with α helical conformation. Dephasing of the four Ala labeling show similar dephasing buildup trends, with dephasing $(\Delta S/S_0)_{d10>d8>d4}$. There are dephasing buildups for d10 and d8, and no dephasing buildups for d4 labeled samples. At τ = 48ms, $(\Delta S/S_0)_{d10:d8} \approx$ 4:3, 2:1, 2:1 and 3:2 ratio for A5, A7, A17 and A19, respectively. The bigger dephasing with d10 than d8 labeling supports that there are major contacts with d10 then with d8. The substantial experimental dephasing buildups show exponential trends for A5, A7 and A17, and are fitting

with equation $A \times (1 - e^{-\gamma\tau})$. It's not exponential buildup trend for A17 data, which need to be fitted by other fitting methods to find out the inter-nuclear distance, which will be used to calculate the membrane location of the labeled ^{13}CO nucleus. The similar buildup extent at longer dephasing time with much slower buildup rate might suggest a single longer inter-nuclear distance.

To summarize, our studies show helical secondary structure of KALP peptide at A5, A7, A17 and A19 residue. Membrane contact study between the peptide backbone and specific regions of membrane show similar membrane contacts at A5, A7 and A17 residue, with major contact with membrane center PC_d10 and minor contact with PC_d8. A19 has similar dephasing value at longer dephasing time (τ = 48ms) for PC_d10, d8 and d4 labeling, but with a much slower buildup, which suggests a longer ^{13}C-^{2}H inter-nuclear distance, and thus A19 is much further away from membrane center. Figure 3.35 shows a membrane location model of KALP peptide consistent with our experiment results. The hydrophobic length of LA residues is 25.5Å, which is shorter than the ~ 31Å of the DPPC membrane hydrophobic thickness.[39, 40] The lysine sidechains are pointing out to interact with the aqueous phase near the phosphate group, and the hydrophobic length of the peptide is extended by lysine sidechains. This is consistent with the proposed snorkeling effect of charged residues like lysine in transmembrane peptides.[41] The different membrane locations are probably due to different snorkeling geometries of the lysine. According to the dephasing at τ=48ms, the molecular population for making close contact with PC_d10 relative to PC_d8 is ~ 3:2 for all A5, A7, A17 and A19 residues.

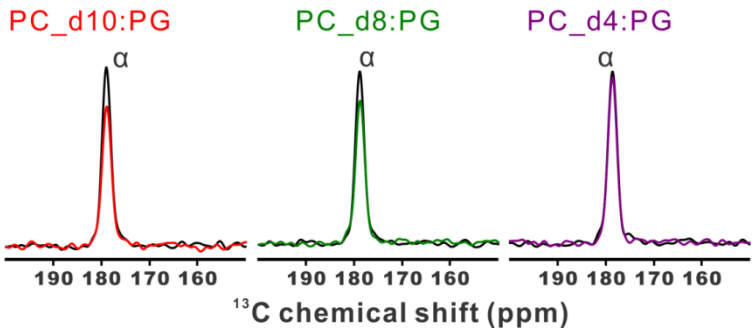

Figure 3.27 ^{13}C-detect / ^{2}H-dephase REDOR S_0 (black) and S_1 (colored) experimental spectra for KALP_A5c at τ = 40ms. The data is processed with 100 Hz Gaussian line broadening and polynomial baseline correction. PC: PG =4:1 mole ratio.

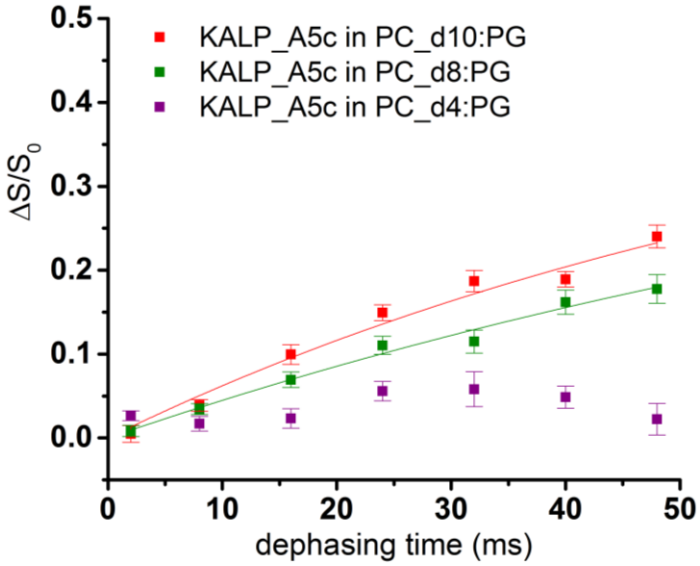

Figure 3.28 The KALP_A5c dephasing buildup of $\Delta S/S_0$ (colored squares) with error bars vs dephasing time. S_0 and S_1 is integration through 3ppm integration window. The colored line is the best fit exponential buildup curve fitted by $A \times (1 - e^{-\gamma\tau})$. PC: PG =4:1 mole ratio.

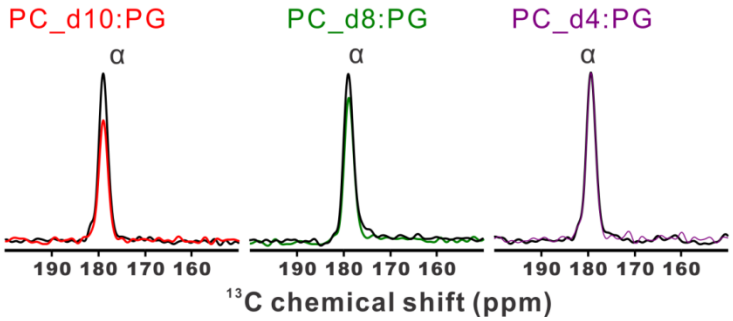

Figure 3.29 ^{13}C-detect / ^{2}H-dephase REDOR S_0 (black) and S_1 (colored) experimental spectra for KALP_A7c at τ = 40ms. The data is processed with 100 Hz Gaussian line broadening and polynomial baseline correction. PC: PG =4:1 mole ratio.

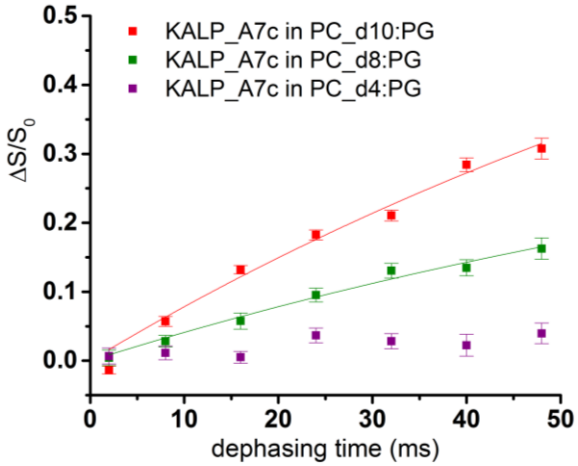

Figure 3.30 The KALP_A7c dephasing buildup of $\Delta S/S_0$ (colored squares) with error bars vs dephasing time. S_0 and S_1 is integration through 3ppm integration window. The colored line is the best fit exponential buildup curve fitted by $A \times (1 - e^{-\gamma\tau})$. PC: PG =4:1 mole ratio.

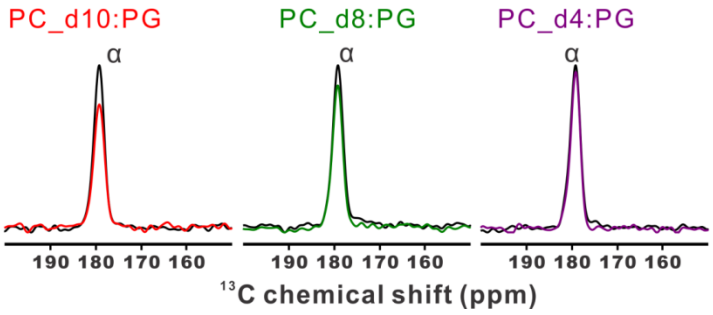

Figure 3.31 ^{13}C-detect / ^{2}H-dephase REDOR S_0 (black) and S_1 (colored) experimental spectra for KALP_A17c at τ = 40ms. The data is processed with 100 Hz Gaussian line broadening and polynomial baseline correction. PC: PG =4:1 mole ratio.

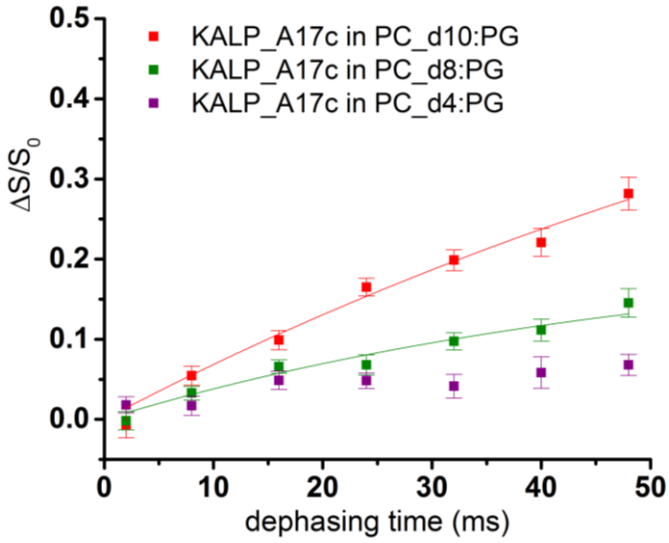

Figure 3.32 The KALP_A17c dephasing buildups of $\Delta S/S_0$ (colored squares) with error bars vs dephasing time. S_0 and S_1 is integration through 3ppm integration window. The colored line is the best fit exponential buildup curve fitted by $A \times (1 - e^{-\gamma\tau})$. PC: PG =4:1 mole ratio.

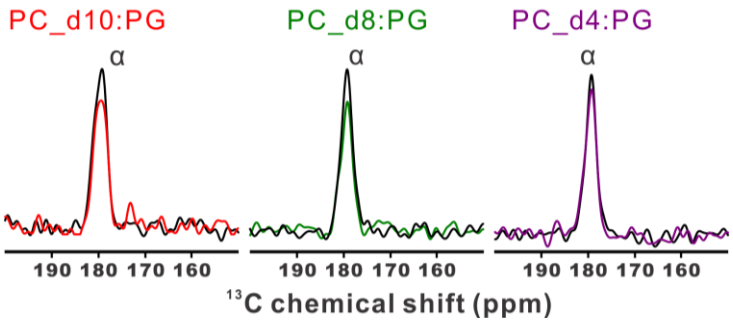

Figure 3.33 ^{13}C-detect / ^{2}H-dephase REDOR S_0 (black) and S_1 (colored) experimental spectra for KALP_A19c at τ = 40ms. The data is processed with 100 Hz Gaussian line broadening and polynomial baseline correction. PC: PG =4:1 mole ratio.

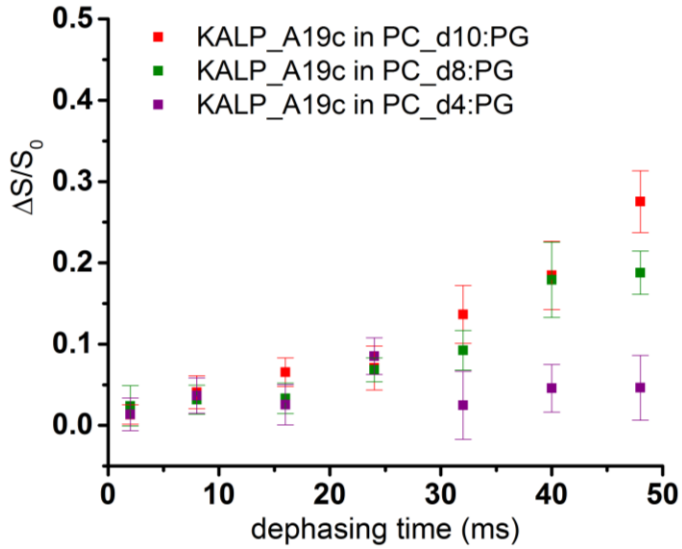

Figure 3.34 The KALP_A19c dephasing buildup of $\Delta S/S_0$ (colored squares) with error bars vs dephasing time. S_0 and S_1 is integration through 3ppm integration window. PC: PG =4:1 mole ratio.

Table 3.7 Best-fit exponential buildup parameters for KALP in membrane without CHOL [a]

Peptide	Membrane	A	γ (Hz)	r (Å)
A5	PC_d8:PG	0.47 (21)	10 (5)	6.8 (1.2)
A5	PC_d10:PG	0.47 (22)	14 (8)	6.0 (1.2)
A7	PC_d8:PG	0.44 (26)	10 (7)	6.8 (1.6)
A7	PC_d10:PG	0.84 (73)	10 (10)	6.8 (2.3)
A17	PC_d8:PG	0.22 (9)	19 (10)	5.5 (1.0)
A17	PC_d10:PG	0.72 (40)	10 (7)	6.8 (1.5)

[a] A and γ are fitting parameters for experimental dephasing buildup from fitting equation of $A \times (1 - e^{-\gamma\tau})$, and r is calculated as $d = 3\gamma/2 = 4642/r^3$. The membrane composition is PC: PG (4:1) with ~ 1μmol peptide.

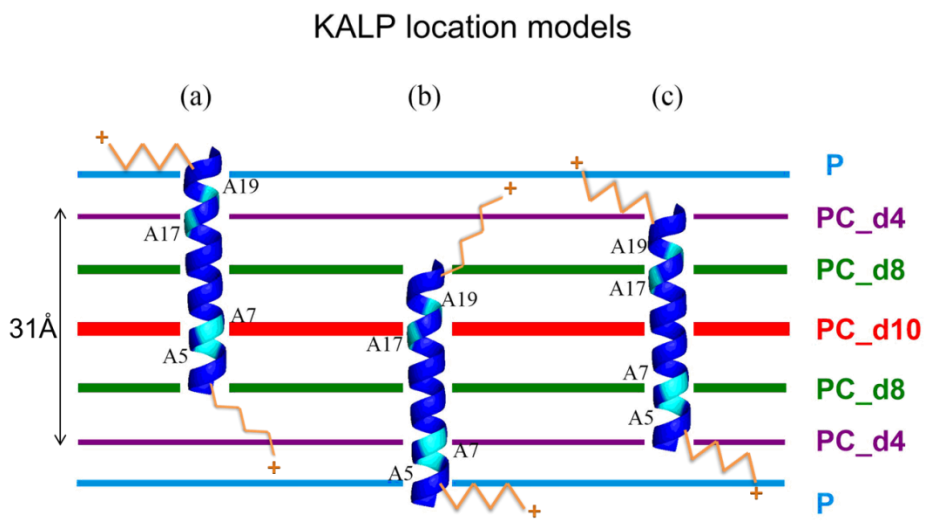

(d) KALP sequence: Acetyl-GKKLALALALALALALALALKKA-NH_2

Figure 3.35 The membrane location model for KALP peptide with one representative lysine sidechain near N- and C- terminal. (a) Major populations of A5 and A7 have close contact to PC_d10 located near the membrane center. (b) Major populations of A17 and A19 have close contact to PC_d10 located near the membrane center, but with A19 further away to PC_d10 compared to A17. (c) Significant populations of A5, A7, A17 and A19 make close contact of PC_d8. (d) Amino acid sequence for KALP peptide. Snorkeling effect of terminal lysine sidechains help extend the hydrophobic length of the peptide by pointing out to the aqueous surface near the phosphate group. The molecular population of (a): (b): (c) ≈ 3:3:2, because the dephasing for PC_d10: PC_d8 is ~ 3:2 for all A5, A7, A17 and A19 residues at τ=48ms. There isn't substantial dephasing buildup for PC_d4 might because the snorkeling effect of lysing sidechains might make lysine sidechains displace PC_d4 and thus enlarge the inter-nuclear distance between labeled ^{13}CO and PC_d4 and is beyond the ~ 8Å detection limit of ^{13}C-^{2}H REDOR.

REFERENCES

REFERENCES

1. Dupuy, A.D. and D.M. Engelman, *Protein area occupancy at the center of the red blood cell membrane.* Proceedings of the National Academy of Sciences of the United States of America, 2008. **105**(8): p. 2848-2852.

2. Michalek, M., C. Aisenbrey, and B. Bechinger, *Investigation of membrane penetration depth and interactions of the amino-terminal domain of huntingtin: refined analysis by tryptophan fluorescence measurement.* European Biophysics Journal with Biophysics Letters, 2014. **43**(8-9): p. 347-360.

3. Lin, P.H., et al., *Membrane attachment and structure models of lipid storage droplet protein 1*. Biochimica Et Biophysica Acta-Biomembranes, 2014. **1838**(3): p. 874-881.

4. Su, Y., R. Mani, and M. Hong, *Asymmetric insertion of membrane proteins in lipid bilayers by solid-state NMR paramagnetic relaxation enhancement: A cell-penetrating peptide example.* Journal of the American Chemical Society, 2008. **130**(27): p. 8856-8864.

5. Gabrys, C.M. and D.P. Weliky, *Chemical shift assignment and structural plasticity of a HIV fusion peptide derivative in dodecylphosphocholine micelles.* Biochimica Et Biophysica Acta-Biomembranes, 2007. **1768**(12): p. 3225-3234.

6. Jaroniec, C.P., et al., *Structure and dynamics of micelle-associated human immunodeficiency virus gp41 fusion domain.* Biochemistry, 2005. **44**(49): p. 16167-16180.

7. Li, Y.L. and L.K. Tamm, *Structure and plasticity of the human immunodeficiency virus gp41 fusion domain in lipid micelles and bilayers.* Biophysical Journal, 2007. **93**(3): p. 876-885.

8. Gabrys, C.M., et al., *Solid-State Nuclear Magnetic Resonance Measurements of HIV Fusion Peptide (CO)-C-13 to Lipid P-31 Proximities Support Similar Partially Inserted Membrane Locations of the alpha Helical and beta Sheet Peptide Structures.* Journal of Physical Chemistry A, 2013. **117**(39): p. 9848-9859.

9. Qiang, W., M.L. Bodner, and D.P. Weliky, *Solid-state NMR Spectroscopy of human immunodeficiency virus fusion peptides associated with host-cell-like membranes: 2D correlation spectra and distance measurements support a fully extended conformation and models for specific antiparallel strand registries.* Journal of the American Chemical Society, 2008. **130**(16): p. 5459-5471.

10. Yang, J., C.M. Gabrys, and D.P. Weliky, *Solid-state nuclear magnetic resonance evidence for an extended beta strand conformation of the membrane-bound HIV-1 fusion peptide.* Biochemistry, 2001. **40**(27): p. 8126-8137.

11. Toke, O., et al., *Secondary structure and lipid contact of a peptide antibiotic in phospholipid Bilayers by REDOR.* Biophysical Journal, 2004. **87**(1): p. 662-674.

12. Xie, L., et al., *Residue-specific membrane location of peptides and proteins using specifically and extensively deuterated lipids and C-13-H-2 rotational-echo double-resonance solid-state NMR.* Journal of Biomolecular Nmr, 2013. **55**(1): p. 11-17.

13. Schmidt, A., R.A. McKay, and J. Schaefer, *INTERNUCLEAR DISTANCE MEASUREMENT BETWEEN DEUTERIUM (I = 1) AND A SPIN-1/2 NUCLEUS IN ROTATING SOLIDS.* Journal of Magnetic Resonance, 1992. **96**(3): p. 644-650.

14. Gullion, T., R. Kishore, and T. Asakura, *Determining dihedral angles and local structure in silk peptide by C-13-H-2 REDOR.* Journal of the American Chemical Society, 2003. **125**(25): p. 7510-7511.

15. Hirsh, D.J., et al., *A new monofluorinated phosphatidylcholine forms interdigitated bilayers.* Biophysical Journal, 1998. **75**(4): p. 1858-1868.

16. Qiang, W., Y. Sun, and D.P. Weliky, *A strong correlation between fusogenicity and membrane insertion depth of the HIV fusion peptide.* Proceedings of the National Academy of Sciences of the United States of America, 2009. **106**(36): p. 15314-15319.

17. Xie, L., *Solid State Nuclear Magnetic Rosonance Studies of Structures and Membrane Locations of Peptides*, in *Chemistry*. 2014, Michigan State University.

18. Jia, L.H., et al., *REDOR solid-state NMR as a probe of the membrane locations of membrane-associated peptides and proteins.* Journal of Magnetic Resonance, 2015. **253**: p. 154-165.

19. Sack, I., et al., *Solid-state NMR determination of peptide torsion angles: Applications of H-2-dephased REDOR.* Journal of the American Chemical Society, 2000. **122**(49): p. 12263-12269.

20. Schmick, S.D. and D.P. Weliky, *Major Antiparallel and Minor Parallel beta Sheet Populations Detected in the Membrane-Associated Human Immunodeficiency Virus Fusion Peptide.* Biochemistry, 2010. **49**(50): p. 10623-10635.

21. Freed, E.O., et al., *A MUTATION IN THE HUMAN-IMMUNODEFICIENCY-VIRUS TYPE-1 TRANSMEMBRANE GLYCOPROTEIN-GP41 DOMINANTLY INTERFERES WITH FUSION AND INFECTIVITY.* Proceedings of the National Academy of Sciences of the United States of America, 1992. **89**(1): p. 70-74.

22. Qiang, W. and D.P. Weliky, *HIV Fusion Peptide and Its Cross-Linked Oligomers: Efficient Syntheses, Significance of the Trimer in Fusion Activity, Correlation of beta Strand Conformation with Membrane Cholesterol, and Proximity to Lipid Headgroups.* Biochemistry, 2009. **48**(2): p. 289-301.

23. Gullion, T., *Introduction to rotational-echo, double-resonance NMR.* Concepts in Magnetic Resonance, 1998. **10**(5): p. 277-289.

24. Zheng, Z., et al., *Conformational flexibility and strand arrangements of the membrane-associated HIV fusion peptide trimer probed by solid-state NMR spectroscopy.* Biochemistry, 2006. **45**(43): p. 12960-12975.

25. Bak, M., J.T. Rasmussen, and N.C. Nielsen, *SIMPSON: A general simulation program for solid-state NMR spectroscopy.* Journal of Magnetic Resonance, 2000. **147**(2): p. 296-330.

26. Xie, L., et al., *Multiple Locations of Peptides in the Hydrocarbon Core of Gel-Phase Membranes Revealed by Peptide C-13 to Lipid H-2 Rotational-Echo Double-Resonance Solid-State Nuclear Magnetic Resonance.* Biochemistry, 2015. **54**(3): p. 677-684.

27. Zhang, H.Y., S. Neal, and D.S. Wishart, *RefDB: A database of uniformly referenced protein chemical shifts.* Journal of Biomolecular Nmr, 2003. **25**(3): p. 173-195.

28. Brugger, B., et al., *The HIV lipidome: A raft with an unusual composition.* Proceedings of the National Academy of Sciences of the United States of America, 2006. **103**(8): p. 2641-2646.

29. Schimick, S., *High resolution tertiary structure of the membrane-associated HIV fusion peptides by solid state nuclear magnetic resonance*, in *Chemistry*. 2012, Michigan State University.

30. Banerjee, K. and D.P. Weliky, *Folded Monomers and Hexamers of the Ectodomain of the HIV gp41 Membrane Fusion Protein: Potential Roles in Fusion and Synergy Between the Fusion Peptide, Hairpin, and Membrane-Proximal External Region.* Biochemistry, 2014. **53**(46): p. 7184-7198.

31. Lorizate, M., et al., *Comparative lipidomics analysis of HIV-1 particles and their producer cell membrane in different cell lines.* Cellular Microbiology, 2013. **15**(2): p. 292-304.

32. Qiang, W., J. Yang, and D.P. Weliky, *Solid-state nuclear magnetic resonance measurements of HIV fusion peptide to lipid distances reveal the intimate contact of beta strand peptide with membranes and the proximity of the Ala-14-Gly-16 region with lipid headgroups.* Biochemistry, 2007. **46**(17): p. 4997-5008.

33. Ratnayake, P.U., et al., *pH-dependent vesicle fusion induced by the ectodomain of the human immunodeficiency virus membrane fusion protein gp41: Two kinetically distinct processes and fully-membrane-associated gp41 with predominant beta sheet fusion peptide conformation.* Biochimica Et Biophysica Acta-Biomembranes, 2015. **1848**(1): p. 289-298.

34. Ghosh, U., et al., *Closed and Semiclosed Interhelical Structures in Membrane vs Closed and Open Structures in Detergent for the Influenza Virus Hemagglutinin Fusion Peptide*

and Correlation of Hydrophobic Surface Area with Fusion Catalysis. Journal of the American Chemical Society, 2015. **137**(24): p. 7548-7551.

35. Lai, A.L., et al., *Fusion Activity of HIV gp41 Fusion Domain Is Related to Its Secondary Structure and Depth of Membrane Insertion in a Cholesterol-Dependent Fashion.* Journal of Molecular Biology, 2012. **418**(1-2): p. 3-15.

36. Ratnayake, P.U., et al., *Full-length trimeric influenza virus hemagglutinin II membrane fusion protein and shorter constructs lacking the fusion peptide or transmembrane domain: Hyperthermostability of the full-length protein and the soluble ectodomain and fusion peptide make significant contributions to fusion of membrane vesicles.* Protein Expression and Purification, 2016. **117**: p. 6-16.

37. Morris, K.F., X.F. Gao, and T.C. Wong, *The interactions of the HIV gp41 fusion peptides with zwitterionic membrane mimics determined by NMR spectroscopy.* Biochimica Et Biophysica Acta-Biomembranes, 2004. **1667**(1): p. 67-81.

38. Pereira, F.B., et al., *Permeabilization and fusion of uncharged lipid vesicles induced by the HIV-1 fusion peptide adopting an extended conformation: Dose and sequence effects.* Biophysical Journal, 1997. **73**(4): p. 1977-1986.

39. de Planque, M.R.R., et al., *Sensitivity of single membrane-spanning alpha-helical peptides to hydrophobic mismatch with a lipid bilayer: Effects on backbone structure, orientation, and extent of membrane incorporation.* Biochemistry, 2001. **40**(16): p. 5000-5010.

40. de Planque, M.R.R., et al., *Different membrane anchoring positions of tryptophan and lysine in synthetic transmembrane alpha-helical peptides.* Journal of Biological Chemistry, 1999. **274**(30): p. 20839-20846.

41. Strandberg, E., et al., *Lipid dependence of membrane anchoring properties and snorkeling behavior of aromatic and charged residues in transmembrane peptides.* Biochemistry, 2002. **41**(23): p. 7190-7198.

Chapter 4 - Preferential Contacts of HFP with CHOL vs PC lipid

4.1 Introduction

CHOL is an important component in membranes.[1] HIV is an enveloped virus, and CHOL constitutes about 30mol % in both HIV host cell plasma membrane and HIV virus membrane.[2] Studies have shown that depletion of cellular CHOL reduces HIV-1 binding to cells and inhibits HIV virus induced cell-cell fusion.[3] The significance of CHOL on HIV makes it important to study how CHOL interfere with HIV induced fusion. HIV infection is initiated via viral gp120 binding to host cell CD4 receptor and co-receptor sequentially, which leads to conformational change of gp120 and get gp41 exposed to interact the host cell membrane and catalyze membrane fusion. Protein gp41 undergoes extended pre-hairpin intermediate (PHI) and folds into final hairpin or six helical bundle state (SHB) (see figure 1.16 in chapter 1).[4-8] The HIV gp41 N-terminal fusion peptide region (HFP) itself can induce both lipid mixing and contents leakage of vesicles.[9-13] Both HFP_V2E and gp41_V2E mutant abrogate membrane fusion.[14-16] Thus HFP has been widely studied as a model protein to understand its structure and function in HIV-host cell membrane fusion. HFP induced model membrane fusion studies indicate that there is faster fusion in membranes that contain CHOL and more fusion when there is more CHOL.[12, 17-19] The vesicle fusion rate is faster for three different oligomer states of HFP, monomer, dimer and trimer in membrane with CHOL than in membrane without CHOL.[18] Vesicle fusion studies suggest that membranes with a coexistence of liquid ordered and liquid disordered domains undergo more fusion, and fluorescence microcopy studies suggests that HFP binds to membranes and promotes membrane fusion at the interface between CHOL rich liquid ordered domains and liquid disordered domains.[17] Although all these studies have illustrated that CHOL is important to HFP induced efficient membrane fusion, there is little

information about how HFP contact the nearby lipid and the affinity between HFP and the membrane CHOL.

To study contact and affinity between HFP and membrane CHOL, $^{13}C–^{2}H$ rotational echo double resonance (REDOR) solid-state NMR is employed to measure the dipolar couplings (d's) between ^{13}CO–HFP and ^{2}H–CHOL in this thesis. The d depends on the $^{13}C–^{2}H$ inter-nuclear distance (r) as $d(Hz)=4642/r(Å)^3$.[20-22] HFP sequence in gp41 studied is AVGIGALFLGFLGAAGSTMGARS. The model membrane is 1, 2-dipalmitoyl-sn-glycero-3-phosphocholine (PC): 1, 2-dipalmitoyl-sn-glycero-3-phospho-(1'-rac-glycerol) (sodium salt) (PG) in 4:1mol ratio typically with 33% CHOL. This composition reflects features of HIV host cell membrane including significant fraction of PC lipid, anionic lipid fraction of ~ 0.15, and CHOL fraction of ~ 0.3.[2] To study the HFP-CHOL contact, we also studied membrane with 20 % CHOL and 11 % CHOL.

HFP forms majorly β sheet conformation in membrane with ~ 30mol % CHOL.[23] Therefore, one advantage of Gly-^{13}CO labeling in the β sheet is a Gly-^{13}CO chemical shift (~171 ppm) different from lipid and natural abundance chemical shifts of other residues (~175 ppm).[24, 25] There are distributions of antiparallel registry length of the first 16 residues of HFP in membrane with a total fraction of ~ 30% of antiparallel 16→1/1→16 and 17→1/1→17 registries.[23, 26] The ^{13}CO labeled at G16 (G16c) spectrum also has a higher chemical shift (~174 ppm) β sheet peak that might due to HFP molecules with shorter antiparallel β sheet registries that do not include G16 residue.[27] The membrane is ^{2}H labeled either at PC lipids or CHOL displayed in chapter 3. In membrane without protein, PC_d10 and Chol_d7 deuterons are located near the membrane center, PC_d4 and Chol_d6 deuterons are located near the membrane surface, while

PC_d8 deuterons are located in the middle of PC lipid acyl chain. The overall preferential contact with CHOL vs PC is through comparing experimental dephasing data with CHOL labeling and PC lipid labeling. All the REDOR data was acquired with sample temperature at about −30 °C to minimize sample motion which would reduce signal intensity and dephasing by increasing T_2 relaxation rate and reducing dipolar coupling, respectively.[27, 28]

4.2 Results

4.2.1 Experimental $^{13}C–^{2}H$ REDOR results for HFP_G5, G10 and G16c

The contact between HFP and membrane components is evaluated with same membrane composition but different ^{2}H membrane locations, shown in chapter 2. In Membrane PC: PG: CHOL (8:2:5) which contains ~33mol% CHOL, G5c has biggest dephasing with Chol-d7, significant dephasing with PC_d10 and relatively smaller dephasing with PC_d8, which suggests closer contact between G5c and Chol_d7 deuterons than PC_d10 and PC_d8 deuterons (figure 4.1). Since the deuteron ratio is 7:16 in sample with Chol_d7: sample with PC_d10 and the deuteron membrane location is similar at least in membrane without protein, the bigger dephasing in membrane with Chol_d7 than PC_d10 evidences preferential contact with Chol_d7 compared to PC_d10. The greater dephasing in membrane with PC_d10 and Chol_d7 than PC_d8 suggests most HFP G5 ^{13}CO is deeply inserted into the membrane hydrophobic core, assuming that the membrane structure locally around peptide is similar to the structure in the absence of peptide. The contact between G5c and membrane is also assessed with smaller CHOL content. In membrane with PC: PG: CHOL (8:2:2.5) which contains ~ 20% CHOL, comparable dephasing is obtained with either Chol_d7 or PC_d10 deuteron labeling where the deuteron ratio of Chol_d7: PC_d10 is only 7: 32 (figure 4.2). The CHOL amount is further reduced to ~ 11mol %

with membrane PC: PG: CHOL (8:2:1.25), and significant dephasing is still observed (figure 4.2), which further supports considerable preferential contact between G5c and Chol_d7.

Similar dephasing trend is also observed at G10 ^{13}CO (figure 4.3). In membrane with PC: PG: CHOL (8:2:2.5) which contains ~ 20% CHOL, comparable dephasing is observed with either Chol_d7 or PC_d10 deuteron labeling where the deuteron ratio is only 7:32. The dephasing buildups are also similar to G5c (figure 4.2), which suggests similar contact with Chol_d7 between G10 and G5 ^{13}CO.

Previous studies show that G16 in HFP is majorly located near the phosphorous head group region. Our G16 ^{13}CO REDOR dephasing plots all show minimal dephasing in membrane PC: PG: CHOL (8:2:5) with deuteron labeling in PC_d10, d8, d4 and Chol_d7 (figure 4.4), which indicates that most G16 ^{13}CO don't have close contact with membrane hydrophobic core and is thus not inserted into the membrane interior. However, G16 ^{13}CO shows significant dephasing in the same membrane with Chol_d6 deuterons labeling which is located near the membrane surface (figure 4.5).[27, 29, 30] Smaller amount of CHOL (20mol %) containing membrane is also tested (figure 4.5), and the dephasing is only reduced by ~ 20%, which supports preferential contact between G16c and Chol_d6. If there is no preferential contact between G16c and Chol_d6 compared to PC, there would be less or equal dephasing with Chol_d6 labeling than with PC_d4 labeling because Chol_d6: PC_d4 = 5:8 and the corresponding deuterons ratio is 30:32.

The substantial dephasing buildups are semi-quantitatively fitted to exponential buildup equation $A \times (1 - e^{-\gamma\tau})$. A is the fraction of molecule with $d \approx 3\gamma/2$ (fully explained in chapter 3).[31] The exponential fitting approach is chosen majorly due to T_1 relaxation effects of ^{2}H (shown in (table

4.1)). The data is also alternatively fitted with isolated $^{13}CO–^{2}H$ spin pairs with a single dipolar coupling (d) by SIMPSON (table 4.2). The data is well fitted by fitting approach ***Π*** (discussed in chapter 3) with 3 populations, two fractions with different d's and the rest population with d=0. Experimental parameters are incorporated into the SIMPSON simulation, including the MAS frequency, radio frequency fields of the pulses, ^{13}C chemical shift offset and anisotropy and the ^{2}H quadrupole anisotropy. But the SIMPSON program does not take relaxation into account.[32]

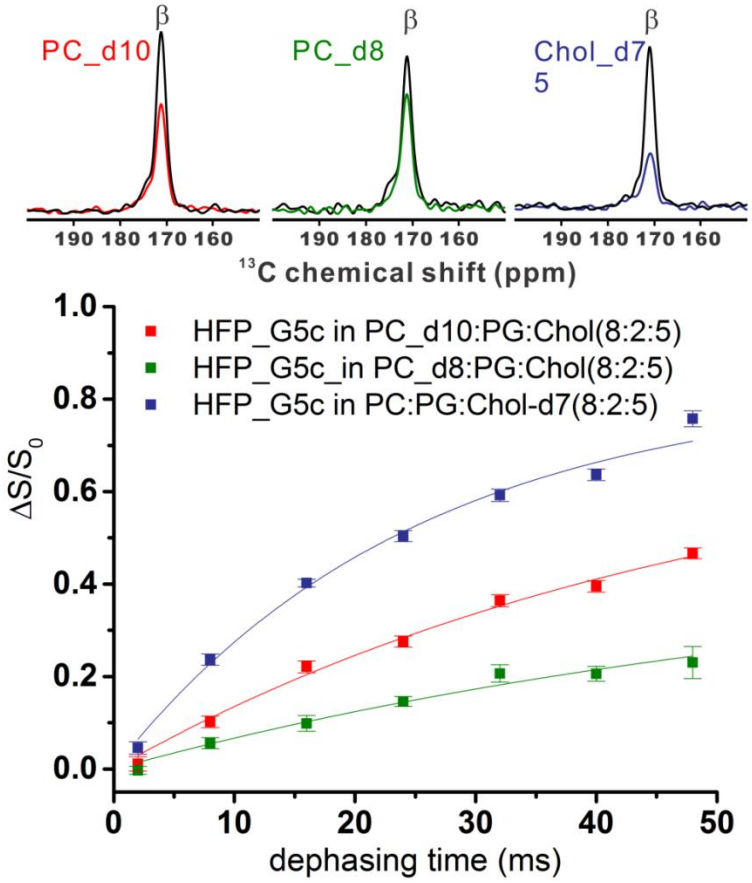

Figure 4.1 ^{13}C-detect / ^{2}H-dephase REDOR S_0 (black) and S_1 (colored) experimental spectra (top panel) of membrane - associated HFP_G5c at τ = 40ms and quantitative $\Delta S/S_0$ buildups for the major β peak in membrane with different ^{2}H labeling. The colored line is best fitted curve by equation of $A \times (1 - e^{-\gamma\tau})$.

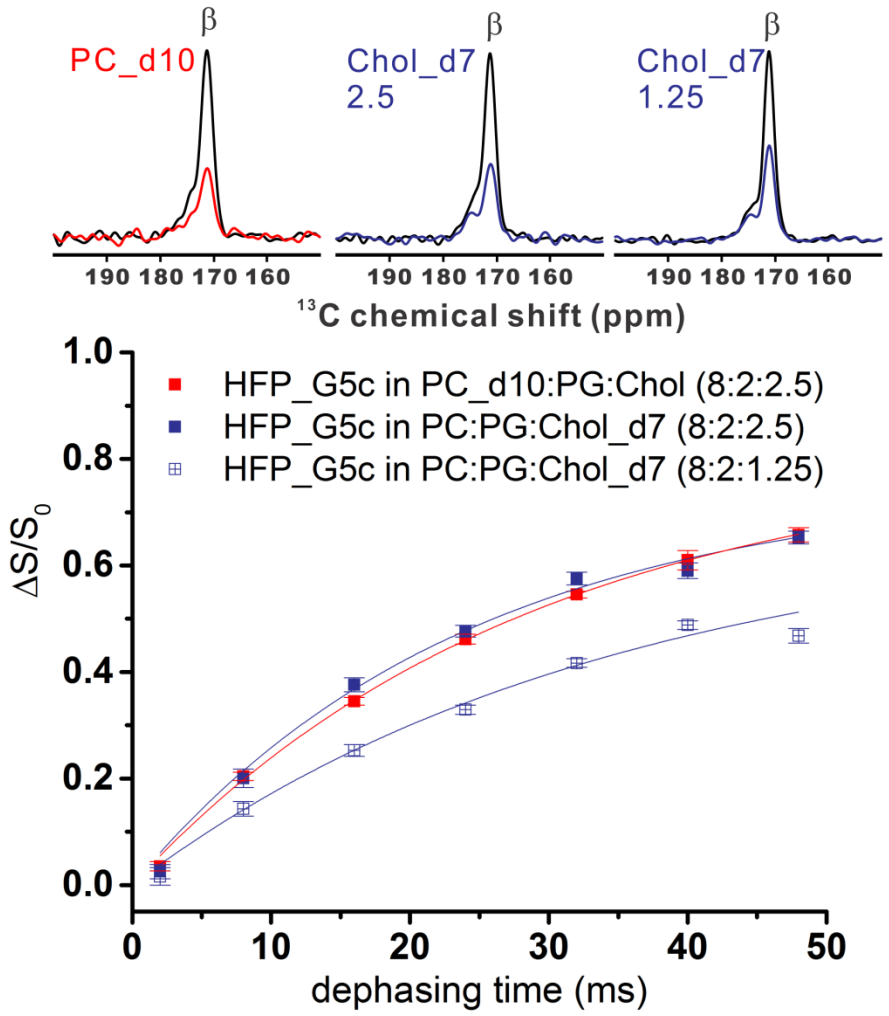

Figure 4.2 ^{13}C-detect / ^{2}H-dephase REDOR S_0 (black) and S_1 (colored) experimental spectra (top panel) of membrane – associated HFP_G5c at τ = 40ms and quantitative $\Delta S/S_0$ buildups for the major β peak in membrane with different ^{2}H labeling. The colored line is best fitted curve by equation of $A \times (1 - e^{-\gamma\tau})$.

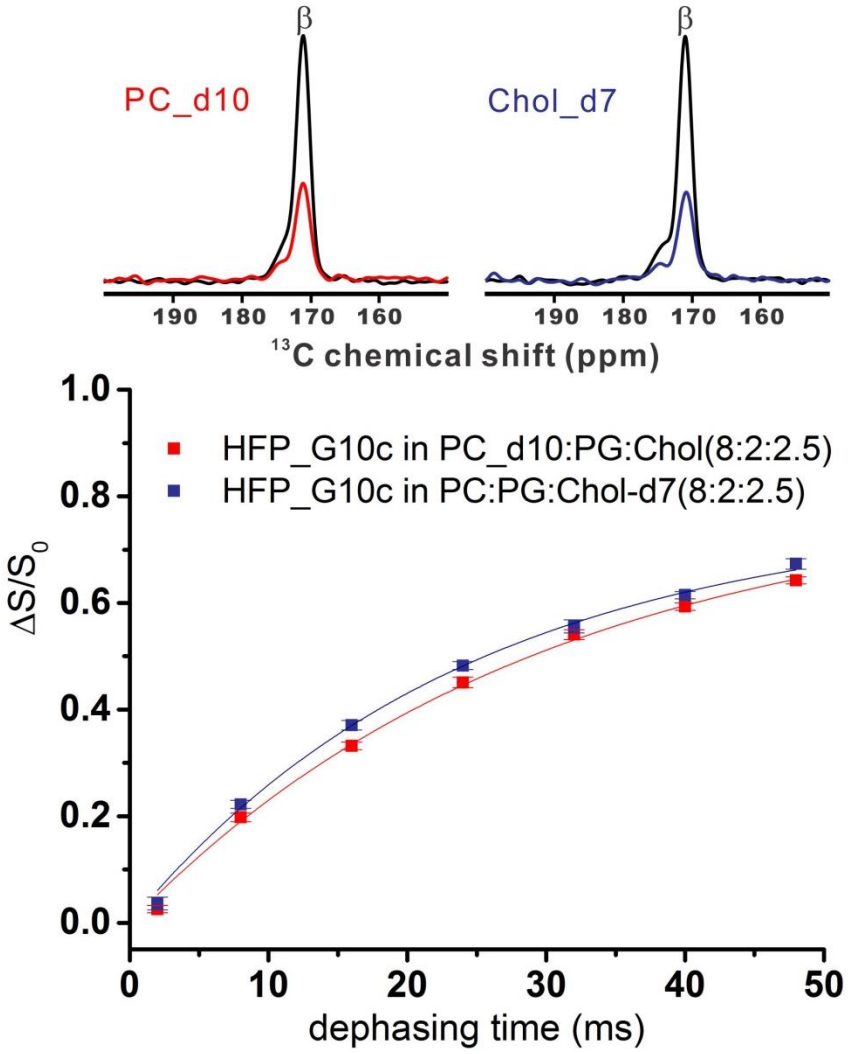

Figure 4.3 ^{13}C-detect / ^{2}H-dephase REDOR S_0 (black) and S_1 (colored) experimental spectra (top panel) of membrane – associated HFP_G10c at τ = 40ms and quantitative $\Delta S/S_0$ buildups for the major β peak in membrane with different ^{2}H labeling. The colored line is best fitted curve by equation of $A \times (1 - e^{-\gamma\tau})$.

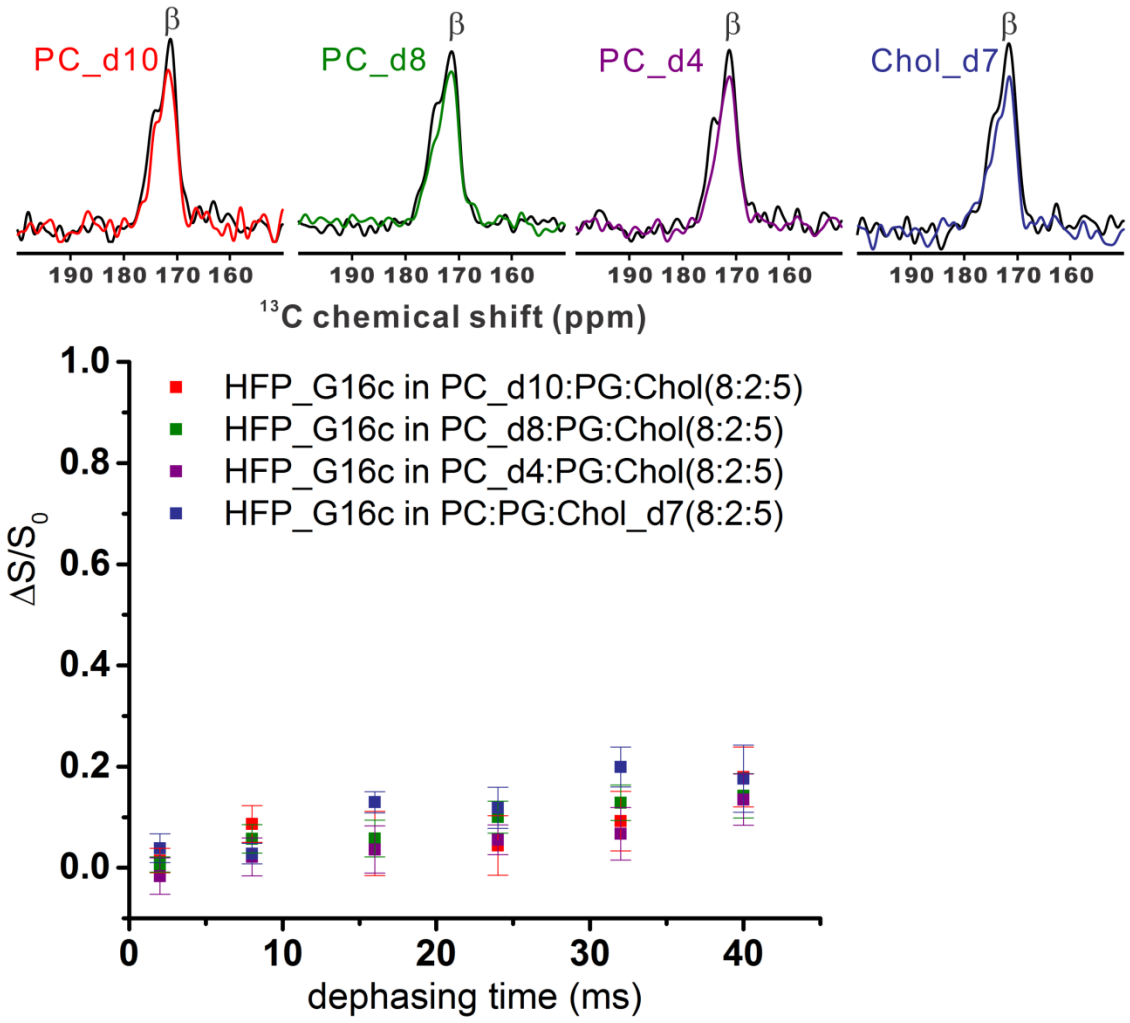

Figure 4.4 ^{13}C-detect / ^{2}H-dephase REDOR S_0 (black) and S_1 (colored) experimental spectra (top panel) of membrane – associated HFP_G16c at τ = 40ms and quantitative $\Delta S/S_0$ buildups for the major β peak in membrane with different ^{2}H labeling.

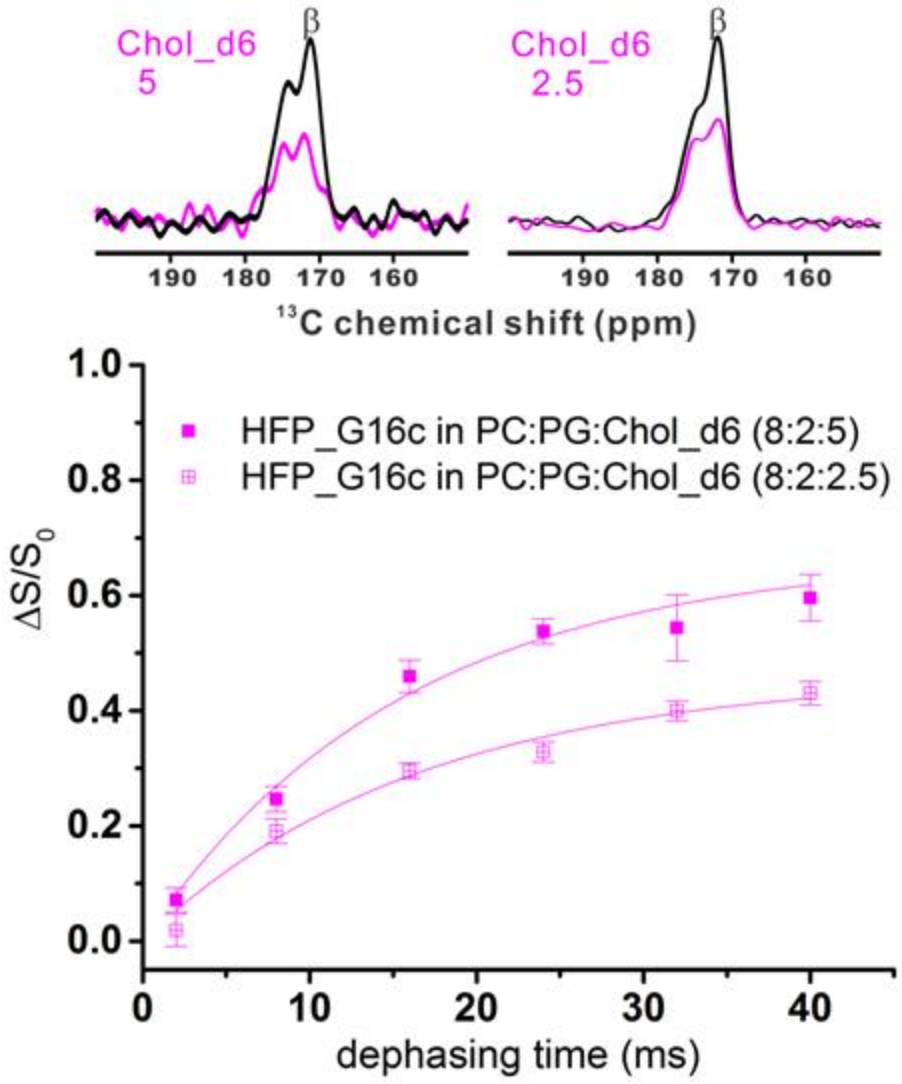

Figure 4.5 ^{13}C-detect / ^{2}H-dephase REDOR S_0 (black) and S_1 (colored) experimental spectra (top panel) of membrane – associated HFP_G16c at τ = 40ms and quantitative $\Delta S/S_0$ buildups for the major β peak at 171 ppm in membrane with different ^{2}H labeling. The colored line is best fitted curve by equation of $A \times (1 - e^{-\gamma\tau})$.

Table 4.1 Best-fit exponential buildup parameters for HFP in membrane with CHOL [a]

Peptide	PC lipid label	f_{Chol}	A	γ (Hz)	r (Å)
G5c	PC_d8	0.33	0.46 (25)	16 (11)	5.8 (1.4)
G5c	PC_d10	0.33	0.77 (11)	20 (4)	5.4 (4)
G5c	Chol_d7	0.33	0.83 (5)	40 (5)	4.3 (2)
G5c	PC_d10	0.20	0.81 (3)	35 (2)	4.5 (1)
G5c	Chol_d7	0.20	0.75 (4)	42 (5)	4.2 (2)
G5c	Chol_d7	0.11	0.68 (9)	29 (7)	4.7 (4)
G10c	PC_d10	0.20	0.80 (4)	34 (3)	4.5 (1)
G10c	Chol_d7	0.20	0.77 (2)	41 (2)	4.2 (1)
G16c	Chol_d6	0.33	0.67 (5)	64 (10)	3.6 (2)
G16c	Chol_d6	0.20	0.46 (3)	61 (10)	3.7 (2)

[a] A and γ are fitting parameters for experimental dephasing buildup from fitting equation of $A \times (1 - e^{-\gamma\tau})$, and r is calculated as $d = 3\gamma/2 = 4642/r^3$. The peak analyzed is the major β peak. The sample typically contains ~ 1μmol peptide with peptide: phospholipid ratio of 1:50. Phospholipid is DPPC: DPPG with 4:1 mole ratio. f_{Chol} is the CHOL amount relative to the total amount of lipids including CHOL.

Table 4.2 Alternative SIMPSON simulation results [a]

Peptide	PC lipid label	f_{Chol}	f_1	d_1/Hz	r_1/ Å	f_2	d_2 /Hz	r_2/ Å
G5c	PC_d8	0.33	0.24	54	4.4	0.43	19	6.3
G5c	PC_d10	0.33	0.07	80	3.9	0.24	24	5.8
G5c	Chol_d7	0.33	0.44	81	3.9	0.56	22	6.0
G5c	PC_d10	0.20	0.34	85	3.8	0.58	22	6.0
G5c	Chol_d7	0.20	0.39	81	3.9	0.53	23	5.9
G5c	Chol_d7	0.11	0.23	66	4.1	0.47	23	5.9
G10c	PC_d10	0.20	0.33	83	3.8	0.58	22	6.0
G10c	Chol_d7	0.20	0.37	83	3.8	0.57	23	5.9
G16c	Chol_d6	0.33	0.40	77	3.9	0.48	33	5.2
G16c	Chol_d6	0.11	0.36	78	3.9	0.29	21	6.0

[a] distance r was calculated from $r= (4642/d)^{1/3}$. The membrane is DPPC: DPPG with 4:1 mole ratio. f_{Chol} is the CHOL amount relative to the total amount of lipids. The best fitting results are based on minimum χ^2 achieved.

4.2.2 Free energy of preferential contact of HFP with CHOL vs PC

The membrane in our studies contains ~7–30mol % cholesterol, and there are liquid-ordered and solid-ordered phase separations at room temperature according to the DPPC/CHOL binary phase

diagram.[33] The CHOL: PC ratio is 0.30:0.70 and 0.07:0.93 in liquid-ordered and solid-ordered phases, respectively. There would be experimental dephasing as long as HFP ^{13}CO nucleus makes contact with at least one labeled molecule. The average dephasing value (C) of 8-48ms or 8-40ms (when 48ms data isn't measured) is a more reliable metric of peptide ^{13}CO-membrane ^{2}H contact. The error of C is calculated from equation $\sigma(C) = \frac{1}{n}\sqrt{\sum_{i=1}^{i=n}\sigma^2_{\left(\frac{\Delta S}{S_0}\right)_i}}$ and n=5 and 6 for average dephasing of 8–40ms and 8–48ms, respectively (table 4.3). G5c and G10c show 90% of maximum C (in sample of PC_d10: PG with 4:1 mole ratio) in both PC_d10: PG: CHOL and PC: PG: Chol_d7 membranes with 8:2:2.5 ratios. We consider a model that the nucleus contacts two molecules. Because d depends on $1/r^3$, the dipolar coupling is dominated by the closest coupled spin pair. Therefore, dephasing for contact of ^{13}CO with two ^{2}H labeled molecules is considered equivalent to dephasing with one labeled molecule because there are many ^{2}H nuclei in a labeled molecule. The fractional probabilities (P) for HFP contacting a nearby lipid which result in dephasing in our samples are statistically calculated (table 4.4). The C's depend strongly on PC: CHOL ratios in our samples which evidence peptide binding to both gel and liquid-ordered phases because there is significant dephasing buildup for HFP in pure gel phase membrane (f_{Chol}= 0%), pure liquid- ordered phase membrane (f_{Chol}= 33%) and a mixture of both phases membrane (f_{Chol}= 20%). The C values also support preferential binding of HFP to CHOL vs PC. For example, C_{Chol_d7}:C_{PC_d10} ≈ 1.7 and P_{Chol}: P_{PC} ≈ 0.7 for PC: PG: CHOL (8:2:5) and C_{Chol_d7}:C_{PC_d10} ≈ 1.0 and P_{Chol}: P_{PC} ≈ 0.4 for PC: PG: CHOL (8:2:2.5). To evaluate the preferential contact of HFP to CHOL, we consider that C_{PC}= P_{PC} × B and C_{Chol} = P_{Chol} × W × B where B is a proportionality constant and W is the preference for peptide binding to CHOL vs PC. W is evaluated from comparison of C and P values for different samples. For the same peptide labeling and membrane composition, W = (C_{Chol} × P_{PC}) / (C_{PC} × P_{Chol}). A model for W is

$W = \exp(-\Delta G_{Chol\_PC}/RT)$ where ΔG_{Chol_PC} is the free energy difference between peptide contact with CHOL vs PC. Then $\Delta G_{PC\text{-}Chol} = RT \times \ln(\langle \Delta S/S_0 \rangle_{Chol\text{-}d7} / \langle \Delta S/S_0 \rangle_{PC\text{-}d10} \times P_{PC}/P_{Chol})$ for the same peptide labeling and membrane composition, and $\langle \Delta S/S_0 \rangle$ is the average dephasing of 8-48ms dephasing times, which is also denoted as C values. For a typical W=2.5 and T=300 K, $\Delta G \approx$ 0.57(5) kcal.mol^{-1} for all 6 independent samples, and the number in the parenthesis is the standard deviation, which is 0.05 kcal/mol (table 4.5).

Table 4.3 C values for different peptide and membrane labeling [a]

Peptide	PC lipid label	f_{Chol}	C value
G5c	PC_d8	0.33	0.157 (8)
G5c	PC_d10	0.33	0.304 (5)
G5c	PC_d10	0.33	0.272 (6)[b]
G5c	Chol_d7	0.33	0.522 (5)
G5c	PC_d10	0.20	0.471 (5)
G5c	PC_d10	0.20	0.433 (5)[b]
G5c	Chol_d7	0.20	0.479 (6)
G5c	Chol_d7	0.11	0.350 (4)
G10c	PC_d10	0.20	0.460 (3)
G10c	Chol_d7	0.20	0.487 (4)
G16c	Chol_d6	0.33	0.477 (16)[b]
G16c	Chol_d6	0.20	0.329 (8)[b]

[a] The C values are typically the average dephasing $\langle \Delta S/S_0 \rangle$ of 8-48ms dephasing times, except for G16c samples, it's 8-40ms dephasing times. The phospholipid composition is PC: PG (4:1), and f_{Chol} the fraction of CHOL of total lipids. Example C value of 0.157 (8) means C value is 0.157 with error of ± 0.008.

[b] The C values is the average dephasing $\langle \Delta S/S_0 \rangle$ of 8-40ms dephasing times.

Table 4.4 Fractional probabilities of ^{13}CO making contact to PC or CHOL with two molecules contact model [a]

Membrane	P_{PC}	P_{Chol}
PC: PG: CHOL (8:2:5)	0.782	0.556
PC: PG: CHOL (8:2:2.5)	0.870	0.360
PC: PG: CHOL (8:2:1.25)	0.917	0.210

[a] The fractional probabilities are based on a model that the ^{13}CO nucleus contacts two molecules. $P_{PC}=f_{PC}^2+2\times f_{PC}(f_{Chol}+f_{PG})= f_{PC}^2+2\times f_{PC}(1-f_{PC})= f_{PC}(2-f_{PC})$, similarly, $P_{Chol}= f_{Chol}(2-f_{Chol})$. f_{PC} and f_{Chol} are the mole fraction of PC and CHOL in the relevant membrane compositions, respectively.

Table 4.5 $\Delta G_{PC\text{-}Chol}$ values (the energy difference for peptide binding to PC vs CHOL) for different samples

Peptide label	PC: PG: CHOL	Membrane labels	$\Delta G_{PC\text{-}CHOL}$/kcal×mol^{-1}
G5c	8:2:5	PC_d10 or Chol_d7	0.53
G5c	8:2:2.5	PC_d10 or Chol_d7	0.54
G5c	8:2:1.25	PC_d10 or Chol_d7	0.65[a]
G10c	8:2:2.5	PC_d10 or Chol_d7	0.56
G5c, G16c	8:2:5	PC_d10, Chol_d6	0.62[b]
G5c, G16c	8:2:2.5	PC_d10, Chol_d6	0.53[b]

[a] Calculation is done with C_{PC_d10} =0.517 which is obtained from sample G5c in PC_d10:PG (4:1).

[b] Calculation is done by comparison of sample between G5c with PC_d10 labeling and G16c with Chol_d6 labeling and based on ^{13}CO contact with one lipid model, and $\Delta G_{PC\text{-}Chol}$ = $RT\times\ln(\langle\Delta S/S_0\rangle_{Chol\text{-}d6}/\langle\Delta S/S_0\rangle_{PC\text{-}d10}\times f_{PC}/f_{Chol})$, and $\langle\Delta S/S_0\rangle$ is the average dephasing of 8-40ms dephasing times.

4.2.3 CHOL binding to two strands antiparallel HFPs predicted by Swiss Dock and two sets of REDOR experimental distance constraints

Prediction of the most favorable sites of interaction between CHOL and the antiparallel HFP motif (HFP-antiβ) is performed by using the Swiss Dock web service (http://www.swissdock.ch/docking) with default settings.[34-36] The HFP–antiβ motif is built by sidechain mutation to the 16–residue HFP sequence in PyMOL (The PyMOL Molecular Graphics System, Version 1.2r2, Schrödinger, LLC) from two adjacent long strands in the beta-barrel outer membrane protein G (OmpG) (Protein Data Bank (PDB) entry 2iww).[37, 38] The OmpG sequences of ^{82}DFSFGLTGGFRNYGY^{97}H and ^{106}TANMQRWKIAPDWDV^{121}K are both mutated to N-terminal HFP 16–residue sequence AVGIGALFLGFLGAAG. The antiparallel β strand backbone structures of OmpG sequences are maintained. Any van der Waals overlaps between side chains are alleviated by using alternative favorable side–chain orientations from Dunbrack's backbone-dependent rotamer library, as implemented in PyMOL.[39, 40] Both the energy–minimized (HFP-$_{\text{antiβmin}}$) and non–energy–minimized (HFP-$_{\text{antiβ}}$) states of HFP–antiβ are used as input to Swiss Dock, with energy minimization performed with default parameters by the YASARA energy minimization server (http://www.yasara.org/minimizationserver.htm).[41] Developed by crystallographers working with computational chemists, this energy minimization tool maintains good stereochemistry in the protein and ligand, as well as improving interactions between the two molecules.

CHOL ligand structures for docking are obtained from ZINC database entry 3875383 (http://zinc.docking.org) and from a CHOL molecule bound to the crystal structure of human β2-adrenergic receptor, a membrane bound G protein-coupled receptor, PDB 2rh1.[42-45] In both cases, the stereochemistry of CHOL is confirmed to be correct. A panel of all 17 low–energy

(favorable) conformations of the 2rh1 CHOL molecule is obtained by using Omega2 software version 2.3.2 (OpenEye Scientific Software, Inc., Santa Fe, NM; http://www.eyesopen.com).[46, 47] For clarity in the following data tables, the CHOL structure from the ZINC database is referred as CHOL, and the panel of all favorable CHOL conformers from the PDB entry 2rh1 cholesterol structure is labeled Chol17.

For predicting favored interactions between a ligand such as CHOL and the HFP protein, Swiss Dock samples alternative ligand binding modes relative to the protein surface (e.g., HFP-antiβ) by dihedral sampling, filters out redundant or poorly interacting orientations of the ligand, and then sorts the dockings by their Simple-Fitness values (the CHARMM22 energy). The most favorable orientations are then minimized by using the CHARMM force field, and the exact CHARMM22 energy is calculated. This includes the bonded and non-bonded (electrostatic and van der Waals interaction) energy of protein and ligand, and the non-bonded interaction energy between the protein and the ligand. Finally, Swiss Dock spatially clusters the energy–minimized dockings by RMSD, using a distance cutoff of 2Å. Within a cluster, each binding mode is ranked according to its effective energy, which also includes the fast analytical continuum treatment of solvation (FACTS) energy, such that the rank #0 docking in each cluster represents the lowest energy configuration in that cluster.[34, 36, 48]

For identification of dockings that are consistent with the REDOR–identified interaction between CHOL and HFPs, the coordinates of the lowest energy CHOL docking from each spatial cluster are saved in a separate PDB-formatted file, and the peptide backbone carbonyl carbon to CHOL ^{1}H distances are analyzed in PyMOL. Table 4.6 summarizes the results. Those meeting a 4–5 Å distance between the CHOL isopropyl ^{1}Hs and the Gly5 or Gly10 ^{13}CO, or between one or more of the Chol-2,2,3,4,4,6 protons and Gly16 or Ala1 ^{13}CO, are considered to match the ^{13}CO–^{2}H

REDOR experimental data and are sent to YASARA for energy minimization. After energy minimization, CHOL– HFP–antiβ atomic coordinates are saved as PDB files following deletion of the shell of water molecules. The final energy values of the docking conformers that meet at least 2 REDOR distance constraints within 4–5 Å are found to lie within a favorable range of −8535 $kJ.mol^{-1}$ to −9454 $kJ.mol^{-1}$ (more favorable), though these energy values should be considered approximate rather than absolute.

A summary of the docking modes that resulted is given in table 4.7. More binding orientations relative to HFP-antiβ resulted when experimental distance constraints up to 4–6 Å are considered, but these additional binding modes are distributed all around HFP–antiβ without showing preferential binding in any region(s) and are deemed nonspecific. Further analysis focused on those docking modes that meet the more stringent criteria of matching at least two experimental distance constraints within 4–5 Å.

Table 4.6 Dockings of CHOL with HFP–antiβ resulting from different protocols

Protein model	CHOL model	Number of Swiss Dock docking modes	Number of docking modes matching at least 2 experimental distance constrains within 4–5 Å	Number of docking modes matching at least 1 experimental distance constrains within 4–6 Å
HFP-$_{antiβ}$	CHOL	12	1	7
HFP-$_{antiβ}$	Chol17	14	2	4
HFP-$_{antiβmin}$	CHOL	6	1	3
HFP-$_{antiβmin}$	Chol17	14	4	7

Docked CHOL molecules that match at least two REDOR 4–5 Å distance constraints to HFP–antiβ (HFP-antiβ and HFP-antiβmin) are analyzed together in PyMOL to define the most favorable sites of interaction (figure 4.6). The minimized energies of each docking are listed in table 4.7, as well as the side chains in HFP–antiβ participating in each interaction of the lowest energy docking from each cluster. There are two distinct interaction footprints on HFP–antiβ, one around Ala1–Gly5 showing the highest catchment, including seven dockings (position 1), and a second around Ala6–Gly10 containing only one docking (position 2). These positions reflect two different ways of two distance constraints being satisfied. In the first docking position,

either Chol–2,2,3,4,4,6 protons around the hydroxyl group contact the Ala1 carbonyl carbon and the CHOL isopropyl tail contacts the Gly5 carbonyl carbon in the same strand of HFP, or the CHOL isopropyl tail contacts the Gly5 carbonyl carbon in one strand and the Gly10 carbonyl carbon in the other strand of HFP. In the second docking position, the CHOL isopropyl tail contacts the Gly5 carbonyl carbon in one strand and the Gly10 carbonyl carbon in the other strand of HFP. Here we label the residues in one strand of HFP with sentence case (e.g., Gly) and the residues in the second strand with capitals (e.g., GLY) to distinguish them. ILE4, GLY5 and LEU7 sidechains are in frequent contact with cholesterol across all eight dockings.

The most energetically favorable docking (-9453.8 kJ.mol^{-1}) is selected as the representative from the seven dockings overlapping in the first (Ala1–Gly5) position (bold purple in position 1, figure 4.6). In this docking, cholesterol makes sidechain contacts with residues VAL2, ILE4, and LEU7 in one chain and Gly10 and Leu12 in the other (figure 4.7-b). Since the sequence of the two HFP strands is the same, there is also a symmetry–related position in which cholesterol interacts with the same residues in the other strand. The original and symmetry–related positions of this docking are also shown (figure 4.7-c), and can be occupied concurrently. Furthermore, considering the possibility that multiple HFPs together form a larger antiparallel beta sheet imbedded in the membrane, cholesterol binding in this position and its symmetry–related position would not interfere with the growth of a beta sheet (figure 4.8-a). However, the second position for cholesterol binding, in the Ala6–Gly10 region (Chol location shown in green, figure 4.8-b) blocks the main–chain hydrogen bonding edge of the strand and thus would inhibit beta sheet expansion.

Table 4.7 Energies of CHOL dockings meeting at least two experimental distance constraints within 5Å [a]

Protein model	CHOL model	Energy / ($kJ.mol^{-1}$)	Satisfied REDOR distance constraints [a]	Side chains within 4 Å of CHOL
HFP-$_{anti\beta}$	CHOL	−9247.0	GLY5–Chol_d7, Gly10–Chol_d7	Leu7,Leu9,Gly10,Phe11,Leu12
HFP-$_{anti\beta}$	Chol17	−9453.8	GLY5–Chol_d7, Gly10–Chol_d7	Gly10,Leu12,VAL2,ILE4,GLY5 ,LEU7
		−9209.5	GLY5–Chol_d7, ALA1–Chol_d6	NA
HFP-$_{anti\beta min}$	CHOL	−8750.2	GLY5–Chol_d7, ALA1–Chol_d6	VAL2,GLY3,ILE4,GLY5,LEU7
HFP-$_{anti\beta min}$	Chol17	−9014.3	GLY5–Chol_d7, Gly10–Chol_d7	Leu12,ILE4,GLY5,LEU7
		−8964.7	GLY5–Chol_d7, Gly10–Chol_d7	NA
		−8535.7	GLY5–Chol_d7, ALA1–Chol_d6	NA
		−8816.6	GLY5–Chol_d7, ALA1–Chol_d6	NA

[a] Chol_d7 refers to cholesterol deuterated at isopropyl 1H, and Chol_d6 refers to Chol deuterated at 2,2,3,4,4,6 – ^{1}H. HFP-$_{anti\beta}$ and HFP-$_{anti\beta min}$ side chains within 4 Å contact distance of CHOL are listed for the most energetically favorable member of each docking cluster from Swiss Dock.

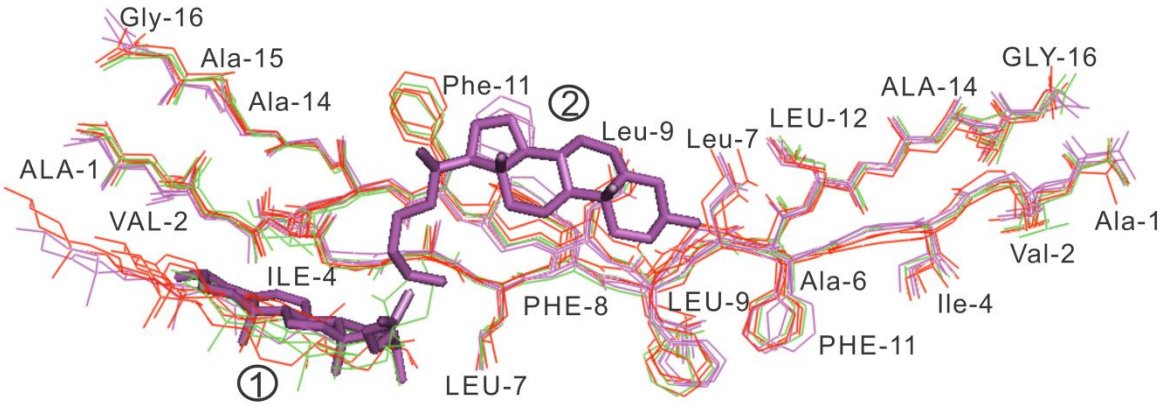

Figure 4.6 Eight favorable dockings of CHOL (colored tubes) that meet two REDOR 4–5 Å distance constraints: the YASARA energy minimized predicted HFP-$_{antiβ}$ and HFP-$_{antiβmin}$ structures (drawn as lines, with residues labeled) in complex with the corresponding CHOL binding mode are colored red for the least energetically favorable group (-8535 to -8841 kJ·mol^{-1}), green for the intermediate energy group (-8841 to -9147 kJ.mol^{-1}) and purple, for the most favorable group (−9147 to −9454 kJ.mol^{-1}). Note the high occupancy of seven favorable CHOL dockings spanning Ala1–Gly5 (position 1, lower left), with just one docking occupying position 2 (top center), as shown by thick purple tubes for the two most favorable dockings. CHOL interactions with HFP residues are listed earlier in this chapter.

(a)

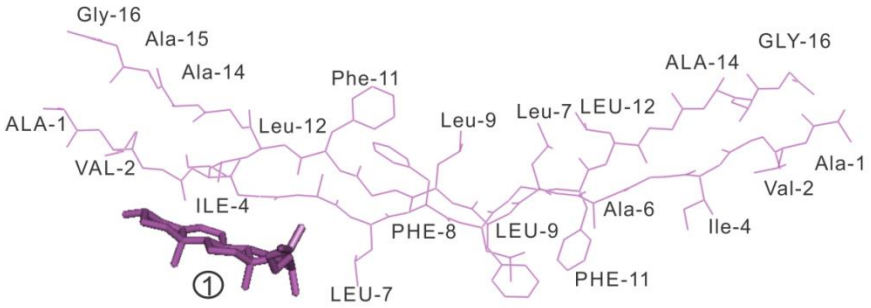

(b)

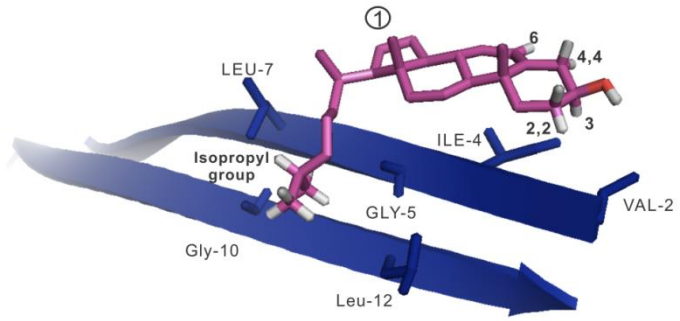

(c)

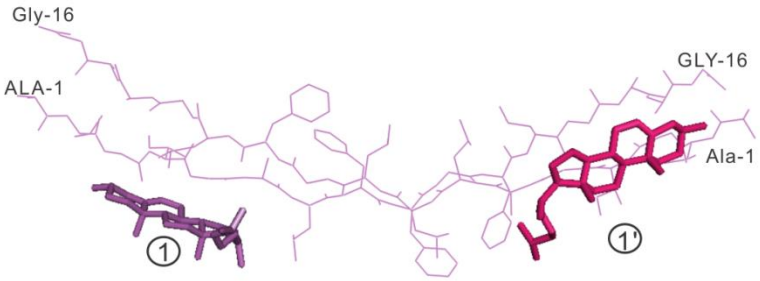

Figure 4.7 The most favorable CHOL binding mode relative to HFP-antiβ: (a) CHOL binding mode (purple tubes) is shown relative to the two HFP strands (sticks). (b) Details of HFP-antiβ side chain interactions with CHOL protons monitored by REDOR (shown in white and labelled). The binding mode is the same as shown for location 1 above, while rotated by roughly 180° about the horizontal and vertical axes to enable viewing from above. (c) Same CHOL binding mode shown above (position 1, purple), plus its symmetry mate at the opposite end of HFP-$_{antiβ}$ (position 1', magenta).

(a) (b)

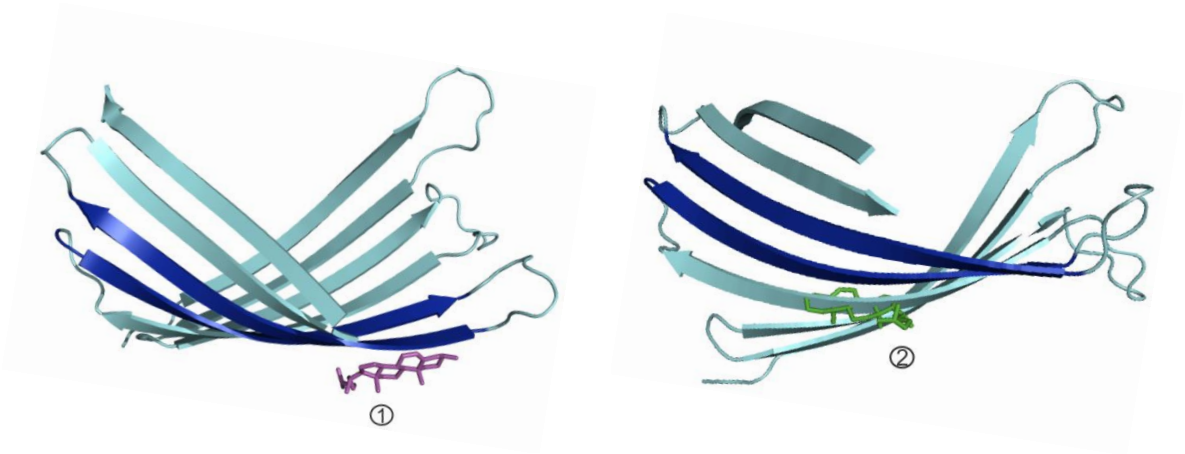

Figure 4.8 The HFP–antiβ structural model in complex with (a) CHOL in its dominant favorable position (position 1, purple tubes, as shown in Figure above) and (b) in the alternative binding mode (position 2, shown here in green tubes). The two strands of HFP-$_{\text{anti}\beta}$ (dark blue) with cholesterol bound are shown in the context of a multi-stranded beta barrel structure (light blue strands, from PDB entry 2iww) to explore the extent to which the two CHOL positions are consistent with formation of a larger (more than two–stranded) antiparallel β sheet structure by HFPs. The first cholesterol position (a) and its symmetry mate (not shown) would be compatible with formation of a larger sheet structure by HFPs if the last four residues, GAAG, of every second peptide in the sheet did not pair with the adjacent beta strand and shifted out of the way. The second CHOL site (b) would clearly block the addition of a beta strand (shown by interpenetration between CHOL and the light–blue beta strand) and thus would preclude formation of a larger sheet by HFPs.

4.2.4 Favorable CHOL binding geometry on the concave surface of an HFP–antiβ sheet

It's also possible that CHOL is located on top of HFP-antiβ with extended sheet formation. All binding positions on top of HFP–antiβ without blocking sheet extension predicted from Swiss Dock are screened out. Most of the binding has CHOL located near the center residues of the HFP strands. The distances between CHOL and HFPs at the sites measured by REDOR are analyzed. Only the green with energy of −9080.4 kJ.mol^{-1} (energy within intermediate energy group (−8841 to −9147 kJ.mol^{-1})) and purple with energy of −9228.5 kJ.mol^{-1} (energy within most favorable group (−9147 to −9454 kJ.mol^{-1}) ones have within 5Å distance between CHOL and HFP at one of the sites measured by REDOR (table 4.8, figure 4.9). It's between CHOL isopropyl ^{1}Hs and G5/G10 for green/purple colored binding respectively. Among the populated CHOL binding positions, the purple one is chosen as the representative of the most energy favorable binding position for CHOL located on the concave surface of HFP-antiβ. In this docking, CHOL makes sidechain contacts with Leu7 and Leu9 in one strand, and PHE8, GLY10 and LEU12 in the other (figure 4.10-b). This binding mode might interfere with neighboring sheet extension as seen when superimposing this binding geometry on PDB 2iww (figure 4.11). However, it only needs space to accommodate the terminal CH_3 protons of CHOL. It's still possible to have this CHOL binding geometry if the neighbor strands accommodate the terminal CH_3 protons of cholesterol during bigger sheet formation.

Table 4.8 CHOL dockings meeting at least one experimental distance constraints within 5 Å on the concave surface of an HFP-antiβ sheet

Protein model	CHOL model	Energy (kJ.mol^{-1})	Satisfied REDOR distance constraints	Sidechains within 4Å of CHOL	Docking location
HFP-$_{antiβmin}$	CHOL	−9080.4	Gly5–Chol_d7	NA	4
HFP-$_{antiβmin}$	Chol17	−9228.5	GLY10–Chol_d7	Leu7, Leu9, PHE8, GLY10, LEU12	3

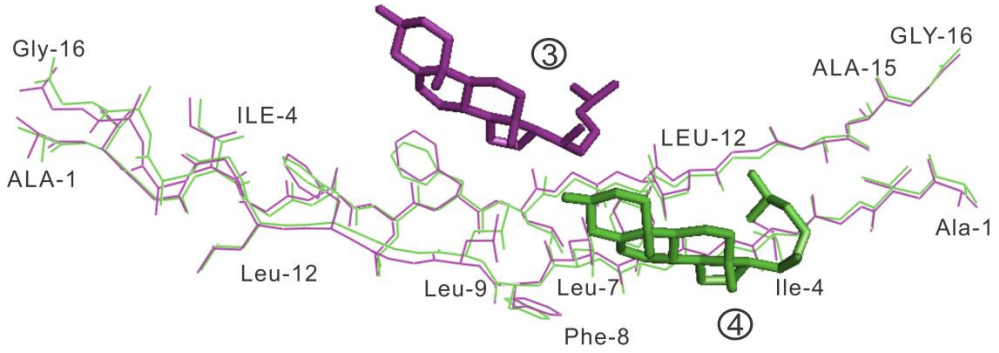

Figure 4.9 Favorable dockings of CHOL (colored tubes) on the concave surface of HFP–antiβ: Only the purple and green ones have within 5 Å distance between CHOL and HFP at one of the sites measured by REDOR. There are eight favorable dockings predicted by Swiss Dock with CHOL located on the concave surface of HFP-antiβ without blocking sheet extension.

(a)

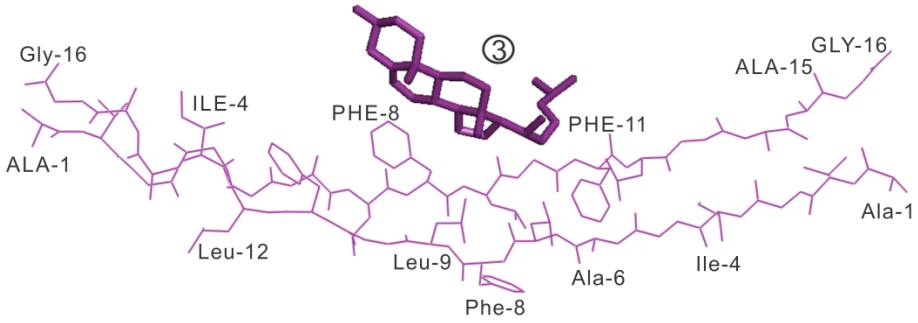

(b)

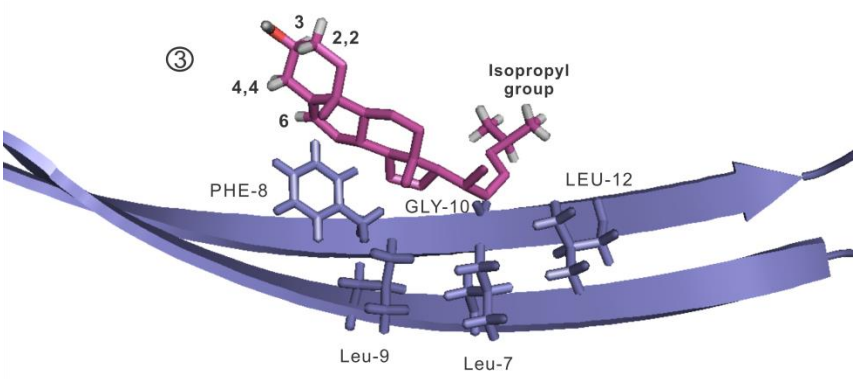

Figure 4.10 The most favorable CHOL binding mode (purple tubes, location 3) for CHOL located on the concave surface of HFP-antiβ, (a) the geometry of the most favorable CHOL binding to the two stranded HFPs, (b) details of HFP-antiβ side chain interactions with CHOL protons monitored by REDOR (shown in white and labelled).

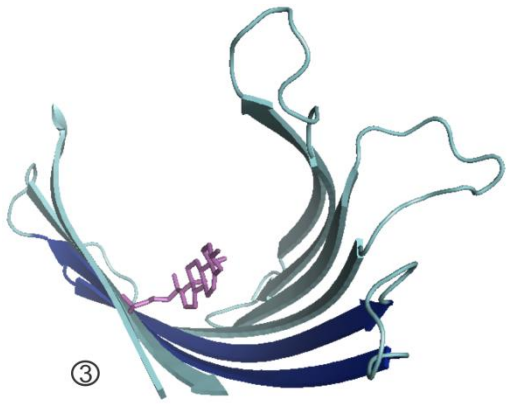

Figure 4.11 Superimposition of this purple colored favorable binding (location 3) on PDB 2iww, the purple colored CHOL is from the most favorable binding location 3. It's still possible to have this CHOL binding geometry if the neighbor strands accommodate the terminal CH_3 protons of CHOL during bigger sheet formation.

In summary, ^{13}C-^{2}H REDOR SSNMR reveals preferential contact between HFP and CHOL vs PC lipid. Energy favorable contact between two strands antiparallel HFP and CHOL is successfully modeled by Swiss Dock, energy minimization, and filtered by REDOR experimental results. There are two energetic favorable models of close contact between HFP and CHOL (Figure 4.7a and Figure 4.10 a). The models are consistent with REDOR experimental results of G5/Chol_d7 and/or G10/Chol_d7 results. The contact models reveal tilted and curved-up tail orientation of Chol_d7. Fusion may be catalyzed by matching the curvature of lipids contacting HFPs with the membrane curvature during the fusion intermediates like the stalk.[49] The antiparallel HFPs make lipid tail closer to the membrane surface and could reduce activation energy of joining of the outer leaflets of viral and host cell membrane.[50] The HFP preferential contact to CHOL vs PC lipid may increase fusion through two features of CHOL vs PC: one is that CHOL has greater intrinsic curvature, and the other one is that CHOL

is a shorter molecule and the tail is closer to the membrane surface. The study of HFP contact to CHOL vs PC lipid supports that this ^{13}C-^{2}H REDOR SSNMR method can also be applied to study other proteins – CHOL contact with residue specific labeling.

REFERENCES

REFERENCES

1. Chapman, D., *PHASE-TRANSITIONS AND FLUIDITY CHARACTERISTICS OF LIPIDS AND CELL-MEMBRANES.* Quarterly Reviews of Biophysics, 1975. **8**(2): p. 185-235.

2. Lorizate, M., et al., *Comparative lipidomics analysis of HIV-1 particles and their producer cell membrane in different cell lines.* Cellular Microbiology, 2013. **15**(2): p. 292-304.

3. Liao, Z.H., et al., *Lipid rafts and HIV pathogenesis: Host membrane cholesterol is required for infection by HIV type 1.* Aids Research and Human Retroviruses, 2001. **17**(11): p. 1009-1019.

4. White, J.M., et al., *Structures and mechanisms of viral membrane fusion proteins: Multiple variations on a common theme.* Critical Reviews in Biochemistry and Molecular Biology, 2008. **43**(3): p. 189-219.

5. Sackett, K., et al., *Hairpin Folding of HIV gp41 Abrogates Lipid Mixing Function at Physiologic pH and Inhibits Lipid Mixing by Exposed gp41 Constructs.* Biochemistry, 2009. **48**(12): p. 2714-2722.

6. Kilby, J.M., et al., *Potent suppression of HIV-1 replication in humans by T-20, a peptide inhibitor of gp41-mediated virus entry.* Nature Medicine, 1998. **4**(11): p. 1302-1307.

7. Furuta, R.A., et al., *Capture of an early fusion-active conformation of HIV-1 gp41.* Nature Structural Biology, 1998. **5**(4): p. 276-279.

8. Chan, D.C. and P.S. Kim, *HIV entry and its inhibition.* Cell, 1998. **93**(5): p. 681-684.

9. Cheng, S.F., et al., *The fusion peptide domain is the primary membrane-inserted region and enhances membrane interaction of the ectodomain of HIV-1 gp41.* Molecular Membrane Biology, 2010. **27**(1): p. 31-44.

10. Durell, S.R., et al., *What studies of fusion peptides tell us about viral envelope glycoprotein-mediated membrane fusion.* Molecular Membrane Biology, 1997. **14**(3): p. 97-112.

11. Epand, R.M., *Fusion peptides and the mechanism of viral fusion.* Biochimica Et Biophysica Acta-Biomembranes, 2003. **1614**(1): p. 116-121.

12. Lai, A.L., et al., *Fusion Activity of HIV gp41 Fusion Domain Is Related to Its Secondary Structure and Depth of Membrane Insertion in a Cholesterol-Dependent Fashion.* Journal of Molecular Biology, 2012. **418**(1-2): p. 3-15.

13. Yang, J., C.M. Gabrys, and D.P. Weliky, *Solid-state nuclear magnetic resonance evidence for an extended beta strand conformation of the membrane-bound HIV-1 fusion peptide.* Biochemistry, 2001. **40**(27): p. 8126-8137.

14. Gabrys, C.M., et al., *Solid-State Nuclear Magnetic Resonance Measurements of HIV Fusion Peptide (CO)-C-13 to Lipid P-31 Proximities Support Similar Partially Inserted Membrane Locations of the alpha Helical and beta Sheet Peptide Structures.* Journal of Physical Chemistry A, 2013. **117**(39): p. 9848-9859.

15. Freed, E.O., et al., *A MUTATION IN THE HUMAN-IMMUNODEFICIENCY-VIRUS TYPE-1 TRANSMEMBRANE GLYCOPROTEIN-GP41 DOMINANTLY INTERFERES WITH FUSION AND INFECTIVITY.* Proceedings of the National Academy of Sciences of the United States of America, 1992. **89**(1): p. 70-74.

16. Delahunty, M.D., et al., *Mutational analysis of the fusion peptide of the human immunodeficiency virus type 1: Identification of critical glycine residues.* Virology, 1996. **218**(1): p. 94-102.

17. Yang, S.T., et al., *HIV gp41-mediated membrane fusion occurs at edges of cholesterol-rich lipid domains.* Nature Chemical Biology, 2015. **11**(6): p. 424-+.

18. Yang, J., et al., *Oligomeric beta-structure of the membrane-bound HIV-1 fusion peptide formed from soluble monomers.* Biophysical Journal, 2004. **87**(3): p. 1951-1963.

19. Qiang, W. and D.P. Weliky, *HIV Fusion Peptide and Its Cross-Linked Oligomers: Efficient Syntheses, Significance of the Trimer in Fusion Activity, Correlation of beta Strand Conformation with Membrane Cholesterol, and Proximity to Lipid Headgroups.* Biochemistry, 2009. **48**(2): p. 289-301.

20. Gullion, T., *Introduction to rotational-echo, double-resonance NMR.* Concepts in Magnetic Resonance, 1998. **10**(5): p. 277-289.

21. Gullion, T. and J. Schaefer, *ROTATIONAL-ECHO DOUBLE-RESONANCE NMR.* Journal of Magnetic Resonance, 1989. **81**(1): p. 196-200.

22. Schmidt, A., R.A. McKay, and J. Schaefer, *INTERNUCLEAR DISTANCE MEASUREMENT BETWEEN DEUTERIUM (I = 1) AND A SPIN-1/2 NUCLEUS IN ROTATING SOLIDS.* Journal of Magnetic Resonance, 1992. **96**(3): p. 644-650.

23. Schmick, S.D. and D.P. Weliky, *Major Antiparallel and Minor Parallel beta Sheet Populations Detected in the Membrane-Associated Human Immunodeficiency Virus Fusion Peptide.* Biochemistry, 2010. **49**(50): p. 10623-10635.

24. Qiang, W., M.L. Bodner, and D.P. Weliky, *Solid-state NMR Spectroscopy of human immunodeficiency virus fusion peptides associated with host-cell-like membranes: 2D correlation spectra and distance measurements support a fully extended conformation and models for specific antiparallel strand registries.* Journal of the American Chemical Society, 2008. **130**(16): p. 5459-5471.

25. Zhang, H.Y., S. Neal, and D.S. Wishart, *RefDB: A database of uniformly referenced protein chemical shifts.* Journal of Biomolecular Nmr, 2003. **25**(3): p. 173-195.

26. Schimick, S., *High resolution tertiary structure of the membrane-associated HIV fusion peptides by solid state nuclear magnetic resonance*, in *Chemistry*. 2012, Michigan State University.

27. Jia, L.H., et al., *REDOR solid-state NMR as a probe of the membrane locations of membrane-associated peptides and proteins.* Journal of Magnetic Resonance, 2015. **253**: p. 154-165.

28. Ghosh, U., et al., *Closed and Semiclosed Interhelical Structures in Membrane vs Closed and Open Structures in Detergent for the Influenza Virus Hemagglutinin Fusion Peptide and Correlation of Hydrophobic Surface Area with Fusion Catalysis.* Journal of the American Chemical Society, 2015. **137**(24): p. 7548-7551.

29. Qiang, W., Y. Sun, and D.P. Weliky, *A strong correlation between fusogenicity and membrane insertion depth of the HIV fusion peptide.* Proceedings of the National Academy of Sciences of the United States of America, 2009. **106**(36): p. 15314-15319.

30. Qiang, W., J. Yang, and D.P. Weliky, *Solid-state nuclear magnetic resonance measurements of HIV fusion peptide to lipid distances reveal the intimate contact of beta strand peptide with membranes and the proximity of the Ala-14-Gly-16 region with lipid headgroups.* Biochemistry, 2007. **46**(17): p. 4997-5008.

31. Xie, L., et al., *Multiple Locations of Peptides in the Hydrocarbon Core of Gel-Phase Membranes Revealed by Peptide C-13 to Lipid H-2 Rotational-Echo Double-Resonance Solid-State Nuclear Magnetic Resonance.* Biochemistry, 2015. **54**(3): p. 677-684.

32. Bak, M., J.T. Rasmussen, and N.C. Nielsen, *SIMPSON: A general simulation program for solid-state NMR spectroscopy.* Journal of Magnetic Resonance, 2000. **147**(2): p. 296-330.

33. Sankaram, M.B. and T.E. Thompson, *CHOLESTEROL-INDUCED FLUID-PHASE IMMISCIBILITY IN MEMBRANES.* Proceedings of the National Academy of Sciences of the United States of America, 1991. **88**(19): p. 8686-8690.

34. Grosdidier, A., V. Zoete, and O. Michielin, *Fast Docking Using the CHARMM Force Field with EADock DSS.* Journal of Computational Chemistry, 2011. **32**(10): p. 2149-2159.

35. Grosdidier, A., V. Zoete, and O. Michielin, *SwissDock, a protein-small molecule docking web service based on EADock DSS.* Nucleic Acids Research, 2011. **39**: p. W270-W277.

36. Grosdidier, A., V. Zoete, and O. Michielin, *EADock: Docking of small molecules into protein active sites with a multiobjective evolutionary optimization.* Proteins-Structure Function and Bioinformatics, 2007. **67**(4): p. 1010-1025.

37. Yildiz, O., et al., *Structure of the monomeric outer-membrane porin OmpG in the open and closed conformation.* Embo Journal, 2006. **25**(15): p. 3702-3713.

38. Berman, H.M., et al., *The Protein Data Bank.* Nucleic Acids Research, 2000. **28**(1): p. 235-242.

39. Dunbrack, R.L. and M. Karplus, *BACKBONE-DEPENDENT ROTAMER LIBRARY FOR PROTEINS - APPLICATION TO SIDE-CHAIN PREDICTION.* Journal of Molecular Biology, 1993. **230**(2): p. 543-574.

40. Bower, M.J., F.E. Cohen, and R.L. Dunbrack, *Prediction of protein side-chain rotamers from a backbone-dependent rotamer library: A new homology modeling tool.* Journal of Molecular Biology, 1997. **267**(5): p. 1268-1282.

41. Krieger, E., et al., *Improving physical realism, stereochemistry, and side-chain accuracy in homology modeling: Four approaches that performed well in CASP8.* Proteins-Structure Function and Bioinformatics, 2009. **77**: p. 114-122.

42. Irwin, J.J., et al., *ZINC: A Free Tool to Discover Chemistry for Biology.* Journal of Chemical Information and Modeling, 2012. **52**(7): p. 1757-1768.

43. Irwin, J.J. and B.K. Shoichet, *ZINC - A free database of commercially available compounds for virtual screening.* Journal of Chemical Information and Modeling, 2005. **45**(1): p. 177-182.

44. Hanson, M.A., et al., *A specific cholesterol binding site is established by the 2.8 angstrom structure of the human beta(2)-adrenergic receptor.* Structure, 2008. **16**(6): p. 897-905.

45. Cherezov, V., et al., *High-resolution crystal structure of an engineered human beta(2)-adrenergic G protein-coupled receptor.* Science, 2007. **318**(5854): p. 1258-1265.

46. Hawkins, P.C.D. and A. Nicholls, *Conformer Generation with OMEGA: Learning from the Data Set and the Analysis of Failures.* Journal of Chemical Information and Modeling, 2012. **52**(11): p. 2919-2936.

47. Hawkins, P.C.D., et al., *Conformer Generation with OMEGA: Algorithm and Validation Using High Quality Structures from the Protein Databank and Cambridge Structural Database.* Journal of Chemical Information and Modeling, 2010. **50**(4): p. 572-584.

48. Haberthur, U. and A. Caflisch, *FACTS: Fast analytical continuum treatment of solvation.* Journal of Computational Chemistry, 2008. **29**(5): p. 701-715.

49. Tristram-Nagle, S., et al., *HIV Fusion Peptide Penetrates, Disorders, and Softens T-Cell Membrane Mimics.* Journal of Molecular Biology, 2010. **402**(1): p. 139-153.

50. Larsson, P. and P.M. Kasson, *Lipid Tail Protrusion in Simulations Predicts Fusogenic Activity of Influenza Fusion Peptide Mutants and Conformational Models.* Plos Computational Biology, 2013. **9**(3): p. 9.

Chapter 5 - HFP Effect on Membrane Motion by ^{2}H-NMR Studies

5.1 Introduction

^{2}H - NMR is a useful tool to study the structure and motions of lipids as well as membrane protein-lipids interactions in biological membranes.[1, 2] ^{2}H and ^{1}H are chemically equivalent and ^{2}H substitution of ^{1}H is not perturbing the native lipids and protein membrane environment.[3-5] Thus, it is advantageous to study membrane structure and motion changes by ^{2}H - NMR. We analyze the membrane motion through quadrupolar splitting ($\Delta\nu_Q$) and deuteron relaxation (T_2 and T_1) studies.

Deuteron is a spin 1 nucleus, and there are two allowed transitions: $m_s = 1 \rightarrow 0$ and $m_s = 0 \rightarrow -1$, which corresponds to the Pake doublet resonance in the spectrum. $\Delta\nu_Q$ is the peak splitting between the Pake doublets corresponding to a certain C-D bond orientation relative to $\mathbf{B_0}$. There is discussion of the orientation dependence of the quadrupolar energy in chapter 1 quadrupolar coupling interaction section. The ^{2}H spectrum can provide information about the C-D bond vector fluctuations by deuterium order parameter (S_{CD}).

$$\Delta\nu_Q = \frac{3}{4} \times \left(\frac{e^2qQ}{h}\right) \times S_{CD} = \frac{3}{4}\chi_Q S_{CD} \qquad 5.1$$

χ_Q is the static quadrupolar coupling constant. For aliphatic C-D bond, χ_Q is ~ 170 kHz.[6, 7] The order parameter is S_{CD}. $S_{CD} = \frac{1}{2} < 3\cos^2\theta - 1 >$, and θ is the angle between the C-D bond and the lipid principal reorientation axis which is the membrane normal. It is hard to get the $\Delta\nu_Q$ for each individual deuteron along the per-deuterated lipid acyl chain because individual peaks are broad and not well resolved in the static powder pattern spectrum (Figure 5.2) for un-oriented lipid vesicles. De-Pake-ing is one method to convert the un-oriented spectrum into 0°- oriented spectrum with well-resolved peaks from the FID.[8] To calculate S_{CD} for ^{2}Hs attached at

different carbon positons along the acyl chain, we use the peak splitting of the Pake doublet from the de-Paked spectrum. The more motion, the less ordered of C-D bond. Similarly, the less motion, the more ordered of C-D bond. Bigger $\Delta\nu_Q$ gives bigger S_{CD}. There is more motion toward the acyl chain terminus, and S_{CD} for lipid decreases along the carbon positon toward the membrane center. Perturbation of lipid motion can be analyzed by comparison of S_{CD} in membrane without and with HFP or/and CHOL.

Besides quadrupolar splitting and segmental order parameter, deuteron relaxation times are also sensitive to molecular motions. Relaxation is the process to return to the thermal equilibrium. In NMR, after pulses are applied, the nuclei relax to the Boltzmann equilibrium with rates of $1/T_2$ and $1/T_1$.

$$M_x(t) = M_x(0)exp\left(-\frac{t}{T_2}\right);\ M_y(t) = M_y(0)exp\left(-\frac{t}{T_2}\right) \quad 5.2$$

$$M_z(t) - M_z(0) = (M_z(0) - M_0)exp\left(-\frac{t}{T_1}\right) \quad 5.3$$

T_2 is the transverse or spin-spin relaxation time and T_1 is the longitudinal or spin lattice relaxation time. T_2 is sensitive to slow motions with $\tau_C >> \omega_0^{-1}$, and T_1 is sensitive to fast motions with $\tau_C << \omega_0^{-1}$, where τ_C is the molecular correlation time.[9, 10]

In this study, we are using ^2H NMR method to investigate the effect of HFP on membrane structure and motion in different model membranes. Membrane without and with CHOL is used to study the CHOL catalysis on HFP induced membrane fusion from membrane motion view. We use DMPC-d54 to probe the PC motion including segmental order parameter S_{CD} and T_2 relaxation rates in membrane both without and with CHOL. It is interesting to study the membrane with CHOL because studies have shown that presence of CHOL could catalyze HFP

induced fusion and previous studied in chapter 4 in this thesis support that HFP has preferential contact with CHOL vs PC.[11, 12] In membrane with CHOL, we investigate CHOL motion by T_2 and T_1 relaxation studies. In DMPC/DMPG/CHOL membrane, we investigated both DMPC and CHOL motion. Besides, we also studied CHOL motion in POPC/POPG/CHOL membrane, which is the most commonly use membrane composition for viral protein induced vesicle fusion assay.[13]

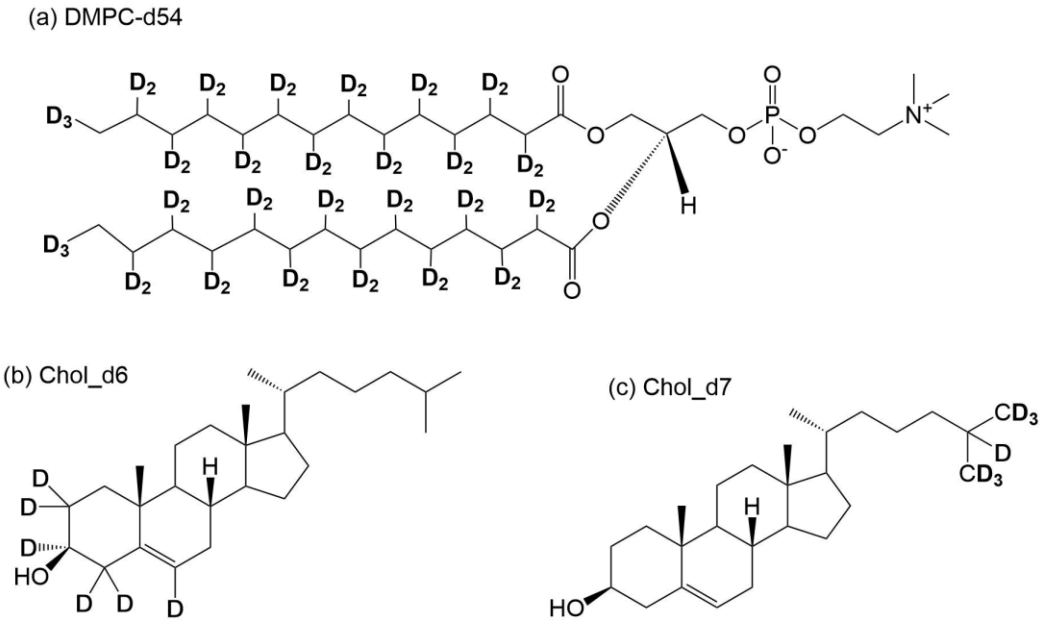

Figure 5.1 Chemical structures of deuterated PC and CHOL used for ^{2}H NMR study: (a) DMPC-d54, (b) Chol_d6 and (c) Chol_d7.

5.2 Experimental conditions

Samples are prepared by oganic cosolubilization method, see chapter 2 for details. The percentage of CHOL is mole percentage, and HFP percentage is mole of HFP relative to the total moles of PC and PG. DMPC-d54 and Chol_d6 ^{2}H NMR spectrum at variable temperatures are acquired by solid echo (quecho) experiment. Chol_d6 and Chol_d7 are used in another

membrane copositon. The chemical structure of the deuterated PC and CHOL are displayed. The pulse sequence of quecho experiment is shown in Chaper 2. For spectra at different temperatures, the sample is equlibrated for ~30 minutes with rotor inside the probe at each target temperature. The data is acquired typically with τ = 40 μs and τ_1 = 21 μs to gain best signal intensity and minimize pulse ringdown interference. For DMPC-d54 and Chol_d6/d7 ^{2}H T_2 studies, the data are acquired for different τ and τ_1 with same constant delay increments. For Chol_d7 T_1 relaxation studies, the data are acquired for each τ_1 with fixed increments for one set of τ_1 array. 90° and 180° pulses are optimized using D_2O with the transmiter frequency set at 61.2023333 MHz. The data is acquired at Varian 9.4 tesla NMR spectromete. Typical parameters are 3.0 μs 90° pulse, 6.3 μs 180° pulse, 0.9 rf amplification and 1s pulse delay. For DMPC-d54 studies, 2.1 μs 90° pulse is used with 0.4 rf amplification. The rabi frequency for 90° ^{2}H pulse is calculated from equation: $\frac{\gamma B_1}{2\pi} = \frac{1}{4 \times pw90X}$, and is 83 kHz and 119 kHz for 3 μs and 2.1 μs 90° pulse, respectively.

5.3 Results

5.3.1 Solid echo or quecho experimental results for DMPC/DMPG membrane without and with CHOL/ HFP

5.3.1.1 ^{2}H - NMR spectra features for DMPC-d54 and Chol_d6

In order to help understand membrane motions perturbed by HFP in membrane without and with CHOL, ^{2}H spectra of DMPC-d54 are taken in membrane without and with CHOL or/and HFP at different temperatures (Figures 5.2- 5.5). We add ~ 20 % DMPG to reflect the negative charged membrane composition in HIV host cells, and assist HFP membrane binding through electrostatic interaction because the peptide is positively charged. Pure DMPC-d54 has a phase transition temperature of ~ 23 °C.

In membrane without CHOL and HFP, Figure 5.2 shows a clear phase transition of DMPC-54 between 21 °C and 25 °C as evidenced from the spectrum shape change. The spectrum at 21 °C is broad because the experimental temperature is below the phase transition temperature of the PC and the PC is in gel phase with less C- ^{2}H bond motion. At 21 °C with addition of 4% HFP, the spectrum becomes significantly narrower and the peaks are similarly resolved compared to the spectra taken at higher temperatures. This indicates that HFP increases PC motion below the transition temperature. For the spectrum taken from 25 °C to 37 °C, the spectra are narrower and well resolved because the temperature is above the phase transition temperature and the membrane is in liquid disordered phase. In presence of HFP, the overall spectra become a little bit narrower, and the individual peaks become broader and less resolved.

In membrane with ~ 33% CHOL and without HFP, figure 5.3 does not show a phase transition of the membrane because the membrane is in liquid ordered phase with the presence of 33% CHOL at the temperature range studied. With addition of 4% HFP, all spectra become broader at different temperatures that support that HFP increase membrane order. In addition of 1% HFP, DMPC-d54 ^{2}H spectrum becomes narrower with individual peaks broader. For Chol_d6, the spectrum is similar without and with 2% HFP.

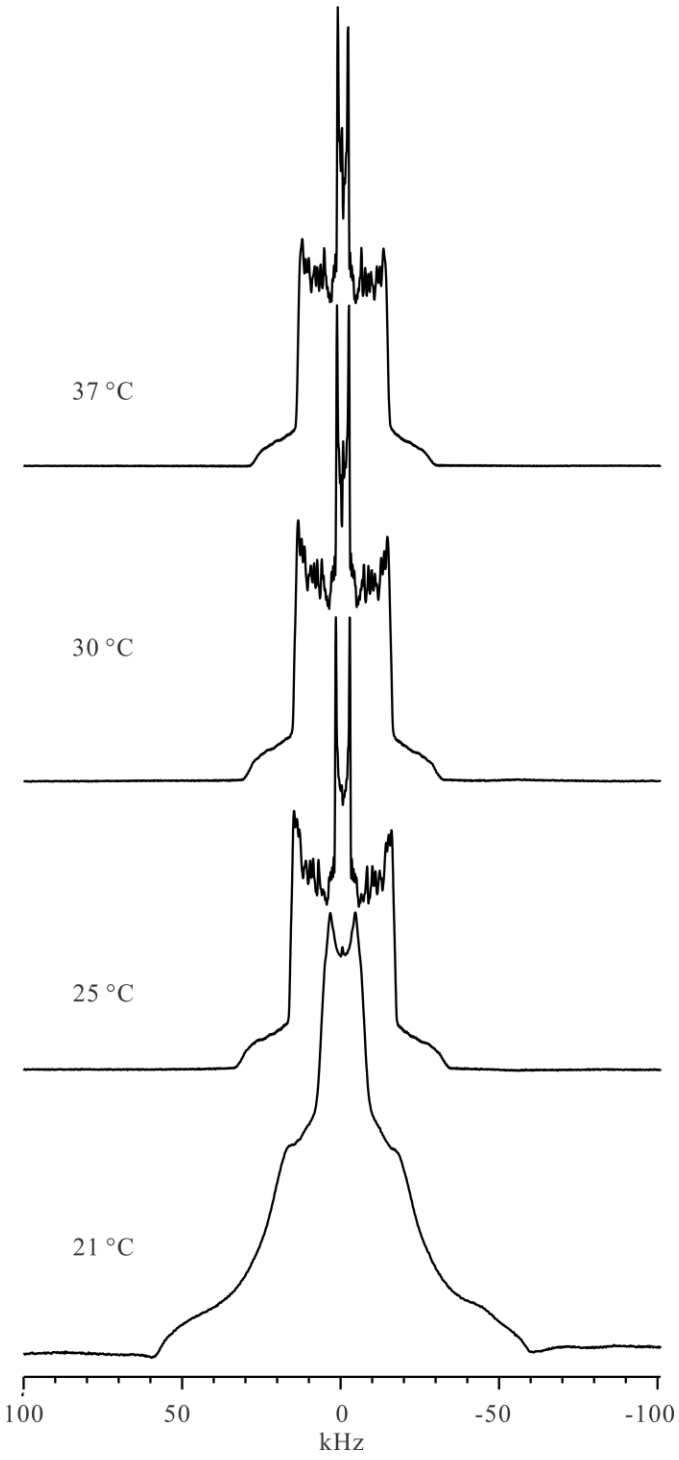

Figure 5.2 ^{2}H - NMR spectra of DMPC-d54 taken at different temperature in membrane of DMPC: DMPG= 40: 10μmol at pH 7.4.

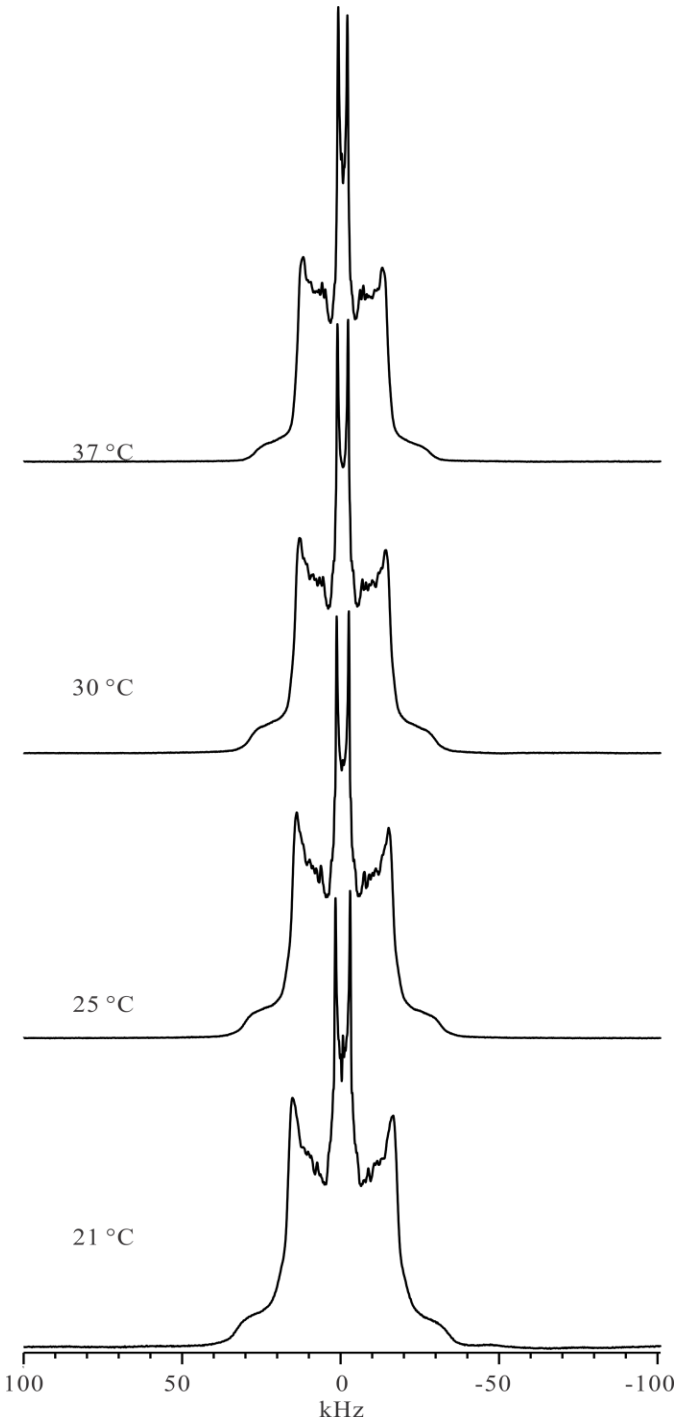

Figure 5.3 ^{2}H - NMR spectra of DMPC-d54 taken at different temperature in membrane of DMPC: DMPG= 40: 10µmol with ~ 2µmol HFP at pH 7.4.

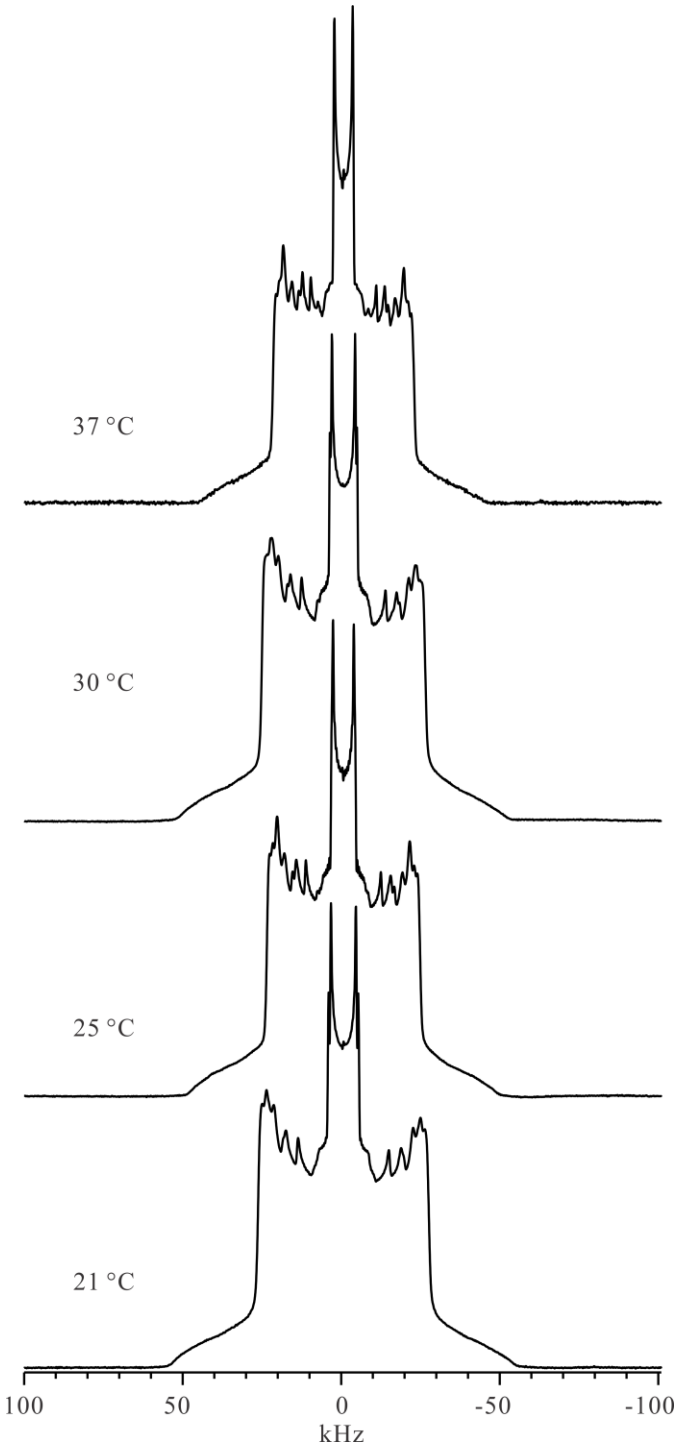

Figure 5.4 ^{2}H - NMR spectra of DMPC-d54 taken at different temperature in membrane of DMPC: DMPG: CHOL = 40: 10: 25μmol at pH 7.4.

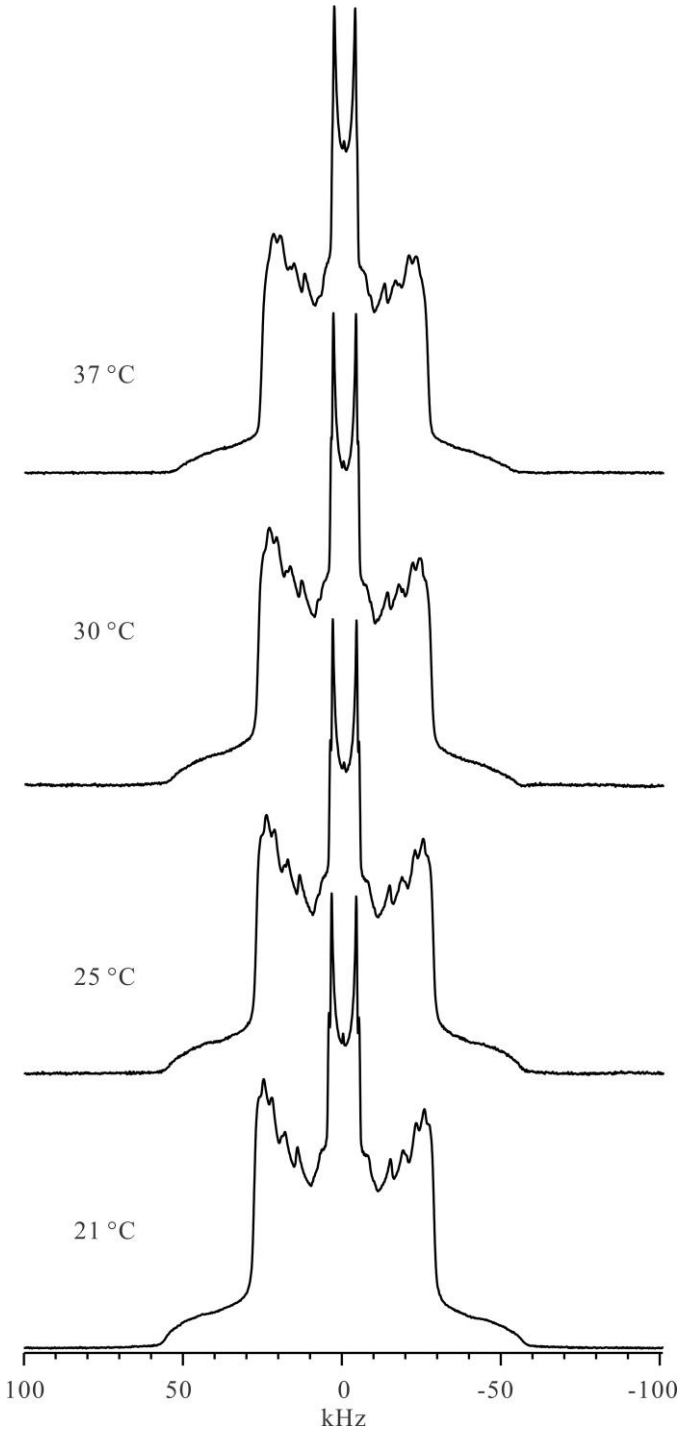

Figure 5.5 ^{2}H - NMR spectra of DMPC-d54 taken at different temperature in membrane of DMPC: DMPG: CHOL = 40: 10: 25μmol with ~ 2μmol HFP at pH 7.4.

5.3.1.2 DMPC-d54 Segmental order parameters at 37 °C

We investigated the effect of HFP on segmental order parameter of DMPC-d54 in membrane without and with 33% CHOL at physiological temperature 37 °C and physiological pH 7.4. Compared to membrane without HFP, the overall ^{2}H spectrum of DMPC-d54 becomes narrower with addition of 4% HFP in membrane without CHOL. There is similar spectrum feature with addition of 1% HFP in membrane with CHOL. The narrowing of the spectrum indicates disordering of the lipid acyl chain. On the contrary, the spectrum becomes significantly broader with addition of 4% HFP in membrane with CHOL, which suggests ordering of the lipid acyl chain in this condition.

However, the DMPC-d54 ^{2}H spectrum results from all the ^{2}Hs in the molecule. In order to get the quadrupolar splitting for each ^{2}H along the acyl chain, the spectrum need to be de-convoluted (de-Paked) to get better-resolved individual peaks. Figures 5.6-5.8 show representative overall ^{2}H powder pattern spectra of DMPC-d54, and figures 5.10- 5.12 show de-Paked spectra of DMPC-d54 without and with HFP. From the de-Paked spectrum, order parameter for each ^{2}H along the acyl chain is calculated as $S_{CD} = \Delta\nu_Q/(\frac{3}{4}\chi_Q)$, where $\chi_Q = \frac{e^2qQ}{h}$, and is the Qradrupolar coupling constant in Hz. For aliphatic C-^{2}H bond, χ_Q is 170 kHz. Figure 5.14 shows the percentage change of ^{2}H order parameter relative to the pure membrane. In presence of 4% HFP, the ^{2}H order parameter decreases ~ 1-10% along the acyl chain in membrane without CHOL, and increases about 20% to 30% along the acyl chain in membrane with 33% CHOL. In presence of 1% HFP, the ^{2}H order parameter decreases ~ 2 - 7% along the acyl chain in membrane with 33% CHOL. There is greater effect toward the terminal of the acyl chain. Order parameter change toward the terminal ^{2}H indicates perturbation of HFP down to the membrane center, which is consistent with REDOR results.

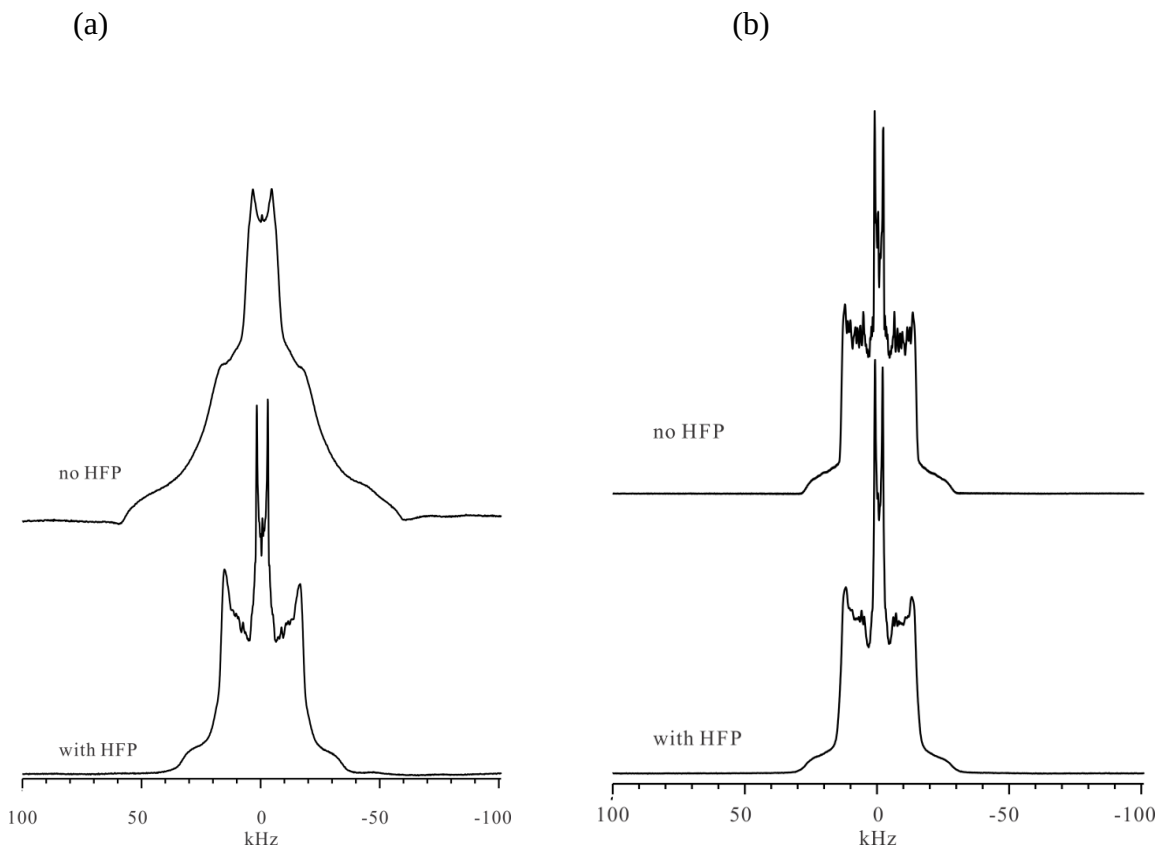

Figure 5.6 ^{2}H - NMR spectra of DMPC-d54 without and with HFP at (a) 21°C and (b) 37°C in membrane without CHOL at pH 7.4. Pure lipids are DMPC-d54: DMPG (40: 10μmol). HFP: lipids ratio is 1:25.

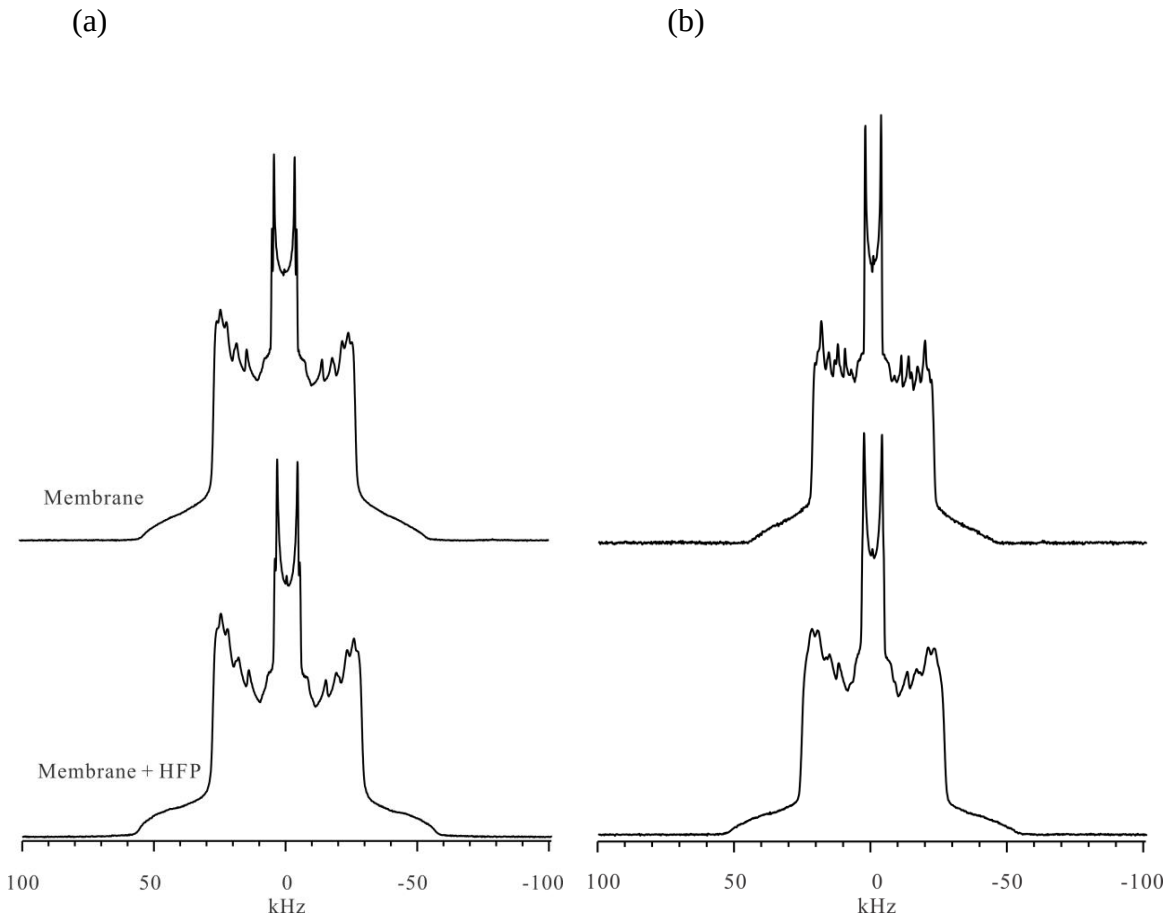

Figure 5.7 ^{2}H - NMR spectra of DMPC-d54 without and with HFP at (a) 21°C and (b) 37°C in membrane containing 33% CHOL at pH 7.4. Membrane is DMPC-d54: DMPG: CHOL (40: 10: 25μmol). HFP: lipids ratio is 1:25.

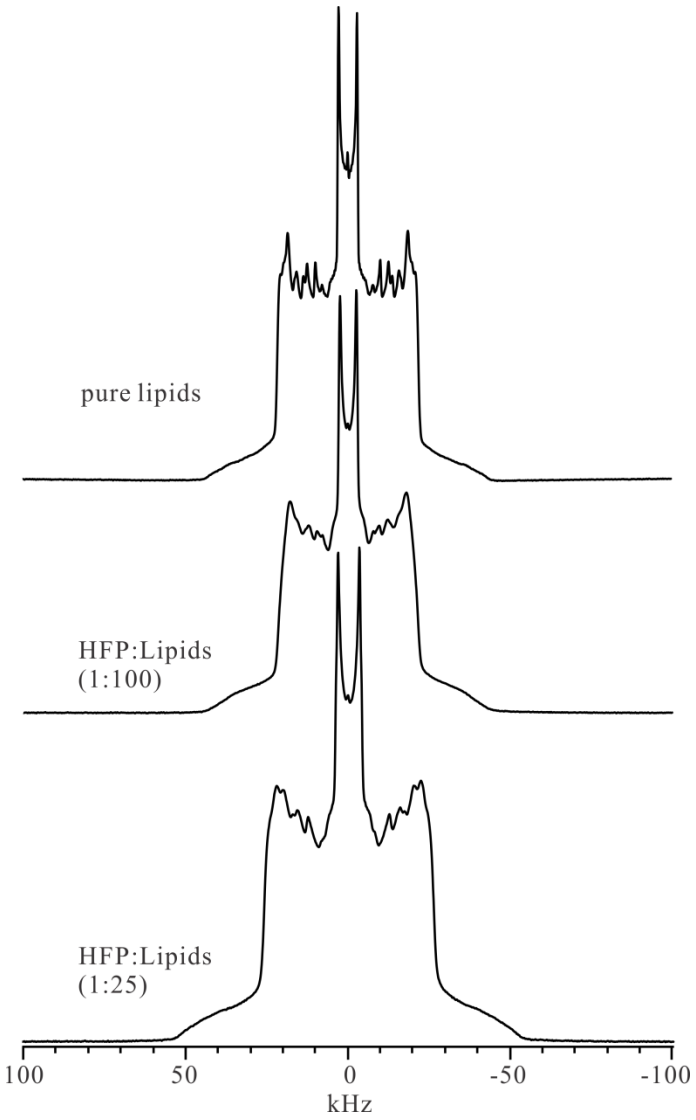

Figure 5.8 ^{2}H - NMR spectra of DMPC-d54 without (top) and with different peptide to lipids mole ratios, 1: 100 (middle) and 1: 25 (bottom) at 37°C and pH 7.4. Pure lipids are DMPC-d54: DMPG: CHOL with 40:10:25μmol.

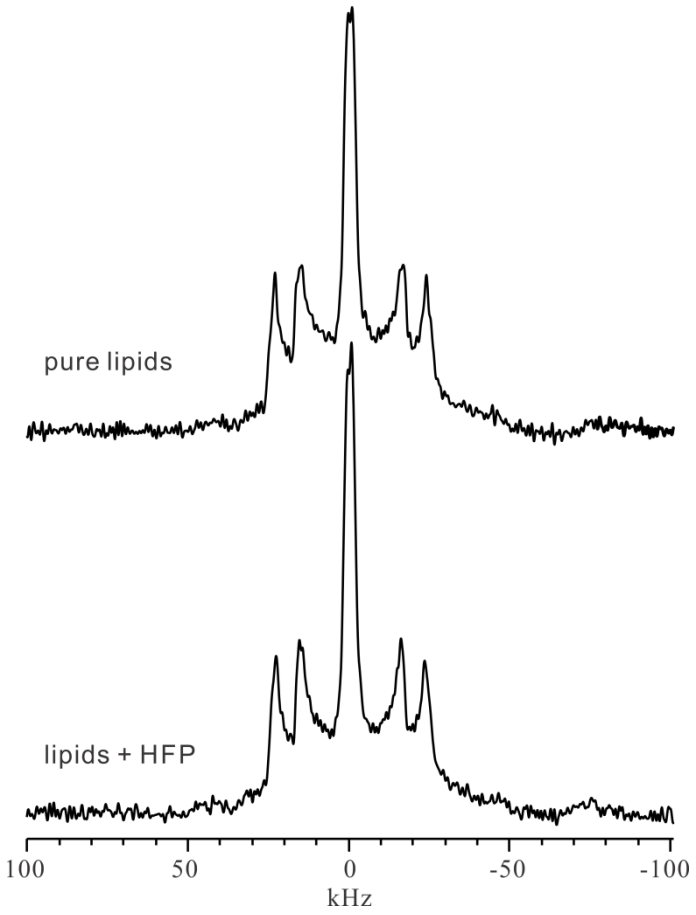

Figure 5.9 Chol_d6 ^{2}H-NMR spectra, without (top) and with HFP (bottom) at 37°C and pH 7.4, pure lipids are DMPC: DMPG: Chol_d7 with 40:10:25μmol. HFP: lipids mole ratio is 1:50, and lipids do not include CHOL.

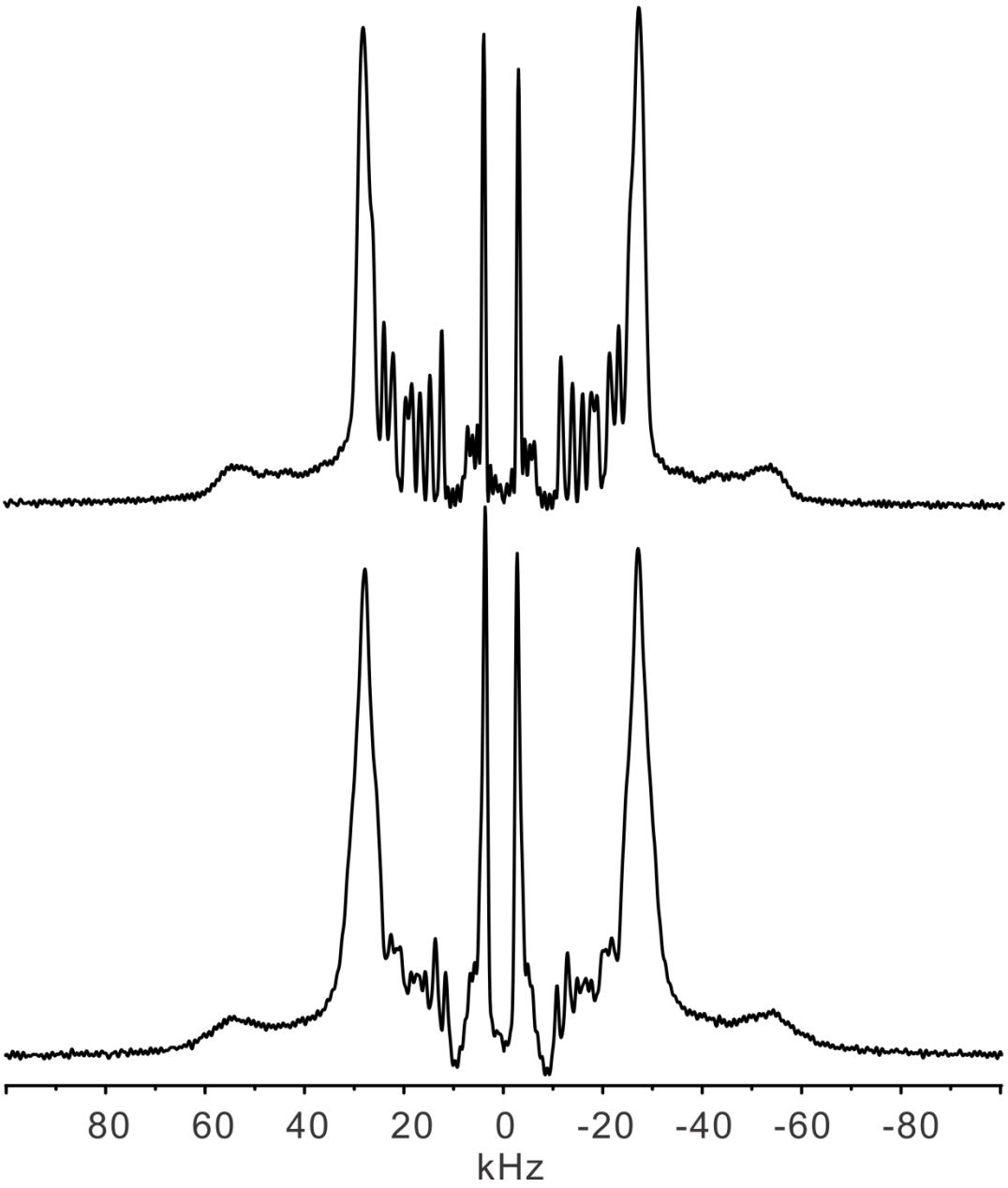

Figure 5.10 DMPC-d54 de-Paked spectra, without (top) and with HFP (bottom) at 37°C and pH 7.4. The membrane is DMPC-d54: DMPG with 40:10μmol. HFP: lipids ratio is 1:25.

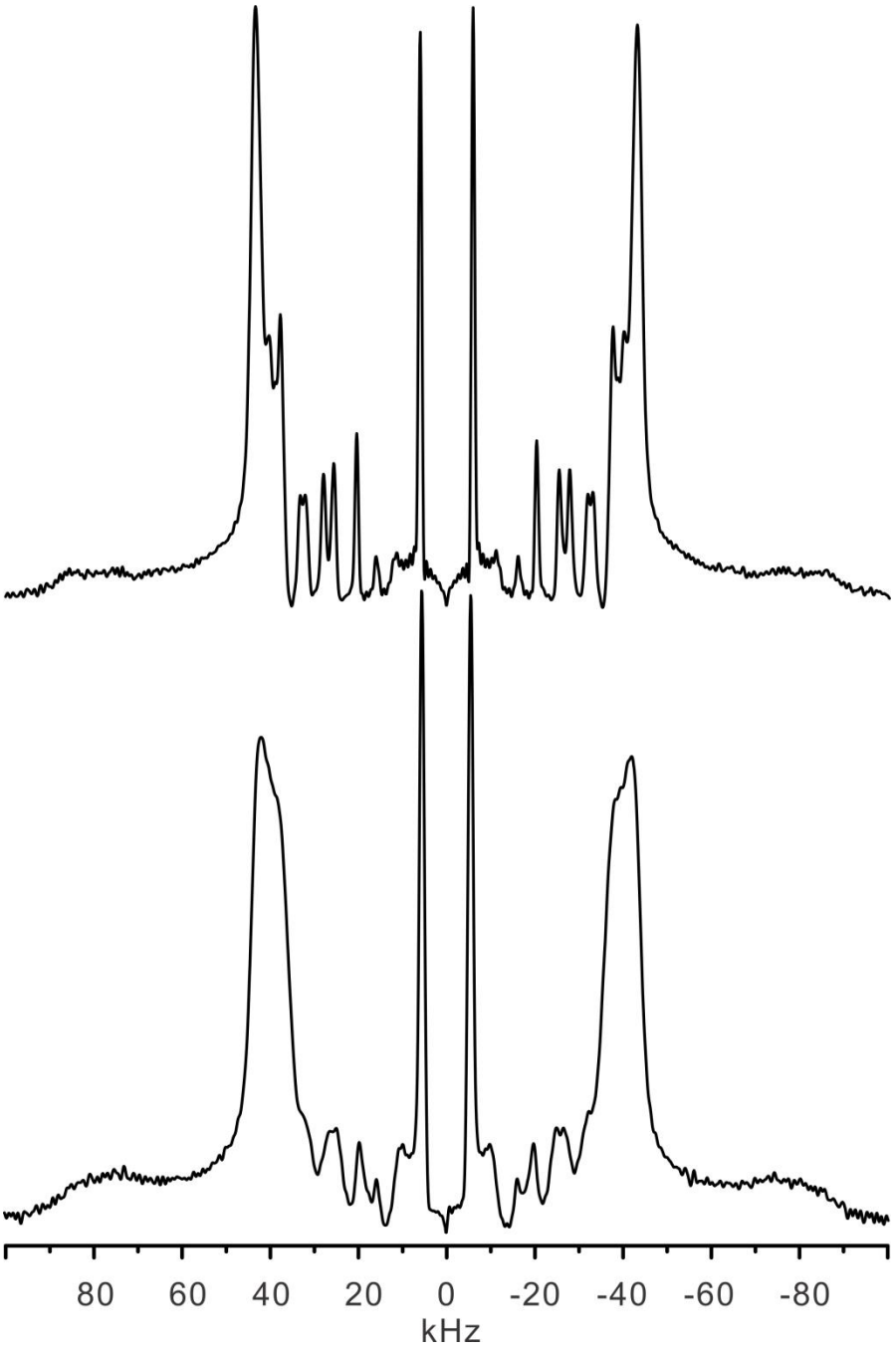

Figure 5.11 DMPC-d54 de-Paked spectra, without (top) and with HFP (bottom) at 37°C and pH 7.4. The membrane is DMPC-d54: DMPG: CHOL with 40:10:25μmol. HFP: lipids ratio is 1:100.

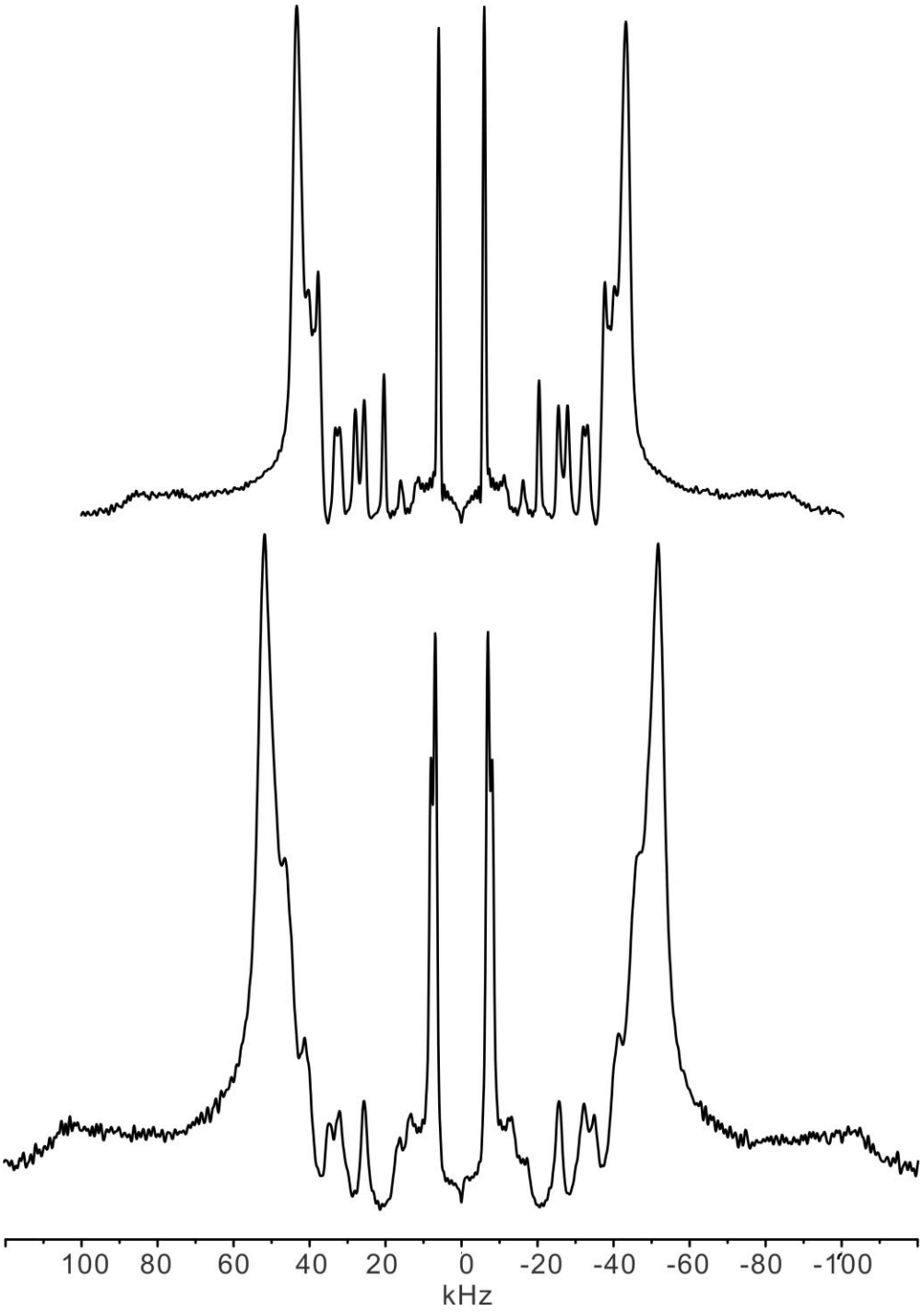

Figure 5.12 DMPC-d54 de-Paked spectra, without (top) and with HFP (bottom) at 37°C and pH 7.4. The membrane is DMPC-d54: DMPG: CHOL with 40:10:25μmol. HFP: lipids ratio is 1:25.

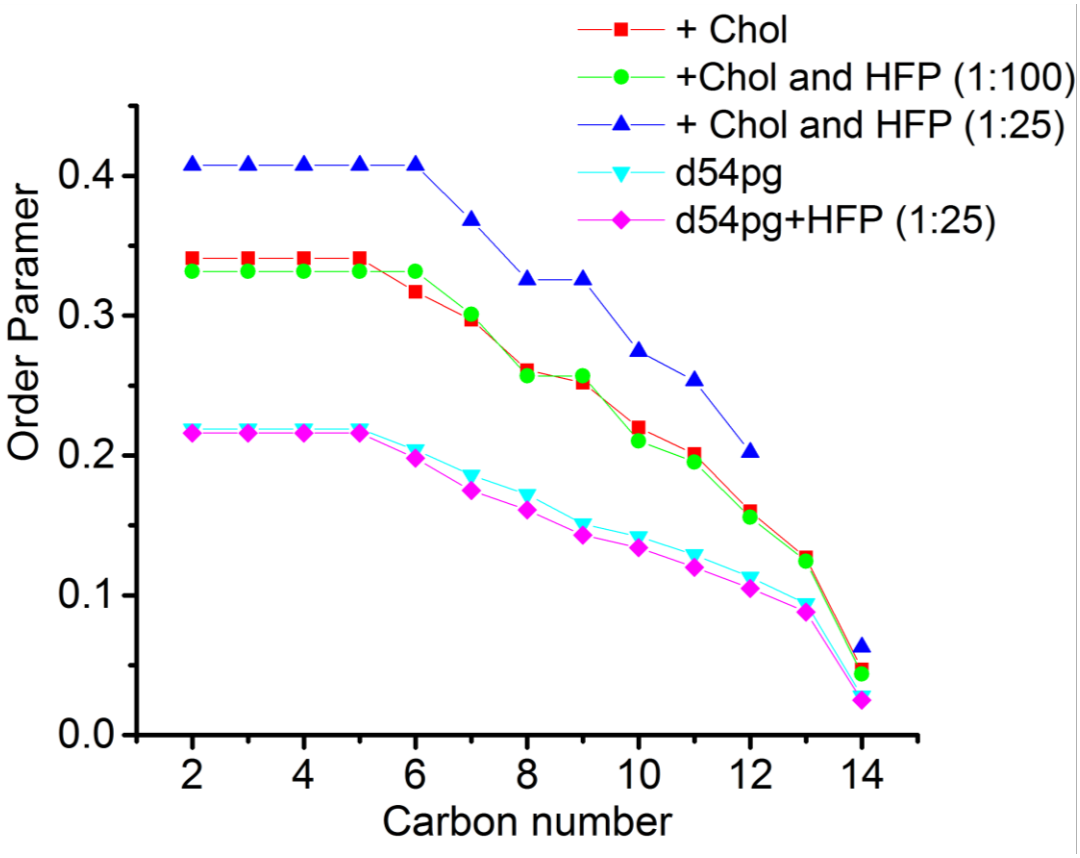

Figure 5.13 HFP effects on the DMPC-d54 order parameters profile in membrane with and without CHOL at 37°C and pH 7.4. HFP decreases the order parameters along the acyl chain of the lipid in membrane of DMPC-d54 (d54) and DMPG (pg) with 1:25 peptide to lipids ratio, and membrane with additional 33% CHOL (+Chol) with 1:100 peptide to lipids ratio. However, HFP increases the order parameters along the acyl chain of the lipid with 1:25 peptide to lipids ratio in the membrane containing 33% CHOL.

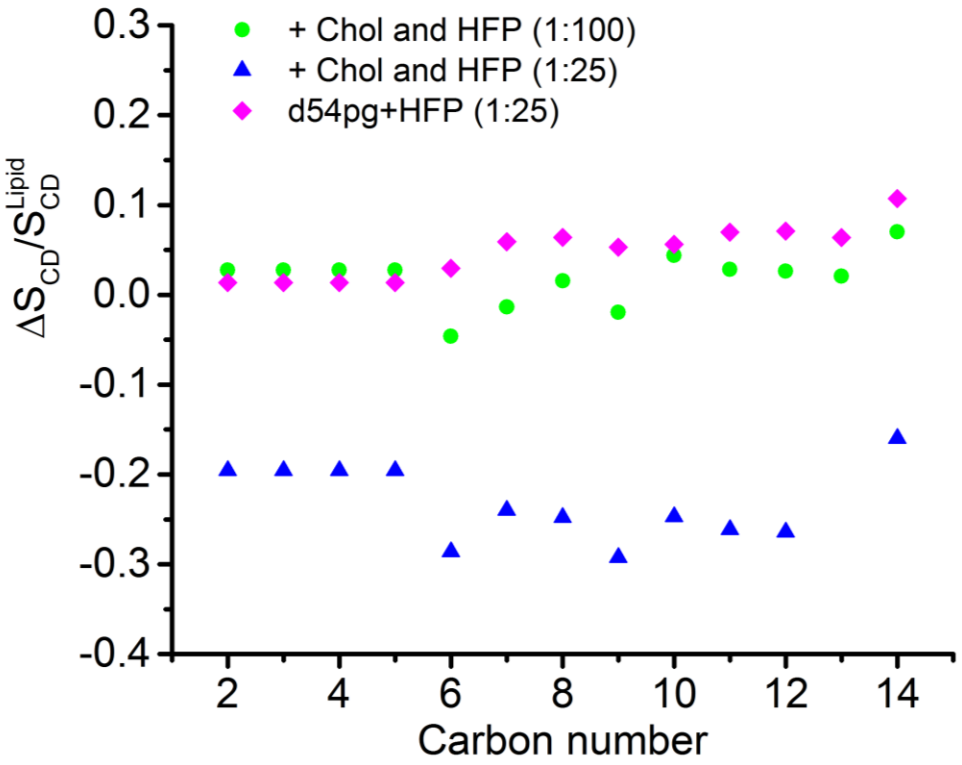

Figure 5.14 HFP effects on the order parameter change of DMPC-d54 along the lipid acyl chain compared to pure membrane with and without CHOL at 37 °C and pH 7.4. $\Delta S_{CD} = S_{CD}^{Lipid} - S_{CD}^{(Lipid+ HFP)}$. Positive value indicates decreased order parameter and negative value indicates increased order parameter compared to pure membrane without HFP. The plot color and shape are consistent with previous figure.

5.3.1.3 Transverse relaxation studies of DMPC-d54 and Chol_d6

Samples are prepared by oganic cosolubilization method, see chapter 2 for details. To evaluate the effect of HFP on membrane motion and the role of CHOL, we study the transverse relaxation (T_2 relaxation) by quecho experiments. For each sample, τ and τ_1 were arrayed with same delay increments. We hydrated the sample with pH 7.4 buffer and study PC motion with DMPC-d54 in membrane both without and with CHOL. We used Chol_d6 for CHOL motion in membrane containing 33% CHOL. We study DMPC-d54 at different temperatures and Chol_d6 at 37 °C.

Figure 5.15 and Figure 5.21 shows representative stack plots of FID of DMPC-d54 and Chol_d6, respectively. Figure 5.16 to 5.20 show representative stack plots of processed spectra of DMPC-d54 for CD_3 and outer CD_2 peak intensity. Both FID intensity and processed peak intensity show exponential decay. We fit the echo intensity of FID to get the overall T_2 that has contributions from all the ^{2}Hs for both DMPC-d54 and Chol-d6. CD_3 and CD_2 peak intensity from processed spectra are used to get CD_3 and CD_2 ^{2}H T_2. Below phase transition temperature, CD_2 peak intensity is weak and decays very fast, so we did not analyze the T_2 at 21 °C. CD_3 peak intensity has contribution from CD_3 and CD_2 deuterons, the T_2 analyzed for CD_3 would also contains part effect from CD_2. Since CD_2 T_2 is much shorter than CD_3, inclusion of CD_2 peak intensity would make the measured CD_3 T_2 smaller than the actual value.

We fit the data by equation:

$$I(2\tau) = I(0) \times \exp\left(-\frac{2\tau}{T_2}\right) + A \qquad 5.1$$

$I(2\tau)$ is the experimental measured echo or peak intensity, and $2\tau = \tau + \tau 1$ + data shift points × dwell time. I(0) and T_2 are fitting parameters, and A is the fitting offset. Figures 5.22 to 5.25 display T_2 fittings from echo intensity for DMPC-d54 in different sample compositions at various temperatures. Figure 5.26 shows representative T_2 fitting from echo intensity, CD_3 peak intensity and CD_2 peak intensity. Figure 5.27 displays representative fitting plots for membrane without and with HFP for Chol_d6 at 37 °C. The best-fit T_2s from different samples at various temperatures are in Table 5.1. Adding HFP will generally decrease PC T_2, except for sample of HFP in membrane composed of DMPC-d54 and DMPG at 21 °C. We compared the T_2s in membrane with 33% CHOL, shown in Table 5.2. Adding HFP causes T_2 reduction for both Chol_d6 and DMPC-D54. There is much bigger reduction for PC than Chol_d6. The T_2

reduction is a little smaller with 1% HFP than 4% HFP when fitting with echo intensity, but similar for CD_3 and CD_2.

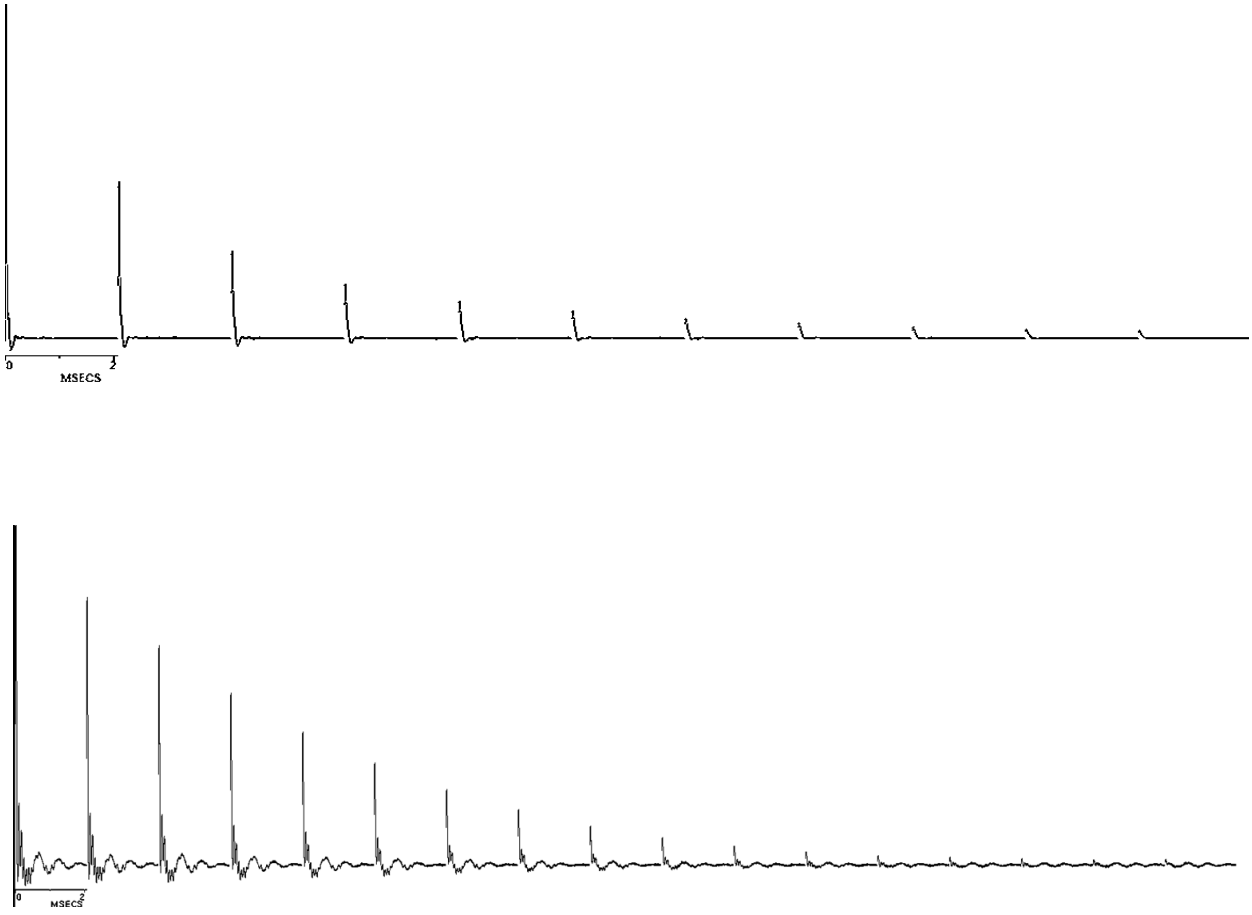

Figure 5.15 Representative stacked FID plots DMPC-d54 in membrane of DMPC-d54: DMPG without HFP at 21°C (top) and 37°C (bottom) in static. The ^2H FIDs were obtained by varying τ and τ_1. For each τ and τ_1, the number of scans was 5000 (top) and 1000 (bottom), respectively.

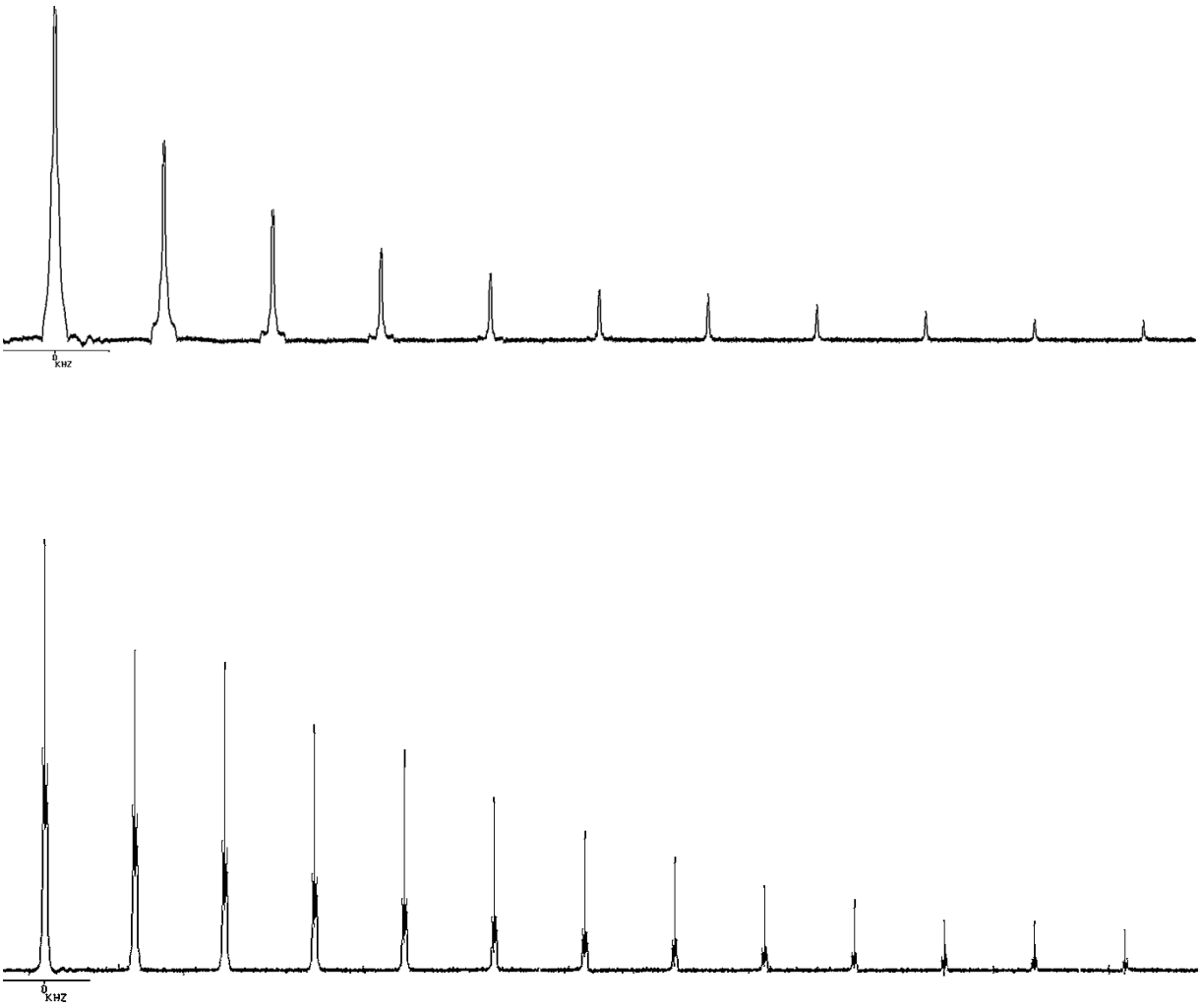

Figure 5.16 Representative stacked spectrum plots DMPC-d54 in membrane of DMPC-d54: DMPG without HFP at 21°C (top) and 37°C (bottom) at pH 7.4 in static. The ^{2}H spectra were obtained by varying τ and τ_1. For each τ and τ_1, the number of scans was 5000 (top) and 1000 (bottom), respectively. All spectra were processed with 200 Hz line broadening, data shift = -11.

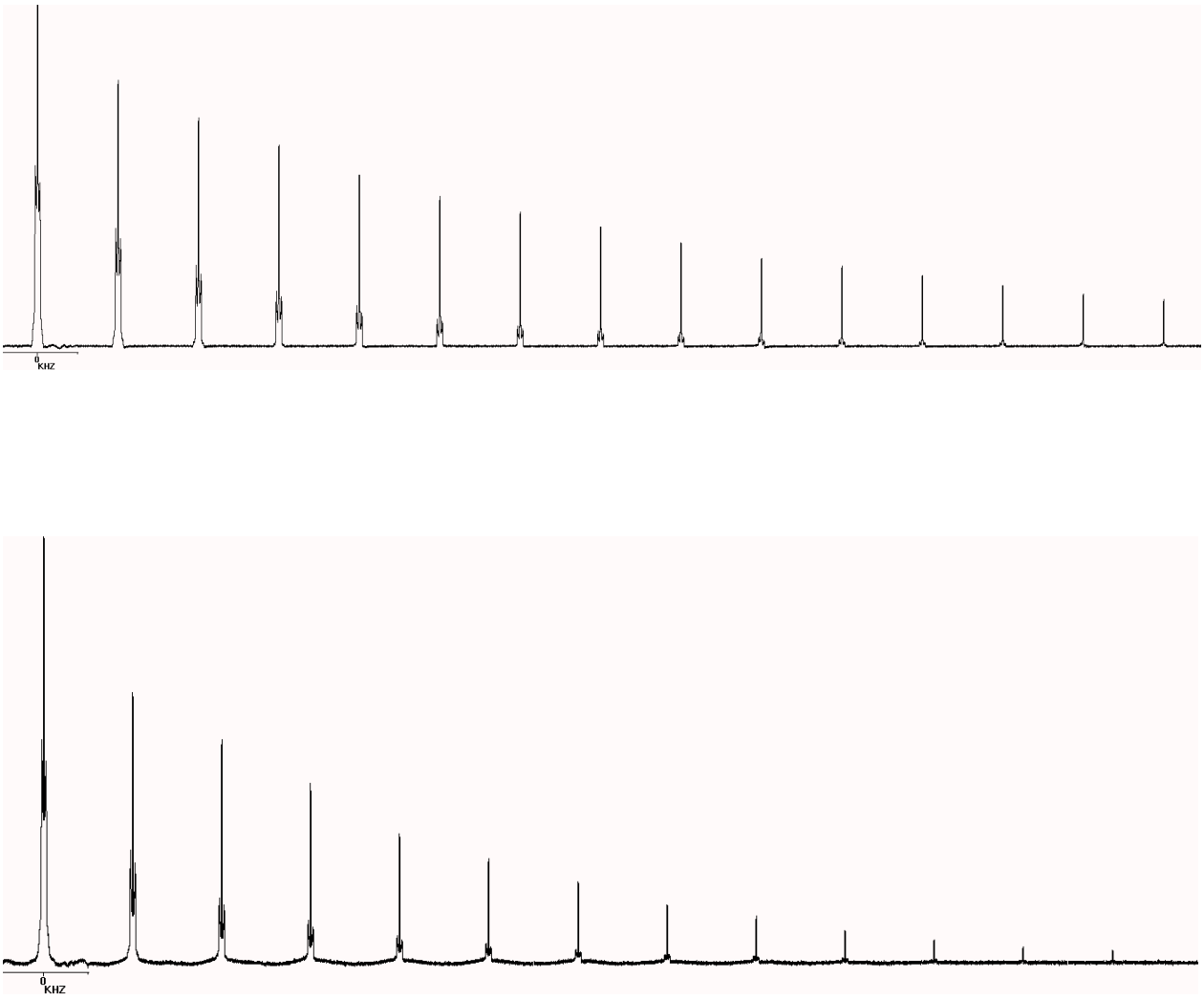

Figure 5.17 Representative stacked spectrum plots DMPC-d54 in membrane of DMPC-d54: DMPG with 2µmol HFP at 21°C (top) and 37°C (bottom) and pH 7.4 in static. The ^{2}H spectra were obtained by varying τ and τ_1. The top spectra were arrayed to τ = 750 and τ_1 = 731 µs. The bottom spectra were arrayed to τ = 1360 µs and τ = 1341 µs. For each τ and τ_1, the number of scans was 5000 (top) and 1000 (bottom), respectively. All spectra were processed with DC offset correction, data shift = -11. We processed the bottom spectra additionally with polynomial baseline correction of the order 5.

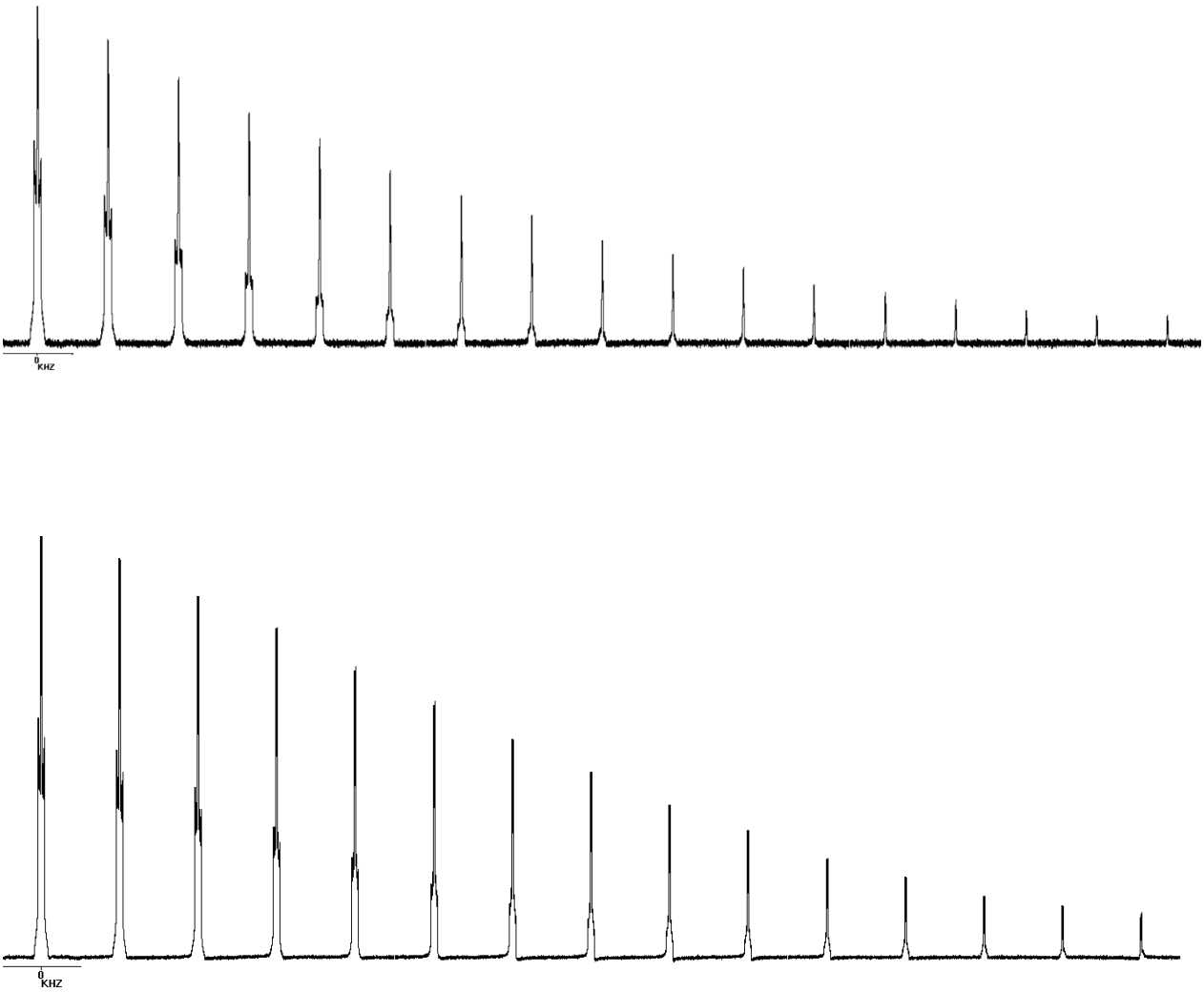

Figure 5.18 Representative stacked spectrum plots DMPC-d54 in membrane of DMPC-d54: DMPG: CHOL (8:2:5) without HFP at 21°C (top) and 37°C (bottom) and pH 7.4 in static. The ^{2}H spectra were obtained by varying τ and τ_1. The top spectra were arrayed to τ = 1340 and τ_1 = 1321 μs. The bottom spectra were arrayed to τ = 1320 μs and τ = 1301 μs. For each τ and τ_1, the number of scans was 1000. All spectra were processed with DC offset correction, data shift = -11.

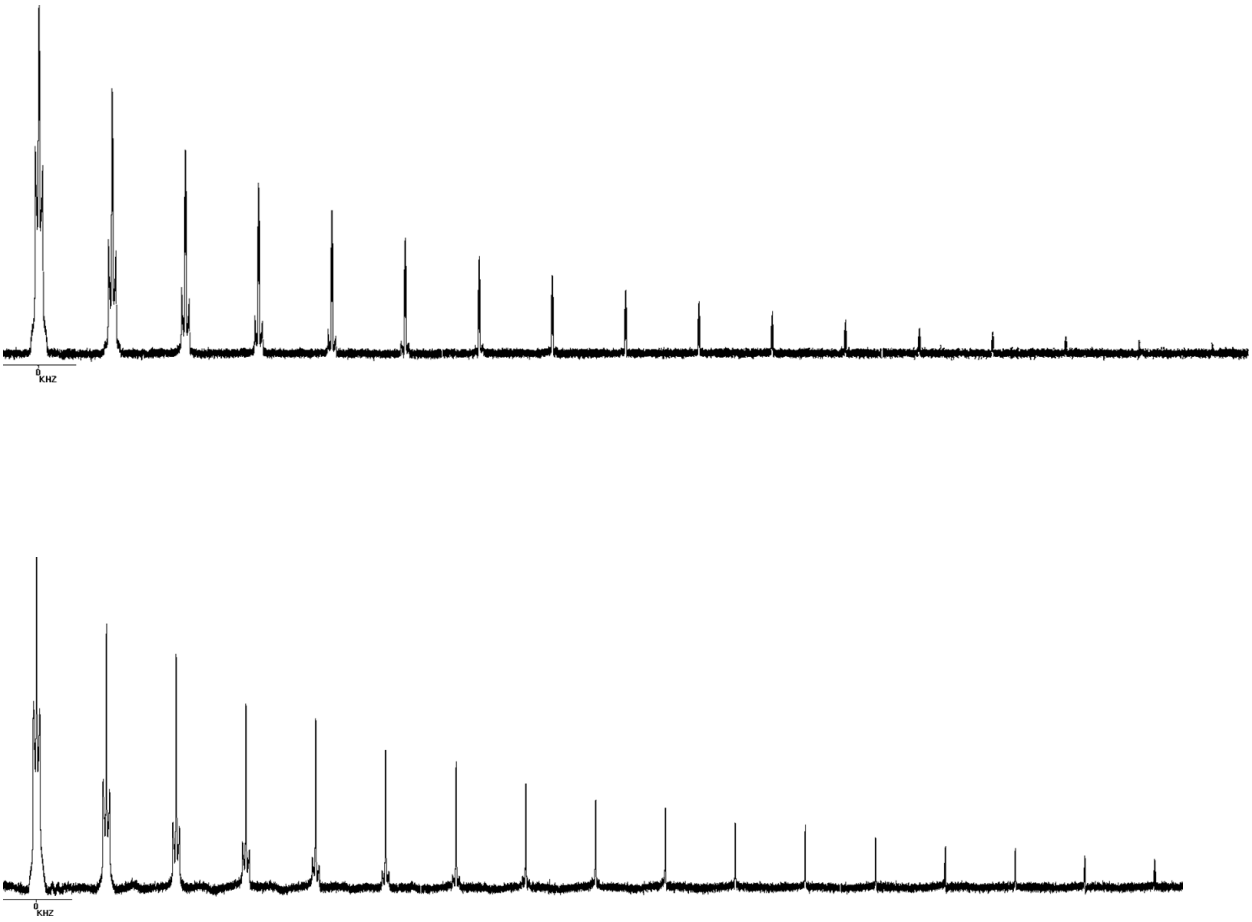

Figure 5.19 Representative stacked spectrum plots DMPC-d54 in membrane of DMPC-d54: DMPG: CHOL (8:2:5) with 2µmol HFP at 21°C (top) and 37°C (bottom) and pH 7.4 in static. The ^{2}H spectra were obtained by varying τ and τ_1. The top spectra were arrayed to τ = 1340 and τ_1 = 1321 µs. The bottom spectra were arrayed to τ = 1000 µs and τ = 981µs. For each τ and τ_1, the number of scans was 1000. All spectra were processed with DC offset correction, data shift = -11.

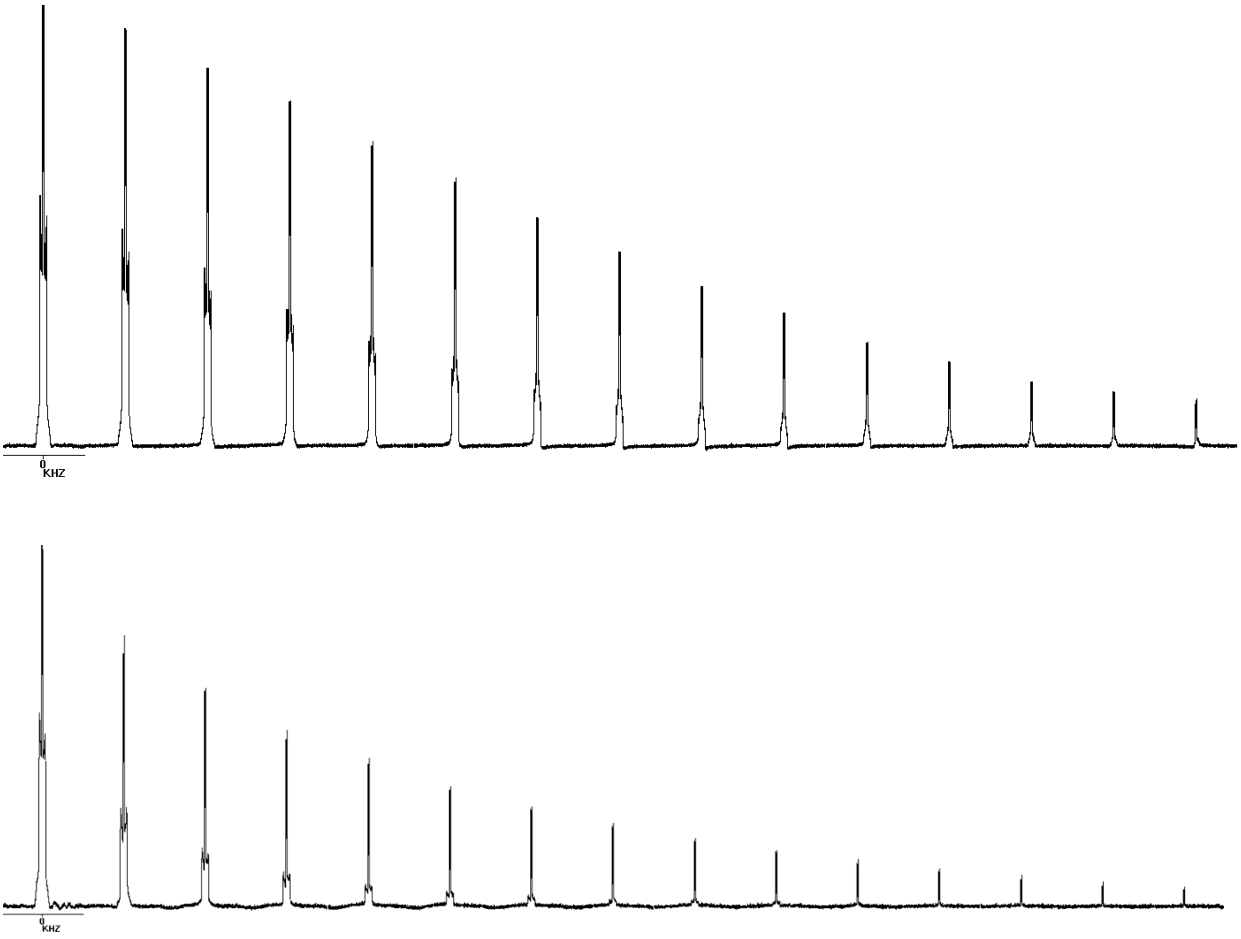

Figure 5.20 Representative stacked spectrum plots DMPC-d54 in membrane of DMPC-d54: DMPG: CHOL (8:2:5) without (top) and with HFP (HFP: phospholipids= 1:100) (bottom) at 37°C (bottom) and pH 7.4 in static. The ^{2}H spectra were obtained by varying τ and τ_1. The top spectra were arrayed to τ = 1320 and τ_1 = 1301 μs. The bottom spectra were arrayed to τ = 1160 μs and τ = 1141μs. For each τ and τ_1, the number of scans was 1000. All spectra were processed with DC offset correction, data shift = -11. We processed the bottom spectra with additional 200 Hz Gaussian line broadening and polynomial baseline correction of the order 5.

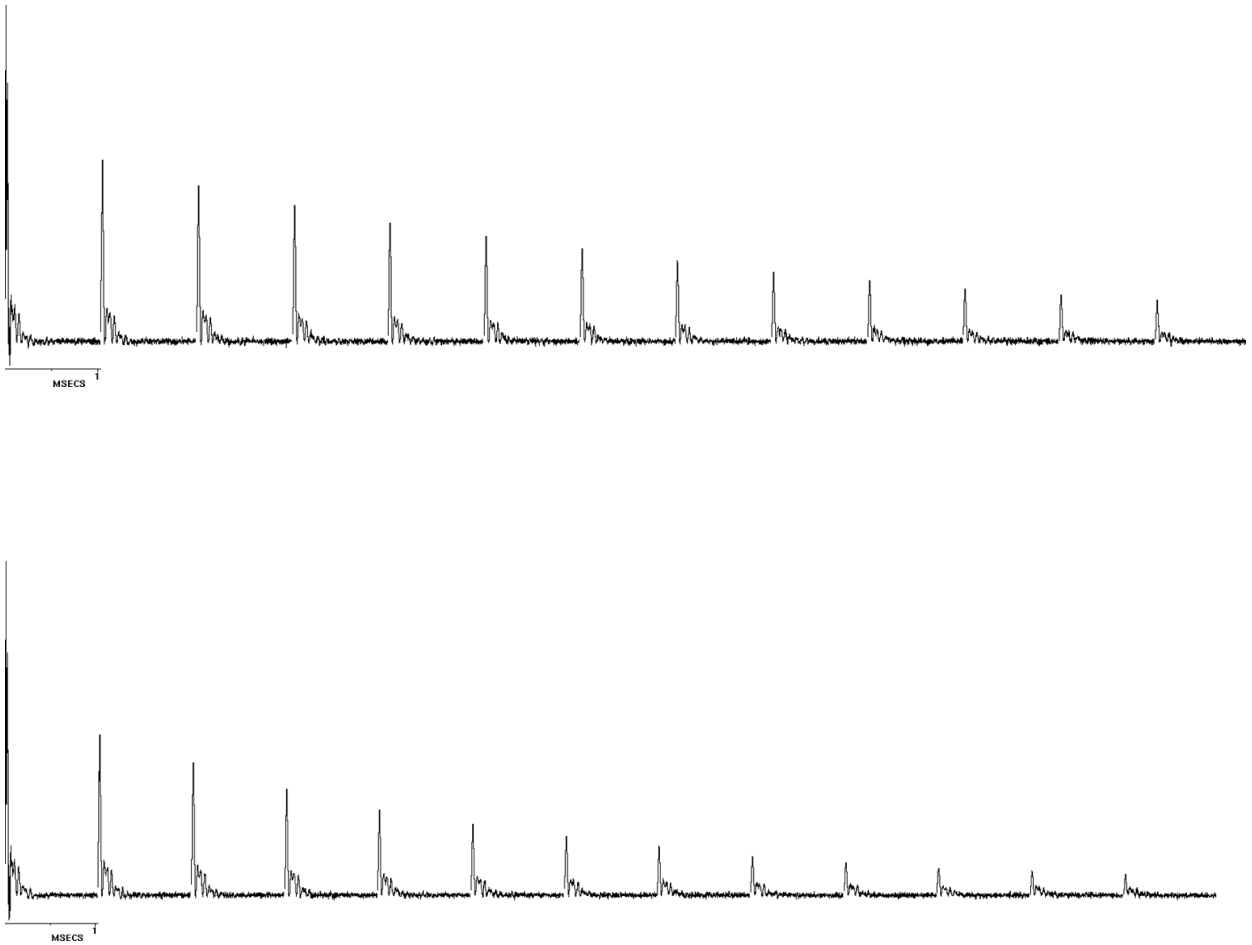

Figure 5.21 Stacked spectrum plots Chol_d6 in membrane of DMPC: DMPG: Chol_d6 (8:2:5) without (top) and with (bottom) 1µmol HFP at 37°C and pH 7.4 in static. The ^{2}H spectra were obtained by varying τ and τ_1. The spectra were arrayed to τ = 340 and τ_1 = 321 µs. For each τ and τ_1, the number of scans was 10000.

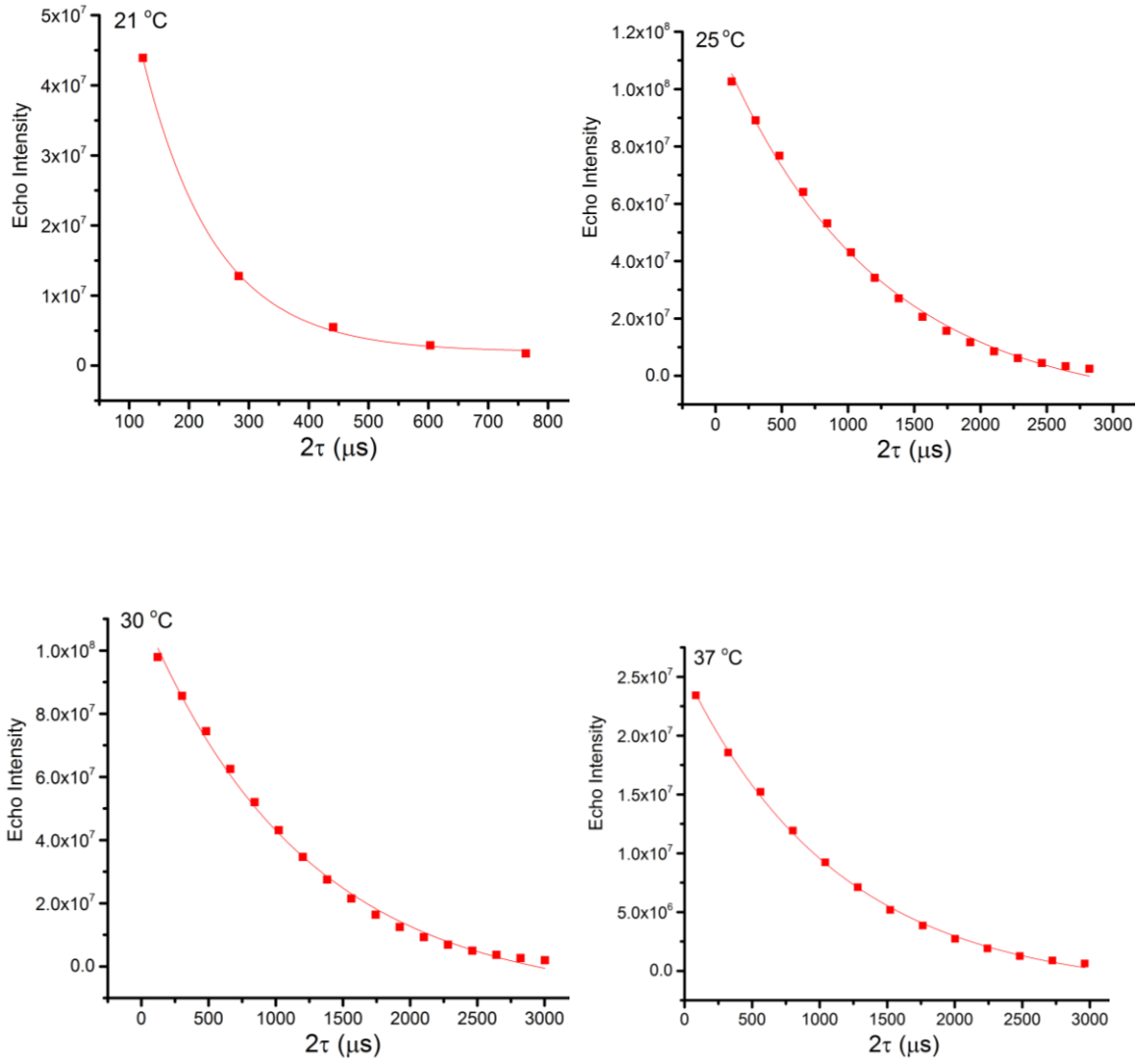

Figure 5.22 Quecho experimental (red squares) and best fit (red lines) plots of tip intensity of echo FID vs 2τ for DMPC-d54 in membrane of DMPC-d54: DMPG without HFP under static conditions at different temperatures and pH 7.4. The data are fitted with $I(2\tau) = I(0) \times \exp(-2\tau/T_2) + A$, where A is the fitting offset.

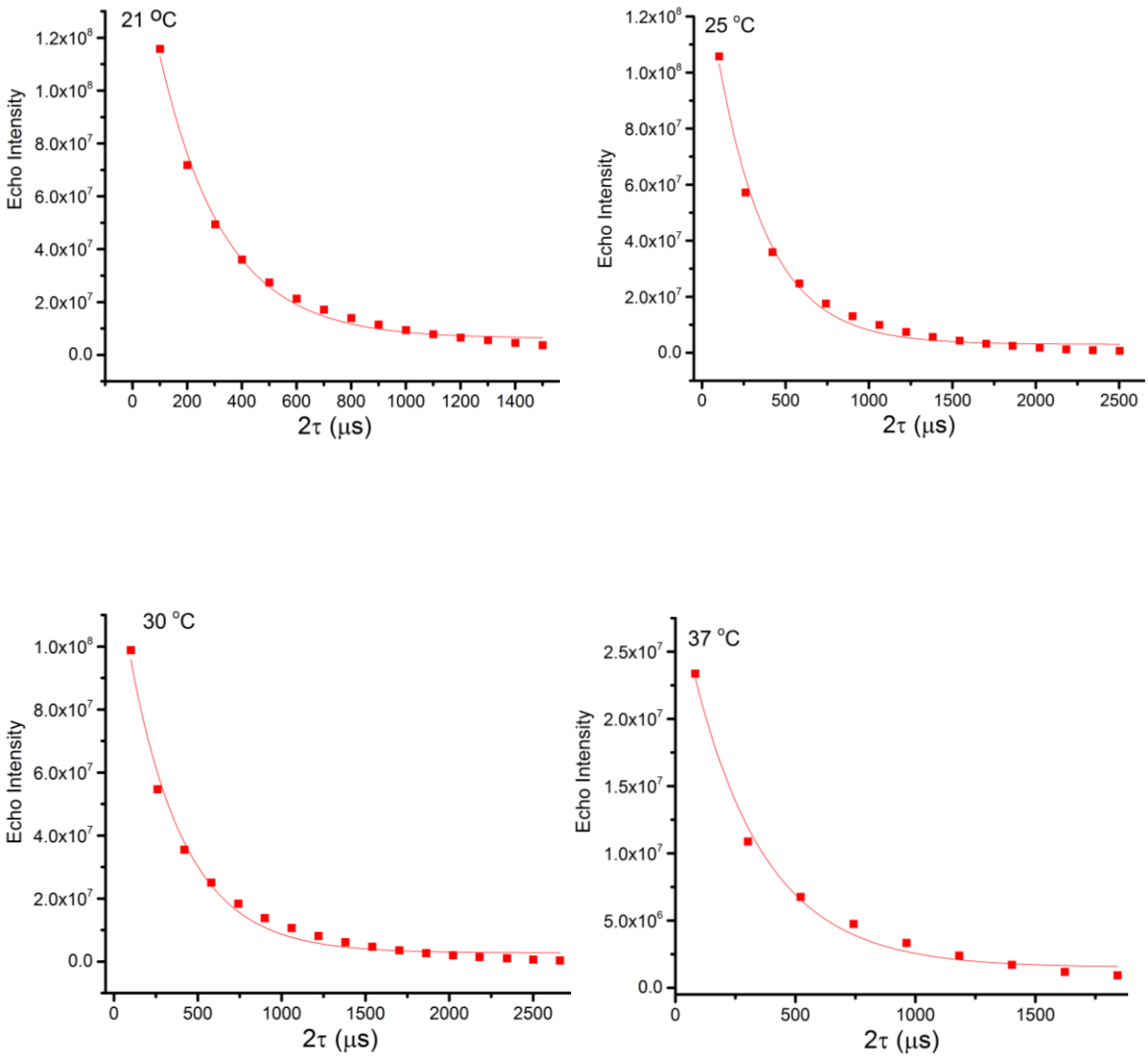

Figure 5.23 Quecho experimental (red squares) and best fit (red lines) plots of tip intensity of DMPC-d54 echo FID vs 2τ in membrane of DMPC-d54: DMPG with HFP under static conditions at different temperatures and pH 7.4. The HFP: lipids mole ratio is 1:25. The data are fitted by equation $I(2\tau) = I(0) \times \exp(-2\tau/T_2) + A$, where A is the fitting offset. There are some fitting deviations relative to experimental data because there are fast decay components (CD_2) and slow decay components (CD_3).

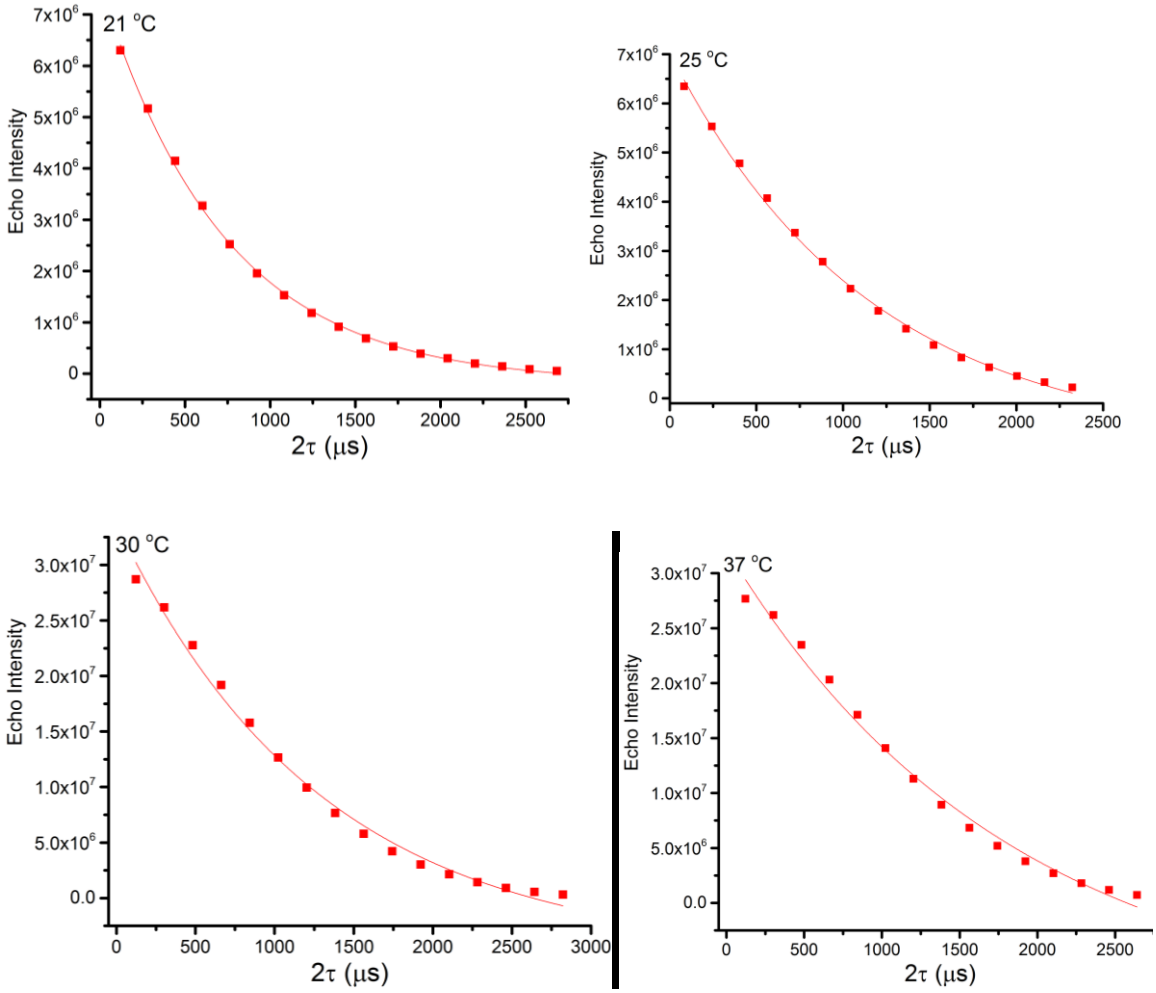

Figure 5.24 Quecho experimental (red squares) and best fit (red lines) plots of tip intensity of echo FID vs 2τ for DMPC-d54 in membrane of DMPC-d54: DMPG: CHOL (8:2:5 mole ratio) without HFP under static conditions at different temperatures and pH 7.4. The data are fitted by equation $I(2\tau) = I(0) \times \exp(-2\tau/T_2) + A$, where A is the fitting offset. There are some fitting deviations relative to experimental data because there are fast decay components (CD_2) and slow decay components (CD_3).

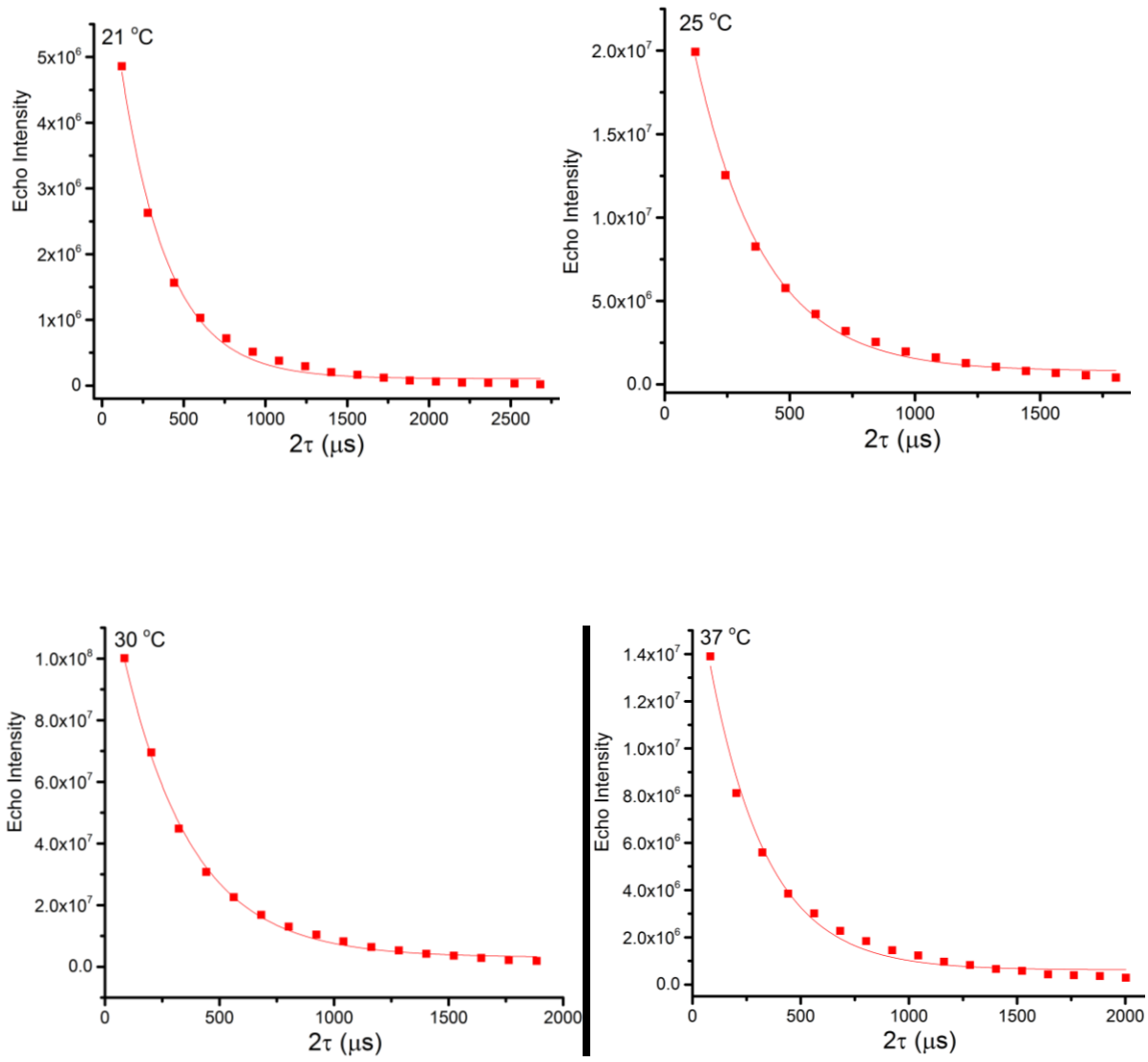

Figure 5.25 Quecho experimental (red squares) and best fit (red lines) plots of tip intensity of DMPC-d54 echo FID vs 2τ in membrane of DMPC-d54: DMPG: CHOL (8:2:5 mole ratio) with HFP under static conditions at different temperatures and pH 7.4. The HFP: phospholipids mole ratio is 1:25. The data are fitted by equation $I(2\tau) = I(0) \times \exp(-2\tau/T_2) + A$, where A is the fitting offset.

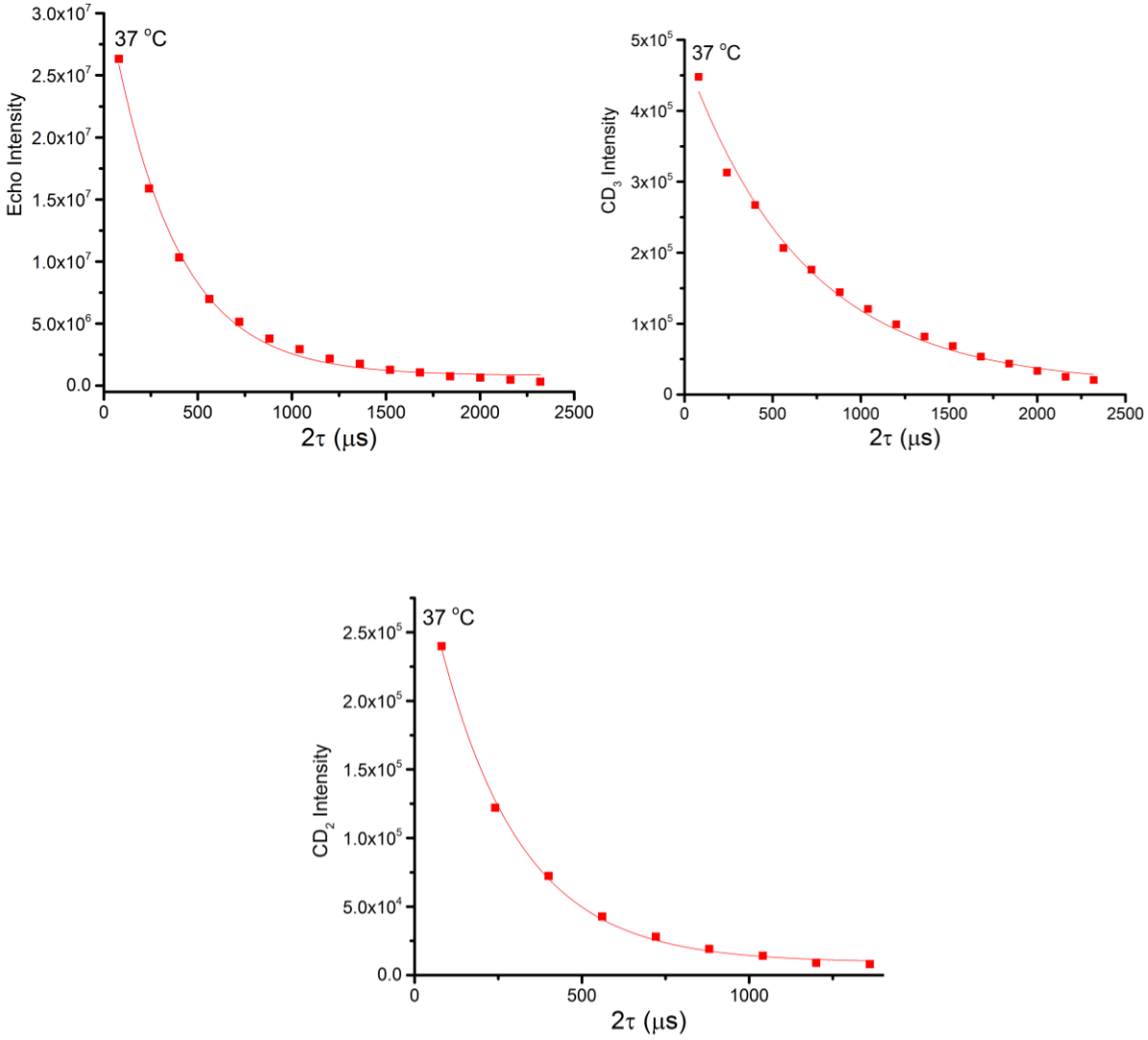

Figure 5.26 Quecho experimental (red squares) and best fit (red lines) plots of DMPC-d54 echo tip intensity of FID, CD_3 and CD_2 peak intensity vs 2τ in membrane of DMPC-d54: DMPG: CHOL (8:2:5 mole ratio) with HFP under static conditions at 37 °C and pH 7.4. The HFP: phospholipids mole ratio is 1:100. The data are fitted by equation $I(2\tau) = I(0) \times \exp(-2\tau/T_2) + A$, where A is the fitting offset.

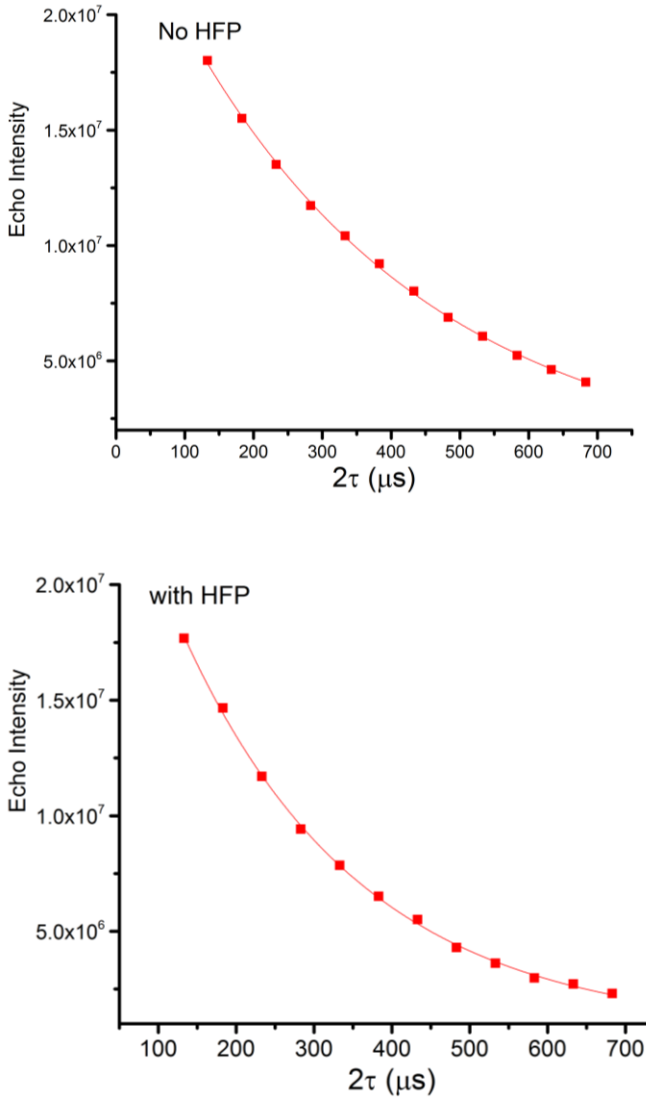

Figure 5.27 Quecho experimental (red squares) and best fit (red lines) plots of Chol_d6 FID echo tip intensity vs 2τ in membrane of DMPC: DMPG: Chol_d6 (8:2:5 mole ratio) with and without HFP under static conditions at 37 °C and pH 7.4. The HFP: phospholipids mole ratio is 1:50. The data are fitted by equation $I(2\tau) = I(0) \times \exp(-2\tau/T_2) + A$, where A is the fitting offset.

Table 5.1 The HFP effects on DMPC-d54 best-fit ^2H T_2 (μs) in membrane without and with CHOL by quecho experiments. The fitting errors are in parenthesis.

Temperature (°C)	d54pg	HFP/d54pg (1:25)	d54pgChol	HFP/d54pgChol (1:25)	
21	120 (6)	235 (11)	726 (14)	289 (11)	echo
	158 (7)	541 (50)	1255 (53)	710 (24)	CD_3
	NA	247 (5)	519 (16)	265 (6)	CD_2
25	1170 (61)	301 (16)	1153 (56)	273 (9)	echo
	1333 (108)	735 (46)	2060 (147)	663 (36)	CD_3
	1000 (25)	304 (4)	674 (58)	259 (2)	CD_2
30	1206 (61)	327 (18)	1292 (112)	298 (7)	echo
	1465 (119)	685 (42)	1935 (242)	726 (31)	CD_3
	991 (29)	322 (7)	807 (57)	241 (5)	CD_2
37	1140 (36)	302 (26)	1818 (265)	264 (13)	echo
	1206 (114)	715 (63)	2767 (454)	678 (53)	CD_3
	901 (28)	329 (16)	1140 (144)	222 (10)	CD_2

Table 5.2 HFP effects on best-fit ^2H T_2 (μs) of Chol_d6 and DMPC-d54 in membrane with 33% CHOL studied by quecho experiment at 37 °C and pH 7.4. The fitting errors are in parenthesis. The ratio is HFP: phospholipids mole ratio. NA means not applied.

T_2/ μs	dmpcpgChol_d6	HFP/ dmpcpgChol_d6 (1:50)	d54pgChol	HFP/ d54pgChol (1:100)	HFP/ d54pgChol (1:25)
echo	358 (13)	230 (7)	1818 (265)	345 (13)	264 (13)
CD_3	NA	NA	2767 (454)	671 (48)	678 (53)
CD_2	NA	NA	1140 (144)	242 (9)	222 (10)

5.3.2 CHOL motion in POPC/POPG/CHOL membrane without and with HFP

It is interesting to study CHOL motion in POPC/POPG/CHOL membrane system with 33% CHOL because this is a common membrane composition used to study the fusion activity of fusion peptides and proteins of virus such as HIV and Influenza.[14-17] Studies have shown that presence of CHOL can catalyze HFP induced vesicle fusion.[11, 12] We study HFP perturbation on CHOL motion by T_2 and T_1 relaxation. We analyzed T_2 relaxation for both Chol_d6 and Chol_d7, T_1 relaxation for Chol_d7. In membrane with HFP, the HFP: phospholipids mole ratio is ~ 1:50.

5.3.2.1 Transverse relaxation studies of Chol_d6

We studies Chol_d6 T_2 relaxation at 37 °C and pH 7.4. Figure 5.28 shows the stacked plots of FID without and with HFP. We got T_2 by fitting the echo intensity with equation $I(2\tau) = I(0) \times \exp(-2\tau/T_2) + A$, shown in Figure 5.29 and Table 5.3.

Adding HFP reduces T_2 of Chol_d6 fitting from echo intensity. The reduction extent is similar compared to DMPC/DMPG/CHOL membrane system. We investigated the spectrum features at −5°C, 0 °C, 25 °C, 37 °C and 45 °C, shown in figure 5.30. The spectrum becomes broader when the temperature decreases, and this is consistent with less motional averaging of quadrupolar couplings at lower temperature. However, the spectrum is not significantly different at and higher than 0 °C, because the phase transition temperature of POPC and POPG is −2 °C. However, the spectrum at −5 °C has much worse signal/noise ratio compared to spectrum taken at 37 °C with similar number of scans. This is due to less motion at the temperature below the phase transition temperature of the membrane.

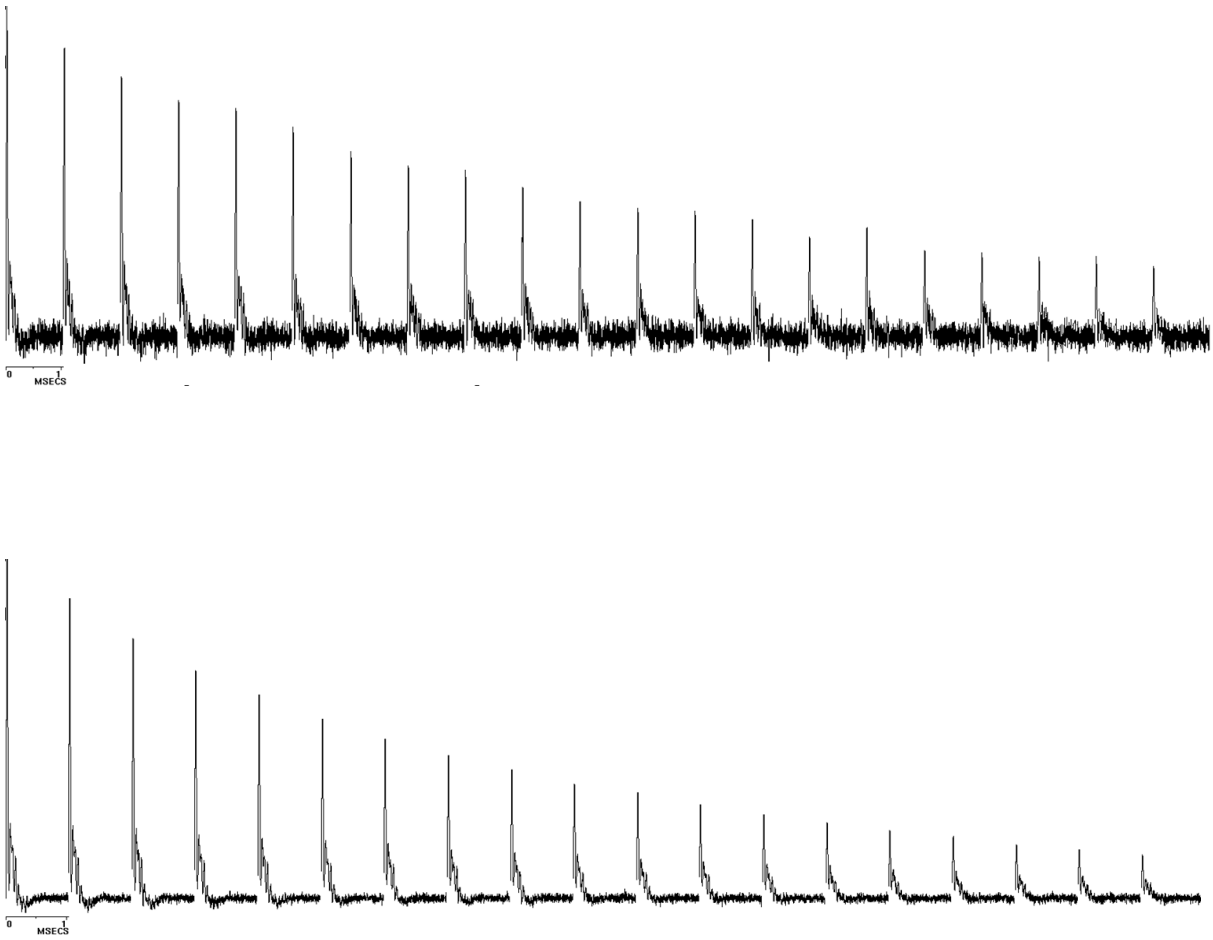

Figure 5.28 Stacked spectrum plots Chol_d6 in membrane of POPC: POPG: Chol_d6 (8:2:5) without (top) and with (bottom) HFP at 37°C and pH 7.4 in static. The ^{2}H spectra were obtained by varying τ and τ_1. The top spectra were arrayed to τ = 330 and τ_1 = 311 μs, and the bottom spectra were arrayed to τ = 300 and τ_1 = 281 μs. For each τ and τ_1, the number of scans was 4000. (File location: mb4b…./102416, Chold6popcpg_withHFP_102716 on mb4b)

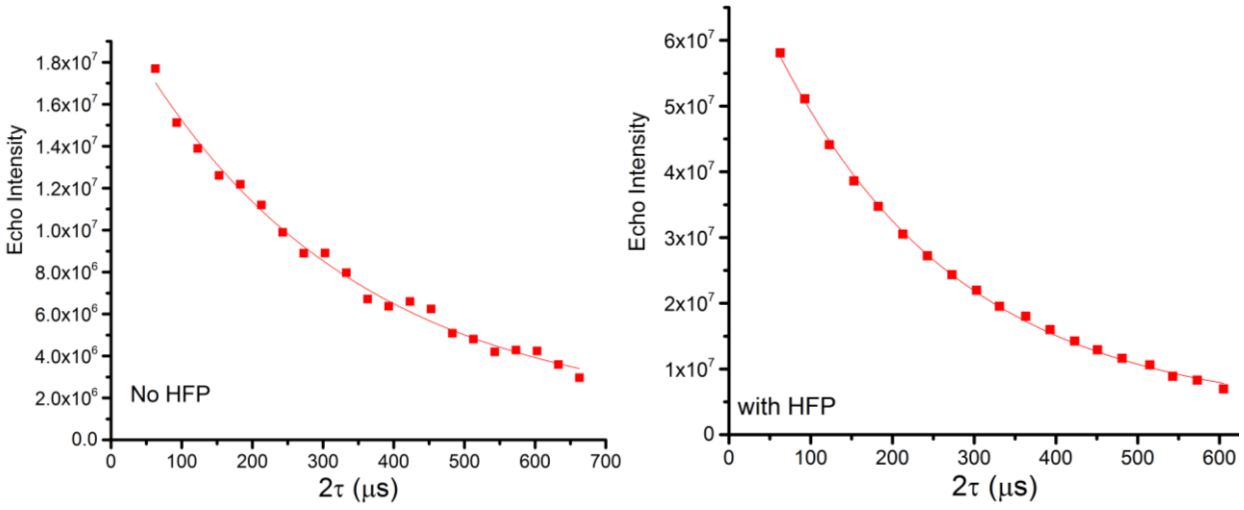

Figure 5.29 Quecho experimental (red squares) and best fit (red lines) plots of Chol_d6 FID echo tip intensity vs 2τ in membrane of POPC: POPG: Chol_d6 (8:2:5 mole ratio) with and without HFP under static conditions at 37 °C and pH 7.4. The HFP: phospholipids mole ratio is 1:50. The data are fitted by equation $I(2\tau) = I(0) \times \exp(-2\tau/T_2) + A$, where A is the fitting offset. (File location: mb4b…./102416, Chold6popcpg_withHFP_102716 on mb4b)

Table 5.3 HFP effects on best-fit Chol_d6 ^{2}H T_2 (μs) of in POPC: POPG membrane with 33% Chol_d6 studied by quecho experiment at 37 °C and pH 7.4. The fitting errors are in parenthesis. We got the best fit T_2 by fitting the echo intensity. The ratio is HFP: phospholipids mole ratio.

T_2/μs	No HFP	with HFP: phospholipids (1:50)
echo	312 (28)	224 (6)

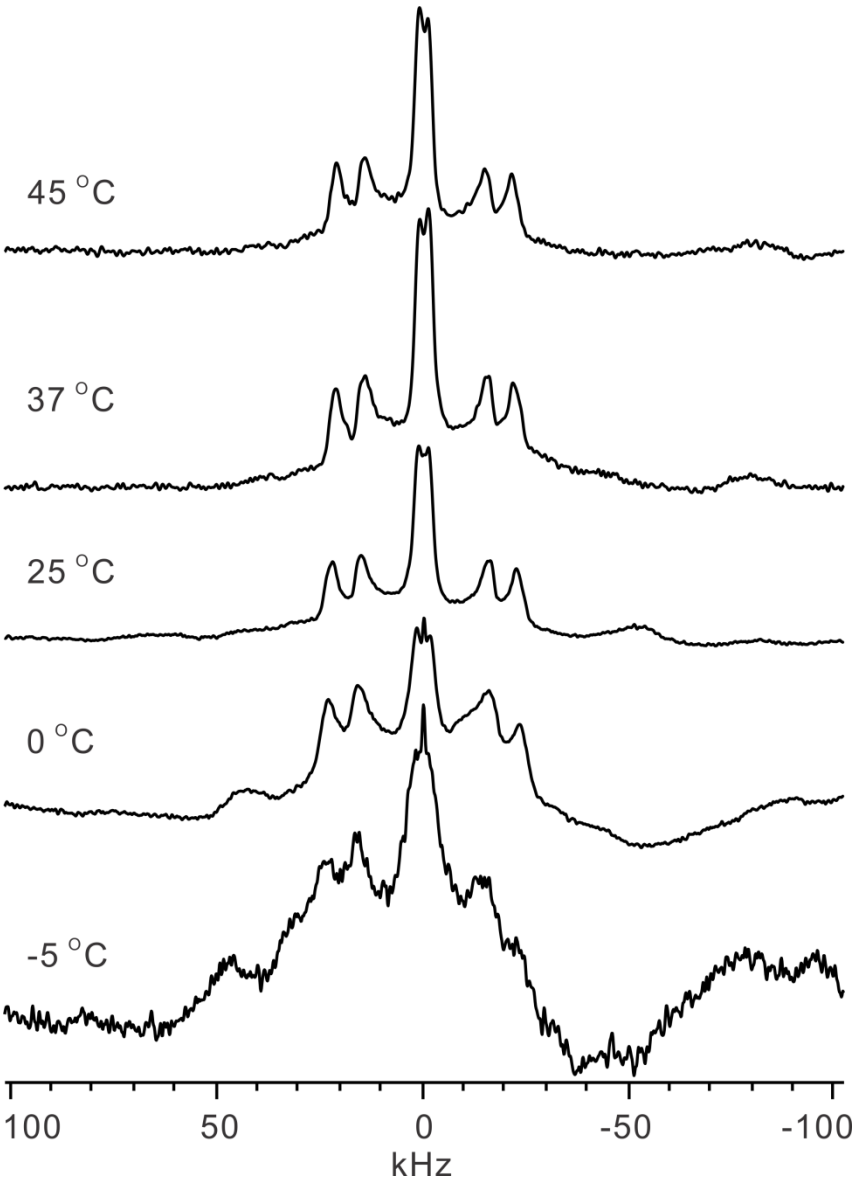

Figure 5.30 Stacked spectrum plots Chol_d6 in membrane of POPC: POPG: Chol_d6 (8:2:5) with HFP at different temperatures and pH 7.4 in static. The ^{2}H spectra were obtained by varying τ and τ_1. We processed the spectra with data shift, DC offset, 500 Hz Gaussian line broadening, and baseline correction of the order 5. The number of scans was typically 10000. It is 35000 for 25 °C and 80000 for 0 °C.

5.3.2.2 Transverse relaxation studies of Chol_d7

To evaluate the effect of HFP on the CHOL hydrocarbon tail motion, we investigated the transverse relaxation (T_2) at different temperatures: - 50°C, 5°C, 25°C, 37°C and 45°C. We fit the peak intensity of CD_3 ($I_{2\tau}$) to get best fit T_2. The fitting equation is $\ln(I_{2\tau}) = \ln I_0 - \frac{2\tau}{T_2}$, where $\ln I_0$ and T_2 are the fitting parameters and $2\tau = \tau + \tau 1+$ data shift points × dwell time. Figure 5.31 and 5.32 display stack plots of processed spectra without and with HFP at - 50°C and 37 °C, respectively. Figures 5.33 to 5.35 show the fitting plots at different temperatures without and with HFP. Table 5.4 displays the best-fit T_2 values. The T_2 values at - 50°C are much smaller in membrane both without and with HFP compared to the other higher temperatures studied. This is due to less motion at the temperature below the PC phase transition temperature (−2 °C). At - 50°C, presence of HFP increases T_2, which suggests that presence of HFP increases the CHOL tail motion. However, at and above 5 °C, there is similar T_2 at different temperatures for the same sample, and similar T_2 without and with HFP, which suggests that HFP does not affect the CHOL tail motion at the temperature above the POPC phase transition temperature.

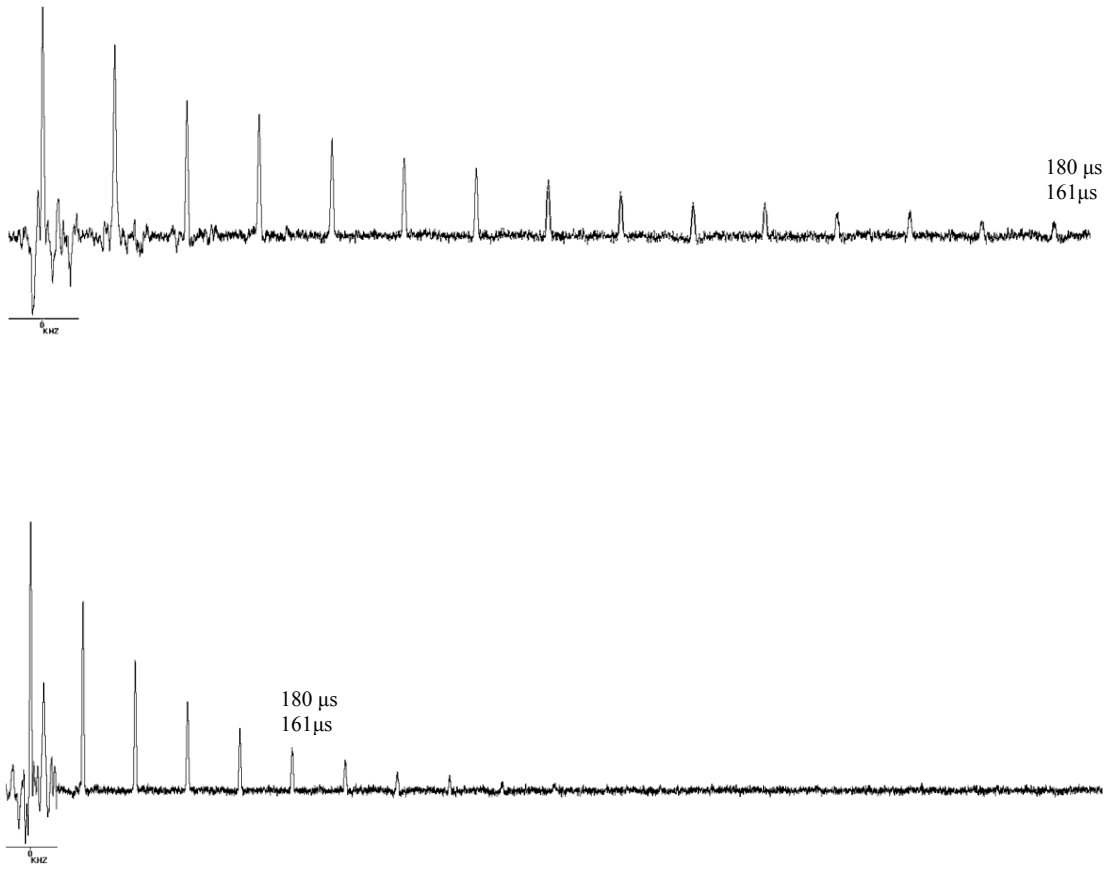

Figure 5.31 Stacked spectrum plots Chol_d7 in membrane of POPC: POPG: Chol_d7 (8:2:5) without and with HFP at -50°C and pH 7.4 in static. HFP to phospholipids ratio is 1:50. The ^{2}H spectra were obtained by varying τ and τ_1. For each τ and τ_1, the number of scans was 2000 (top) and 800 (bottom). We processed the data with -10 data shift pts, 2000 Hz Gaussian line broadening and polynomial baseline correction of the order 5.

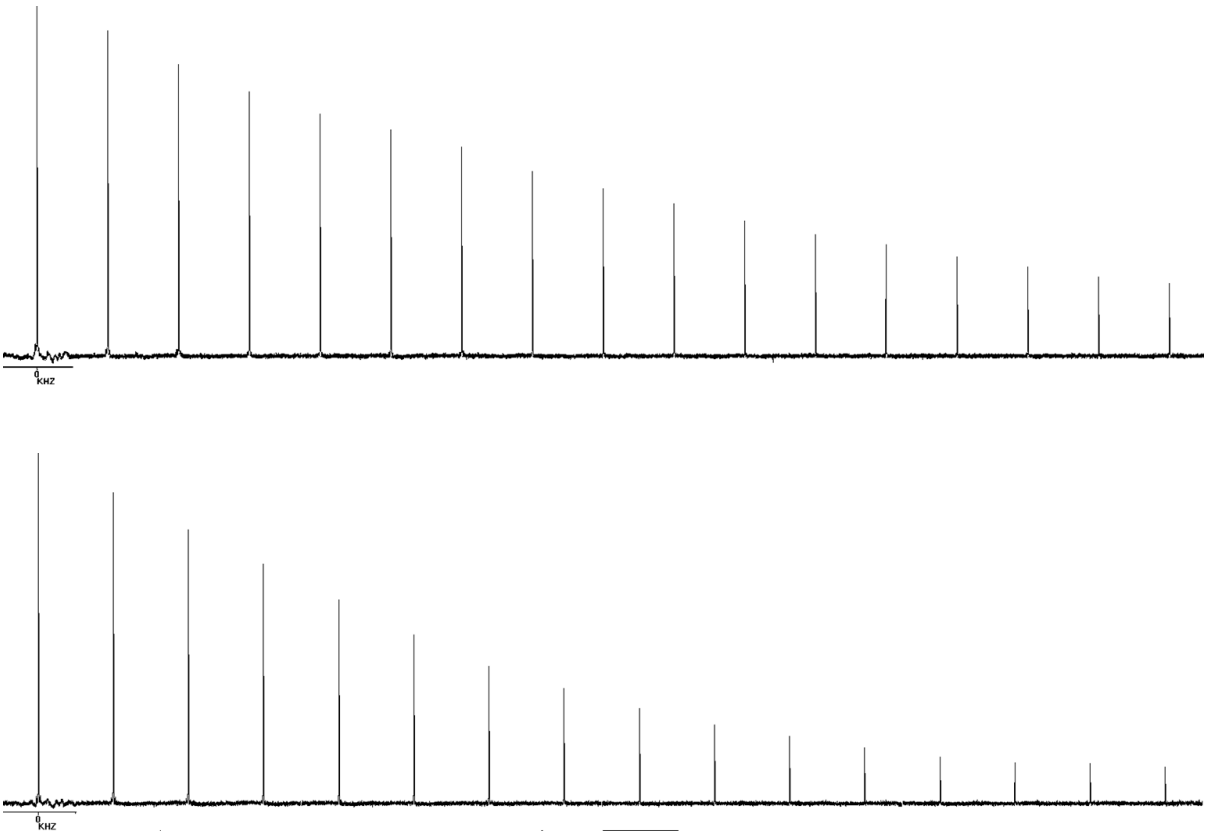

Figure 5.32 Stacked spectrum plots Chol_d7 in membrane of POPC: POPG: Chol_d7 (8:2:5) without and with HFP at 37°C and pH 7.4 in static. HFP to phospholipids ratio is 1:50. We acquired the ^{2}H spectra by varying τ and τ_1. We arrayed τ and τ_1 to 1000 and 975 μs (top), 1540 and 1521 μs (bottom). For each τ and τ_1, the number of scans was 800. We processed the data with -11 data shift pts, 500 Hz Gaussian line broadening and polynomial baseline correction of the order 5.

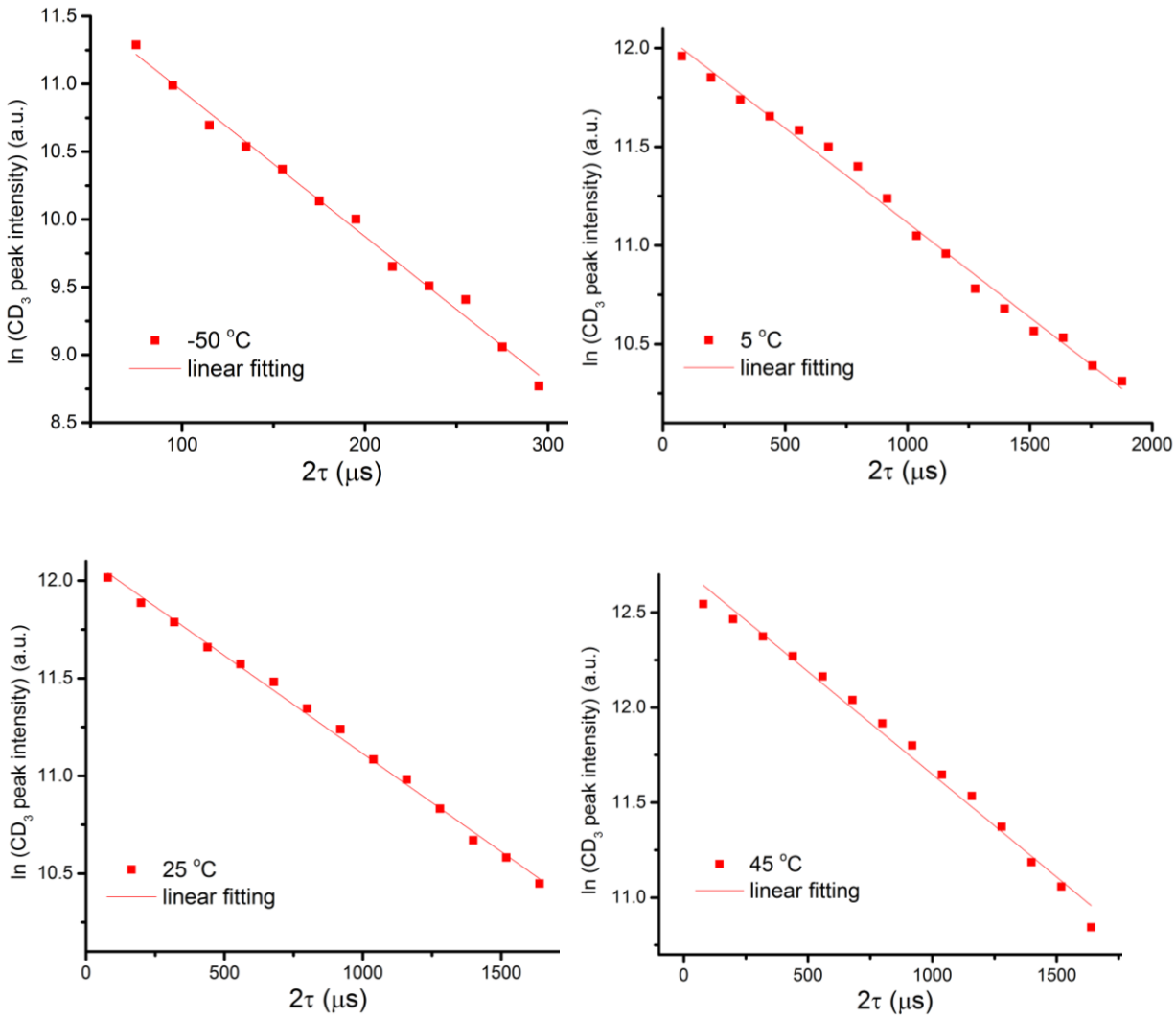

Figure 5.33 Fitting plots of Chol_d7 ln (CD_3 peak intensity) from membrane of POPC: POPG: Chol_d7 (8:2:5) without HFP at different temperatures and pH 7.4. We acquired the data in static condition.

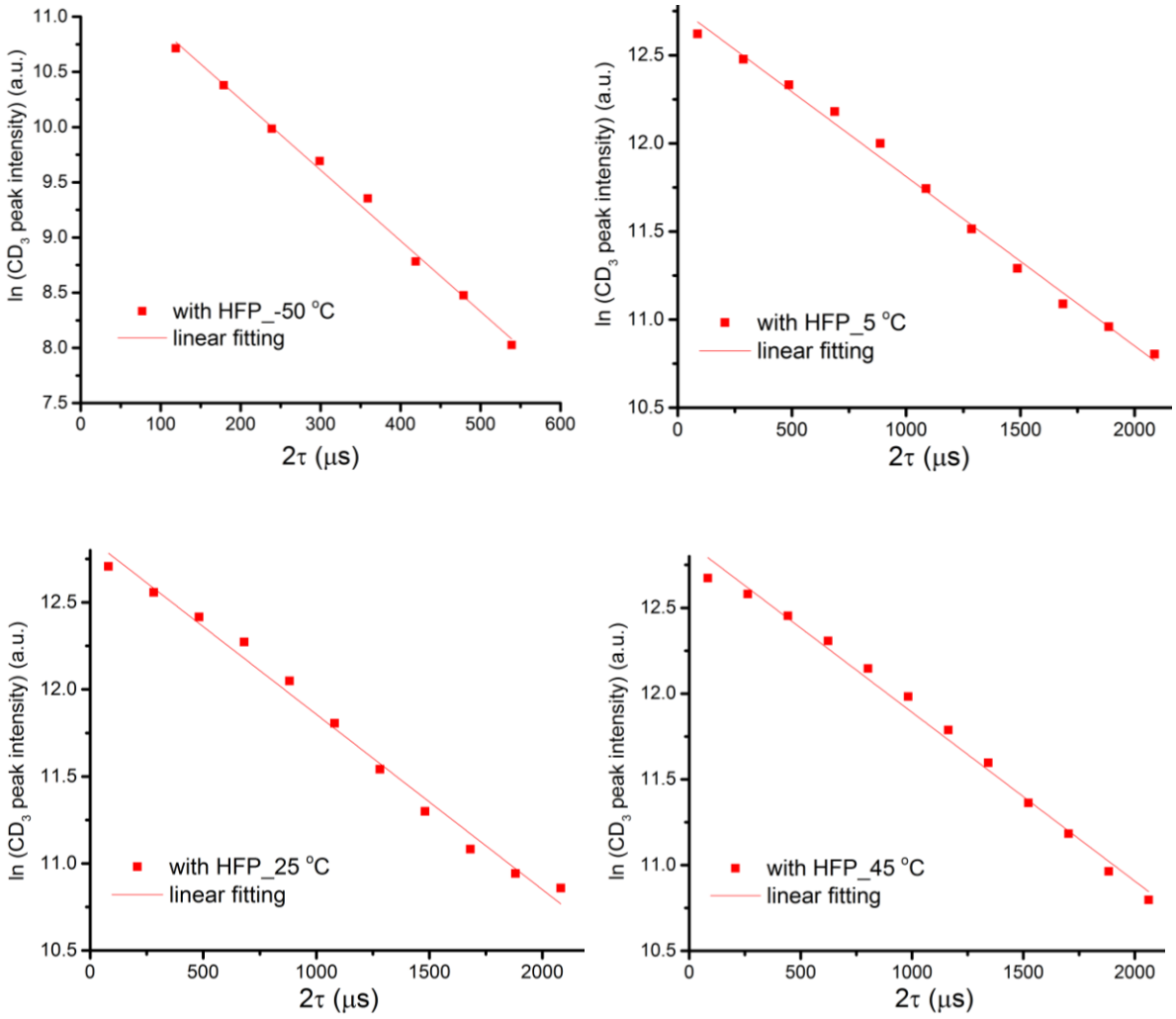

Figure 5.34 Fitting plots of Chol_d7 ln (CD_3 peak intensity) from membrane of POPC: POPG: Chol_d7 (8:2:5) with HFP at different temperatures and pH 7.4 in static.

(a) no HFP (b) with HFP

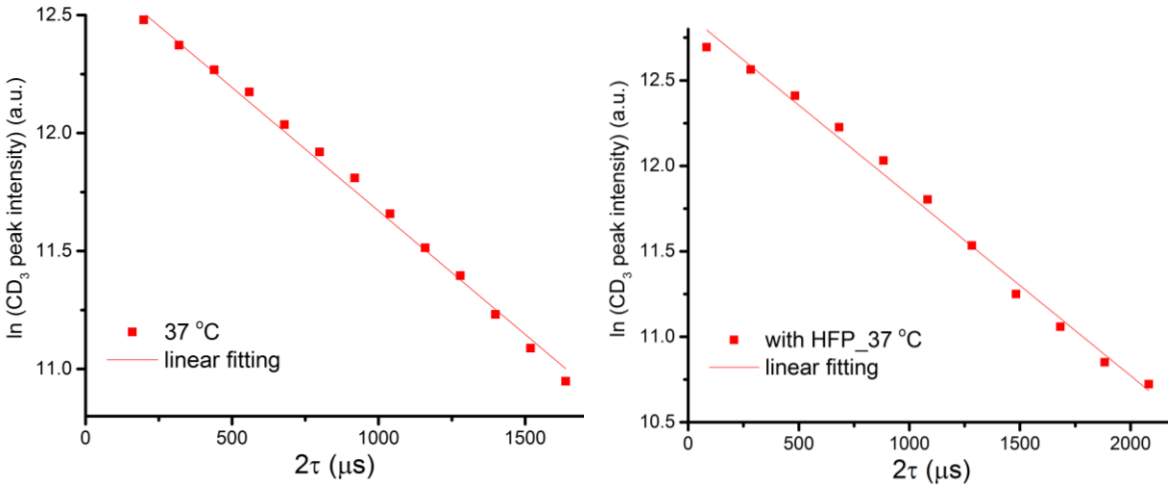

Figure 5.35 Fitting plots of Chol_d7 ln (CD_3 peak intensity) from membrane of POPC: POPG: Chol_d7 (8:2:5) without HFP (a) and with HFP (b) at 37 °C and pH 7.4 in static.

Table 5.4 Best-fit Chol_d7 ^2H T_2 (μs) values at different temperatures without and with HFP, uncertainties are in parenthesis. T_2 was fitted with ln (CD_3 peak intensity) vs 2τ.

Temperature (°C)	T_2	T_2 (with HFP)
−50	93(2)	157(4)
5	1043(25)	1040(26)
25	1000(17)	990(30)
37	952(22)	943(26)
45	926(28)	1016 (30)

5.3.2.3 Spin lattice relaxation studies of Chol_d7

To evaluate the effect of HFP on the CHOL hydrocarbon tail motion, we investigated the spin lattice relaxation (T_1) for Chol_d7 at different temperatures: - 50°C, 5°C, 25°C, 37°C and 45°C. The sample is POPC/POPG/Chol_d7 without and with HFP. Chol_d7 composition is 33%, and HFP: phospholipids ratio is ~ 1:50. The Chol_d7 T_1 is studied in static and pH 7.4 by t1D_ir pulsed sequence, which is inversion-recovery followed by quecho. The pulse sequence is π – τ1– (π/2)x – τ2 – (π/2)y – τ3 – acquisition, shown in Figure 5.36. The data is acquired by arraying τ1 and τ2 and τ3 are fixed at 50 μs. For each τ1 within the array, the number of acquisition is the

same and is typically 3000 scans. We processed the data with Gaussian line broadening, data shift and polynomial baseline correction. Figure 5.37 and 5.38 display representative FID and stacked plots of processed spectra for Chol_d7 without and with HFP, respectively. Chol_d7 spectrum has two pairs of horns (Pake doublet), one pair has bigger intensity with ~ 1.6 kHz peak splitting corresponding to the six CD_3 deuterons, and the other pair has much smaller intensity with ~ 26 kHz peak splitting corresponding to the CD deuteron present in Chol_d7. Chol_d7 T_1 is typically from the CD_3 peak intensity fitting. At - 50°C in pure membrane, the sample temperature is ~ - 30°C, the peaks are broader, and the CD_3 peak two horns are not resolved due to less motional averaging of quadrupolar anisotropy at lower temperature. Therefore, the integrated peak intensity is used, and the integration is with 300-ppm integration width centered at the peak center. The peak intensity is fitted vs τ1 by the equation:

$$I(\tau 1) = I_0 + \Delta I \times (1 - \exp(-\frac{\tau 1}{T_1})) \qquad 5.2$$

Where I(τ1) is the experimental peak intensity, I_0, ΔI and T_1 are fitting parameters. I_0 is I (τ1=0), ΔI = I (τ1→∞) – I (τ1=0). Figures 5.39 to 5.41 show the best-fit plots. Table 5.4 show best-fit T_1 values. At and above 5 °C, presence of HFP does not affect Chol_d7 T_1. T_1 is slightly shorter with HFP at - 50°C.

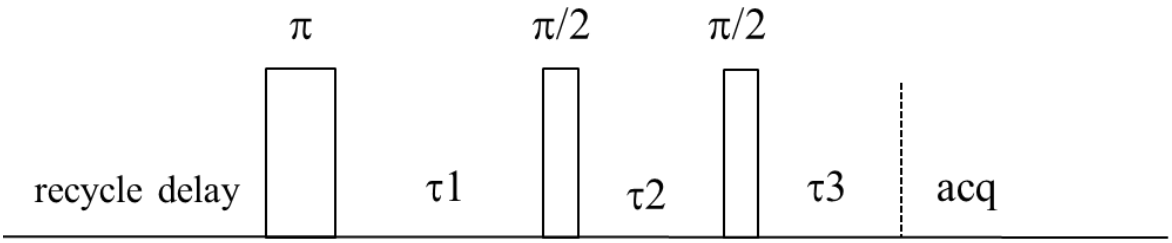

Figure 5.36 "t1D_ir" pulse sequence for T_1 relaxation study.

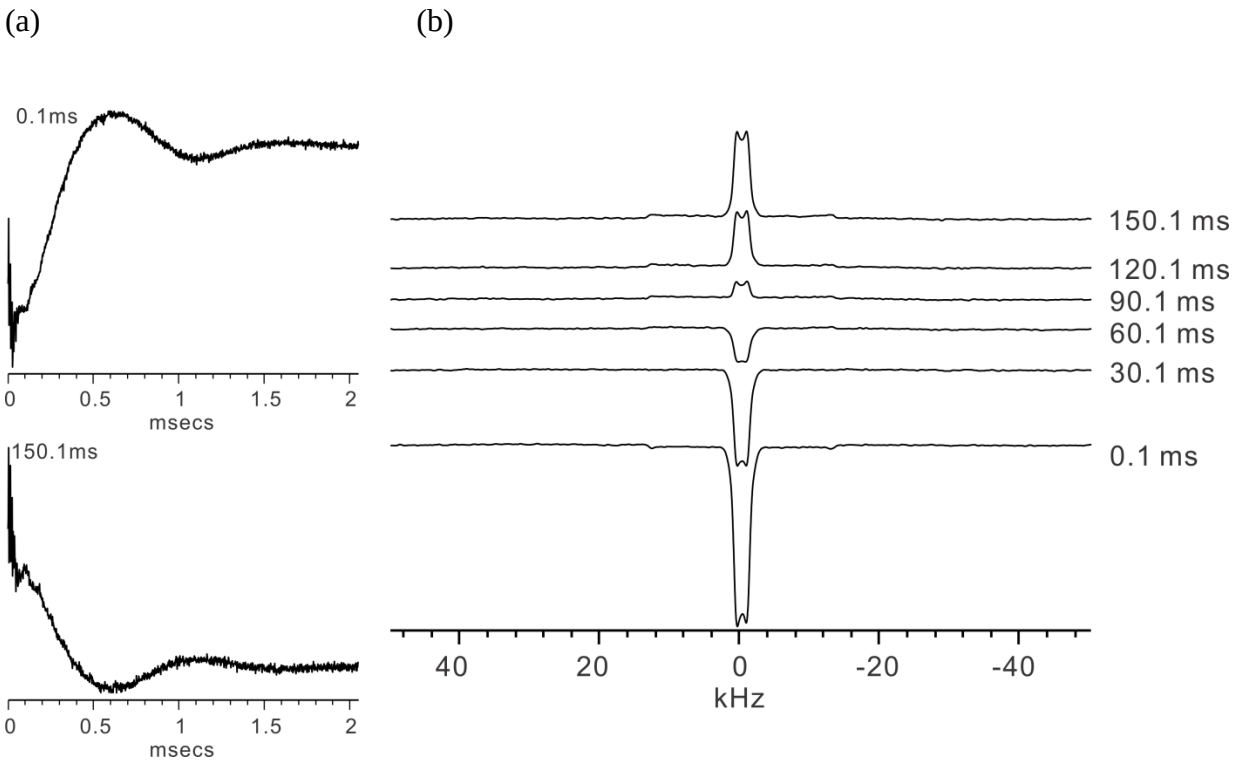

Figure 5.37 "t1D_ir" experimental (red squares) of Chol_d7 from membrane of POPC: POPG: Chol_d7 (8:2:5) without HFP at 37 °C and pH 7.4 in static. The number of scans is 3000 for each τ1. (a) ^{2}H FID for τ1 = 0.1 and 150.1ms, (b) Chol_d7 ^{2}H spectra for τ1 = 0.1 through 150.1ms. We did not show spectra for τ1 = 180.1 through 510.1ms for view simplicity. All Spectra are processed with 500 Hz Gaussian line broadening, -7 data shift points, and polynomial baseline correction of order 5.

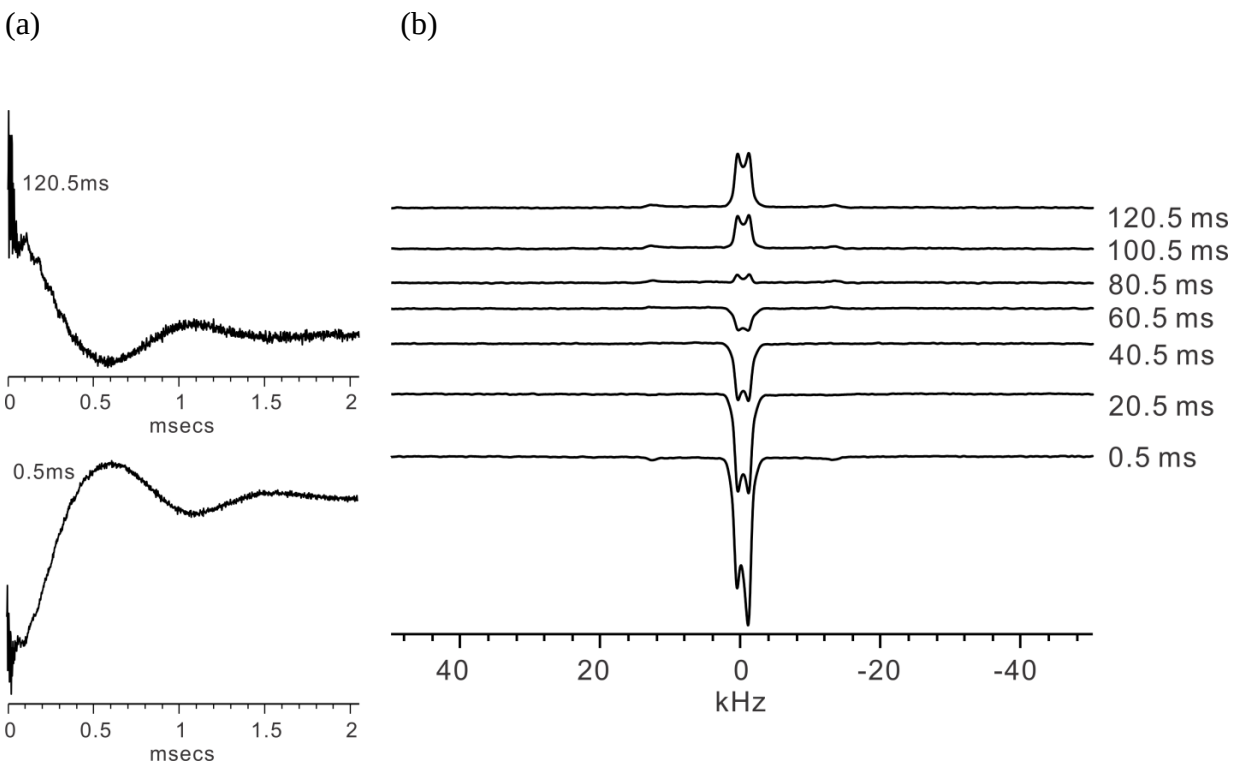

Figure 5.38 "t1D_ir" experimental (red squares) of Chol_d7 from membrane of POPC: POPG: Chol_d7 (8:2:5) with HFP at 37 °C and pH 7.4 in static. The HFP to phospholipids mole ratio is 1:50. The number of scans is 3000 for each τ1. (a) ^{2}H FID for τ1 = 0.5 and 120.5ms, (b) Chol_d7 ^{2}H spectra for τ1 = 0.5 through 120.5ms. We did not show spectra for τ1 = 140.5 through 340.5ms for view simplicity. We processed the spectra with 500 Hz Gaussian line broadening, data shift of -12, and polynomial baseline correction of order 5.

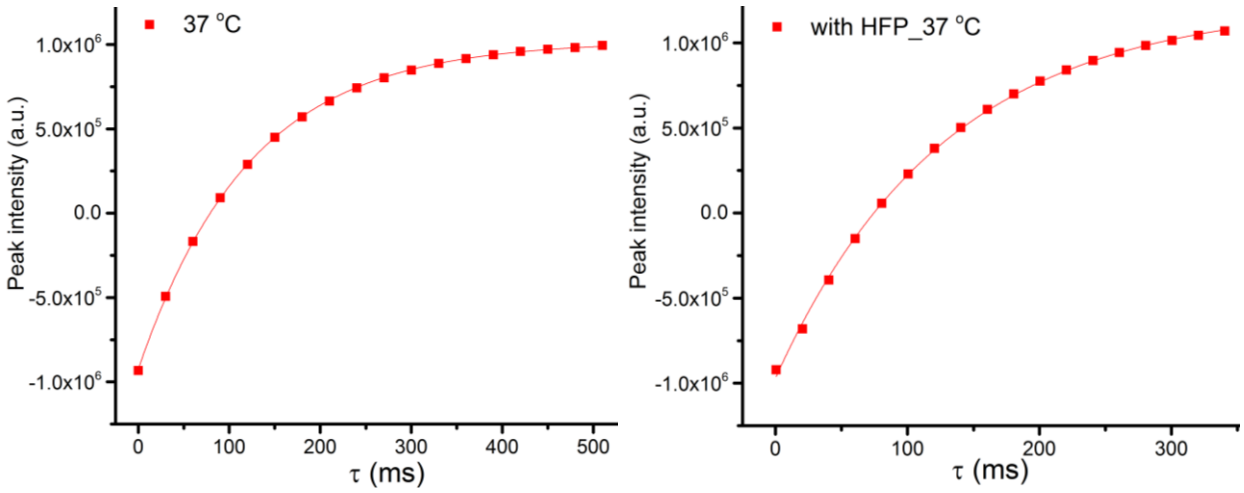

Figure 5.39 "t1D_ir" experimental (red squares) and best fit (red line) of Chol_d7 CD_3 peak intensity vs τ1 from membrane of POPC: POPG: Chol_d7 (8:2:5) without and with HFP at 37 °C and pH 7.4 in static. HFP: phospholipids mole ratio is 1:50.

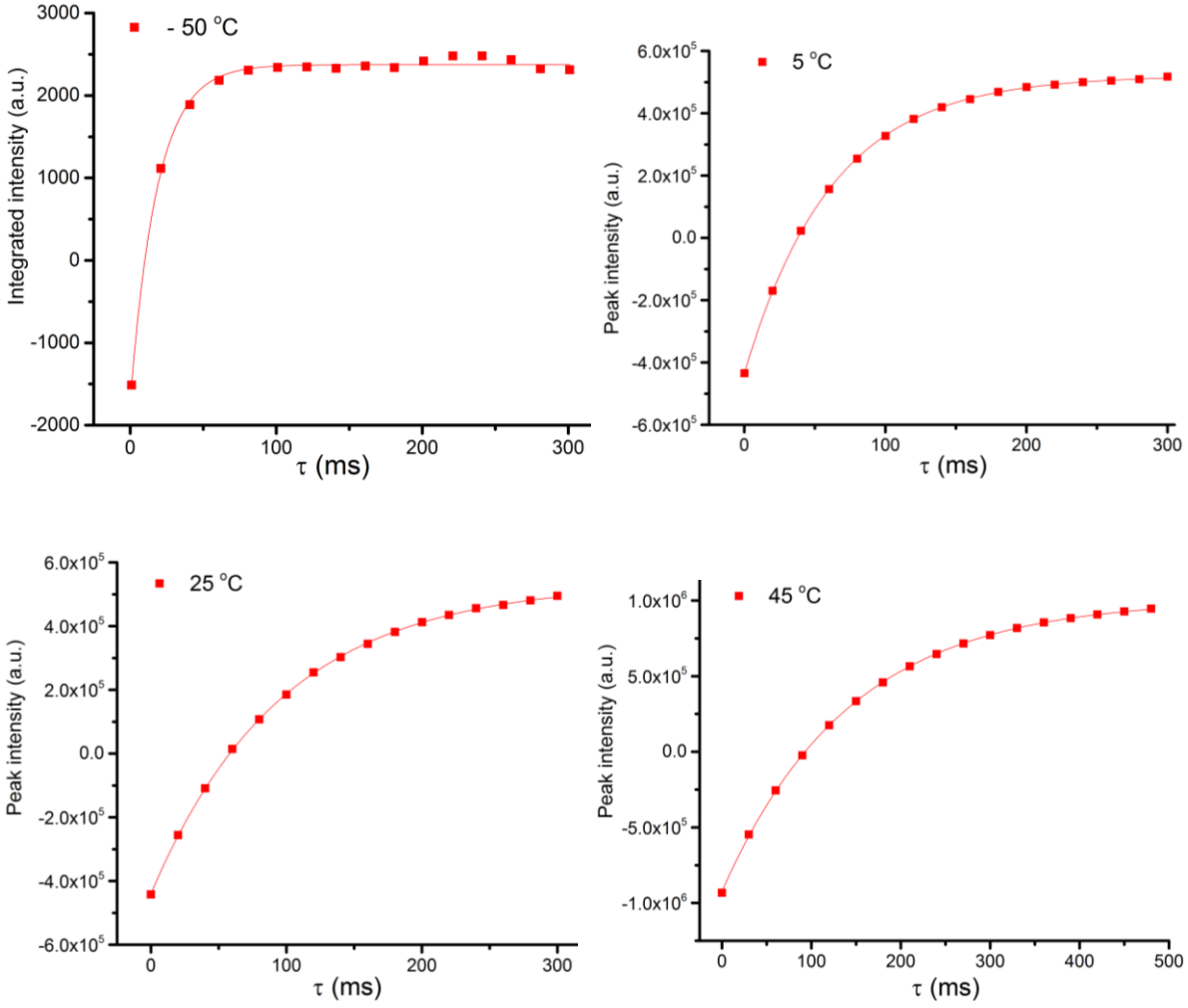

Figure 5.40 "t1D_ir" experimental (red squares) and best fit (red line) of Chol_d7 CD_3 peak intensity vs τ1 from membrane of POPC: POPG: Chol_d7 (8:2:5) without HFP at different temperatures and pH 7.4 in static.

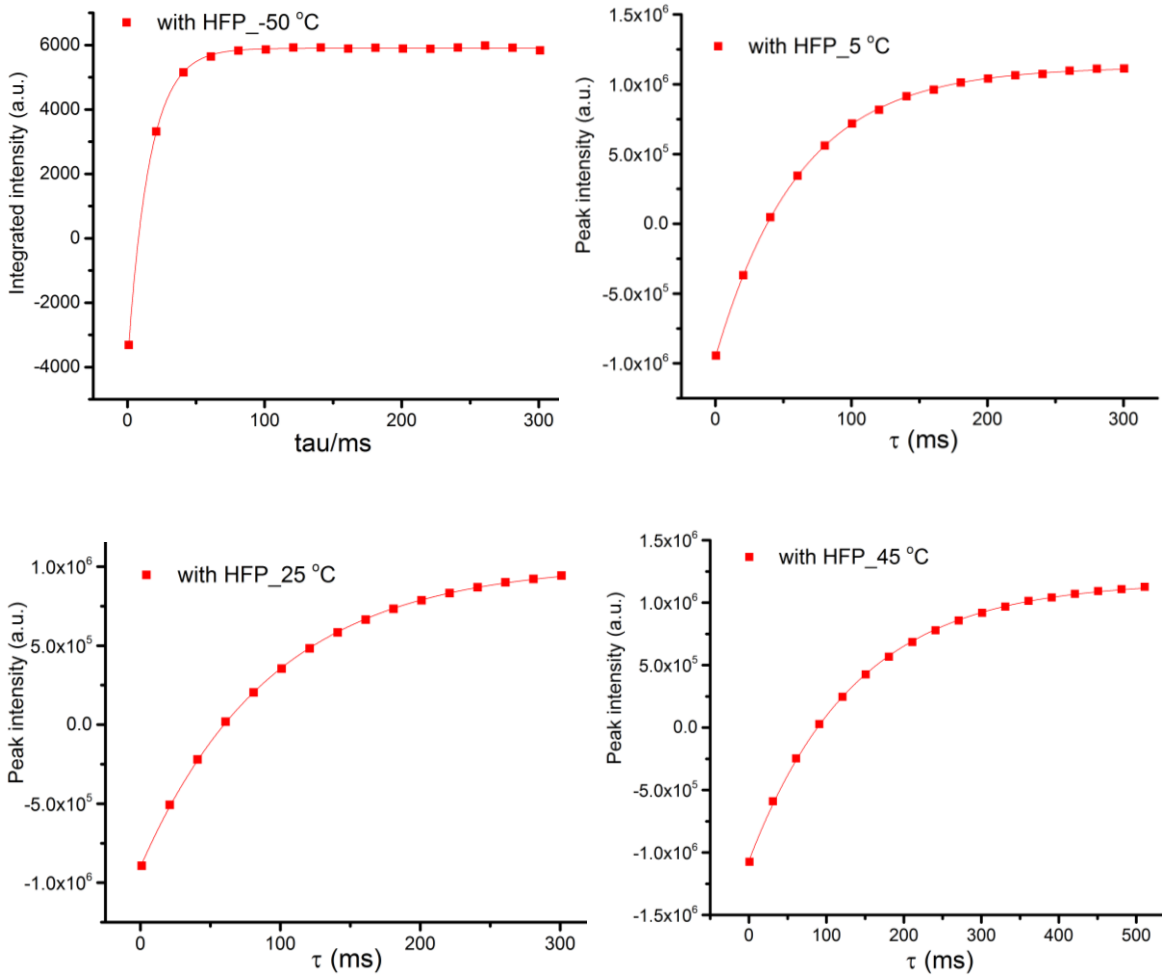

Figure 5.41 "t1D_ir" experimental (red squares) and best fit (red line) of Chol_d7 CD_3 peak intensity vs τ1 from membrane of POPC: POPG: Chol_d7 (8:2:5) with HFP at different temperatures and pH 7.4 in static. HFP: phospholipids mole ratio is 1:50.

Table 5.5 Best-fit Chol_d7 CD_3 T_1 (ms) values at different temperatures, uncertainties are in parenthesis. T_1 was fitted with the CD_3 peak intensity vs τ1.

Temperature (°C)	T_1/ms	T_1 (with HFP)/ms
−50	18.4(7)	15.8(2)
5	62(1)	62(1)
25	97(1)	94(1)
37	122 (1)	128(3)
45	143(1)	137(1)

5.4 Discussion

The static quecho experiments studied in this chapter is majorly to investigate the membrane motions including PC and CHOL perturbed by HFP. Our earlier REDOR results have shown that HFP has preferential contact to CHOL vs PC when associated with membrane at several residue sites along the peptide chain. Specifically, that is G5 and G10 residues inserted deeply into the membrane center has preferential contact to Chol_d7 terminal deuterons than PC_d10 terminal deuterons near the membrane center, and G16 has preferential contact to Chol_d6 deuterons than PC_d4 deuterons near the membrane surface. However, there is little information about how

CHOL catalyze HFP induced membrane fusion. To help understand this, we investigate how HFP perturbs membrane motion in membrane both without and with CHOL in this study by ^{2}H - NMR.

5.4.1 HFP disrupts lipid acyl chain packing in membrane both without and with CHOL

To study the CHOL effect on HFP-membrane interaction, we used DMPC-d54 with per-deuterated acyl chain. We added anionic lipid to reflect the negatively charged membrane of HIV host cell. To investigate the effect of HFP on membrane motion, we studied membrane both without and with CHOL. In membrane with CHOL, 33% CHOL represents the typical CHOL composition in HIV host cell membrane. For all the ^{2}H spectra at different temperatures and different membrane composition, the overall spectrum shape is similar without and with HFP, which suggests that the anionic membrane remains lamellar membrane phase in addition of HFP regardless of CHOL. Instead of powder pattern spectrum, a narrow (~ 200Hz FWHM) isotropic deuteron peak is likely corresponding to formation of isotropic, non-lamellar lipid phase.[18, 19] In membrane without CHOL, the spectrum individual peaks become broader and less resolved in presence of HFP, and there is ~ 0.75 kHz line broadening due to shorter T_2 with 4% HFP. In membrane without CHOL, at 21 °C, the broad spectrum indicates that the membrane is in gel phase. However, the static spectrum becomes much narrower with sharp peaks similar to the spectrum at higher temperature when the membrane is in liquid disordered phase. These results indicate that HFP lowers the DMPC-d54 phase transition temperature in anionic membrane without CHOL because the phase transition temperature of DMPC-d54 is 23 °C. Similar effect has been observed for Influenza peptide at pH 5.0.[20] In membrane with 33% CHOL, the spectrum feature at 37 °C is similar with earlier studied of HFP in LM3 membrane at 35 °C by Jun Yang and Charles GABRYS. Adding HFP makes individual peaks broader and less resolved,

and there is ~ 0.90 kHz line broadening due to shorter T_2 with 4% HFP. However, the peak splitting is ~ 10% smaller for CD_3 peak, and ~ 3% smaller for the CD_2 peak in presence of 1% HFP, while the peak splitting is ~ 15% bigger for CD_3, and ~ 20% bigger for CD_2 in presence of 4% HFP. In membrane without CHOL, the peak splitting is ~ 10% smaller for CD_3 peak and almost the same for CD_2 peak in presence of 4% HFP. The results with 4% HFP in the membrane without and with CHOL suggest a role of CHOL in membrane fusion. CHOL restricts fast motion of PC because the spectrum is broader with CHOL. HFP slightly increases fast motion of lipids in membrane without CHOL, but restrict the fast motions of lipids with CHOL.

Table 5.6 Peak splitting for CD_3 and CD_2 of DMPC-d54 powder pattern spectrum at 37 °C

Membrane	CD_3 peak splitting /kHz	CD_2 peak splitting /kHz	HFP amount
d54pg	3.23	25.68	0%
	2.89 (10 % ↓)	25.66 (0 %)	4%
d54pgCHOL	5.71	37.29	0%
	5.07 (10% ↓)	36.16 (3% ↓)	1%
	6.58 (15% ↑)	44.70 (20% ↑)	4%

De-Pake-ing the data gives better-resolved spectra. Figures 5.10 to 5.12 show the de-Paked spectra. The peaks with the smallest and biggest $\Delta\nu_Q$ comes from the terminal CD_3 deuterons near the membrane center and CD_2 deuterons near the membrane surface, respectively. The largest $\Delta\nu_Q$ peak corresponds to deuterons from C2 to C5. Other well-resolved peaks are from deuterons attached from C6 to C13, with smaller $\Delta\nu_Q$ coming from carbon positions closer to the membrane center. There are similar trends of $\Delta\nu_Q$ for middle deuterons.

In membrane without CHOL, HFP decreases acyl chain order of lipid by ~ 1-10% with 4% HFP. However, HFP increases acyl chain order of lipid by ~ 20-30% in membrane with CHOL with 4%

HFP (figure 5.14). The opposite effect of HFP on membrane lipid acyl chain ordering is because CHOL can help regulate the membrane ordering.[21] Adding HFP perturbs the local membrane packing, CHOL is a smaller molecule relative to phospholipids, and able to pack well to the void space between HFP and nearby lipid molecule, and thus restricts the motion of lipids and increase acyl chain order parameter of lipid. From these results, CHOL probably catalyze membrane fusion by stabilizing the high-energy membrane intermediate states and thus lowering the energy barrier to achieve the membrane fusion intermediate states. While in membrane without CHOL, HFP perturbs membrane packing, the less than 10% of lipid acyl chain disordering is probably due to the local lipids nearby HFP. From the order parameter profile of lipid acyl chain, HFP affects order parameter down to the membrane center independent of CHOL, which is consistent with the earlier major deeply inserted HFP membrane location model in membrane both without and with CHOL. The deeply inserted membrane location is responsible for fusion.

In membrane with 33% CHOL, HFP perturbs DMPC-d54 acyl chain order dependent on HFP concentrations. Specifically, with 1% and 4% HFP, lipid acyl chain order decreases and increases, respectively. Figure 5.13 and figure 5.14 shows the order parameter and order parameter change induced by HFP. In presence of 1% HFP, HFP increases membrane disorder along the whole acyl chain, and with greater disordering extent toward the membrane center. In presence of 4% HFP, HFP increases membrane order also along the whole lipid acyl chain, and with bigger ordering extent from middle of acyl chain toward the membrane center. Both 1% and 4% HFP affect lipid acyl chain packing down to the lipid tail at the membrane center.

5.4.2 Transverse relaxation studies of PC and CHOL

To study the effect of HFP on lipid transverse relaxation (T_2), we used DMPC-d54 in anionic membrane both without and with 33% CHOL. Except in membrane without HFP at 21 °C, adding HFP generally decreases PC T_2 ~ 68 % independent of CHOL fitted from echo, CD_3 and CD_2 intensity. In membrane without HFP at 21°C, adding HFP increased PC T_2 fitted from echo, CD_3 and CD_2 intensity while CD_2 T_2 is not determined in membrane without HFP because the intensity is too weak and decays too fast due to broad CD_2 spectrum in gel phase. T_2 at and above 25 °C is similar for the same sample. We also compared the PC T_2 with different concentrations of HFP. For 1% and 4% HFP, T_2 fitted form echo intensity is ~ 23% smaller or the T_2 relaxation rate is ~ 23% faster with 4% HFP relative to with 1% HFP. However, T_2 fitted from CD_3 and CD_2 peak intensity is similar. These results suggest that the T_2 effect of HFP on CD_3 and CD_2 effect is the same with smaller and larger quantities of HFP, while larger quantities of HFP has bigger T_2 decrease on other CD_2s along the acyl chain other than the terminal CD_2s (C2-C5). To investigate the effect of HFP on CHOL transverse relaxation (T_2), where both Chol_d6 and Chol_d7 where the deuterons are located near the membrane surface and membrane center, respectively. In membrane with 33% CHOL at 37 °C, the Chol_d6 T_2 is similar in DMPC and POPC membranes fitted from echo intensity. In DMPC membrane, T_2 is 358 (13) and 230 (7) for without and with HFP respectively. In POPC membrane, T_2 is 312 (28) and 224 (6) for without and with HFP respectively. The T_2 decreases or the T_2 relaxation rate increases ~ 35% and ~ 28% in DMPC and POPC membrane, respectively. We studied the T_2 of Chol_d7 with POPC in anionic membrane with 33% CHOL, which is the most common membrane composition for vesicle fusion study of viral fusion peptides and proteins. At - 50°C, the T_2 increases in presence of 2% HFP. At temperature above and including 5 °C, the T_2 is similar

without and with HFP, and is similar for the same sample regardless of temperature increasing. These results suggest that the effect of HFP on Chol_d7 motion change is negligible on the time scale of ~ 10^{-4} s.

T_2 for DMPC-d54 and Chol_d6 decrease probably because the membrane curvature changes by presence of HFP when it interacts with the membrane. With greater membrane curvature, the C-D bond will experience more orientation diversity relative to the external magnetic field. Thus, the quadrupolar field will have greater change, leading to faster relaxation and shorter T_2. T_2 increases for DMPC-d54 in gel phase anionic membrane without CHOL and Chol_d7 in POPC anionic membrane in presence of HFP, which is because HFP increases nearby C-D bond axial rotation and the increased motion leads to the observed longer T_2. However, the fast axial CD_3 bond rotation and longitudinal diffusion induced by increased temperature overcomes the effect induced by HFP, so the T_2 is similar without and with HFP.

Interestingly, the T_2 for DMPC-d54 decreases independent of CHOL, which suggests that HFP induce membrane curvature independent of CHOL and helps explain HFP induce fusion in membrane both without and with HFP.[11] The T_2 decreases or the T_2 relaxation rate increases ~ 75% by 4% HFP in membrane without CHOL, and the T_2 decreases or the T_2 relaxation rate increases ~ 85% by 4% HFP in membrane with CHOL. The greater reduction in T_2 in membrane with CHOL might due to greater membrane curvature induced by HFP in presence of CHOL. The greater membrane curvature facilitates faster transition into the membrane fusion intermediate states because of the smaller energy gap between the curved membrane and the fusion intermediate states and leading to increased membrane fusion rate.

5.4.3 Spin lattice relaxation studies of Chol_d7

To investigate the spin lattice relaxation (T_1 relaxation) for Chol_d7, we studied OPC/POPG membrane with 33% CHOL at various temperatures. We analyzed the CD_3 deuterons. At - 30°C, T_1 decreases (or T_1 relaxation rate) slightly (~ 8%) in presence of ~ 2% HFP. This result indicates that HFP restricts T_1 relaxation of Chol_d7 CD_3 deuterons. This is probably because the interaction between HFP and Chol_d7 restricts the fast rotational and translational motions of the CD_3 that interacts with HFP. This is consistent with the preferential contact between HFP and CHOL vs PC observed at - 30°C. At and above 5 °C, T_1 is similar without and with HFP. T_1 is longer for the same sample at higher temperature due to increased motion.

REFERENCES

REFERENCES

1. Seelig, J. and P.M. Macdonald, *PHOSPHOLIPIDS AND PROTEINS IN BIOLOGICAL-MEMBRANES - H-2 NMR AS A METHOD TO STUDY STRUCTURE, DYNAMICS, AND INTERACTIONS.* Accounts of Chemical Research, 1987. **20**(6): p. 221-228.

2. Salnikov, E.S., A.J. Mason, and B. Bechinger, *Membrane order perturbation in the presence of antimicrobial peptides by H-2 solid-state NMR spectroscopy.* Biochimie, 2009. **91**(6): p. 734-743.

3. Xie, L., et al., *Multiple Locations of Peptides in the Hydrocarbon Core of Gel-Phase Membranes Revealed by Peptide C-13 to Lipid H-2 Rotational-Echo Double-Resonance Solid-State Nuclear Magnetic Resonance.* Biochemistry, 2015. **54**(3): p. 677-684.

4. Jia, L.H., et al., *REDOR solid-state NMR as a probe of the membrane locations of membrane-associated peptides and proteins.* Journal of Magnetic Resonance, 2015. **253**: p. 154-165.

5. Xie, L., et al., *Residue-specific membrane location of peptides and proteins using specifically and extensively deuterated lipids and C-13-H-2 rotational-echo double-resonance solid-state NMR.* Journal of Biomolecular Nmr, 2013. **55**(1): p. 11-17.

6. Brown, M.F. and G.D. Williams, *MEMBRANE NMR - A DYNAMIC RESEARCH AREA.* Journal of Biochemical and Biophysical Methods, 1985. **11**(2-3): p. 71-81.

7. Seelig, J. and W. Niederberger, *DEUTERIUM-LABELED LIPIDS AS STRUCTURAL PROBES IN LIQUID-CRYSTALLINE BILAYERS - DEUTERIUM MAGNETIC-RESONANCE STUDY.* Journal of the American Chemical Society, 1974. **96**(7): p. 2069-2072.

8. Sani, M.A., et al., *A practical implementation of de-Pake-ing via weighted Fourier transformation.* Peerj, 2013. **1**: p. 8.

9. Bloom, M. and E. Sternin, *TRANSVERSE NUCLEAR-SPIN RELAXATION IN PHOSPHOLIPID-BILAYER MEMBRANES.* Biochemistry, 1987. **26**(8): p. 2101-2105.

10. Harris, R.K., *Nuclear Magnetic Resonance Spectroscopy*. Longman Scientific & Technical. 1986, England.

11. Rong Yang, M.P., ‡ Francis J. Castellino,‡ and David P. Weliky*,†, *A Trimeric HIV-1 Fusion Peptide Construct Which Does Not Self-Associate in Aqueous Solution and Which Has 15-Fold Higher Membrane Fusion Rate.* Journal of American Chemical Society, 2004. **126**(45): p. 14722-14723.

12. Yang, S.T., et al., *HIV gp41-mediated membrane fusion occurs at edges of cholesterol-rich lipid domains.* Nature Chemical Biology, 2015. **11**(6): p. 424-+.

13. Gabrys, C.M., et al., *Solid-State Nuclear Magnetic Resonance Measurements of HIV Fusion Peptide (CO)-C-13 to Lipid P-31 Proximities Support Similar Partially Inserted Membrane Locations of the alpha Helical and beta Sheet Peptide Structures.* Journal of Physical Chemistry A, 2013. **117**(39): p. 9848-9859.

14. Ratnayake, P.U., et al., *Full-length trimeric influenza virus hemagglutinin II membrane fusion protein and shorter constructs lacking the fusion peptide or transmembrane domain: Hyperthermostability of the full-length protein and the soluble ectodomain and fusion peptide make significant contributions to fusion of membrane vesicles.* Protein Expression and Purification, 2016. **117**: p. 6-16.

15. Ratnayake, P.U., et al., *pH-dependent vesicle fusion induced by the ectodomain of the human immunodeficiency virus membrane fusion protein gp41: Two kinetically distinct processes and fully-membrane-associated gp41 with predominant beta sheet fusion peptide conformation.* Biochimica Et Biophysica Acta-Biomembranes, 2015. **1848**(1): p. 289-298.

16. Sackett, K., et al., *Hairpin Folding of HIV gp41 Abrogates Lipid Mixing Function at Physiologic pH and Inhibits Lipid Mixing by Exposed gp41 Constructs.* Biochemistry, 2009. **48**(12): p. 2714-2722.

17. Lai, A.L., et al., *Fusion Activity of HIV gp41 Fusion Domain Is Related to Its Secondary Structure and Depth of Membrane Insertion in a Cholesterol-Dependent Fashion.* Journal of Molecular Biology, 2012. **418**(1-2): p. 3-15.

18. Gabrys, C.M., et al., *Nuclear magnetic resonance evidence for retention of a lamellar membrane phase with curvature in the presence of large quantities of the HIV fusion peptide.* Biochimica Et Biophysica Acta-Biomembranes, 2010. **1798**(2): p. 194-201.

19. Yang, J., et al., *Solid state NMR measurements of conformation and conformational distributions in the membrane-bound HIV-1 fusion peptide.* Journal of Molecular Graphics & Modelling, 2001. **19**(1): p. 129-135.

20. Ghosh, U., *Solid State NMR Studies of Structure and Dynamics of Membrane Associated Influenza Fusion Peptides*, in *Chemistry*. 2016, Michigan State University.

21. Yang, S.T., et al., *The role of cholesterol in membrane fusion.* Chemistry and Physics of Lipids, 2016. **199**: p. 136-143.

Chapter 6 - Summary and Future work

Over the last ~ 4 years I have been mainly working on two projects:

(1) Using ^{13}C-^{2}H REDOR NMR method as a probe to study the membrane locations of HFP constructs including wildtype, HFP_V2E mutant and HFP_L9R mutant, and transmembrane peptide KALP.

(2) Using ^{2}H-static NMR method to study the membrane dynamics of lipid bilayer affected by the presence of HFP.

6.1 Summary of ^{13}C-^{2}H REDOR as a probe for membrane location study and future work of HFP

To study the membrane locations of HFP constructs and KALP in the membrane hydrophobic core, the peptide backbone is ^{13}CO labeled at specific residue and membrane is selectively deuterated at different regions of the lipid acyl chain or CHOL (labeling scheme see figure 2.). We study the peptide membrane contacts by ^{13}C- ^{2}H REDOR.[1-4]

The experimental REDOR dephasing supports multiple membrane locations for both HFP wildtype and HFP_V2E mutant in DPPC: DPPG (4:1) membrane. In membrane containing ~ 33% deuterated CHOL, there is similar multiple membrane locations for HFP wildtype in DOPC: DOPG and POPC: POPG membranes compared to DPPC: DPPG membranes. These results for HFP wildtype suggest that the multiple membrane locations distribution is robust and probably regardless of the membrane composition. The multiple membrane locations of KALP are because of the hydrophobic mismatch between the KALP hydrophobic length and the membrane and the resultant snorkeling effect of lysine sidechains to the membrane head-group region.

As for the HFP wildtype membrane location study, an interesting discovery is that HFP has preferential contact to neighboring CHOL than lipid acyl chain. In DPPC: DPPG: CHOL (8:2:5) with HFP_G5c, there is ~2 times dephasing with Chol_d7 labeling than with PC_d10 (deuterated DPPC) labeling, where the deuterons are both located near the membrane center without peptides. The dephasing is comparable with Chol_d7 labeling and PC_d10 labeling when the membrane components ratio is DPPC: DPPG: CHOL= 8:2:2.5. HFP_G10c give similar dephasing compared to HFP_G5c in membrane DPPC: DPPG: CHOL= 8:2:2.5. HFP_G16c also has preferential contact to Chol_d6 than lipid acyl chains near the membrane surface. The preferential contact of HFP to CHOL vs PC might shed some light on understanding the increased fusion in membrane with CHOL vs without CHOL. CHOL increase fusion via two features of CHOL vs PC: (1) CHOL has greater intrinsic curvature which is more favorable in membrane intermediate state during fusion; (2) CHOL tail is closer to the membrane surface because CHOL is shorter.[5]

For future work of HFP, it will be interesting to study the residue specific membrane locations of HFP in the membrane hydrophobic core using larger gp41 constructs including the HFP region. The larger gp41 construct can be FP-Hairpin (FP-NHR-Loop-CHR) or FP-HM (FP-NHR-Loop-CHR-MPER). We can study the membrane location in membrane with and without CHOL. In membrane with CHOL, we can compare the dephasing with PC_d10 and Chol_d7, or PC_d4 with Chol_d6 to see whether there is preferential contact of FP in the larger gp41 constructs to CHOL vs PC. In membrane containing ~ 33% CHOL, greater or similar dephasing with deuterated CHOL than deuterated PC would support preferential contact to CHOL, while about half or less dephasing with deuterated CHOL compared to PC would be consistent with no preferential contact to CHOL.

6.2 Summary of membrane motions perturbed by HFP and future work

My second project is to investigate the changes in membrane structure and motions in presence of HFP. We use per-deuterated PC (DMPC-d54) and deuterated CHOL (Chol_d6 and Chol_d7) to investigate the change by evaluating the spectrum and T_2 and T_1 relaxation times by ^{2}H- NMR. We observed powder pattern of DMPC-d54 even in presence of 4% HFP suggests that the membrane maintains the lamellar bilayer structure. The spectrum changes are CHOL and peptide quantity dependent.

For changes of DMPC-d54, addition of HFP broadens the fine peaks in DMPC-d54 spectrum. In membrane without CHOL, the CD_3 and CD_2 peak splitting is narrower with HFP relative to without HFP in membrane without CHOL and the acyl chain order parameter decreases less than 5% along the acyl chain with 4% HFP relative to without HFP. However, in membrane with ~ 33% CHOL, the peak splitting is significantly broader and the acyl chain order parameter increases about 20% to 30% with HFP relative to without HFP. Therefore, HFP increases the motion on the time scale of ~ 10^{-5}s of membrane without CHOL, and decreases the motion on the time scale of ~ 10^{-5}s of membrane with CHOL. HFP generally decreases DMPC-d54 T_2 ~ 68 % independent of CHOL above the DMPC phase transition temperature. With 1% and 4% HFP, T_2 fitted form echo intensity is ~ 23% smaller with 4% HFP relative to with 1% HFP. For changes of Chol_d6, in membrane with 33% CHOL at 37 °C, the Chol_d6 T_2 is similar in DMPC and POPC membranes. The T_2 decreases ~ 35% and ~ 28% in DMPC and POPC membrane, respectively. These results suggest that presence of HFP restricts the motion of Chol_d6 and there is little effect of membrane composition on Chol_d6 motion while the membrane is likely in liquid ordered phase both in POPC/CHOL membrane and in DMPC/CHOL membrane at 37 °C.[6, 7] For changes of Chol_d7, for temperature above and including 5 °C, the T_2 is similar

without and with HFP, and is similar for the same sample regardless of temperature increasing. The decreased T_2 of DMPC-d54 and Chol_d6 is probably due to increased membrane curvature in presence of HFP. And the similar T_2 for Chol_d7 indicates that the effect of HFP on Chol_d7 motion is negligible. Chol_d6 has the deuteron on the rigid ring system, and would have slow motions, while Chol_d7 have deuterons in the isopropyl tail which has fast axial rotation of the C-D bond.

For future work, it will be interesting to study the structure and motion changes in membrane induced by HFP_V2E and HFP_L9R mutants to correlate the membrane change induced by HFP constructs and fusogenicity. It's worthwhile to study the membrane both without and with CHOL to understand the role of CHOL in fusion. It's also interesting to study the membrane change induced by FP using larger gp41 constructs. The larger gp41 constructs can be FP-Hairpin (FP-NHR-Loop-CHR) and FP-HM (FP-NHR-Loop-CHR-MPER) and the corresponding non-fusogenicity V2E and fusogenicity L9R mutants.

REFERENCES

REFERENCES

1. Gullion, T., *Introduction to rotational-echo, double-resonance NMR.* Concepts in Magnetic Resonance, 1998. **10**(5): p. 277-289.

2. Xie, L., et al., *Multiple Locations of Peptides in the Hydrocarbon Core of Gel-Phase Membranes Revealed by Peptide C-13 to Lipid H-2 Rotational-Echo Double-Resonance Solid-State Nuclear Magnetic Resonance.* Biochemistry, 2015. **54**(3): p. 677-684.

3. Jia, L.H., et al., *REDOR solid-state NMR as a probe of the membrane locations of membrane-associated peptides and proteins.* Journal of Magnetic Resonance, 2015. **253**: p. 154-165.

4. Xie, L., et al., *Residue-specific membrane location of peptides and proteins using specifically and extensively deuterated lipids and C-13-H-2 rotational-echo double-resonance solid-state NMR.* Journal of Biomolecular Nmr, 2013. **55**(1): p. 11-17.

5. Zimmerberg, J. and M.M. Kozlov, *How proteins produce cellular membrane curvature.* Nature Reviews Molecular Cell Biology, 2006. **7**(1): p. 9-19.

6. Almeida, P.F.F., W.L.C. Vaz, and T.E. Thompson, *LATERAL DIFFUSION IN THE LIQUID-PHASES OF DIMYRISTOYLPHOSPHATIDYLCHOLINE CHOLESTEROL LIPID BILAYERS - A FREE-VOLUME ANALYSIS.* Biochemistry, 1992. **31**(29): p. 6739-6747.

7. Thewalt, J.L. and M. Bloom, *PHOSPHATIDYLCHOLINE - CHOLESTEROL PHASE-DIAGRAMS.* Biophysical Journal, 1992. **63**(4): p. 1176-1181.

APPENDICES

APPENDIX A

Preparation and characterization of FPHM_V2E mutant of gp41 ectodomain

A.1 Preparation of FPHM_V2E mutant

Figure A.1 shows the FPHM_V2E mutant amino acid and DNA sequence. Studies have shown that V2E mutant in gp41 eliminates cell-cell fusion.[1] We study the structure and oligomeric state of FPHM_V2E mutant to help understand gp41 catalyzed fusion. FPHM amino acid sequence is shown in figure 1.16, and is from residue 512 to 683 according to g160 sequence numbering for the HXB2 laboratory strain of HIV, and the region from residue 582 to 627 in gp41 is replaced with SGGRGG loop which does not affect the SHB assembly.[2-4] Crystal structure shows flexible (crystallography disordered) structure from residue 601 to 613 and helical structure from residue 582 to 600 and 614 to 627.[5] PHM_V2E mutant is engineered through point mutation of FPHM by polymerase chain reaction (PCR) using FPHM template DNA and designed primers including the point mutation. FPHM template plasmid is extracted from overnight grown cells. Primers are designed including the V2E point mutation. The forward primer sequence is 5' - CAT ATG GCC GAG GGT ATC GGT G - 3'. The reverse primer sequence is 5' – CAC CGA TAC CCT CGG CCA TAT G - 3'. After PCR, DNP1 enzyme is added to the final PCR product to cleave mother template DNA (FPHM DNA). We run the PCR product on agarose gel and compare with DNA ladder to check successfulness of the mutation. The successful PCR product with the point mutation is taken up by BL21 (DE3) competent cells. Then we incubate the cells on agar plate overnight in the incubator at 37 °C. Colony on the agar plate is picked to grow overnight in 100mL LB at 37 °C. Glycerol stocks were made with 1mL cell cultures and 50% glycerol and stored at -80°C.[6] The plasmid is extracted from overnight grown cells using plasmid extraction kit (Promega) and sent for DNA sequencing to check the successfulness of the V2E point mutation.

To express the protein, glycerol stocks of the cells containing the FPHM_V2E mutant plasmid is incubated overnight in 50mL LB with 50mg/L kanamycin antibiotic at 37 °C with stirring at 180 rpm. Then the culture is added to 1L fresh LB in baffled flask. Expression of the protein is induced by adding isopropyl β–D-1-thiogalactopyranoside (IPTG) to a final concentration of 2mM after the cell culture $OD_{600} \approx 0.8$. After 5hrs protein expression, the cells are harvested by centrifugation at 9000g for 10mins at 4 °C. The cell pellets are stored at -20 °C until use.

(a) FPHM_V2E amino acid sequence:

AEGIGALFLGFLGAAGSTMGARSMTLTVQARQLLSGIVQQQNNLLRAIEAQQHLLQLTV
WGIKQLQARILSGGRGGWMEWDREINNYTSLIHSLIEESQNQQEKNEQELLELDKWASL
WNWFNITNWLWYIKGGGGGGLEHHHHHH

(b) FPHM_V2E DNA sequence:

GCCGAGGGTATCGGTGCTCTGTTCCTGGGTTTCCTGGGTGCTGCTGGTTCGACGATG
GGTGCCCGCTCAATGACGCTGACGGTCCAAGCACGTCAGCTGCTGAGCGGCATTGT
GCAGCAACAGAACAATCTGCTGCGCGCGATCGAAGCCCAACAGCATCTGCTGCAGC
TGACCGTTTGGGGTATTAAACAACTGCAGGCTCGTATCCTGAGCGGCGGTCGCGGCG
GTTGGATGGAATGGGATCGTGAAATTAACAATTATACGAGCCTGATTCACTCTCTGA
TCGAAGAAAGTCAAAACCAACAGGAGAAAAACGAACAGGAACTGCTGGAACTGGA
CAAATGGGCCTCCCTGTGGAACTGGTTTAACATTACGAACTGGCTGTGGTACATCAA
AGGCGGCGGTGGCGGTGGTCTCGANCACCACCACCACCAC

Figure A1 FPHM_V2E amino acid and DNA sequences. The C-terminal GGGGGGLEHHHHHH residues are non-native tag. SGGRGG is the engineered loop.

To get purified FPHM_V2E protein, ~ 4g cell pellet is tip sonicated in ~ 40mL pH 7.4 PBS buffer (10mM Na_2HPO_4 + 2mM KH_2PO_4 + 3mM KCl + 140mM NaCl). Sonication is done with 60% amplitude for 0.6s and followed by 0.4s rest for 1min. And there are 5 rounds × 1min sonication separated by 1min rest. Then the inclusion bodies which are rich in the FPHM_V2E proteins are separated from the rest part of the cells by centrifugation at 48000g for 20mins at 4 °C. The inclusion bodies are subject for another 2 rounds of sonication in PBS buffer followed by centrifugation. Next, the inclusion body pellets are solubilized in 8M Urea + 0.8% N-lauroylsarcosine (SRC) + 0.5% SDS PBS buffer (solubilization buffer) by tip sonication. Sonication is done with 70% amplitude for 0.8s and followed by 0.2s rest for 1min. And there are 5 rounds × 1min sonication separated by 1min rest. There is no visible solid after the mixture is centrifuged at 48000g for 20 mins at 4 °C which supports complete solubilization.

The protein is purified affinity chromatography. First, 1mL Co^{2+} affinity resin is added to the ~ 40mL solutions containing the FPHM_V2E protein. Then the mixture is agitated for 2hrs at ambient temperature to allow protein binding to the resin. Next, the protein bound resin is separated from solution through fritted column and followed by 1mL × 4 rounds solubilization buffer wash. Then the protein is eluted with solubilization buffer + 250mM imidazole (elution buffer). The protein is quantitated with A_{280}, and the purification yield is ~ 0.7 mg from 1L culture. Figure A.2 shows the SDS-PAGE of purification products. The elution shows pure band around 15kDa and is consistent with FPHM_V2E molecular weight. This band is submitted to MSU Proteomics Facility center to identify the FPHM_V2E by trypsin digestion and analysis of the resultant peptides. There is 88% amino acid coverage which identifies FPHM_V2E.

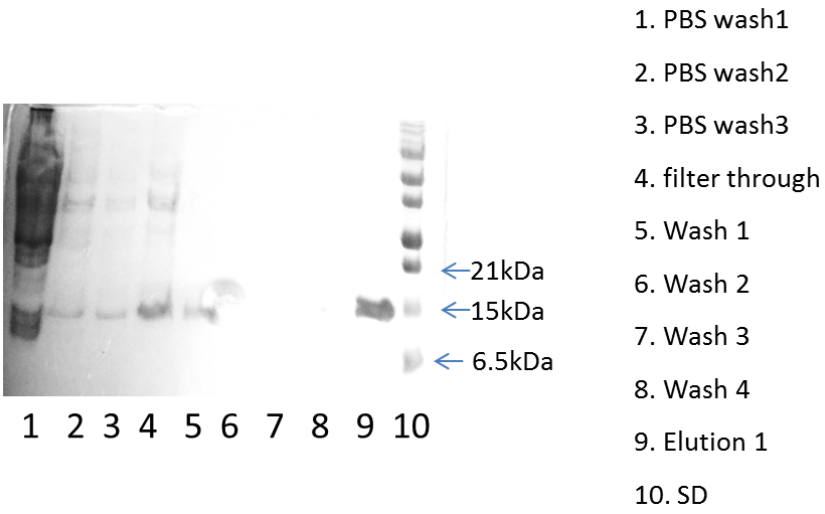

Figure A2 SDS-PAGE of FPHM_V2E mutant. PBS wash is the supernatant of the inclusion bodies in PBS buffer at pH 7.4. Filter through and wash 1-4 is in solubilization buffer, and Elution 1 is in solubilization buffer + 250mM imidazole.

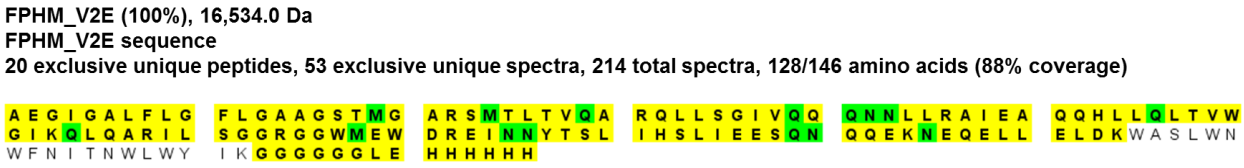

Figure A3 Proteomics results of the SDS-PAGE band corresponding to FPHM_V2E protein. Green color shaded M means there is detection of digested short peptides including oxidation (+16). Green color shaded Q and N means there is detection of digested short peptides including deamidated Q and N (+1) respectively. Green color shaded E means there is detection of digested short peptides including dehydrated E (-18).

A.2 Structure and oligomeric state of FPHM_V2E mutant

Before structural characterization of the protein, the protein eluent is refolded by adding equal volume of ice-cold buffer (10mM Tris-HCl, 0.17% decylmaltoside (DM), 2mM EDTA, and 1M

L-arginine at pH 8.0).[6] The mixture is agitated overnight at 4 °C followed by ~ 4 days dialysis against CD-buffer (10mM Tris-HCl + 0.2% SDS at pH 7.4) with 4 times buffer change. We use CD spectroscopy to characterize the secondary structure of the protein. Typical parameters include: protein concentration of ~ 14 μM, 1mm path-length and 260-185 nm spectral range with 1nm band width and 1s response time. Each spectrum is accumulation of 3 scans. Each scan is baseline subtracted, and baseline is absorbance from CD-buffer only. The CD spectrum shows two minima at 208nm and 222nm, which is consistent with overall α- helical secondary structure. According to the mean residue molar elipticity at 222 nm (θ_{222}), the protein is 45% helical according to the maximum θ_{222}value of -33,000 for α helix.[7] There are 146 residues totally in the FPHM_V2E sequence, and helicity of NHR (residue 535- 581) and CHR (residue 628-662) accounts for 56% helicity. HFP_V2E has partial helical structure from some residues like L9, L12 and A14 in membrane bilayer.[8] The 45% helicity is probably from NHR and CHR, and the decreased helicity is likely due to SDS denaturation of the protein. To get the melting temperature, the CD spectrum is taken from 25 °C to 90 °C with 5 °C increment. The mean residue molar elipticity at 222 nm is plotted. The protein is still helical at 90 °C and the melting temperature is above 90 °C.

To get the oligomeric state of FPHM_V2E, protein solution is analyzed by gel filtration chromatography. The protein eluent is dialyzed against gel-filtration-buffer (10mM Tris-HCl + 0.2% SDS + 150mM NaCl at pH 7.4) for ~ 4days with 4 times buffer change after refolding. The instrument is Pathfinder 20 instrument (Bio-Rad) with Superdex 200 increase column (General Electric). The column is equilibrated with gel-filtration-buffer before running protein sample. The protein concentration is ~0.9 mg/mL protein concentration. Eluent flow rate is 0.3mL/min. Detection is A_{280nm}. There is a single peak and peak is eluted at 14.23mL which corresponds to

molecular weight of 99kDa and FPHM_V2E is likely in trimeric state with molecular weight of 50kDa, and the rest 49kDa corresponds to SDS detergent molecules. SDS aggregation number is ~62, which corresponds to 17.8kDa mass per micelle. The 49kDa of SDS detergent molecules is ~ 3 micelles size. Then in the trimer peak, the FPHM_V2E protein: SDS micelle is ~1:1 mole ratio.

Table A1 Mean residue molar elipticity of FPHM_V2E at 222nm (θ_{222}) (deg.cm^2.dmol^{-1}.residue^{-1}) at different temperatures

Temperature/ °C	θ_{222}/ deg.cm^2.dmol^{-1}.residue^{-1}
25	-15079
30	-15008
35	-14691
40	-13928
45	-13632
50	-13443
55	-13316
60	-13016
65	-12803
70	-12407
75	-12164
80	-11804
85	-11598
90	-11337

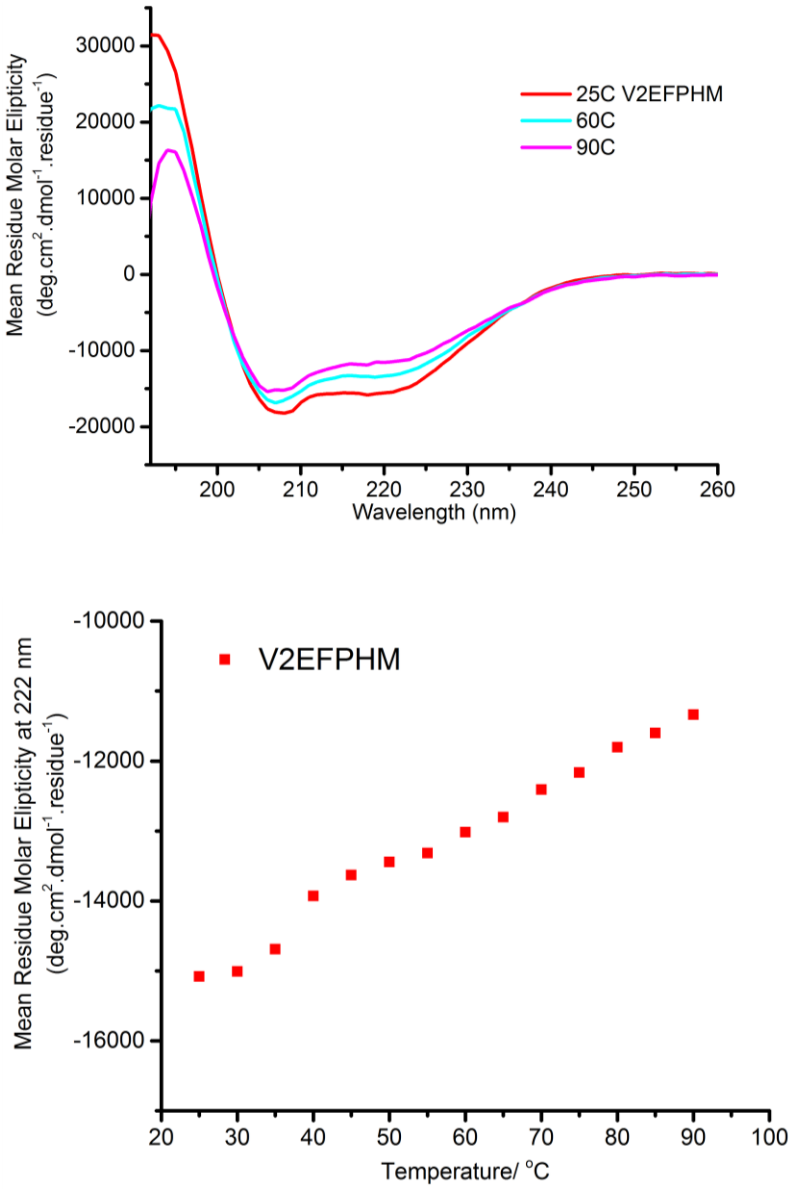

Figure A4 CD spectroscopy of FPHM_V2E (top panel) and melting temperature (bottom panel) in 10mM tris(hydroxymethyl)aminomethane (Tris-HCl) + 0.2% SDS at pH 7.4. The melting temperature plot is based on the mean residue molar elipticity at 222nm.

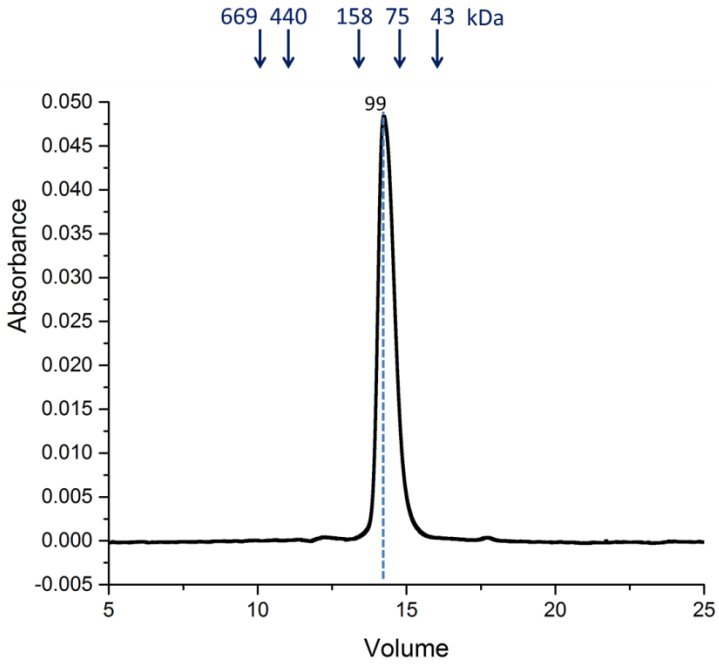

Figure A5 Gel filtration chromatograph of FPHM_V2E in 10mM Tris-HCl + 0.2% SDS + 150mM NaCl at pH 7.4. The highest peak is eluted at 14.23mL and corresponds to molecular weight of 99kDa.

A.3 Lipid mixing assay of FPHM_V2E mutant in POPC: CHOL (2:1) vesicle at pH 7.4

Lipid mixing assay of FPHM_V2E is done with POPC: CHOL (2:1) ratio. Lipids are dissolved in chloroform. Chloroform is removed by N_2 gas followed by vacuum pumping. The lipid film is dissolved in 1mL pH 7.4 buffer (5mM HEPES + 10mM MES), and homogenized by 10 freeze-thaw cycles. The mixture is then extruded through membrane film with 100nm pore size ~ 20 times. There are non-labeled lipids and fluorescent labeled lipids. The fluorescent labeled lipid also contained 2mol % fluorescent lipid N-(7-nitro-2, 1, 3-benzoxadiazol-4-yl) (ammonium salt) dipalmitoylphosphatidylethanolamine (N-NBD-PE) and 2mol % quenching lipid N-(lissamine rhodamine B sulfonyl) (ammonium salt) dipalmitoylphosphatidylethanolamine (N-Rh-PE). Labeled and unlabeled lipids are mixed in 1: 9 ratios to achieve total phospholipid (POPC)

concentration ≈ 150μM. The vesicle solution is stirred at 37 °C. Protein to lipids ratio is 1:300. The fluorescence is measured with 467nm excitation and 530nm detection. The baseline fluorescence is F_0, protein stock solution (40μM in CD-buffer (10mM Tris-HCl + 0.5% SDS at pH 7.4)) is added at time 0, and there is increased fluorescence $\Delta F(t) = F(t)-F_0$ because the distance between fluorescent and quenching lipids is longer in the fused vesicle (labeled + unlabeled) than in the original labeled vesicle. The asymptotic fluorescence is usually reached by ~ 600s. Then 12μL 10 % Triton X-100 is added to achieve the maximum fluorescence (ΔFmax). % lipid mixing $=\Delta F(t)/ \Delta Fmax \times 100$. There is ~ 0.5% lipid mixing with protein: lipids ratio of 1:300. However, FPHM wildtype induces ~ 4% lipid mixing under same conditions from Shuang Liang's work in our group. Our result supports that FPHM_V2E mutant of gp41 is nonfusogenic.

For future work, the protein structure characterization and lipid mixing assay need to be repeated to check consistency. Comparing with FPHM wild type is necessary to gain insight on structure and fusion correlation. For lipid mixing assay, it is interesting to study the negatively charged vesicles, and study fusion at low pH to compare the electrostatic and hydrophobicity contribution to FPHM induced fusion.

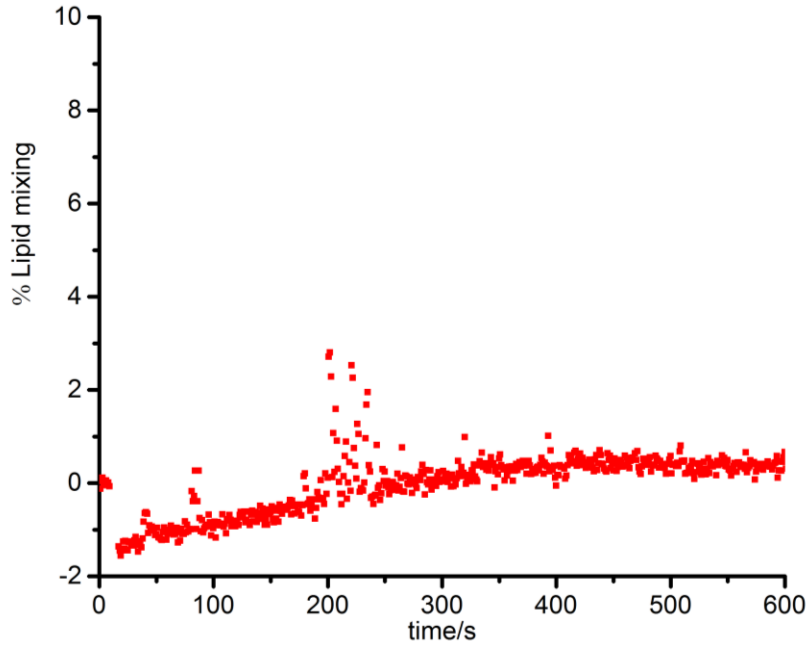

Figure A6 Lipid mixing assay of FPHM_V2E in POPC: CHOL= 2:1 vesicles at pH 7.4. Protein: Lipids = 1:300 mole ratio.

APPENDIX B

NMR file locations

Figure 3.3

/export/home/hapi0/mb4c/data/Lihui/13C2H/HFP/HFP_041213

Figure 3.4

/export/home/hapi0/mb4c/data/Lihui/13C2H/HFP/HFP_053113 (organic)

/export/home/hapi0/mb4c/data/Lihui/13C2H/HFP/HFP_051713 (aqueous)

Figure 3.5

/export/home/hapi0/mb4c/data/Lihui/13C2H/HFP/HFP_053113 (organic)

/export/home/hapi0/mb4c/data/Lihui/13C2H/HFP/HFP_051713 (aqueous)

Figure 3.6

/export/home/hapi0/mb4c/data/Lihui/13C2H/HFP/HFP_053113 (- 30 °C)

/export/home/hapi0/mb4c/data/Lihui/13C2H/HFP/HFP_071613 (0 °C)

Figure 3.7 and Figure 3.8

/export/home/hapi0/mb4c/data/Lihui/13C2H/HFP/HFP_041213 (PC_d10)

/export/home/hapi0/mb4c/data/Lihui/13C2H/HFP/HFP_042513 (PC_d8)

/export/home/hapi0/mb4c/data/Lihui/13C2H/HFP/HFP_050813 (PC_d4)

/export/home/hapi0/mb4c/data/Lihui/13C2H/HFP/HFP_053113 (PC_d10: PG)

/export/home/hapi0/mb4c/data/Lihui/13C2H/HFP/HFP_090313 (PC_d8: PG)

/export/home/hapi0/mb4c/data/Lihui/13C2H/HFP/HFP_040814 (PC_d4: PG)

Figure 3.9 and Figure 3.10

/export/home/hapi0/mb4c/data/Lihui/13C2H/HFP/HFP_112713 (PC_d10: PG)

/export/home/hapi0/mb4c/data/Lihui/13C2H/HFP/HFP_121713 (PC_d8: PG)

/export/home/hapi0/mb4c/data/Lihui/13C2H/HFP/HFP_122613 (PC_d4: PG)

Figure 3.12

/export/home/hapi0/mb4c/data/Lihui/13C2H/HFP/HFP_051214 (PC: PG: Chol_d7)

/export/home/hapi0/mb4c/data/Lihui/13C2H/HFP/HFP_052614 (PC: PG: Chol_d6)

Figure 3.13

/export/home/hapi0/mb4c/data/Lihui/13C2H/HFP/HFP_061614 (PC: PG: Chol_d7)

/export/home/hapi0/mb4c/data/Lihui/13C2H/HFP/HFP_060214 (PC: PG: Chol_d6)

Figure 3.15 and Figure 3.16

/export/home/hapi0/mb4c/data/Lihui/13C2H/HFP/ G10c_050216 (Chol_d7 5)

/export/home/hapi0/mb4c/data/Lihui/13C2H/HFP/G10c_051416 (Chol_d6 5)

/export/home/hapi0/mb4c/data/Lihui/13C2H/HFP/ G10c _101415 (Chol_d7 2.5)

Figure 3.17 and Figure 3.18

/export/home/hapi0/mb4c/data/Lihui/13C2H/HFP/ G16c_052616 (Chol_d6)

/export/home/hapi0/mb4c/data/Lihui/13C2H/HFP/G16c_060316 (Chol_d7)

Figure 3.19 and Figure 3.20

/export/home/hapi0/mb4c/data/Lihui/13C2H/HFP/ HFP_070714 (Chol_d7)

/export/home/hapi0/mb4c/data/Lihui/13C2H/HFP/G16c_071714 (Chol_d6)

Figure 3.22

/export/home/hapi0/mb4c/data/Lihui/13C2H/HFP/V2E_031214 (PC_d10: PG)

/export/home/hapi0/mb4c/data/Lihui/13C2H/HFP/V2E_031914 (PC_d8: PG)

/export/home/hapi0/mb4c/data/Lihui/13C2H/HFP/V2E_032714 (PC_d4: PG)

Figure 3.25

/export/home/hapi0/mb4c/data/Lihui/13C2H/HFP/HFP_012714 (PC_d10: PG)

/export/home/hapi0/mb4c/data/Lihui/13C2H/HFP/HFP_011414 (PC_d8: PG)

/export/home/hapi0/mb4c/data/Lihui/13C2H/HFP/HFP_010214 (PC_d4: PG)

Figure 3.26

/export/home/hapi0/mb4c/data/Lihui/13C2H/HFP/HFP_022214 (PC_d10: PG)

/export/home/hapi0/mb4c/data/Lihui/13C2H/HFP/HFP_021214 (PC_d8: PG)

/export/home/hapi0/mb4c/data/Lihui/13C2H/HFP/HFP_030314 (PC_d4: PG)

Figure 3.27 and Figure 3.28

/export/home/hapi0/mb4c/data/Lihui/13C2H/KALP/A5c_033115 (PC_d10: PG)

/export/home/hapi0/mb4c/data/Lihui/13C2H/KALP/A5c_040815 (PC_d8: PG)

/export/home/hapi0/mb4c/data/Lihui/13C2H/KALP/A5c_041515 (PC_d4: PG)

Figure 3.29 and Figure 3.30

/export/home/hapi0/mb4c/data/Lihui/13C2H/KALP/A7c_031315 (PC_d10: PG)

/export/home/hapi0/mb4c/data/Lihui/13C2H/KALP/A7c_021315 (PC_d8: PG)

/export/home/hapi0/mb4c/data/Lihui/13C2H/KALP/A7c_022015 (PC_d4: PG)

Figure 3.31 and Figure 3.32

/export/home/hapi0/mb4c/data/Lihui/13C2H/KALP/A17c_082815 (PC_d10: PG)

/export/home/hapi0/mb4c/data/Lihui/13C2H/KALP/A17c_092315 (PC_d8: PG)

/export/home/hapi0/mb4c/data/Lihui/13C2H/KALP/A17c_090915 (PC_d4: PG)

Figure 3.33 and Figure 3.34

/export/home/hapi0/mb4c/data/Lihui/13C2H/KALP/A19c_073015 (PC_d10: PG)

/export/home/hapi0/mb4c/data/Lihui/13C2H/KALP/A19c_081815 (PC_d8: PG)

/export/home/hapi0/mb4c/data/Lihui/13C2H/KALP/A19c_081015 (PC_d4: PG)

Figure 4.1

/export/home/hapi0/mb4c/data/Lihui/13C2H/HFP/HFP_042614 (PC_d10: PG: CHOL)

/export/home/hapi0/mb4c/data/Lihui/13C2H/HFP/HFP_081114 (PC_d8: PG: CHOL)

/export/home/hapi0/mb4c/data/Lihui/13C2H/HFP/HFP_051214 (PC: PG: Chol_d7)

Figure 4.2

/export/home/hapi0/mb4c/data/Lihui/13C2H/HFP/HFP_090814 (PC_d10)

/export/home/hapi0/mb4c/data/Lihui/13C2H/HFP/HFP_091614 (Chol_d7 2.5)

/export/home/hapi0/mb4c/data/Lihui/13C2H/HFP/HFP_112014 (Chol_d7 1.25)

Figure 4.3

/export/home/hapi0/mb4c/data/Lihui/13C2H/HFP/HFP_010815 (PC_d10)

/export/home/hapi0/mb4c/data/Lihui/13C2H/HFP/HFP_121914 (Chol_d7)

Figure 4.4

/export/home/hapi0/mb4c/data/Lihui/13C2H/HFP/HFP_072814 (PC_d10)

/export/home/hapi0/mb4c/data/Lihui/13C2H/HFP/HFP_081814 (PC_d8)

/export/home/hapi0/mb4c/data/Lihui/13C2H/HFP/HFP_080414 (PC_d4)

/export/home/hapi0/mb4c/data/Lihui/13C2H/HFP/HFP_061614 (Chol_d7)

Figure 4.5

/export/home/hapi0/mb4c/data/Lihui/13C2H/HFP/HFP_060214 (Chol_d6 5)

/export/home/hapi0/mb4c/data/Lihui/13C2H/HFP/HFP_120614 (Chol_d6 2.5)

Figure 5.2

/export/home/hapi0/mb4c/data/Lihui/DMPCPG/21C_one_ 021517

/export/home/hapi0/mb4c/data/Lihui/DMPCPG/25C_one _021317

/export/home/hapi0/mb4c/data/Lihui/DMPCPG/30C_one _021417

/export/home/hapi0/mb4c/data/Lihui/DMPCPG/d54dmpg_one_113016 (37 °C)

Figure 5.3

/export/home/hapi0/mb4c/data/Lihui/DMPCPG/21C_one_withHFP_021617

/export/home/hapi0/mb4c/data/Lihui/DMPCPG/25C_one_withHFP_021817

/export/home/hapi0/mb4c/data/Lihui/DMPCPG/30C_one_withHFP_022017

/export/home/hapi0/mb4c/data/Lihui/DMPCPG/d54dmpg_one_withHFP_120116 (37 °C)

Figure 5.4

/export/home/hapi0/mb4c/data/Lihui/DMPCPGChol/21C_one_d54pgchol_ 020217

/export/home/hapi0/mb4c/data/Lihui/DMPCPGChol/25C_one_d54pgchol_ 020117

/export/home/hapi0/mb4c/data/Lihui/DMPCPGChol/30C_one_d54pgchol_ 013117

/export/home/hapi0/mb4c/data/Lihui/DMPCPGChol/d54_noHFP_091516_one (37 °C)

Figure 5.5

/export/home/hapi0/mb4c/data/Lihui/DMPCPGChol/2umolHFP/21C_one_020617

/export/home/hapi0/mb4c/data/Lihui/DMPCPGChol/2umolHFP/25C_one_020817

/export/home/hapi0/mb4c/data/Lihui/DMPCPGChol/2umolHFP/30C_one_020917

/export/home/hapi0/mb4c/data/Lihui/DMPCPGChol/2umolHFP/d54pgchol_one_withHFP_1227

16 (37°C)

Figure 5.6

/export/home/hapi0/mb4c/data/Lihui/DMPCPG/21C_one_ 021517

/export/home/hapi0/mb4c/data/Lihui/DMPCPG/21C_one_withHFP_021617

/export/home/hapi0/mb4c/data/Lihui/DMPCPG/d54dmpg_one_113016 (37 °C)

/export/home/hapi0/mb4c/data/Lihui/DMPCPG/d54dmpg_one_withHFP_120116 (37 °C)

Figure 5.7

/export/home/hapi0/mb4c/data/Lihui/DMPCPGChol/21C_one_d54pgchol_ 020217

/export/home/hapi0/mb4c/data/Lihui/DMPCPGChol/2umolHFP/21C_one_020617

/export/home/hapi0/mb4c/data/Lihui/DMPCPGChol/d54_noHFP_091516_one (37 °C)

/export/home/hapi0/mb4c/data/Lihui/DMPCPGChol/2umolHFP/d54pgchol_one_withHFP_122716 (37°C)

Figure 5.8

/export/home/khafre0/mb4b/data/Lihui/d54 _noHFP_one_101716 (pure lipids)

/export/home/khafre0/mb4b/data/Lihui/d54 _withHFP_one_101516 (1:100)

/export/home/khafre0/mb4b/data/Lihui/2umolHFP/d54 _withHFP_one_102416 (1:25)

Figure 5.9

/export/home/hapi0/mb4c/data/Lihui/DMPCPGChol/Chold6_noHFP_090216 (pure lipids)

/export/home/hapi0/mb4c/data/Lihui/DMPCPGChol/Chold6_withHFP_090816 (lipids+HFP)

Figure 5.15

/export/home/hapi0/mb4c/data/Lihui/DMPCPG/21C_T2_2_ 021417 (21 °C)

/export/home/hapi0/mb4c/data/Lihui/DMPCPG/d54dmpg_113016 (37 °C)

Figure 5.16

Same as figure 5.15

Figure 5.17

/export/home/hapi0/mb4c/data/Lihui/DMPCPG/21C_T2_withHFP_ 021617 (21 °C)

/export/home/hapi0/mb4c/data/Lihui/DMPCPG/d54dmpg_withHFP_120116 (37 °C)

Figure 5.18

/export/home/hapi0/mb4c/data/Lihui/DMPCPGChol/21C_T2_d54pgchol_ 020317 (21 °C)

/export/home/hapi0/mb4c/data/Lihui/DMPCPGChol/37C_T2_2_ 021017 (37 °C)

Figure 5.19

/export/home/hapi0/mb4c/data/Lihui/DMPCPGChol/2umolHFP/21C_T2_ 020617 (21 °C)

/export/home/hapi0/mb4c/data/Lihui/DMPCPGChol/2umolHFP/d54pgchol_withHFP_122716 (37 °C)

Figure 5.20

/export/home/hapi0/mb4c/data/Lihui/DMPCPGChol/37C_T2_2_021017 (without HFP)

/export/home/hapi0/mb4c/data/Lihui/DMPCPGChol/d54_wihHFP_090716 (HFP:PL= 1:100)

Figure 5.21

/export/home/hapi0/mb4c/data/Lihui/DMPCPGChol/Chold6_090216

/export/home/hapi0/mb4c/data/Lihui/DMPCPGChol/Chold6_withHFP_090816

Figure 5.22

/export/home/hapi0/mb4c/data/Lihui/DMPCPG/21C_T2_2_021417 (21 °C)

/export/home/hapi0/mb4c/data/Lihui/DMPCPG/25C_T2_021217 (25 °C)

/export/home/hapi0/mb4c/data/Lihui/DMPCPG/30C_T2_021317 (30 °C)

/export/home/hapi0/mb4c/data/Lihui/DMPCPG/d54dmpg_113016 (37 °C)

Figure 5.23

/export/home/hapi0/mb4c/data/Lihui/DMPCPG/21C_T2_withHFP_021617 (21 °C)

/export/home/hapi0/mb4c/data/Lihui/DMPCPG/25C_T2_withHFP_021817 (25 °C)

/export/home/hapi0/mb4c/data/Lihui/DMPCPG/30C_T2_withHFP_021917 (30 °C)

/export/home/hapi0/mb4c/data/Lihui/DMPCPG/d54dmpg_withHFP_120116 (37 °C)

Figure 5.24

/export/home/hapi0/mb4c/data/Lihui/DMPCPGChol/21C_T2_d54pgchol_020317 (21 °C)

/export/home/hapi0/mb4c/data/Lihui/DMPCPGChol/25C_T2_d54pgchol_020217 (25 °C)

/export/home/hapi0/mb4c/data/Lihui/DMPCPGChol/30C_T2_2_ 020917 (30 °C)

/export/home/hapi0/mb4c/data/Lihui/DMPCPGChol/37C_T2_2_ 021017 (37 °C)

Figure 5.25

/export/home/hapi0/mb4c/data/Lihui/DMPCPGChol/2umolHFP/21C_T2_020617 (21 °C)

/export/home/hapi0/mb4c/data/Lihui/DMPCPGChol/2umolHFP/25C_T2_020717 (25 °C)

/export/home/hapi0/mb4c/data/Lihui/DMPCPGChol/2umolHFP/30C_T2_020817 (30 °C)

/export/home/hapi0/mb4c/data/Lihui/DMPCPGChol/2umolHFP/d54pgchol_withHFP_122716 (37 °C)

Figure 5.26

/export/home/hapi0/mb4c/data/Lihui/DMPCPGChol/d54_wihHFP_090716

Figure 5.27

Same as figure 5.21

Figure 5.28 and Figure 5.29

/export/home/khafre0/mb4b/data/Lihui/Chold6popcpg_102416 (no HFP)

/export/home/khafre0/mb4b/data/Lihui/Chold6popcpg__withHFP_102716 (with HFP)

Figure 5.30

/export/home/hapi0/mb4c/data/Lihui/Chold6_070516/Chold6_45C_071216 (45 °C)

/export/home/hapi0/mb4c/data/Lihui/Chold6_070516/Chold6_37C_071216 (37 °C)

/export/home/hapi0/mb4c/data/Lihui/Chold6_070516/Chold6_25C_070516 (25 °C)

/export/home/hapi0/mb4c/data/Lihui/Chold6_070516/Chold6_0C_070616 (0 °C)

/export/home/hapi0/mb4c/data/Lihui/Chold6_070516/Chold6_-5C_070816 (-5 °C)

Figure 5.31

/export/home/hapi0/mb4c/data/Lihui/Chold7_m_080216/Chold7_-50C_T2array2_080316 (no HFP)

/export/home/hapi0/mb4c/data/Lihui/Chold7_062716/Chold7_-50C_T2array_071816 (with HFP)

Figure 5.32

/export/home/hapi0/mb4c/data/Lihui/Chold7_m_080216/Chold7_37C_T2_080816 (no HFP)

/export/home/hapi0/mb4c/data/Lihui/ Chold7_062716/Chold7_37C_T2array_072816 (with HFP)

Figure 5.33

/export/home/hapi0/mb4c/data/Lihui/Chold7_m_080216/Chold7_-50C_T2array2_080316 (-50 °C)

/export/home/hapi0/mb4c/data/Lihui/Chold7_m_080216/Chold7_5C_T2_080316 (5 °C)

/export/home/hapi0/mb4c/data/Lihui/Chold7_m_080216/Chold7_25C_T2_080316 (25 °C)

/export/home/hapi0/mb4c/data/Lihui/Chold7_m_080216/Chold7_45C_T2_080916 (45 °C)

Figure 5.34

/export/home/hapi0/mb4c/data/Lihui/Chold7_062716/Chold7_-50C_T2array_071816 (-50 °C)

/export/home/hapi0/mb4c/data/Lihui/Chold7_062716/Chold7_5C_T2array_072216 (5 °C)

/export/home/hapi0/mb4c/data/Lihui/Chold7_062716/Chold7_25C_T2array_072116_1 (25 °C)

/export/home/hapi0/mb4c/data/Lihui/Chold7_062716/Chold7_45C_T2array_072916 (45 °C)

Figure 5.35

Same as figure 5.32

Figure 5.37

/export/home/hapi0/mb4c/data/Lihui/Chold7_m_080216/Chold7_37C_T1_080816

Figure 5.38

/export/home/hapi0/mb4c/data/Lihui/Chold7_062716/Chold7_37C_T1array_072816

Figure 5.39

Same as figure 5.37 and figure 5.38

Figure 5.40

/export/home/hapi0/mb4c/data/Lihui/Chold7_m_080216/Chold7_-50C_T1array_080216 (-50 °C)

/export/home/hapi0/mb4c/data/Lihui/Chold7_m_080216/Chold7_5C_T1_081016 (5 °C)

/export/home/hapi0/mb4c/data/Lihui/Chold7_m_080216/Chold7_25C_T1_080516 (25 °C)

/export/home/hapi0/mb4c/data/Lihui/Chold7_m_080216/Chold7_45C_T1_080916 (45 °C)

Figure 5.41

/export/home/hapi0/mb4c/data/Lihui/Chold7_062716/Chold7_-50C_T1array_071816

/export/home/hapi0/mb4c/data/Lihui/Chold7_062716/Chold7_5C_T1array_072216

/export/home/hapi0/mb4c/data/Lihui/Chold7_062716/Chold7_25C_T1array_072116

/export/home/hapi0/mb4c/data/Lihui/Chold7_062716/Chold7_45C_T1array_072916

APPENDIX C

Data for fitting

Table C1 HFP_G10 and HFP_G16 dephasing $\Delta S/S_0$ in POPC: POPG: Chol_d7/d6, the data is processed with 100Hz Gaussian line broadening and integration width of 3ppm for G10, and 1ppm for G16.

	HFP_G10 in POPC:PG:Chol_d7 (8:2:5)		HFP_G10 in POPC:PG:Chol_d7 (8:2:2.5)		HFP_G10 in POPC:PG:Chol_d6 (8:2:5)		HFP_G16 in POPC:PG:Chol_d6 (8:2:5)		HFP_G16 in POPC:PG:Chol_d7 (8:2:5)	
Dephasing time/ms	ΔS/So	error of ΔS/So	ΔS/So	error of ΔS/So	ΔS/So	error of ΔS/So	ΔS/So	error of ΔS/So	ΔS/So	error of ΔS/So
2	0.0079	0.0168	-0.0047	0.0146	-0.0059	0.0135	0.0311	0.0252	0.0086	0.0169
8	0.1168	0.0087	0.0612	0.0122	0.0412	0.0173	0.1033	0.0269	0.0335	0.0291
16	0.2188	0.0109	0.0921	0.0161	0.0478	0.0123	0.1642	0.0273	0.0424	0.0201
24	0.3007	0.0177	0.1302	0.0133	0.0770	0.0210	0.2010	0.0381	0.1026	0.0267
32	0.3659	0.0269	0.1948	0.0288	0.1148	0.0179	0.3335	0.0178	0.1964	0.0344
40	0.4349	0.0232	0.1980	0.0216	0.0915	0.0320	0.3767	0.0142	0.2267	0.0338
48	0.4931	0.0552	0.2513	0.0266	0.1713	0.0304				

Table C2 HFP_G5 dephasing $\Delta S/S_0$ in DOPC: DOPG: Chol_d7/d6 (8:2:5), the data is processed with 100Hz Gaussian line broadening and 2ppm integration width.

	Chol_d7		Chol_d6	
Dephasing time/ms	ΔS/So	error of ΔS/So	ΔS/So	error of ΔS/So
2	0.0000	0.0170	0.0030	0.0137
8	0.0773	0.0182	0.0155	0.0189
16	0.1271	0.0203	0.0357	0.0121
24	0.2373	0.0297	0.0569	0.0474
32	0.2988	0.0330	0.1047	0.0375
40	0.4630	0.0622	0.2088	0.0558

Table C3 HFPL9R_G5 and G10 dephasing $\Delta S/S_0$ in DPPC: DPPG (4:1), the data is processed with 100Hz Gaussian line broadening and 3ppm integration width.

	HFPL9R_G5 with PC_d10		HFPL9R_G5 with PC_d8		HFPL9R_G5 with PC_d4	
Dephasing time/ms	ΔS/So	error of ΔS/So	ΔS/So	error of ΔS/So	ΔS/So	error of ΔS/So
2	0.0275	0.0075	-0.0041	0.0091	0.0970	0.0117
8	0.1528	0.0183	0.0058	0.0199	0.1628	0.0128
16	0.2804	0.0213	0.1259	0.0260	0.1958	0.0119
24	0.4246	0.0339	0.0485	0.0314	0.2497	0.0232
32	0.5086	0.0392	0.1393	0.0530	0.3566	0.0283
40	0.5901	0.0481	0.0980	0.0769	0.3859	0.0363
48	0.7171	0.1157	0.2282	0.1044	0.4305	0.0727

	HFPL9R_G10 with PC_d10		HFPL9R_G10 with PC_d8		HFPL9R_G10 with PC_d4	
Dephasing time/ms	ΔS/So	error of ΔS/So	ΔS/So	error of ΔS/So	ΔS/So	error of ΔS/So
2	0.0397	0.0127	-0.0056	0.0113	0.1024	0.0098
8	0.2081	0.0135	0.0269	0.0189	0.1156	0.0097
16	0.4095	0.0184	0.0906	0.0223	0.1689	0.0117
24	0.6029	0.0184	0.0852	0.0261	0.2041	0.0126
32	0.7384	0.0112	0.1121	0.0321	0.2249	0.0240
40	0.8231	0.0216	0.1589	0.0251	0.2378	0.0325
48	0.8946	0.0404	0.1826	0.0499	0.3213	0.0514

Table C4 KALP_A5, A7, A17 and A19 dephasing $\Delta S/S_0$ in DPPC: DPPG (4:1), the data is processed with 100Hz Gaussian line broadening and 3ppm integration width.

	A5 with PC_d10		A5 with PC_d8		A5 with PC_d4	
Dephasing time/ms	ΔS/So	error of ΔS/So	ΔS/So	error of ΔS/So	ΔS/So	error of ΔS/So
2	0.0048	0.0099	0.0084	0.0068	0.0265	0.0058
8	0.0388	0.0070	0.0344	0.0064	0.0170	0.0089
16	0.0995	0.0116	0.0694	0.0093	0.0234	0.0115
24	0.1493	0.0094	0.1104	0.0108	0.0559	0.0116
32	0.1871	0.0126	0.1150	0.0138	0.0581	0.0209
40	0.1892	0.0092	0.1619	0.0144	0.0487	0.0131
48	0.2402	0.0136	0.1776	0.0171	0.0224	0.0188

	A7 with PC_d10		A7 with PC_d8		A7 with PC_d4	
Dephasing time/ms	ΔS/So	error of ΔS/So	ΔS/So	error of ΔS/So	ΔS/So	error of ΔS/So
2	-0.0134	0.0058	0.0041	0.0113	0.0067	0.0114
8	0.0570	0.0072	0.0284	0.0083	0.0114	0.0098
16	0.1321	0.0061	0.0576	0.0117	0.0050	0.0086
24	0.1825	0.0073	0.0953	0.0099	0.0367	0.0107
32	0.2106	0.0080	0.1307	0.0106	0.0284	0.0110
40	0.2841	0.0100	0.1348	0.0117	0.0224	0.0158
48	0.3077	0.0149	0.1626	0.0154	0.0397	0.0148

Table C4 (cont'd)

	A17 with PC_d10		A17 with PC_d8		A17 with PC_d4	
Dephasing time/ms	ΔS/So	error of ΔS/So	ΔS/So	error of ΔS/So	ΔS/So	error of ΔS/So
2	-0.0075	0.0154	-0.0018	0.0112	0.0181	0.0103
8	0.0547	0.0119	0.0329	0.0085	0.0171	0.0119
16	0.0990	0.0118	0.0658	0.0084	0.0487	0.0115
24	0.1650	0.0111	0.0681	0.0125	0.0482	0.0095
32	0.1987	0.0130	0.0974	0.0106	0.0414	0.0146
40	0.2207	0.0174	0.1114	0.0136	0.0585	0.0196
48	0.2818	0.0203	0.1453	0.0178	0.0681	0.0131

	A19 with PC_d10		A19 with PC_d8		A19 with PC_d4	
Dephasing time/ms	ΔS/So	error of ΔS/So	ΔS/So	error of ΔS/So	ΔS/So	error of ΔS/So
2	0.0134	0.0121	0.0240	0.0249	0.0137	0.0200
8	0.0408	0.0204	0.0318	0.0179	0.0367	0.0217
16	0.0655	0.0175	0.0333	0.0187	0.0254	0.0248
24	0.0707	0.0270	0.0683	0.0146	0.0852	0.0225
32	0.1366	0.0356	0.0923	0.0244	0.0247	0.0418
40	0.1846	0.0420	0.1790	0.0463	0.0457	0.0293
48	0.2753	0.0380	0.1879	0.0265	0.0463	0.0399

Table C5 DMPC-d54 order parameter (S_{CD}) in d54: DMPG (4:1) and d54: DMPG: CHOL (8:2:5) without and with HFP, and the order parameter percentage change by HFP.

$\Delta S_{CD} = S_{CD}^{Lipid} - S_{CD}^{(Lipid+ HFP)}$.

C position	d54pg	HFP + d54pg (1:25)	+CHOL	+Chol and HFP (1:100)	+ Chol and HFP (1:25)	ΔS_{CD} (d54pg+ HFP (1:25))	ΔS_{CD} (+ Chol and HFP (1:100))	ΔS_{CD} (+ Chol and HFP (1:25))
2	0.219	0.216	0.341	0.332	0.408	0.014	0.028	-0.196
3	0.219	0.216	0.341	0.332	0.408	0.014	0.028	-0.196
4	0.219	0.216	0.341	0.332	0.408	0.014	0.028	-0.196
5	0.219	0.216	0.341	0.332	0.408	0.014	0.028	-0.196
6	0.204	0.198	0.317	0.332	0.408	0.029	-0.046	-0.286
7	0.186	0.175	0.297	0.301	0.368	0.059	-0.014	-0.240
8	0.172	0.161	0.261	0.257	0.326	0.064	0.016	-0.248
9	0.151	0.143	0.252	0.257	0.326	0.053	-0.019	-0.292
10	0.142	0.134	0.22	0.210	0.274	0.056	0.044	-0.247
11	0.129	0.12	0.201	0.195	0.254	0.070	0.028	-0.262
12	0.113	0.105	0.16	0.156	0.202	0.071	0.027	-0.264
13	0.094	0.088	0.127	0.124		0.064	0.021	
14	0.028	0.025	0.047	0.044	0.055	0.107	0.070	-0.160

Table C6 DMPC-d54 T_2 fitting data for echo, CD_3 and CD_2 for both without and with HFP at different temperature. The membrane is d54: DMPG= 4:1 mol ratio.

	21°C					
time/μs	echo intensity	CD3 peak intensity	time/ μs	echo intensity (HFP: PL= 1:25)	CD3 peak intensity (HFP: PL= 1:25)	CD2 peak intensity (HFP: PL= 1:25)
101	63057788	691988.312	101	115802128	2135285.5	1128808.5
181	29523848	406958.406	201	71780360	1612765.875	736819.812
263	16641136	267603.156	303	49382440	1391027	506400.656
341	10358777	179660.125	401	36058856	1245675.875	345419.438
421	7093353	136698.203	501	27391492	1072072.375	252804.359
501	5218229	100800.125	601	21214256	892813.25	169144.359
581	3733626	76095.414	701	17113696	816511.875	127413.523
661	2830889	62065.859	801	13937489	745940.625	94968.844
741	2301231	47807	901	11411520	646773.188	72931.93
821	1702988	34504.895	1001	9378537	542748.812	57735.293
903	1537200	27966.346	1101	7740526	481930.781	39720.156
			1201	6470418	438686.75	30024.465
			1301	5560921	378197.5	22200.453
			1401	4489041	315689.594	
			1501	3629461	272308.406	

Table C6 (cont'd)

	25°C						
time/μs	echo intensity	CD3 peak intensity	CD2 peak intensity	time/ μs	echo intensity (HFP: PL= 1:25)	CD3 peak intensity (HFP: PL= 1:25)	CD2 peak intensity (HFP: PL= 1:25)
123	102638784	2026801.25	1144891	103	105781664	1996271.875	1073387.875
303	89085456	1702830	942213.5	261	57158708	1413117.625	636620.812
483	76725280	1607489.25	776697.438	423	35837136	1199985.375	378250.75
663	64093508	1303193.125	621514.75	583	24722928	1004988.312	234601.484
843	53143176	1185154.5	513685.281	743	17524884	790177.125	150071.406
1023	43038292	1019752.5	408583.469	903	12994199	673512.312	97908.492
1203	34194696	860716.5	340108.438	1063	9936582	565712.375	61229.551
1383	26996276	739432.688	245394.234	1223	7366124	440080.594	41009.828
1563	20587472	599586.812	201877.359	1383	5627005	362828.469	32989.188
1743	15670842	496478.719	142585.859	1543	4321859	301345.438	16505.637
1923	11683965	396061.5	102665.383	1703	3189982	224314.828	39720.156
2103	8540030	337245.562	79838.648	1861	2436088	181833.453	30024.465
2283	6174512	289892.156	56270.645	2023	1753249	148932.031	22200.453
2463	4473311	264372.312		2183	1220028	107132.828	
2643	3339245	251591.453		2343	898252	79102.477	
2823	2453834	245778.141		2503	683723	67685.086	

Table C6 (cont'd)

	30°C						
time/μs	echo intensity	CD3 peak intensity	CD2 peak intensity	time/μs	echo intensity (HFP: PL= 1:25)	CD3 peak intensity (HFP: PL= 1:25)	CD2 peak intensity (HFP: PL= 1:25)
123	97945168	2168760.75	1184524.625	101	98796512	2101625.75	1009767.062
303	85633272	1804549.75	993302.875	261	54628436	1458327	611281.125
483	74481904	1676268.25	820749.25	421	35466788	1185919.5	378962.469
663	62519828	1434212.625	665734.25	581	25012956	1006188.375	245063.312
843	52011936	1200631.75	542333.375	743	18347956	804359.188	164715.953
1023	43123512	1099090.375	456520.156	901	13766222	649429.188	115702.234
1203	34664904	904017.75	342164.969	1061	10600092	551011.062	79574.047
1383	27490000	740479.25	299301.438	1221	8097601	458949.5	57071.07
1563	21481714	639008.625	220743.625	1381	6122391	349215.094	36059.785
1743	16368111	515123.344	158240.828	1541	4697748	286665	26214.693
1923	12453107	429882.125	139159.859	1703	3529706	229169.281	22468.465
2103	9271540	355275.125	97379.008	1863	2652671	176373.281	
2283	6856360	298497.094	78159.414	2023	1982592	134109.656	
2463	4939892	277561.375	62806.781	2181	1433475	106230.781	
2643	3653884			2345	1034288	80250.523	
2823	2611025			2501	620372	63816.102	
3003	1986086			2661	320609	46936.75	

Table C6 (cont'd)

	37°C						
time/μs	echo intensity	CD3 peak intensity	CD2 peak intensity	time/μs	echo intensity (HFP: PL= 1:25)	CD3 peak intensity (HFP: PL= 1:25)	CD2 peak intensity (HFP: PL= 1:25)
83	23420632	614511.688	290392.188	83	23368092	509551.438	265969.75
323	18562896	454312.156	218417.344	303	10879426	321844.75	133845.438
563	15225284	405409.438	169984.75	523	6756645	254588.141	77485
803	11926090	340249.281	131170.984	743	4737914	213737.406	50404.617
1043	9223867	256865.297	100246.281	963	3319797	153440.141	31857.168
1283	7104173	236136.969	76389.078	1183	2391862	115981.594	23216.367
1523	5176301	164442.906	51373.676	1403	1703089	96738.625	15364.001
1763	3844378	130532.312	38250.266	1623	1180113	69017.914	9958.122
2003	2718262	108489.312	27651.395	1843	914771	47562.926	7405.187
2243	1909120	73970.656	26960.746	2063		38422.871	
2483	1256475	67963.414	20812.719	2283		25491.84	
2723	890600	57693.52	12761.95	2503		16364.961	
2963	634516	52292.93	8685.154	2723		14591.285	

Table C7 DMPC-d54 T_2 fitting data for echo, CD_3 and CD_2 for both without and with HFP at different temperature. The membrane is d54: DMPG: CHOL= 8:2:5.

	21°C						
time/ μs	echo intensity	CD3 peak intensity	CD2 peak intensity	time/μs	echo intensity (HFP: PL= 1:25)	CD3 peak intensity (HFP: PL= 1:25)	CD2 peak intensity (HFP: PL= 1:25)
121	6301407	72370.742	41591.008	121	4860291	56084.289	33658.496
283	5166467	65204.785	30029.061	281	2628209	43005.797	18491.996
443	4146610	55714.715	20775.986	441	1563425	33106.707	10292.763
603	3271153	48981.867	14351.056	601	1030302	27663.021	5372.837
763	2519588	42008.625	9594.907	761	718111	23221.93	3298.103
923	1955328	35551.242	6124.931	923	515240	18150.461	1781.744
1083	1526812	31399.668	3877.846	1083	377137	15149.034	
1243	1181775	27149.332		1243	294901	12619.528	
1403	912202	21955.949		1403	201307	10034.387	
1563	685291	18529.879		1563	164014	8021.642	
1723	528695	15252.553		1723	117155	6082.786	
1883	386965	12173.619		1883	77524	4938.036	
2043	297120	9968.1		2043	60258	3905.18	
2203	195505	7988.121		2203	44170	3327.426	
2363	141331	7011.406		2363	42345	2660.875	
2523	87149	6028.201		2523	30900	2019.662	
2683	50449	5629.337		2681	18685	1762.267	

Table C7 (cont'd)

	25°C						
time/μs	echo intensity	CD3 peak intensity	CD2 peak intensity	time/ μs	echo intensity (HFP: PL= 1:25)	CD3 peak intensity (HFP: PL= 1:25)	CD2 peak intensity (HFP: PL= 1:25)
83	6347105	80792.648	44365.863	123	19930866	231827.156	133459.281
243	5532157	73942.883	35725.578	243	12540461	189542.797	84053.414
403	4780424	66615.602	26925.637	363	8251461	153984.156	53628.488
563	4073641	60484.266	19613.178	483	5775383	132002.016	33073.926
723	3370140	52796.312	13957.897	603	4217832	115099.695	21174.137
883	2779965	46467.383	9352.472	723	3192564	97583.891	13608.686
1043	2231754	40227.848	7540.693	843	2539507	87238.836	8325.301
1203	1778664	34618.055	5119.122	963	1964522	74099.109	5900.491
1363	1414178	29852.295	3069.832	1083	1614543	65692.82	3342.039
1523	1084809	24698.77		1203	1270232	54134.52	2740.498
1683	829748	20795.043		1323	1047440	48528.965	1922.136
1843	632355	16854.395		1443	797007	38951.594	
2003	455647	14082.301		1563	676338	34940.828	
2163	327381	11327.173		1683	542335	28156.535	
2323	226087	9006.731		1803	408628	24471.822	

Table C7 (cont'd)

	30°C						
time/μs	echo intensity	CD3 peak intensity	CD2 peak intensity	time/μs	echo intensity (HFP: PL= 1:25)	CD3 peak intensity (HFP: PL= 1:25)	CD2 peak intensity (HFP: PL= 1:25)
123	28706428	364004.906	216588.031	85	100128624	1097857.25	678205.188
303	26174888	342987.312	174189.406	203	69532712	897913.438	427571.5
483	22768650	307423.25	136185.609	323	44843536	751978.562	247767.672
663	19179180	273475.969	100793.07	443	30772500	645994.062	158576.359
843	15775435	237977.25	71622.758	563	22570992	565815.438	94699.414
1023	12660307	204002.781	49457.906	683	16819664	481651.812	62608.941
1203	9940572	180911.469	35640.703	803	13050568	428669.906	41452.617
1383	7662337	146586.031	22334.299	923	10396601	361066.094	28641.406
1563	5786863	121667.305	15393.721	1041	8261454	310768.125	16430.283
1743	4220267	97285.578	9897.642	1163	6420406	269916.812	8570.573
1923	3012119	76122.398		1283	5276130	222875.125	
2103	2140265	62034.441		1403	4230648	183808.906	
2283	1424155	48343.043		1523	3593334	159582.594	
2463	907426	39500.703		1643	2832819	144842.5	
2643	545976	36462.152		1763	2171168	118713.008	
2823	317050	32676.654		1885	1880407	100648.93	

Table C7 (cont'd)

	37°C						
time/μs	echo intensity	CD3 peak intensity	CD2 peak intensity	time/μs	echo intensity (HFP: PL= 1:25)	CD3 peak intensity (HFP: PL= 1:25)	CD2 peak intensity (HFP: PL= 1:25)
123	27683546	413753.312	234696.266	83	13901748	220394.219	123708.883
303	26203104	392187.219	203342.562	203	8110308	161628.469	71819.789
483	23483512	354733.344	166953.391	323	5592441	155021.781	43283.867
663	20314432	323332.188	128196.75	443	3849416	121720.812	29284.15
843	17124336	281276.625	98458.82	563	3013031	112230.75	20009.635
1023	14080315	247663.797	72356.75	683	2273741	91241.977	11001.198
1203	11290925	214235.547	52255.438	803	1839586	75849.367	8655.914
1383	8922532	181751.641	37383.781	923	1452028	68953.648	5539.538
1563	6848299	149601.312	25970.537	1043	1233011	57797.215	
1743	5189815	124471.781	17748.801	1163	964646	52754.32	
1923	3785671	96539.695	10881.546	1283	821070	42714.387	
2103	2695042	78749.055		1403	656531	33184.688	
2283	1791103	59661.094		1523	577684	32935.875	
2461	1191651	51195.496		1643	427749	26385.656	
2641	720066	42218.711		1763	395406	22643.736	
				1883	355069	20892.908	
				2003	288613	18788.369	

Table C8 Chol_d6 T_2 fitting data for echo intensity for both without and with HFP at 37 °C in membrane of DMPC: DMPG: Chol_d6= 8:2:5 and POPC: POPG: Chol_d6= 8:2:5.

	DMPCPGChol_d6		POPCPGChol_d6		
time/μs	Echo intensity	Echo intensity with HFP	time/μs	Echo intensity	Echo intensity with HFP
133	18017108	17682278	63	17700144	58113512
183	15503495	14659419	93	15126436	51097308
233	13510561	11705473	123	13886196	44113644
283	11729365	9425289	153	12606192	38606532
333	10417644	7852361	183	12187828	34709568
383	9214424	6516831	213	11201064	30500508
433	8024377	5504747	243	9895180	27207600
483	6882644	4302516	273	8902792	24344344
533	6071274	3618283	303	8903644	21966172
583	5240645	2983362	333	7972644	19520700
633	4628060	2715867	363	6719492	18031672
683	4085062	2306738	393	6363652	15968128
			423	6591000	14244916
			453	6237668	12931472
			483	5077704	11633468
			513	4801908	10613544
			543	4200040	8870172
			573	4286332	8297860
			603	4244240	6966928
			633	3593688	
			663	2967528	

Table C9 Chol_d7 T_2 fitting data with ln(CD_3 peak intensity) for both without and with HFP at different temperatures. Peak intensity is short as PI.

	-50°C			5°C				25°C			
time/μs	ln(CD3 PI)	time/μs	With HFP	time/μs	ln(CD3 PI)	time/μs	With HFP	time/μs	ln(CD3 PI)	time/μs	With HFP
75	11.290	119	10.899	77	11.959	87	12.631	79	12.016	81	12.680
95	10.989	179	10.714	197	11.852	287	12.443	199	11.886	281	12.549
115	10.695	239	10.379	317	11.739	487	12.254	319	11.788	481	12.381
135	10.538	299	9.986	437	11.654	687	12.052	439	11.659	681	12.224
155	10.371	359	9.692	557	11.584	887	11.815	559	11.572	881	12.033
175	10.135	419	9.355	677	11.500	1087	11.530	679	11.481	1081	11.809
195	10.003	479	8.782	797	11.401	1287	11.277	799	11.345	1281	11.557
215	9.653	539	8.475	917	11.238	1487	11.075	919	11.239	1481	11.289
235	9.509			1037	11.049			1039	11.085	1681	11.067
255	9.409			1157	10.958			1159	10.982	1881	10.903
275	9.059			1277	10.781			1279	10.832	2081	10.799
295	8.770			1397	10.679			1399	10.670		
				1517	10.565			1519	10.582		
				1637	10.532			1639	10.449		
				1757	10.390						
				1877	10.312						

Table C9 (cont'd)

	37°C			45°C			
time/ µs	ln(CD3 PI)	time/ µs	With HFP	time/ µs	ln(CD3 PI)	time/ µs	With HFP
79	12.555	83	12.694	79	12.545	83	12.673
199	12.480	283	12.564	199	12.465	263	12.581
319	12.373	483	12.411	319	12.374	443	12.454
439	12.268	683	12.226	439	12.270	623	12.307
559	12.175	883	12.030	559	12.163	803	12.146
679	12.036	1083	11.803	679	12.039	983	11.982
799	11.920	1283	11.534	799	11.917	1163	11.788
919	11.810	1483	11.250	919	11.801	1343	11.597
1039	11.658	1683	11.060	1039	11.646	1523	11.362
1159	11.514	1883	10.851	1159	11.534	1703	11.183
1279	11.396	2083	10.723	1279	11.373	1883	10.963
1399	11.231			1399	11.186	2063	10.797
1519	11.088			1519	11.058		
1639	10.948			1639	10.844		

Table C10 Chol_d7 T_1 fitting data (CD_3 peak intensity) at different temperatures for both membranes without and with HFP. Peak intensity is short as PI.

	-50°C		5°C			
tau/ms	CD3 PI (300ppm integration)	With HFP (300ppm integration)	tau/ms	CD3 PI	tau/ms	With HFP
1	-1512.9	-3312.4	0.1	-434881.6	0.5	-945151.7
21	1116.0	3315.2	20.1	-169887.3	20.5	-369262.8
41	1888.2	5154.4	40.1	22743.7	40.5	46525.4
61	2184.2	5646.2	60.1	156616.8	60.5	345054.3
81	2307.9	5827.7	80.1	253943.0	80.5	560756.6
101	2340.9	5864.5	100.1	327334.4	100.5	718595.9
121	2347.8	5925.1	120.1	381858.5	120.5	817169.9
141	2329.7	5921.9	140.1	419204.4	140.5	913808.7
161	2358.0	5892.5	160.1	445182.2	160.5	960305.4
181	2337.8	5913.6	180.1	468484.2	180.5	1012877.5
201	2416.7	5892.3	200.1	484320.9	200.5	1039870.8
221	2480.8	5884.3	220.1	491316.6	220.5	1064254.9
241	2481.0	5924.8	240.1	500078.8	240.5	1072906.4
261	2434.8	5984.2	260.1	504772.7	260.5	1096844.9
281	2322.9	5917.3	280.1	509381.3	280.5	1111076.1
301	2311.4	5836.3	300.1	517757.5	300.5	1112866.4

Table C10 (cont'd)

25 ℃			
tau/ms	CD3 PI	tau/ms	With HFP
0.1	-442409.8	1	-893296.7
20.1	-255557.3	21	-507085.4
40.1	-109295.0	41	-219779.4
60.1	14820.2	61	19034.4
80.1	107549.8	81	204182.4
100.1	185117.4	101	354759.8
120.1	254591.7	121	481844.9
140.1	302620.8	141	583910.9
160.1	343963.7	161	664930.5
180.1	381466.1	181	732717.7
200.1	412364.4	201	786209.6
220.1	434873.4	221	832482.4
240.1	455804.0	241	869810.3
260.1	466611.2	261	899894.5
280.1	480669.6	281	921989.6
300.1	495197.5	301	943300.2

Table C10 (cont'd)

	37°C			45°C			
time/μs	ln(CD3 PI)	time/μs	With HFP	time/μs	ln(CD3 PI)	time/μs	With HFP
0.1	-932827.8	0.5	-921270.1	0.1	-932013.2	1	-1075404.5
30.1	-492471.4	20.5	-681174.2	30.1	-546767.1	31	-590307.9
60.1	-167003.8	40.5	-394185.3	60.1	-255563.2	61	-247503.8
90.1	90662.7	60.5	-150763.0	90.1	-23192.2	91	27236.7
120.1	289546.3	80.5	57369.1	120.1	174972.9	121	245609.6
150.1	450398.2	100.5	229344.6	150.1	334353.8	151	425383.2
180.1	570572.6	120.5	379687.8	180.1	458165.5	181	566971.8
210.1	665113.3	140.5	502600.3	210.1	564324.1	211	684175.6
240.1	742972.4	160.5	608695.4	240.1	646277.6	241	779078.9
270.1	802038.3	180.5	699460.5	270.1	715041.6	271	856705.8
300.1	848178.4	200.5	775730.8	300.1	771683.9	301	919107.6
330.1	887415.9	220.5	840829.8	330.1	818654.8	331	967508.3
360.1	916573.1	240.5	895715.1	360.1	854716.3	361	1013582.9
390.1	939465.1	260.5	942620.4	390.1	884128.0	391	1041437.9
420.1	959147.1	280.5	984891.4	420.1	907751.1	421	1069570.9
450.1	971403.8	300.5	1014429.5	450.1	926919.6	451	1091981.4
480.1	981659.6	320.5	1044093.1	480.1	946317.3	481	1108735.9
510.1	994294.1	340.5	1069516.8			511	1126726.9

REFERENCES

REFERENCES

1. Freed, E.O., et al., *A MUTATION IN THE HUMAN-IMMUNODEFICIENCY-VIRUS TYPE-1 TRANSMEMBRANE GLYCOPROTEIN-GP41 DOMINANTLY INTERFERES WITH FUSION AND INFECTIVITY*. Proceedings of the National Academy of Sciences of the United States of America, 1992. **89**(1): p. 70-74.

2. Banerjee, K. and D.P. Weliky, *Folded Monomers and Hexamers of the Ectodomain of the HIV gp41 Membrane Fusion Protein: Potential Roles in Fusion and Synergy Between the Fusion Peptide, Hairpin, and Membrane-Proximal External Region.* Biochemistry, 2014. **53**(46): p. 7184-7198.

3. Sackett, K., et al., *Hairpin Folding of HIV gp41 Abrogates Lipid Mixing Function at Physiologic pH and Inhibits Lipid Mixing by Exposed gp41 Constructs.* Biochemistry, 2009. **48**(12): p. 2714-2722.

4. Tan, K.M., et al., *Atomic structure of a thermostable subdomain of HIV-1 gp41*. Proceedings of the National Academy of Sciences of the United States of America, 1997. **94**(23): p. 12303-12308.

5. Yang, Z.N., et al., *The crystal structure of the SIV gp41 ectodomain at 1.47 angstrom resolution.* Journal of Structural Biology, 1999. **126**(2): p. 131-144.

6. Ratnayake, P.U., et al., *Full-length trimeric influenza virus hemagglutinin II membrane fusion protein and shorter constructs lacking the fusion peptide or transmembrane domain: Hyperthermostability of the full-length protein and the soluble ectodomain and fusion peptide make significant contributions to fusion of membrane vesicles.* Protein Expression and Purification, 2016. **117**: p. 6-16.

7. Greenfield, N., *CITATION CLASSIC - COMPUTED CIRCULAR-DICHROISM SPECTRA FOR THE EVALUATION OF PROTEIN CONFORMATION*. Current Contents/Life Sciences, 1982(26): p. 28-28.

8. Gabrys, C.M., et al., *Solid-State Nuclear Magnetic Resonance Measurements of HIV Fusion Peptide (CO)-C-13 to Lipid P-31 Proximities Support Similar Partially Inserted Membrane Locations of the alpha Helical and beta Sheet Peptide Structures.* Journal of Physical Chemistry A, 2013. **117**(39): p. 9848-9859.